Following the collapse and evolution of cosmological structures in simulations

Michael Bühlmann

UNIVERSITÉ CÔTE D'AZUR

ÉCOLE DOCTORALE
SCIENCES FONDAMENTALES ET APPLIQUÉES

Suivre la formation et l'évolution des structures cosmologiques à l'aide de simulations numériques

Michael Bühlmann

Laboratoire J.-L. Lagrange – Observatoire de la Côte d'Azur

Présentée en vue de l'obtention du grade de docteur en science de la planète et de l'Univers **de l'**Université Côte d'Azur

Dirigée par: Oliver Hahn

Soutenue le: 11 octobre 2019

Devant le jury, composé de:

Raúl Angulo, Professeur, DIPC
Chiara Ferrari, Astronome, OCA
Oliver Hahn, Professeur, UCA
Adrian Jenkins, Professeur, Durham University
Karl-Joakim Rosdahl, Chargé de recherche, CRAL
Romain Teyssier, Professeur, Universität Zürich

European Research Council
Established by the European Commission

Suivre la formation et l'évolution des structures cosmologiques à l'aide de simulations numériques

Jury:

Présidente du jury:
Chiarra Ferrari, Astronome, Laboratoire Lagrange, OCA

Rapporteurs:
Adrian Jenkins, Professeur, Durham University
Romain Teyssier, Professeur, Universität Zürich

Examinateurs:
Raúl Angulo, Professeur, Donostia International Physics Center
Oliver Hahn, Professeur, Laboratoire Lagrange, UCA
Karl-Joakim Rosdahl, Chargé de recherche, CRAL

Résumé / Abstract

Suivre la formation et l'évolution des structures cosmologiques à l'aide de simulations numériques

Les grands relevés observationnels des dernières décennies ont conduit à imposer le modèle ΛCDM comme le modèle cosmologique privilégié pour décrire l'Univers. Dans ce modèle, la matière noire représente la principale composante de la matière de l'Univers, et sa nature inconnue représente l'un des plus grands mystères de la physique contemporaine. La modélisation dynamique de la matière noire par le biais de simulations numérique constitue désormais un outil indispensable pour contraindre ses propriétés et ses origines physiques.

Dans cette thèse, nous étudions différents aspects de l'effondrement gravitationnel des perturbations dans le champ de densité initial, qui mène à une toile cosmique complexe composée de murs, filaments et halos, dans lequel les baryons se condensent et forment les riches structures que nous pouvons observer aujourd'hui. En particulier, nous utilisons des simulations cosmologiques à N-corps et employons une application Lagrangienne depuis les conditions initiales jusqu'aux positions et vitesses finales pour suivre l'évolution du fluide de matière noire.

Dans un premier temps, nous utilisons les propriétés de l'espace des phases de la matière noire pour étudier l'émergence du champ de tenseur de dispersion des vitesses aux grandes échelles. Il transporte les signatures des anisotropies de l'effondrement gravitationnel, ce qui nous permet de déduire une nouvelle méthode de classification de la toile cosmique et de caractériser le champ de vitesse de la matière noire dans ces environment effondrés. Nous montrons ensuite que l'amplitude de la dispersion de vitesse de la matière noire est en bon accord avec les vitesses aléatoires isotropes dans le gaz de baryons chauffé par chocs et traçant la distribution de matière noire. Ceci permettra d'améliorer les prédictions des températures du milieu intergalactique à partir des simulations à N-corps dans des études futures.

Dans un second temps, nous nous concentrons sur l'effondrement de halos gravitationnellement liés et leur origine dans le champ de perturbation initial. Ces « patchs » de proto-halos jouent une rôle important pour des simulations « zoom », c'est-à-dire des simulations qui concentrent les ressources de calculs sur un objet spécifique et requièrent ainsi une connaissance précise du « patch » Lagrangien depuis lequel cet objet se forme. Dans ce cadre nous avons développé une application Web qui permet aux utilisateurs de sélectioner des objets cibles en vue d'être resimulés dans des catalogues de halos extraits de diverses simulations récentes, de récupérer les conditions initiales compatibles à différents codes de simulations raffinées sur leurs proto-halos associé, et de référencer ces conditions initiales dans les publications scientifiques.

Enfin, nous utilisons les jeux de données disponibles de halos et proto-halos associés pour étudier la connexion entre les perturbations initiales, les propriétés intrinsèques des objets effondrés et l'influence de l'environnement à grande échelle.

Mots clés : cosmologie, formation des structures à grande échelle, matière noire, simulations numérique

Following the Collapse and Evolution of Cosmological Structures in Simulations

Observational efforts during the last decades have led to the establishment of the ΛCDM model as the standard model of our Universe. In this model, dark matter represents the majority of the matter content of the Universe, whose unknown nature poses one of the largest mysteries in physics today. A key ingredient for constraining its properties and physical origin from astronomical observations is the modeling of dark matter in cosmological simulations to understand the formation of structures and create accurate predictions.

In this thesis, we study various aspects of the gravitational collapse of perturbations in the initial density field, which leads to an intricate web composed of walls, filaments, and halos, in which baryons condense and form the rich structures that we can observe today. In particular, we use cosmological N-body simulations and exploit the Lagrangian mapping from coordinates in the initial conditions to the late time positions and velocities to follow the evolution of the dark matter fluid.

In a first part, we use the phase-space properties of dark matter to study the emergence of the large-scale velocity dispersion tensor field. It carries the anisotropic signature of gravitational collapse, allowing us to derive a new classification method of the cosmic web and characterize the velocity field of dark matter in these collapsed environments. We then show that the amplitude of the dark matter velocity dispersion is in good agreement with the isotropic random velocities in the shock-heated baryonic gas tracing the dark matter distribution. This will allow improved predictions of temperatures of the intergalactic medium from N-body simulations in future studies.

In a second part, we focus on the collapse of gravitationally bound halos and their origin in the initial perturbation field. These proto-halo patches play an important role for zoom simulations, i.e. simulations that focus computational resources on an individual object of interest and thus require accurate knowledge about the Lagrangian patch from where the object forms. In this regard, we develop a web application, which allows users to find target objects for re-simulation in various halo catalogs of existing state-of-the-art simulations, to retrieve initial conditions for different simulation codes refined on their associated proto-halo, and to reference the initial conditions in scientific publications.

Finally, we exploit the available dataset of halos and associated proto-halos to study the connection between the initial perturbations, intrinsic properties of the collapsed objects, and the influence of the large scale environment.

Keywords: cosmology, structure formation, dark matter, numerical simulations

Contents

Introduction

During the last hundred years, our understanding of the Universe has fundamentally changed. While at the beginning of the last century, scientists argued whether the spiral nebulae were part of our galaxy or if they were distant "island universes", it became undeniably clear that these galaxies were indeed extragalactic systems after Edwin Hubble inferred the distance to the Andromeda nebula using the period-luminosity relation of Cepheid variable stars in 1924 [164]. Only five years later, Hubble made his second fundamental contribution to cosmology by showing that the galaxies are receding from us with a velocity proportional to their distance [163]. This distance – velocity relation is now known as Hubble's law and implies (assuming statistical isotropy and homogeneity of space) that the Universe is expanding.

With the publication of the General Theory of Relativity by Albert Einstein [94] in 1915/1916, a self-consistent model of the Universe was available, connecting the content of the Universe to its geometry via the Einstein field equations. Solutions of these equations for the homogeneous Universe were found a couple years later by Aleksander Friedman [109, 110] and are now known as Friedman world models, which describe the geometry and expansion of the Universe as a function of its energy content.

The expansion of the Universe implied that at very early times, the Universe must have been very dense and hot, such that radiation and (baryonic) matter were tightly coupled via Compton scattering. As the Universe expanded and the photon-baryon fluid would cool, the ionized hydrogen would be able to recombine, and the scattering would eventually become inefficient, allowing photons to free-stream through the Universe. This diffuse background radiation, the cosmic microwave background (CMB), was predicted by Alpher & Herman in 1948 [6], who estimated a black body radiation with a temperature of about 5 K, and detected in 1965 by Penzias & Wilson [248], confirming the thermal history of the Universe. Subsequent observations of the CMB showed that the radiation is uniform over the sky to an accuracy of 10^{-5} and its spectrum follows the Planck spectrum with a remarkable precision, with a black-body temperature of ~ 2.7 K [294].

Another key evidence for the "Big Bang" model of the Universe was the prediction by Hoyle & Tayler in 1964 [162] of chemical abundances of helium and other light isotopes created during the primordial nucleosynthesis, matching the measured abundances accurately. The calculations also showed that there is an upper limit to the mean baryon density, above which less than the observed abundances of ^{2}H and ^{3}He would be generated. This constrained the baryonic matter content of the Universe to $\lesssim 1/10$ of the critical density required for a Universe with a flat geometry.

To model the vast amount of observable structures in our Universe, physicists studied the gravitational collapse of perturbations in the homogeneous background. It was soon found that in an expanding Universe, the growth of such perturbations is only algebraic [201]. Together with the nucleosynthesis constraints on the amount of baryonic matter, the fact that before recombination,

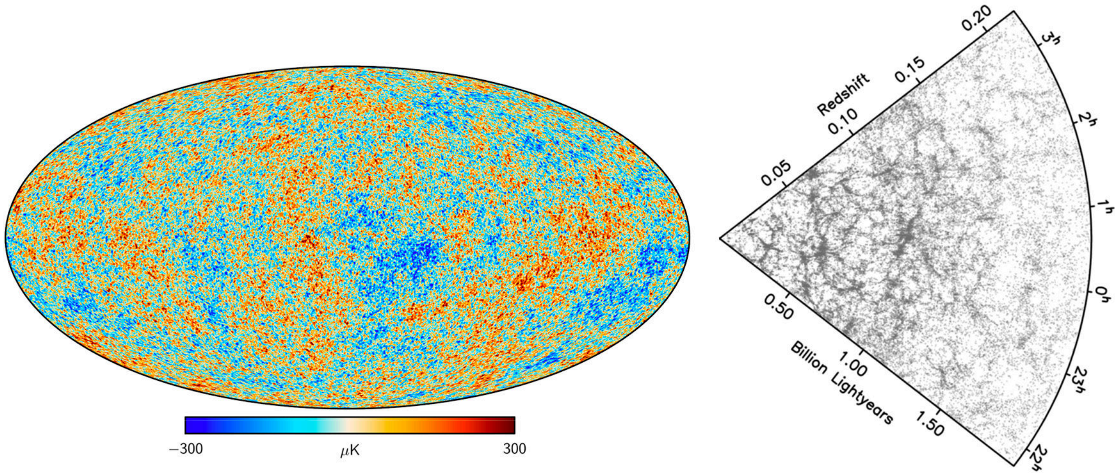

Planck 2018 CMB temperature anisotropy map   2dF Galaxy Redshift Survey

Figure 1: **Left:** full sky map of the anisotropies in the cosmic microwave background temperature, observed with the Planck satellite (image courtesy of ESA and the Planck Collaboration [2]). **Right:** galaxy distribution in the nearby universe from one slice of the 2dF Galaxy Redshift Survey, with clearly visible filamentary structures of the cosmic web (image courtesy of the 2dFGRS team [68]).

pressure support in the photon-baryon fluid would inhibit the growth of baryonic perturbations, and with upper limits on the amplitude of said perturbations at the time of recombination from the non-detection of temperature fluctuations in the CMB, this posed a severe problem to explain the structure in today's Universe.

A solution to these problems was proposed in the form of non-baryonic dark matter which would only interact gravitationally with the baryonic universe. Fluctuations in the dark matter distribution would be able to grow during the radiation dominated era and provide potential wells, into which the baryonic matter would fall into after recombination, lowering the expected temperature fluctuations in the CMB. With the prediction of non-zero rest masses, neutrinos became a natural dark matter candidate. Because of their relativistic nature, free-streaming would, however, erase fluctuations below the scale of the most massive clusters, implying a "top-down" structure formation, where the most massive objects would form first, with smaller objects fragmenting in a later step [89].

An alternative dark matter category originated from extensions to the standard model in particle physics, predicting particles that would decouple from the thermal background after they had become non-relativistic in the early Universe. These kind of dark matter candidates were thus grouped in the *Cold Dark Matter* (CDM) picture, in which structure would form "bottom-up", opposed to the *Hot Dark Matter* (HDM) "top-down" picture of neutrinos. After the discovery of angular fluctuations in the CMB by the COBE satellite in 1992 [294], CDM became the preferred model, since the amplitude of the temperature fluctuations would be too low for structures to form in the HDM picture.

The discovery of the characteristic luminosity profile of Type 1a supernovae [265] and their subsequent use as *standard candles* to estimate cosmological distances allowed to measure Hubble's law with higher accuracy and ultimately lead to the detection of the accelerated expansion of space in 1998 [272, 249]. The acceleration can be attributed to the cosmological constant Λ in Einstein's field equation and is also known as *dark energy*, representing 70% of the Universe's energy content today.

The accelerated expansion of the Universe was later confirmed with measurements of the acoustic peaks in the CMB by the Wilkinson Microwave Anisotropy Probe (WMAP) [32] and measurements of the clustering statistics of the galaxy distribution from redshift surveys such as the 2dF Galaxy Redshift Survey [68], shown in fig. 1. The agreement between the results by these entirely independent cosmological probes has lead to the establishment of the ΛCDM model as the standard model of our Universe. Continuously improved measurements (for example the high precision measurements of the CMB anisotropy measured by the Planck satellite [2], shown in fig. 1) and new galaxy survey catalogs allow us to measure the model parameters with high accuracy, which is why some people are calling this the *era of precision cosmology*.

Despite the success of the ΛCDM model, the picture of our Universe is still incomplete. On the one hand, the model requires a process setting up the initial state of the Universe in a way that creates the cosmos as we can observe it today. It is now generally believed that the Universe underwent an initial inflationary phase [129, 202], in which space expanded exponentially and scaled tiny quantum fluctuations to cosmic scales, the seeds from which galaxies can form. This model also naturally creates a flat spatial geometry and would allow regions of space separated by enormous distances to have been in causal contact before, explaining the homogeneity that we can observe for example in the CMB. On the other hand, the physical nature of dark matter and dark energy, accounting for ~95% of the content of our Universe today, are unknown and form some of the largest mysteries in physics today.

Numerical simulations of structure formation played a crucial role in forming our understanding of the Universe, by allowing to connect the initial perturbations, analytically predicted by theory and measured for example in the CMB, to the collapsed structures in the late time Universe that we observe today. With increasingly larger and more accurate galaxy redshift surveys available in the future, also the need for more accurate modeling rises in order to estimate covariances, study systematics, and test data pipelines. Both larger and more detailed simulations play an important role in creating accurate mock observations. Furthermore, numerical simulations allow us to study the mechanics behind the formation of structures, develop a deeper understanding of the non-linear processes, and create more precise analytical models.

Since dark matter only interacts gravitationally, it is relatively easy and computationally affordable to model structure formation using collisionless N-body simulations. Collapsed structures in the dark matter distribution, the dark matter halos, are the regions where the baryonic gas can cool and condense to form galaxies. Understanding galaxy formation thus requires a precise understanding of the formation, evolution, and structure of the underlying dark matter distribution.

Simulating the physics of the baryonic matter component is in contrast very complex and computationally much more expensive. With the increase of computational power over the last decades, it has become feasible to run such simulations on large scales and to model the formation of galaxies and galaxy clusters with increasingly higher levels of detail and under the addition of additional baryonic processes. However, computational resources still limit the size and dynamic range of such simulations. In this regard, two techniques that we will encounter in this thesis have been developed: first, the dynamic range of simulations can be increased by focusing the computational resources on an object of interest to resolve it with maximum resolution, while still capturing the environmental effects in lower resolution. Such simulations are called zoom simulations and play an important role for example in detailed studies of galaxy formation. A second technique, used to calibrate surveys that require a large number of mock observations, is the prediction of observables from dark matter only simulations. Such techniques include for example the creation of galaxy catalogs from dark matter halo catalogs or the prediction of absorption spectra of distant quasars from the dark matter density. This requires a precise understanding of the connection between the dark matter and the baryonic properties (e.g. densities and temperatures) and will present an ideal application field for machine learning techniques in the future.

Outline of this thesis

In this thesis, we mainly use numerical N-body simulations to study the formation and evolution of structures in our Universe, with a focus on the Lagrangian mapping from the initial conditions to the formed structures, which allows us to follow the evolution of the dark matter fluid during the gravitational collapse.

In a first project, we apply this knowledge to reconstruct the continuous dark matter phase-space distribution in simulations, allowing us to accurately measure and study the velocity distribution function in different environments of the cosmic web. We then apply the measurements of the velocity field to introduce a new classification scheme for the cosmic web and, by comparing dark matter and baryons in a two component simulation, we show how this measurement may help in the future to better predict temperatures in the intergalactic medium.

In a second part, we shift our focus from the large-scale structure to individual gravitationally bound objects, the dark matter halos, and their roots in the initial perturbation field, the proto-halos. These proto-halos play a crucial role in setting up zoom simulations, defining the region with needs to be sampled in higher resolution. The lack of access to such proto-halos from halo catalogs of existing state-of-the-art simulations, and the absence of an easy way of referencing simulations in publications that would allow the community to reproduce, verify, and improve scientific results, motivated the development of an online platform, allowing users to find targets to re-simulate, to create initial conditions focused on these objects, and cite the simulation in scientific articles.

In addition, the connection between proto-halo patches and the final objects encodes the formation histories of the halos under the influence of the large scale environment. Measuring the correlation between the initial patch, the final halo, and the environment thus provides valuable information of the formation process. Furthermore, the ability to accurately predict halo formation from the initial density field is an important ingredient for the fast generation of mock catalogs. To improve such methods, studying the connection between the proto-halo patch and the final halo is crucial.

This thesis is structured as follows: In chapter 1 and chapter 2, we start with a review of the theory of structure formation and the numerical methods used in this work, where we highlight connections to techniques and questions addressed in later chapters.

In chapter 3, we measure the velocity dispersion tensor field that emerges in the dark matter phase-space distribution during gravitational collapse. The anisotropic nature of gravitational collapse is reflected in the anisotropy of the velocity dispersion tensor, leading to a natural classification method of the cosmic web. We provide detailed measurements of the different environments, the orientation and alignment of the velocity dispersion field, and we present a comparison of the dark matter velocity dispersion with the average particle velocity in the baryonic gas, reflected in its local temperature.

In chapter 4, we present the COSMICWEB project, a web platform providing access to initial conditions for zoom simulations from various halo catalogs of existing state-of-the-art simulations. We give a detailed overview of the functionality, the available data, and the architecture of the application, and we walk through the most important components of the platform.

In chapter 5, we analyze the large datasets of halos, their properties, and their proto-halos from the COSMICWEB project to study the connection between the initial perturbations and the final objects. Specifically, we measure the shapes and orientations of the initial regions that later collapse to halos and study the connection to the intrinsic properties of the halo and correlations with their environment. We also measure the mass and environment dependence of the "goodness of fit" of the minimum bounding ellipsoids used to describe the proto-halo patches in COSMICWEB, an important factor determining the computational efficiency of the zoom simulation.

We summarize the main results in chapter 6, including an outlook on future goals and projects.

CHAPTER 1

Cosmological Structure Formation

The development of the theory of General Relativity (GR) by Albert Einstein in 1915 enabled the construction of a comprehensive theory of our Universe during the last century. Observations of the Large Scale Structure (LSS) and the Cosmological Microwave Background (CMB) during the last decades led to the establishment of the ΛCDM model, which has been successfully applied to a large range of phenomena, and has become the standard model in modern cosmology.

The ΛCDM model is based on the assumption that there is no special point or direction in the Universe. This so-called *Cosmological* or *Copernican Principle* manifests itself in a number of observations, such as number-counts of galaxies and the regularity of the CMB with deviations only of the order of 10^{-5}. It is these tiny primordial perturbations on top of the homogeneous background that gravitationally collapse and form the rich structures of the Universe that we see today.

This chapter will give a brief summary of the evolution of the homogeneous universe (1.1), the generation and linear growth of perturbations (section 1.2), quantification of inhomogeneities using correlation functions and power spectra (section 1.3), and models for the non-linear collapse (section 1.4) leading to the formation of dark matter halos (section 1.5). The discussion follows the references [57, 81, 221, 185], with additional references given if needed. We use units in which $c = 1$, and Fourier transformations, unless explicitly defined differently, follow the normalization convention

$$f(x) = \frac{1}{(2\pi)^3} \int \mathrm{d}^3\boldsymbol{k}\; e^{i\boldsymbol{k}\boldsymbol{x}} f(\boldsymbol{k}). \tag{1.1}$$

1.1 The Homogeneous and Isotropic Universe

The FLRW metric

In more mathematical terms, the Cosmological principle means that on large enough scales, the universe appears homogeneous and isotropic, with perturbations around the homogeneous background being small. The discovery of the redshift of galaxies indicating a recession velocity proportional to their distance by Georges Lemaître in 1927 [195] and Edwin Hubble in 1929 [163] implied that the Universe is not static in time but expanding. Hence, the homogeneity only applies to space but not to time.

The most general metric capturing this spatial homogeneity and isotropy (a so-called maximally symmetric three-metric) is the Friedman-Lemaître-Robertson-Walker (FLRW) metric, which in spherical coordinates can be written as

$$\mathrm{d}s^2 = g_{\mu\nu}\mathrm{d}x^\mu \mathrm{d}x^\nu = -\mathrm{d}t^2 + a(t)^2 \left(\mathrm{d}\chi^2 + S_k(\chi)^2 \mathrm{d}\Omega^2\right), \tag{1.2}$$

where $a(t)$ is the scale factor measuring the expansion of the universe, χ is the comoving distance, $\mathrm{d}\Omega^2$ the angular separation, and $k \in \{-1, 0, 1\}$ denotes an an open (negatively curved), flat and closed (positively curved) universe respectively. The function $S_k(\chi)$ depends on the curvature and is defined as

$$S_k(\chi) = \begin{cases} \sinh(\chi) & k = -1 \\ \chi & k = 0 \\ \sin(\chi) & k = +1 \end{cases} \tag{1.3}$$

The scale factor $a(t)$ connects comoving units which remain constant over time and physical units which expand with the Universe by $\mathrm{d}x = a(t)\mathrm{d}\chi$. Choosing $a(t_{\mathrm{now}}) = 1$, comoving units correspond to physical units at the present.

Photons travel on null-geodesics ($\mathrm{d}s^2 = 0$). Hence, the comoving distance that a photon travels from its origin to us is related to the emission time t_{emit} by

$$\chi = \int_{t_{\mathrm{emit}}}^{t_{\mathrm{obs}}} \frac{\mathrm{d}t}{a(t)}. \tag{1.4}$$

The largest separation in the Universe that is causally connected is the longest distance a photon could have traveled since the beginning of the Universe. This distance is known as the *particle horizon*

$$\chi_H(t) = \int_0^t \frac{\mathrm{d}t'}{a(t')}. \tag{1.5}$$

Defining the comoving time through

$$\mathrm{d}\eta = \frac{\mathrm{d}t}{a(t)}, \tag{1.6}$$

we find that for units in which $c = 1$, the conformal time corresponds to the particle horizon. The evolution of $\chi_H = \eta$ in the past Universe is illustrated in fig. 1.1

A direct consequence of the FLRW metric is the *reddening* of electromagnetic and gravitational waves as they propagate: emitted at time t_{emit} and wavelength λ_{emit}, it will be observed at time t_{obs} with wavelength $\lambda_{\mathrm{obs}} = \lambda_{\mathrm{emit}} a(t_{\mathrm{obs}})/a(t_{\mathrm{emit}})$. If the universe is expanding and thus $a(t_{\mathrm{obs}}) > a(t_{\mathrm{emit}})$, the observed wavelength will be longer than at emission and hence remote galaxies appear redder than close-by ones. The redshift parameter is defined as

$$1 + z = \frac{\lambda_{\mathrm{obs}}}{\lambda_{\mathrm{emit}}} = \frac{1}{a}, \tag{1.7}$$

where $a(t_{\mathrm{emit}}) = a$ and we assumed that $a(t_{\mathrm{obs}}) = a(t_{\mathrm{now}}) = 1$. We can rewrite eq. (1.4) in terms of z and obtain

$$\chi = \int_0^{z_{\mathrm{emit}}} \frac{\mathrm{d}z}{H(z)}, \tag{1.8}$$

where we assumed that $z_{\rm obs} = 0$ and introduced the Hubble parameter H defined as

$$H = \frac{\dot{a}}{a}. \tag{1.9}$$

For close-by objects, $H \simeq H_0$ is constant and equal to the current expansion rate of the Universe, and thus we find the famous Hubble-Lemaître law [195, 163] (often referred to as Hubble's law)

$$z \approx H_0 \chi, \tag{1.10}$$

stating a linear relationship between the measured redshift of a galaxy and its distance to us (under the assumption of no peculiar velocities, i.e. $\dot{\chi} = 0$ for both the observed galaxy and us).

The Einstein Equations

According to GR, it is the geometry of space-time that determines the trajectories of its content, and the content that in turn determines the geometry of the space-time. The Einstein field equations (EFE) relate the stress-energy tensor $T_{\mu\nu}$, a measure of the energy and momentum density in the Universe, to the Einstein tensor $G_{\mu\nu}$, a measure of the curvature, by

$$G_{\mu\nu} + \Lambda g_{\mu\nu} = 8\pi G T_{\mu\nu}, \tag{1.11}$$

where G is the gravitational and Λ the cosmological constant.

Following the Cosmological Principle, we require that the content of the Universe is homogeneous and isotropic in its rest frame (which is the comoving frame in which also the metric is homogeneous and isotropic). This is called a perfect fluid for which the energy momentum tensor can be written as

$$T_{\mu\nu} = (p + \rho) U_\mu U_\nu + p g_{\mu\nu}, \tag{1.12}$$

where U^μ is the four-velocity of the fluid, ρ is the energy density and p the pressure measured in the rest frame. The pressure is connected to the energy density via the equation of state (EOS) which in its simplest form is a linear relationship of the form

$$p = w\rho. \tag{1.13}$$

The three most relevant perfect fluids in cosmology are the so-called *dust*, *radiation*, and *dark energy*. Dust refers to cold (non-relativistic) and collisionless matter, thus $w_m = 0$. Examples are the cold dark matter (CDM), but also non-relativistic baryonic matter, stars and galaxies for which the pressure is negligible compared to the energy density. Radiation refers to relativistic content, such as electromagnetic radiation or neutrinos, moving close to the speed of light, and has $w_r = 1/3$[1]. In eq. (1.11), we can also include $\Lambda g_{\mu\nu}$ in the energy stress tensor by requiring $p = -(8\pi G)^{-1}\Lambda$ and $p + \rho = 0$ and thus $w_\Lambda = -1$. The cosmological term can thus be interpreted as dark energy (DE), the energy density of the vacuum.

[1] The equation of state for radiation can be obtained from the electro-magnetic stress tensor in the theory of special relativity valid in a local free-falling frame, see e.g. [81].

The conservation of energy-momentum ${T^{\mu\nu}}_{;\nu} = 0$ implies that

$$\rho \propto a^{-3(1+w)}, \tag{1.14}$$

and thus we have $\rho_m \propto a^{-3}$ for dust, $\rho_r \propto a^{-4}$ for radiation, and $\rho_\Lambda = \text{const}$ for dark energy. The additional factor of a for radiation with respect to dust can be understood from the loss of internal energy (frequency) as the universe expands (cf. redshift). For a universe composed of these three components, radiation will thus dominate if a is small, and dark energy will dominated for large a.

The Friedman equations

We now require the FLRW metric to be a solution of the EFE, which will allow us to compute $a(t)$ as a function of the content of the Universe. Calculating the curvature from the metric and using the perfect fluid representation of the energy momentum tensor, we obtain two equations (one from the time coordinate and one from the isotropic space coordinates). These are the Friedman equations (FE, [109, 110]) and can be written as

$$\left(\frac{\dot{a}}{a}\right)^2 = \frac{8\pi G}{3}\rho - \frac{k}{a^2} \tag{1.15}$$

$$-3\frac{\ddot{a}}{a} = 4\pi G(\rho + 3p), \tag{1.16}$$

where $\dot{\circ}$ denotes the derivative wrt. cosmic time, and where we have absorbed Λ in ρ as dark energy.

Using the Hubble parameter H defined in eq. (1.9) and introducing the critical density

$$\rho_c = \frac{3H^2}{8\pi G}, \tag{1.17}$$

we can rewrite eq. (1.15) in terms of the density parameter $\Omega = \frac{\rho}{\rho_c}$ as

$$\Omega - 1 = \frac{k}{H^2 a^2}. \tag{1.18}$$

The critical density ρ_c is the threshold density between an open ($\rho < \rho_c$), flat ($\rho = \rho_c$), and closed ($\rho > \rho_c$) universe. We can rewrite the curvature term as $\Omega_k = k(Ha)^{-2} = \Omega - 1$ and split the total density parameter $\Omega = \Omega_m + \Omega_r + \Omega_\Lambda$ to obtain the parametrized FE for a universe composed of dust, radiation and dark energy:

$$H^2 = H_0^2 \left(\frac{\Omega_{0,r}}{a^4} + \frac{\Omega_{0,m}}{a^3} + \frac{\Omega_{0,k}}{a^2} + \Omega_{0,\Lambda} \right), \tag{1.19}$$

where $\circ_0$ denotes parameters evaluated in the present Universe. The homogeneous background can thus be parametrized by four parameters, describing the Universe today: $\Omega_{0,m}$ $\Omega_{0,r}$, $\Omega_{0,\Lambda}$ and H_0. Recent observations of the CMB strongly favor a flat universe [67] and we will therefore only consider $\Omega_k = 0$ in the following.

The FE are analytically solvable in the case of a dominant constituent. We will first look at the early universe which is dominated by the radiation density $\Omega_r \gg \Omega_m + \Omega_\Lambda$. In this case, we can integrate eq. (1.19) and obtain

$$a_r(t) \propto t^{1/2} \tag{1.20}$$

As the Universe expands, the matter density becomes more important. The scale factor at which radiation and matter have the same energy density, also known as time of equivalence, is given by

$$\frac{\Omega_{0,r}}{a_{\text{eq}}^4} = \frac{\Omega_{0,m}}{a_{\text{eq}}^3} \quad \Rightarrow \quad a_{\text{eq}} = \frac{\Omega_{0,r}}{\Omega_{0,m}}. \tag{1.21}$$

Recent observations [67] find $z_{\text{eq}} = 3371 \pm 23$ corresponding to $a_{\text{eq}} \sim 3 \times 10^{-4}$.

The Universe then enters the matter dominated era, also known as an Einstein-de Sitter (EdS) universe. The scale factor in such a universe evolves as

$$a_m(t) \propto t^{2/3}. \tag{1.22}$$

At even later times, the Universe will transition to a vacuum-dominated state. The second time of equivalence, when the matter energy density equals the vacuum energy, is given by

$$\frac{\Omega_{0,m}}{a_{\text{eq},2}^3} = \Omega_{0,\Lambda} \quad \Rightarrow \quad a_{\text{eq},2} = \left(\frac{\Omega_{0,m}}{\Omega_{0,\Lambda}}\right)^{1/3}, \tag{1.23}$$

which with current cosmological parameters [67] corresponds to $a_{\text{eq},2} \sim 0.76$ or $z_{\text{eq},2} \sim 0.31$.

A vacuum dominated universe, a so-called de Sitter universe, grows exponentially. Considering a flat universe with $\Omega_\Lambda = 1$ we find

$$a_\Lambda(t) \propto e^{H_0 t}. \tag{1.24}$$

1.2 Linear Growth of Primordial Perturbations

1.2.1 Quantum fluctuations and inflation

A model only considering the epochs of radiation, matter, and dark energy after the Big Bang fails to describe some observations of our Universe. By introducing an initial inflationary period $t_b < t < t_e$, during which the Universe grew exponentially, i.e. a de-Sitter universe for which

$$a(t) = a_e e^{H(t-t_e)}, \tag{1.25}$$

is able to solve the following problems [129, 202]:

Horizon problem: the observed homogeneity of the CMB temperature over the entire sky extends to scales which without inflation were never in causal contact ($\sim$ 2 degrees), and thus could not have thermalized. Inflation causes previously causally connected modes to extend beyond the Hubble radius and enter the horizon again at later times. To solve the Horizon problem, we need $H(t_e - t_b) \simeq 60$ [200, 325].

Flatness problem: the very close to flat geometry of the Universe observed today and the instability of the state $\Omega = 1$ means that at earlier times, the Universe must have been even closer to flatness, requiring fine-tuned initial conditions. Inflation naturally blows up any existing curvature radius and creates a nearly flat universe.

Monopole problem: some theories beyond the standard particle model (grand unified theories, GUT [118]) predict the creation of magnetic monopoles during symmetry-breaking at very high temperatures that however are not observed. Inflation dilutes potential magnetic monopoles.

Structure formation problem: Similar to the Horizon problem, the largest anisotropies observed in the CMB extend to scales beyond causality without inflation. Furthermore, the most massive gravitationally bound structures that we observe would not have had enough time to form if they were not in causal contact before re-entering the particle Horizon.

In the *slow-roll* or *new inflation* model, the exponential expansion is caused by a scalar field ϕ "rolling" down a potential hill $V(\phi)$. Deriving the equation of motion of the field (e.g. [221]), one obtains

$$\ddot{\phi} + 3H\dot{\phi} + \frac{\mathrm{d}V}{\mathrm{d}\phi} = 0, \tag{1.26}$$

under the assumption of spatial homogeneity (i.e. $\nabla\phi = 0$). The energy density and pressure of the field are given by

$$\rho = \frac{1}{2}\dot{\phi}^2 + V(\phi) \tag{1.27}$$

$$p = \frac{1}{2}\dot{\phi}^2 - V(\phi). \tag{1.28}$$

If the field evolves slowly ($\dot{\phi} \ll V(\phi)$), then the equation of state satisfies $p \simeq -\rho$ and an inflationary phase is possible with

$$H^2 = \frac{8\pi G}{3}V(\phi) = \frac{8\pi}{3m_{\mathrm{Pl}}^2}V(\phi), \tag{1.29}$$

where $m_{\mathrm{Pl}} = G^{-1/2}$ is the Planck mass (in units with $\hbar = c = 1$). Most recent Planck observations [254] favor slow-roll models with concave potentials and no evidence has been found for dynamics beyond slow-roll so far.

Inflation provides a natural mechanism for the creation of perturbations arising from fluctuations in the primordial quantum fields. These fluctuations are stretched to observable scales and are the seeds of structure formation. Due to the quantum-mechanical nature of these fluctuations, we can only predict statistical properties. Most theories produce close-to Gaussian perturbations with a power spectrum similar to the Harrison-Zel'dovich spectrum [144, 344]. The exact value is parametrized by the spectral index n_s

$$P(k) \propto k^{n_s}. \tag{1.30}$$

We discuss the initial power spectrum and its meaning in more detail in section 1.3.

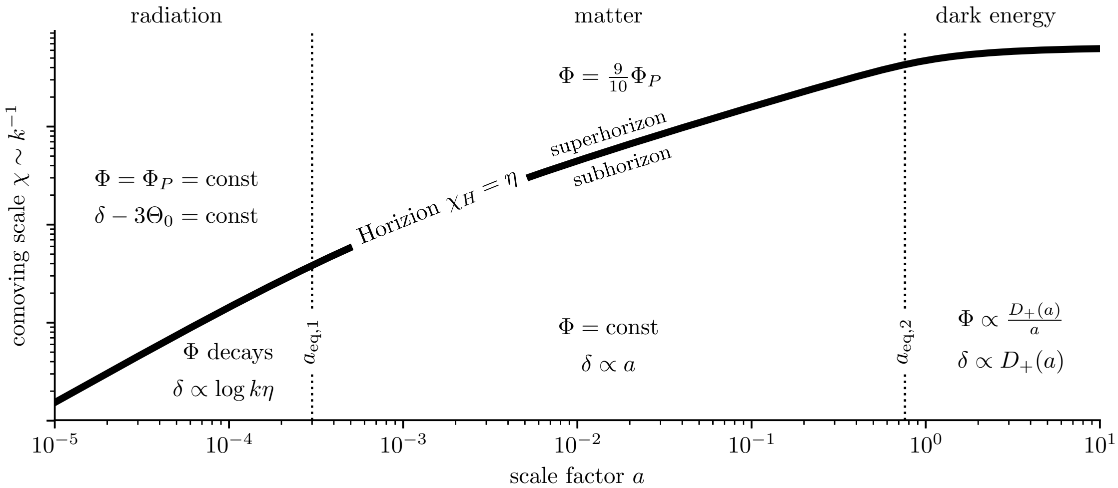

Figure 1.1: Growth of super- and sub-horizon perturbations and potentials in the radiation, matter, and dark energy dominated epochs. Φ denotes metric perturbations in the Newtonian gauge, δ DM perturbations, and Θ_0 the monopole of temperature perturbations of photons.

1.2.2 Relativistic linear perturbation theory

In order to accurately treat the evolution of primordial perturbations, an analysis using full GR is required. In appendix A.1 we outline the main steps in deriving the system of coupled equations, the so-called Einstein-Boltzmann equations, that describe the evolution of the perturbations in the matter and radiation content of our Universe and the perturbations in the metric. In general, these equations have to be numerically integrated. For this purpose, various publicly available codes exist (e.g. [196, 39]). In some limiting cases and under some simplifications, however, we can find analytical approximations. These asymptotic limits are shown in the time-horizon diagram in fig. 1.1 and we briefly summarize them here. More details on the derivation can be found in the appendix and in [81].

On scales larger than the particle horizon, the metric perturbations mainly stay constant, with a decay of $\sim$ 10% after the Universe enters the matter dominated era. Metric perturbations that enter the horizon during the radiation epoch however will decay. Only DM perturbations can grow during that time, while perturbations in the photon-baryon fluid oscillate due to radiation pressure. In the matter dominated era, all matter perturbations can grow and the growth factor $D_+(a) \propto a$ is independent of the mode k. The potential Φ of the metric perturbation remains constant. At late times when dark energy becomes significant, the growth of perturbations slows down and the potentials dilute.

There are therefore two different regimes affecting the primordial perturbations: the scale dependent evolution during the radiation era and horizon crossing, and the scale-independent growth during the matter and dark energy era. The scale dependent growth and effects of the decaying mode (cf. next section) is usually encapsulated in the *transfer function* $T(k, a)$, whereas the *growth function* $D_+(a)$ describes the scale-independent growth, so we can write at linear order

$$\delta(\boldsymbol{k}, a) = \delta(\boldsymbol{k}, a_{\mathrm{in}}) T(k, a) D_+(a), \tag{1.31}$$

for some initial perturbation $\delta(\boldsymbol{k}, a_{\mathrm{in}})$ and some time a well after the regime of the transfer function. To obtain the transfer function $T(k)$, either numerical codes such as CAMB [196] or CLASS [39], or fitting formulae such as the BBKS [20] or the Eisenstein & Hu [95] transfer function have to be used.

In the next section, we will focus on the subhorizon scale in the matter dominated era, where we can neglect GR effects and treat the perturbations in the Newtonian limit (also see the discussion in appendix A.1). We will derive the equations governing the evolution of the perturbations of DM and baryons, and determine the growth function $D_+(a)$.

1.2.3 Linear perturbations in the Newtonian limit

For sub-horizon scales and small metric perturbations Φ, treating the perturbations in the Newtonian limit is a good approximation. This is crucial if we want to treat structure formation numerically with conventional N-body solvers (see next chapter), but also allows us to get a better understanding of physical phenomena in the linear limit which is the goal of this section. A recent analysis of relativistic corrections to this Newtonian approach can for example be found in [102].

Collisionless gas

We consider a self-gravitating, single-species, classical gas, where the motion of each particle is described by the Lagrangian

$$\mathcal{L} = \frac{1}{2} m a^2 \dot{\boldsymbol{x}}^2 - m\Phi, \tag{1.32}$$

where $\boldsymbol{x}$ are the comoving coordinates, $\boldsymbol{p} = \partial\mathcal{L}/\partial\dot{\boldsymbol{x}} = ma\boldsymbol{v}$ are the canonical momenta, and Φ the potential field. The full state of the N particle system is captured in the $6N$-dimensional phase-space. For a macroscopic description however, we do not need to know the position and momentum of individual particles and thus we can represent the state as a phase-space distribution function $f(\boldsymbol{x}, \boldsymbol{p}, t)$ which measures the particle density at $(\boldsymbol{x}, \boldsymbol{p})$ at time t:

$$\mathrm{d}N = f(\boldsymbol{x}, \boldsymbol{p}, t)\, \mathrm{d}^3\boldsymbol{x}\, \mathrm{d}^3\boldsymbol{p}. \tag{1.33}$$

The evolution of f is described by the Boltzmann equation

$$\begin{aligned}\frac{\mathrm{D}f}{\mathrm{D}t} &= \frac{\partial f}{\partial t} + \frac{\partial f}{\partial x_i}\frac{\mathrm{d}x_i}{\mathrm{d}t} + \frac{\partial f}{\partial p_i}\frac{\mathrm{d}p_i}{\mathrm{d}t} \\ &= \frac{\partial f}{\partial t} + \frac{p_i}{ma^2}\frac{\partial f}{\partial x_i} - m\frac{\partial \Phi}{\partial x_i}\frac{\partial f}{\partial p_i} \\ &= \left[\frac{\mathrm{d}f}{\mathrm{d}t}\right]_C,\end{aligned} \tag{1.34}$$

where we used the Lagrangian equations of motion. The term in the last equation is the collision integral measuring the rate at which particles are scattered from a phase-space element $\mathrm{d}^3\boldsymbol{x}\,\mathrm{d}^3\boldsymbol{p}$ located at $(\boldsymbol{x}_1, \boldsymbol{p}_1)$ to another one located at $(\boldsymbol{x}_2, \boldsymbol{p}_2)$ per time interval $\mathrm{d}t$ due to collisions. It is zero in the case of a collisionless gas, such as for dark matter, or for collisional gas in local thermodynamic equilibrium.

We will first study the collisionless Boltzmann equation which is also known as the Vlasov equation. Together with the Poisson equation, they describe the evolution of the phase-space density

$$\frac{\partial f}{\partial t} + \frac{p_i}{ma^2}\frac{\partial f}{\partial x_i} - m\frac{\partial \Phi}{\partial x_i}\frac{\partial f}{\partial p_i} = 0 \tag{1.35}$$

$$\nabla^2\Phi = 4\pi G a^2 \bar{\rho}\delta, \tag{1.36}$$

where the scale-factor $a(t)$ is determined by the FE of the homogeneous background, $\bar{\rho}$ is the background (matter) density and $\delta = \delta\rho/\bar{\rho}$ the local overdensity. Solving the Vlasov equation is difficult and generally has to be done numerically, for example by sampling the phase-space distribution with particles and evolving them with an N-body solver (see next chapter). For small perturbations, we can analyze the system analytically by taking moments of f and the Vlasov equation. Using the first few moments of the phase-space distribution function,

$$n = \frac{a^3\rho}{m} = \frac{a^3\bar{\rho}(1+\delta)}{m} = \int \mathrm{d}^3\boldsymbol{p}\; f(\boldsymbol{x}, \boldsymbol{p}, \boldsymbol{t}) \tag{1.37}$$

$$\langle p_i \rangle = ma\langle v_i \rangle = \frac{1}{n}\int \mathrm{d}^3\boldsymbol{p}\; p_i\; f(\boldsymbol{x}, \boldsymbol{p}, \boldsymbol{t}) \tag{1.38}$$

$$\langle p_i p_j \rangle = m^2a^2\langle v_i v_j \rangle = \frac{1}{n}\int \mathrm{d}^3\boldsymbol{p}\; p_i p_j\; f(\boldsymbol{x}, \boldsymbol{p}, \boldsymbol{t}) \tag{1.39}$$

$$\langle p_i p_j p_k \rangle = m^3a^3\langle v_i v_j v_k \rangle = \frac{1}{n}\int \mathrm{d}^3\boldsymbol{p}\; p_i p_j p_k\; f(\boldsymbol{x}, \boldsymbol{p}, \boldsymbol{t}), \tag{1.40}$$

$$\tag{1.41}$$

where n is the comoving number density, and the corresponding cumulants

$$\sigma^2_{ij} = \langle v_i v_j \rangle - \langle v_i \rangle\langle v_j \rangle \tag{1.42}$$

$$\Sigma^3_{ijk} = \langle v_i v_j v_k \rangle - \langle v_i \rangle\langle v_j \rangle\langle v_k \rangle - \sigma^2_{ij}\langle v_k \rangle - \sigma^2_{jk}\langle v_i \rangle - \sigma^2_{ki}\langle v_j \rangle, \tag{1.43}$$

we find from the first three moments of the Vlasov equation, which after some algebra can be written as [221]

$$\frac{\partial \delta}{\partial t} + \frac{1}{a}\frac{\partial}{\partial x_j}\big((1+\delta)\langle v_j \rangle\big) = 0 \tag{1.44}$$

$$\frac{\partial \langle v_i \rangle}{\partial t} + H\langle v_i \rangle + \frac{\langle v_j \rangle}{a}\frac{\partial \langle v_i \rangle}{\partial x_j} = -\frac{1}{a}\frac{\partial \Phi}{\partial x_i} - \frac{1}{a(1+\delta)}\frac{\partial}{\partial x_j}\left((1+\delta)\sigma^2_{ij}\right) \tag{1.45}$$

$$\frac{\partial \sigma^2_{ij}}{\partial t} + 2H\sigma^2_{ij} + \frac{\langle v_k \rangle}{a}\frac{\partial \sigma^2_{ij}}{\partial x_k} = -\frac{1}{a}\left(\sigma^2_{ik}\frac{\partial \langle v_j \rangle}{\partial x_k} + \sigma^2_{jk}\frac{\partial \langle v_i \rangle}{\partial x_k}\right) - \frac{1}{a(1+\delta)}\frac{\partial}{\partial x_k}\left((1+\delta)\Sigma^3_{ijk}\right). \tag{1.46}$$

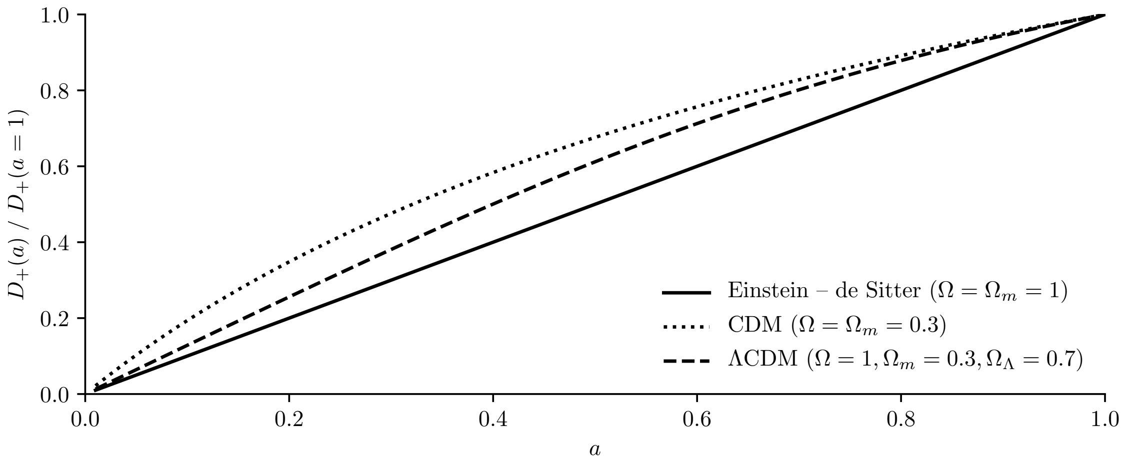

Figure 1.2: Growth factor $D_+(a)$ for an EdS universe in which $D_+(a) \propto a$, an open CDM universe with $\Omega_m = 0.3$ and a flat ΛCDM model with $\Omega_m = 0.3$ and $\Omega_\Lambda = 0.7$ in agreement with current observations [67].

The first equation simply describes the mass conservation, while the second one is the Euler-equation of a collisionless fluid in an expanding universe. The evolution of the velocity dispersion σ_{ij}^2 is determined by the third moment Σ_{ijk}^3 which again depends on the next higher moment, resulting in an infinite hierarchy of equations, the so-called *Boltzmann-hierarchy*. In the following, we will consider two cases under which this infinite hierarchy is truncated: during the single-stream regime of a cold collisionless fluid and the local thermodynamic equilibrium of a collisional gas.

For a cold collisionless fluid in the single-stream regime, we can set $\sigma_{ij}^2 = 0$. Assuming small perturbations so that we can neglect non-linear terms in the perturbative quantities $\delta, \boldsymbol{v}$, and their derivatives, we can differentiate eq. (1.44) and combine with eq. (1.45) and eq. (1.36) to obtain

$$\ddot{\delta} + 2H\dot{\delta} = 4\pi G\bar{\rho}\delta. \tag{1.47}$$

The second term, also called the *Hubble drag*, acts as a friction countering the accelerating collapse of the perturbations.

This second order linear and homogeneous differential equation has two independent solutions which can be combined to the general solution

$$\delta(t) = \delta(0)D_+(t) + \delta(0)D_-(t), \tag{1.48}$$

where $D_+(t)$ is the growing mode (growth factor) and $D_-(t)$ the decaying mode. One can verify[2] that for an EdS universe, $D_+(t) \propto t^{2/3} \propto a$ and $D_-(t) \propto t^{-1} \propto a^{-3.2}$ are the solutions (up to normalization). Therefore, perturbations grow at the same rate as the scale factor in a matter dominated universe. The decaying mode falls of rapidly and can thus be safely ignored at late times.

[2]using the time derivative of $\dot{H} + H^2 = \ddot{a}/a$ and eq. (1.16) to substitute the right-hand side, see e.g. [221]

The growth of the potential perturbations is connected to the density perturbations via the Poisson equation and evolves as $\Phi \propto a^2 \bar{\rho} \delta \propto D_+(a)/a$. In an EdS universe, the potentials thus do not evolve and are frozen in. In general, we can write at linear order

$$\Phi(\boldsymbol{x}, a) = \frac{D_+(a)}{a} \Phi_i, \tag{1.49}$$

for some initial potential field Φ_i, linked to the initial density perturbations via the Poisson equation.

Collisions and the ideal gas

The collision integral in eq. (1.34) accounts for the momentum exchange when particles collide. For an ideal gas, we assume that there are only binary collisions with conserved particle number, total momentum, and total energy. If the mean free path between particle collisions is short, the system will (locally) approach a Maxwell-Boltzmann velocity distribution around the mean velocity $\langle \boldsymbol{v} \rangle$ and therefore Σ^3_{ijk} and the higher order cumulants of the phase-space distribution function are zero. The local velocity distribution function (VDF) can thus be written as

$$f(\boldsymbol{x}, \boldsymbol{v}, t) = \frac{n(\boldsymbol{x}, t)}{\sqrt{(2\pi)^3 \det(\sigma^2)}} \exp\left[-\frac{1}{2} \left(v_i - \langle v_i \rangle \right) \left(\sigma^2_{ij} \right)^{-1} \left(v_j - \langle v_j \rangle \right) \right] \tag{1.50}$$

$$= \frac{n(\boldsymbol{x}, t)}{(2\pi (\mu m_\mathrm{H})^{-1} k_\mathrm{B} T)^{3/2}} \exp\left[-\frac{(\boldsymbol{v} - \langle \boldsymbol{v} \rangle)^2}{2 k_\mathrm{B} T} \right], \tag{1.51}$$

where we assumed in the second step that the collisions will isotropize the velocity distribution function, i.e. $\sigma^2_{ij} = \delta_{ij} k_\mathrm{B} T / (\mu m_\mathrm{H})$, with a spatially varying temperature T, and the average molecular weight μ in units of the atomic hydrogen mass m_H. Instead of using T, we can also describe the system by the isotropic pressure $p = n k_\mathrm{b} T = \rho \,\mathrm{tr}\left(\sigma^2_{ij} \right) / 3$. Unlike the collisionless case where the pressure $p_{ij} = \rho \sigma^2_{ij}$ is anisotropic and dependent on the full Boltzmann hierarchy (cf. eq. (1.45)), the (isotropic) pressure for an ideal gas is fully determined by the first two moments of f, truncating the hierarchy at the second level.

We can now substitute the velocity dispersion σ^2_{ij} with the pressure p (or rather its tensor representation $p_{ij} = p\delta_{ij}/3$) in eq. (1.45). Additionally, we use the equation of state $p = p(\rho, S)$ with the entropy S such that

$$\frac{1}{\bar{\rho}} \frac{\partial p}{\partial x_i} = \frac{1}{\bar{\rho}} \left[\left(\frac{\partial p}{\partial \rho} \right)_S \frac{\partial \rho}{\partial x_i} + \left(\frac{\partial p}{\partial S} \right)_\rho \frac{\partial S}{\partial x_i} \right] \tag{1.52}$$

$$= c_s^2 \frac{\partial \delta}{\partial x_i} + \frac{\sigma}{\bar{\rho}} \frac{\partial S}{\partial x_i}, \tag{1.53}$$

where $c_s^2 = (\partial p / \partial \rho)_S$ is the adiabatic sound speed, and $\sigma = (\partial p / \partial S)_\rho = 2\rho T / 3$ by the first law of thermodynamics for an ideal monoatomic gas. Equation (1.45) becomes the collisional Euler equation

$$\frac{\partial \langle v_i \rangle}{\partial t} + H \langle v_i \rangle + \frac{1}{a} \langle v_j \rangle \frac{\partial \langle v_i \rangle}{\partial x_j} = -\frac{1}{a} \frac{\partial \Phi}{\partial x_i} - \frac{c_s^2}{a} \frac{\partial \delta}{\partial x_i} - \frac{2T}{3a} \frac{\partial S}{\partial x_i}. \tag{1.54}$$

To linear order, individual Fourier modes evolve independently. It is therefore useful to transform the mass conservation, Euler, and Poisson equation to Fourier space. Keeping only linear terms of perturbative quantities we find

$$\text{continuity equation} \quad \dot{\delta} + \frac{i\boldsymbol{k}}{a}\boldsymbol{v} \tag{1.55}$$

$$\text{Euler equation} \quad \dot{\boldsymbol{v}} + H\boldsymbol{v} = -\frac{i\boldsymbol{k}}{a}\left(\Phi + \bar{c}_s^2\delta - \frac{2\bar{T}}{3}S\right) \tag{1.56}$$

$$\text{Poisson equation} \quad k^2\Phi = -4\pi G a^2\bar{\rho}\delta. \tag{1.57}$$

Considering only curl-free velocities[3] such that $\boldsymbol{v} \parallel \boldsymbol{k}$, we can combine the equations to obtain

$$\ddot{\delta} + 2H\dot{\delta} + \left(\frac{c_s^2k^2}{a^2} - 4\pi G\bar{\rho}\right)\delta + \frac{2\bar{T}}{3a^2}k^2S = 0. \tag{1.58}$$

Comparing this result with eq. (1.47), we see that a collisionless gas with negligible velocity stress can be treated as an ideal gas with zero pressure ($c_s = 0, T = 0$). For an ideal gas, both the perturbations in the density δ and in the entropy (connected to pressure perturbations, causing the gas to adiabatically expand and compress) are driving the evolution of the density perturbations. Therefore, there are two initial sources for density fluctuations: isentropic perturbations ($\partial S/\partial x_i = 0$) corresponding to perturbations in the space-time curvature, and isocurvature perturbations ($\delta = 0$) which may be generated by spatial variations in abundance ratios in the early Universe [221].

We will only consider isentropic initial conditions and adiabatic evolution, such that $k^2S_k = 0$. Equation (1.58) has the form of a damped harmonic oscillator with the undamped angular frequency

$$\omega^2 = \frac{c_s^2k^2}{a^2} - 4\pi G\bar{\rho}. \tag{1.59}$$

Thus, the pressure adds a characteristic scale to the system, the *Jeans length*, which we can write in physical units as

$$\lambda_J = \frac{2\pi a}{k_j} = c_s\left(\frac{\pi}{G\bar{\rho}}\right). \tag{1.60}$$

Perturbations smaller than the Jeans length have $\omega^2 > 0$ and thus oscillate (corresponding to an acoustic wave propagating with the sound speed c_s) and will not grow due to the pressure support. Only for modes larger than the Jeans-length, pressure is no longer able to support the gravitational collapse, and in the limit $k \ll k_J$, we recover the solutions of the pressureless gas.

We can define the Jeans mass by relating the wave-length λ to a sphere of radius $\lambda/2$:

$$M_J = \frac{\pi}{6}\bar{\rho}_m\lambda_J^3. \tag{1.61}$$

[3]Taking the curl of eq. (1.54) and only keeping linear terms, one can show that $\nabla\times\boldsymbol{v} \propto a^{-1}$. Therefore, any vorticity (in the linear regime) will decay as the Universe expands. A curl-free vector field can be written as a gradient of a potential field and thus $\boldsymbol{v} \parallel \boldsymbol{k}$.

It can be shown (cf. [221]) that before recombination, when electrons and photons are tightly coupled via Compton scattering and thus baryons and photons behave as a single fluid, the Jeans mass is of the order of superclusters. Only after baryonic matter decouples from radiation ($z \sim 1100$), it drops by several orders of magnitudes to the size of globular clusters. Perturbations on scales smaller than superclusters can thus only grow after recombination.

1.2.4 Zel'dovich approximation

We now go back to the pressureless fluid but we change to a Lagrangian reference frame following the motion of mass elements. We write the position of such an element as a displacement from its initial position $\boldsymbol{q}$ such that

$$\boldsymbol{x}(\boldsymbol{q}, t) = \boldsymbol{q} + \boldsymbol{s}(\boldsymbol{q}, t). \tag{1.62}$$

Assuming a bijective mapping, the mass within the element $\mathrm{d}^3\boldsymbol{q}$ has to be conserved, and thus $\rho(\boldsymbol{x}, t)\ \mathrm{d}^3\boldsymbol{x} = \bar{\rho}(t)\mathrm{d}^3\boldsymbol{q}$. We then have

$$\begin{aligned}
\rho(\boldsymbol{x}(\boldsymbol{q}), t) &= \bar{\rho}(t) \det \left[\frac{\partial x_i(\boldsymbol{q}, t)}{\partial q_j}\right]^{-1} \\
&= \bar{\rho}(t) \det \left[\delta_{ij} + \frac{\partial s_i(\boldsymbol{q}, t)}{\partial q_j}\right]^{-1} \\
&\simeq \bar{\rho(t)} \left(1 - \frac{\partial s_i(\boldsymbol{q}, t)}{\partial q_i}\right),
\end{aligned} \tag{1.63}$$

where in the last step, we assumed small displacements such that $\partial s_i \partial q_j \ll 1$. To linear order, we previously obtained $\rho(\boldsymbol{x}, t) = \bar{\rho}(t)(1 + D_+(t)\delta_i)$, and comparing these equations we find that

$$\delta(\boldsymbol{x}(\boldsymbol{q}), t) \simeq -D_+(t)\nabla \boldsymbol{s}(\boldsymbol{q}, 0) \tag{1.64}$$

$$\nabla \boldsymbol{s}(\boldsymbol{q}, 0) = -\delta_i(\boldsymbol{x}(\boldsymbol{q})) = -\frac{\nabla^2\Phi_i}{4\pi G\bar{\rho}a^3}. \tag{1.65}$$

We can thus write eq. (1.62) as

$$\begin{aligned}
\boldsymbol{x}(\boldsymbol{q}, a) &= \boldsymbol{q} - \frac{D_+(a)}{4\pi G\bar{\rho}a^3}\nabla\Phi_i(\boldsymbol{q}) \\
&= \boldsymbol{q} - D_+(a)\frac{2}{3H^2a^3}\nabla\Phi_i(\boldsymbol{q}) \\
&= \boldsymbol{q} - a\frac{2}{3H_0^2}\nabla\Phi_i(\boldsymbol{q}),
\end{aligned} \tag{1.66}$$

where the last equality holds for an EdS universe (i.e. $\Omega = \Omega_m = 1$ together with and eq. (1.19)). This formulation of linear perturbation theory of a cold and pressureless fluid was developed by Zel'dovich [343] and is known as the Zel'dovich approximation (ZA). It models the evolution of structures in a Lagrangian description where particles travel on straight lines given by the initial density perturbations[4] and the travelled distance is proportional to the growth factor D_+. This linear order approximation can be extended to higher order theories, such as second-order Lagrangian perturbation theory (2LPT, [229, 282]), which give more accurate results in the slightly non-linear regime, and can be used to set up initial conditions for N-body simulations at lower redshifts (see section 2.1.3).

Going back to eq. (1.63) and labeling the real eigenvalues of the symmetric deformation tensor $\nabla \boldsymbol{s}$ as $\lambda_1 \geq \lambda_2 \geq \lambda_3$, we find

$$1 + \delta = \frac{1}{(1 - D_+(a)\lambda_1)(1 - D_+(a)\lambda_2)(1 - D_+(a)\lambda_3)}. \tag{1.67}$$

There are thus up to three singularities during the time evolution, corresponding to the three axes of collapse along the eigenvectors of the deformation tensor. The first collapse (*shell-crossing*) occurs when $D_+(a)\lambda_1 = 1$, forming a two dimensional structure (also called a *wall* or a *Zel'dovich pancake*). At $D_+(a)\lambda_2 = 1$, the structure will collapse along its second axis, forming a filament, before finally the third axis collapses, and a spherical structure (a halo) is formed. In the case of negative eigenvalues or a collapse time larger than the Hubble time, collapse will not happen along this axis. Together with the uncollapsed regions (voids), walls, filaments, and halos form the components of the cosmic web. Since perturbations exist on all scales, the cosmic web has a multi-scale nature, with filaments embedded in walls, and halos embedded in filaments.

In general, the eigenvalues λ_i of the tidal field can be positive or negative. For a Gaussian random field, a useful analytical formula of the joint probability distribution $P(\lambda_1, \lambda_2, \lambda_3)$ has been obtained by Doroshkevich [87], which can be written as [221]

$$P\left(\lambda_1, \lambda_2, \lambda_3\right) \propto \left(\lambda_1 - \lambda_2\right)\left(\lambda_1 - \lambda_3\right)\left(\lambda_2 - \lambda_3\right) \exp\left[-\frac{3}{\sigma^2}\left(I_1^2 + \frac{5}{2}I_2^2\right)\right], \tag{1.68}$$

where $\sigma^2 = \langle \delta^2 \rangle$ is the variance of the overdensity field, $I_1 = \lambda_1 + \lambda_2 + \lambda_3 = \delta$, and $I_2 = \lambda_1\lambda_2 + \lambda_1\lambda_3 + \lambda_2\lambda_3$. Integrating over the distribution yields a probability of 8% of all eigenvalues being negative ($- - -$, corresponding to voids) or positive ($+ + +$, corresponding to halos) and 42% for the mixed states $- - +$ (walls) and $- + +$ (filaments).

Note that the ZA is not valid after the first shell-crossing, as can be seen in the 1D simulation of a plane-wave collapse in fig. 1.3. The ZA predicts that after the formation of the caustic, the particles will simply continue on their trajectories. However, after shell-crossing, the approximation of $\sigma_{ij}^2 = 0$ that we assumed in eq. (1.45) is no longer valid, and all higher moments of the Boltzmann hierarchy have to be considered. We will look in more detail at the generation of velocity dispersion in chapter 3.

The multi-scale nature of perturbations means that different scales will enter the non-linear regime at different times, with small-scale structures collapsing first. By selectively filtering out modes below the non-linear threshold $k < k_{\mathrm{NL}}$, shell-crossing and the consequent "smearing out" of caustics in the ZA can be avoided [66, 276]. This technique is called the truncated ZA and can be applied to studies of the large scale features in the Universe. In practice, the low-pass filtering corresponds to a smoothing of the initial conditions, similar to the truncation of the power spectrum by warm dark matter (cf. section 1.3.2).

[4] Since the velocity is proportional to the gradient of the potential field, velocity flows are irrotational in the ZA. Vorticity can however be generated after shell-crossing [87], when the ZA is no longer valid.

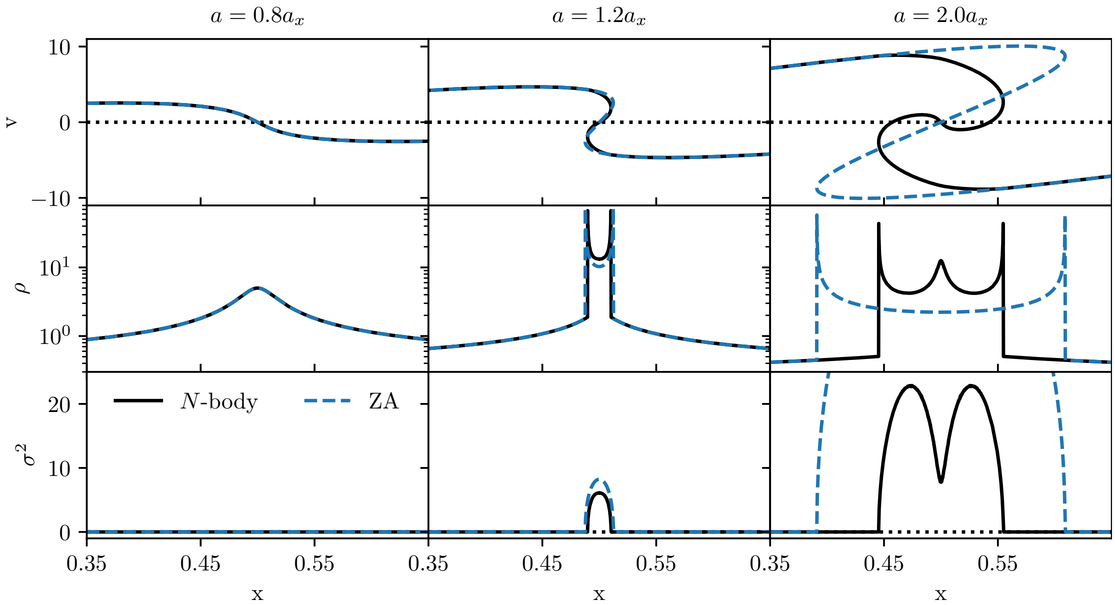

Figure 1.3: Collapse of a 1d plane-wave perturbation in the ZA and the full gravity evolution with a N-body simulation. The top row shows the phase-space distribution (dark matter sheet), the second row the projected density, and the bottom row the velocity dispersion $\sigma^2 = \langle v^2 \rangle - \langle v \rangle^2$. Time is normalized such that the collapse occurs at the scale factor $a = a_x$. After shell-crossing (second column), caustics form in the density distribution where the phase-space distribution goes from a single- to multi-valued distribution, giving rise to velocity dispersion. The ZA is no longer able to predict the evolution of the system and diverges from the true solution, visible at later times (third column).

A further technique to avoid the artificial smearing-out of collapsed regions in the ZA is the adhesion model (see [126, 284, 127, 111] and also [128] for a recent review), in which particles are made to stick together once they enter a caustic. Defining $\boldsymbol{u} = \mathrm{d}\boldsymbol{x}/\mathrm{d}D_+$ and using the ZA, we find along the particle trajectory

$$\frac{\mathrm{D}\boldsymbol{u}}{\mathrm{D}D_+} = \frac{\partial \boldsymbol{u}}{\partial D_+} + (\boldsymbol{u}\nabla)\boldsymbol{u} = 0. \tag{1.69}$$

The stickiness is achieved by adding an artificial viscosity to the equation:

$$\frac{\partial \boldsymbol{u}}{\partial D_+} + (\boldsymbol{u}\nabla)\boldsymbol{u} = \nu\nabla^2\boldsymbol{u}, \tag{1.70}$$

where ν is the viscosity parameter chosen arbitrarily. This equation is known as the Burgers' equation [26, 54] and can be solved analytically for a irrotational velocity field [334]. If we let $\nu \to 0$, we recover the ZA. In structure formation, the adhesion model has been used extensively to study the formation and properties of the large-scale cosmic web (e.g. the evolution of voids [277], filamentary structure [237], and halo mass functions in 2D [318]. However, the approximation cannot predict the dynamics and properties within the structures once they form.

1.3 Statistical Properties of the Overdensity Field

Since the primordial perturbations are thought to originate from random, quantum mechanical processes during the inflationary phase, we can only compare the statistical properties of the cosmic density and velocity fields (and not an individual realization) between theoretical and numerical models and observations. As discussed in section 1.2.1, the primordial perturbations after inflation are predicted to be statistically homogeneous and isotropic and close to Gaussian, following a power law $P(k) \propto k^{n_s}$. In the following, we will introduce the basic quantities of such a Gaussian random field.

1.3.1 Two-point correlators

A simple measure of the clustering of an inhomogeneous universe is the two-point correlation function $\xi(\boldsymbol{x}, \boldsymbol{x}') = \langle \delta(\boldsymbol{x})\delta(\boldsymbol{x}') \rangle$, measuring the expectation value of $\delta(\boldsymbol{x})\delta(\boldsymbol{x}')$ from an underlying stochastic process creating the overdensity field δ. Due to the cosmological principle, ξ can only depend on the distance between $\boldsymbol{x}$ and $\boldsymbol{x}'$ and not the exact location or angle. Hence, we can write

$$\xi(r) = \langle \delta(\boldsymbol{x})\delta(\boldsymbol{x}') \rangle, \tag{1.71}$$

where $r = |\boldsymbol{x} - \boldsymbol{x}'|$. Equivalently, we can define the correlation function in Fourier space and we find

$$\langle \delta(\boldsymbol{k})\delta^\dagger(\boldsymbol{k}') \rangle = (2\pi)^3 \delta_\mathrm{D}(\boldsymbol{k} - \boldsymbol{k}') P(k), \tag{1.72}$$

where δ_D is the Dirac delta-function and $P(k)$ is the power spectrum, which only depends on $k = |\boldsymbol{k}|$ and is real-valued due to rotational symmetry and the reality condition for $\delta(\boldsymbol{x})$. Plugging in the definition of $\delta(\boldsymbol{k})$ as a Fourier transform of $\delta(\boldsymbol{x})$, one can see that the two-point correlation function and the power spectrum are each other's Fourier transform:

$$P(k) = 4\pi \int_{\mathbb{R}_+} \mathrm{d}r \, r^2 \frac{\sin(kr)}{kr} \xi(r) \tag{1.73}$$

$$\xi(r) = \frac{1}{2\pi^2} \int_{\mathbb{R}_+} \mathrm{d}k \, k^2 \frac{\sin(kr)}{kr} P(k), \tag{1.74}$$

and thus both quantities carry the same information and can be used interchangeably (on infinite domains).

For a Gaussian random field, $\xi(r)$ or $P(k)$ determine the field entirely: the probability to find the overdensities $\delta(\boldsymbol{x}_i)$ at N points $\boldsymbol{x}_i$ simultaneously is given by a multivariate Gaussian

$$\mathcal{P}(\delta(\boldsymbol{x}_1), \ldots, \delta(\boldsymbol{x}_N)) = \frac{1}{(2\pi)^{N/2} \det(V)^{1/2}} \exp\left[-\frac{1}{2} \sum_{i,j=1}^{N} \delta(\boldsymbol{x}_i) \left(V^{-1}\right)_{ij} \delta(\boldsymbol{x}_j) \right], \tag{1.75}$$

where the covariance matrix is solely determined by the correlation function: $V_{ij} = \xi(|\boldsymbol{x}_i - \boldsymbol{x}_j|)$. In Fourier space, different $\delta(\boldsymbol{k})$ modes are mutually independent, and their real and imaginary parts are both independent Gaussian variables with mean 0 and variance $P(|\boldsymbol{k}|)/2$ [221] or equivalently with a random phase ϕ and a Rayleigh-distributed modulus μ with variance $P(k)$ [276]:

$$\mathcal{P}(\mu, \phi)\,\mathrm{d}\mu\mathrm{d}\phi = \frac{\mu}{P(k)} \exp\left[-\frac{\mu^2}{2P(k)}\right] \mathrm{d}\mu\, \frac{1}{2\pi}\mathrm{d}\phi. \tag{1.76}$$

Given a power spectrum $P(k)$, this equation can be used to draw independent random numbers in Fourier space, which can then be transformed to real space to obtain a realization of the overdensity field following the power spectrum (also see the discussion on generating initial conditions for simulations, section 2.1.3).

1.3.2 The linear power spectrum

Starting from the primordial power-spectrum $P(k) \propto k^{n_s}$ produced during inflation (cf. section 1.2.1) and combining the scale-dependent evolution of perturbations in the radiation dominated era and outside the horizon described by the transfer function $T(k)$ (section 1.2.2) and the linear, scale-independent evolution described by the growth function D_+ (section 1.2.3), we find that the evolution of the linear power spectrum is given by

$$P_{\mathrm{lin}}(a, k) = A_0 k^{n_s} T^2(a) D_+^2(a), \tag{1.77}$$

where A_0 is the normalization at the present time (since $D_+(a = 1) = 1$ by convention). The full, non-linear power spectrum can be written as $P(k) = P_{\mathrm{lin}}(k) + P_{\mathrm{nl}}(k)$, where $P_{\mathrm{nl}}(k)$ captures the contribution from regions that have entered the non-linear regime. A comparison of the linear power spectrum and the non-linear contributions at late times can be seen in fig. 1.4. Note that the non-linear scale k_{NL}, below which non-linear effects are important, increases to larger modes as time increases.

One way to constrain the amplitude of the power spectrum from observations is to measure the variance of mass (galaxies) that one finds in randomly placed spheres of radius R. Mathematically, this corresponds to measuring the variance of the density field smoothed on the scale R:

$$\delta_R(\boldsymbol{x}) = (\delta * W_R)(\boldsymbol{x}) \tag{1.78}$$

$$\delta_R(\boldsymbol{k}) = \hat{W}_R \delta(\boldsymbol{k}), \tag{1.79}$$

where $\hat{W}_R$ is the Fourier transform of the window function W, which is commonly a tophat or a Gaussian filter. The variance of an overdensity field $\delta(\boldsymbol{x})$ is simply $\sigma^2 = \langle \delta(\boldsymbol{x})^2 \rangle = \xi(0)$, hence we find from eq. (1.74):

$$\sigma^2(R) = \frac{1}{2\pi^2} \int_{\mathbb{R}_+} \mathrm{d}k\, k^2 P(k) \hat{W}_R(k)^2. \tag{1.80}$$

Note that if $P(k)$ does not have a strong cutoff on small scales, the filtered density variance will diverge for $R \to 0$. In such cases, the overdensity field will always be non-linear on some scale and structure can only grow via mergers of non-linear clumps (so-called bottom-up or hierarchical structure formation [242]).

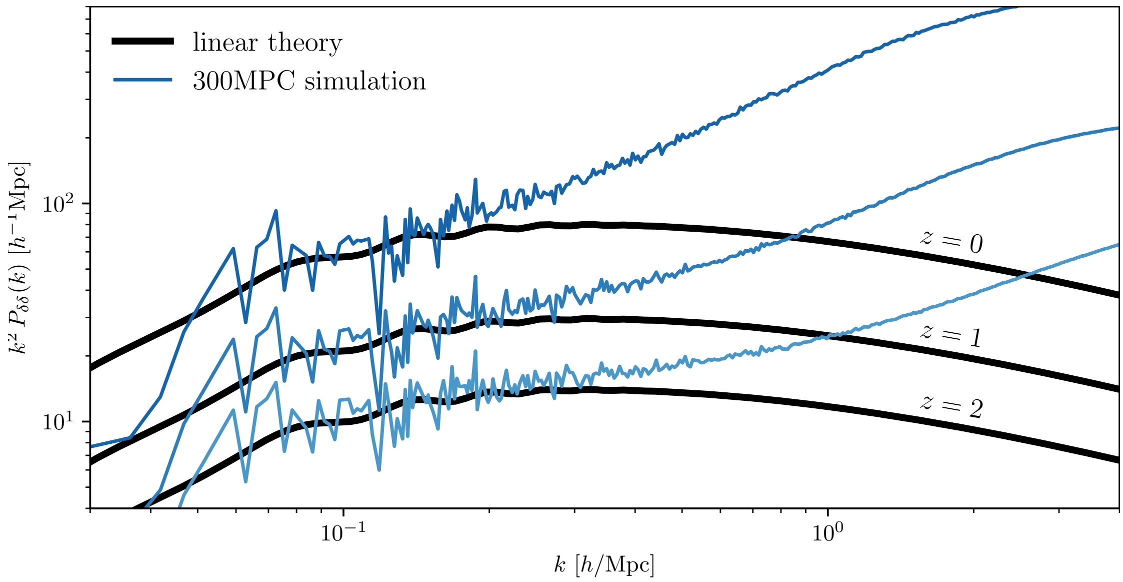

Figure 1.4: Matter distribution power spectra obtained from linear theory and from the 300MPC simulation at redshifts $z = 0, 1$ and 2. The theory spectra were computed using the Eisenstein & Hu [95] transfer function (with Planck 2015 cosmological parameters [67]), which was also used to set up the initial conditions of the simulation (cf. section 2.1.3). Power spectra of the simulation were obtained by projecting the N-body particles onto a mesh with the CIC assignment scheme (cf. section 2.1.2) and deconvolving with the assignment kernel. The noise on large scales is due to the low number of corresponding modes (cosmic variance).

For some applications it is convenient to express σ in terms of contained mass instead of radius, so we will use $\sigma(R)$ and $\sigma(M)$ interchangeably. The typical mass within the filter W_R is just $M = \bar{\rho} \int \mathrm{d}^3\boldsymbol{x}\ W_R(\boldsymbol{x})$, which is $4\pi\bar{\rho}R^3/3$ in the case of a tophat window function.

For historical reasons, the value $\sigma_8 = \sigma(8\ h^{-1}\ \mathrm{Mpc})$ is often used to represent the amplitude of the power spectrum (once the shape of the power spectrum is known, A_0 and σ_8 are easily converted). This convention originates from the observation that for the distribution of galaxies, $\sigma_{\mathrm{gal}}(R) = b\sigma(R) \sim 1$ for $R = 8\ h^{-1}$ Mpc [221], where b is the bias parameter describing the different clustering amplitude of galaxies as tracers of the dark matter distribution.

Truncation by free-streaming in warm and hot dark matter models

Candidates for DM particles can be categorized into hot (HDM), warm (WDM), and cold (CDM) dark matter according to their velocity dispersion, which determines the free-streaming length below which perturbations are erased and gravitational collapse is suppressed. Per definition, the velocity dispersion is negligible for structure formation in the CDM case, whereas for hot DM (e.g. light neutrinos), fluctuations on scales smaller than superclusters are washed out. This implies that in a pure HDM universe, structure would have to form top-down through fragmentation of larger structures (pancakes), which is in contradiction with various observations, such as the incompatible age of galaxies [106], cooling time of the shock-heated baryons during the primary collapse [286], and early measurements of the CMB amplitude [294]. The intermediate range of WDM has gained interest in recent years, as such a DM candidate may alleviate certain tensions between observations and simulations of small scale structures[5] (a review can be found in [53]).

To study the effects of free-streaming on clustering, the Einstein-Boltzmann equations (cf. appendix A.1) including all species have to be (numerically) solved. The result is usually given as a relative transfer function $T_{\mathrm{WDM}}(k)$, measuring the scale dependent modifications to the linear CDM transfer function. In the following, we will use the formula provided by Viel et al. [319] (also see [41]), who find the fitting formula

$$T_{\mathrm{WDM}}(k) \equiv \left[\frac{P_{\mathrm{lin}}^{\mathrm{WDM}}}{P_{\mathrm{lin}}^{\mathrm{CDM}}}\right]^{1/2} \simeq \left[1 + (\alpha k)^{2\mu}\right]^{-5/\mu}, \tag{1.81}$$

where α determines the scale of the suppression and depends on the WDM candidate parameters. For the index μ, values of 1.0 [41] and 1.12 [319] have been used in the literature. For a thermally produced dark matter candidate with particle mass m_{WDM}, the suppression scale can be modeled with

$$\alpha = 0.049 \left[\frac{m_{\mathrm{WDM}}}{\mathrm{keV}}\right]^{-1.11} \left[\frac{\Omega_{\mathrm{WDM}}}{0.25}\right]^{0.11} \left[\frac{h}{0.7}\right]^{1.22} h^{-1}\mathrm{Mpc}. \tag{1.82}$$

For sterile neutrinos, which are not thermally produced, the same formula can be applied but masses have to be translated according to

$$m_{\nu_s} = 4.43\mathrm{keV} \left(\frac{m_{\mathrm{WDM}}}{1\mathrm{keV}}\right)^{4/3} \left(\frac{\Omega_{\mathrm{WDM}}}{0.1225}\right)^{-1/3}. \tag{1.83}$$

Instead of using the suppression scale α, it is convenient to characterize the free-streaming with the scale at which T_{WDM} drops to 1/2, also known as the half-mode scale $k_{\mathrm{WDM}}^{\mathrm{hm}}$ [281, 280]. The half-mode mass can then be obtained from the average mass within a tophat of radius $\pi/k_{\mathrm{WDM}}^{\mathrm{hm}}$:

$$M_{\mathrm{WDM}}^{\mathrm{hm}} = \frac{4\pi}{3}\bar{\rho}\left[\pi\alpha\left(2^{\mu/5} - 1\right)^{-\frac{1}{2\mu}}\right]^3. \tag{1.84}$$

The half-mode mass is where the WDM is expected to first affect the properties of halos [281]. Recent constraints on the mass of sterile neutrinos obtained from Ly-α observations [340] find $m_{\nu_s} \gtrsim 4.17$ keV corresponding to $M^{\mathrm{hm}} \sim 1.8 \times 10^8 h^{-1}\mathrm{M}_\odot$.

1.4 Non-linear Collapse Models

Present-day structures in the Universe, such as DM halos, galaxies, and galaxy clusters, have overdensities $\delta \gg 1$ and are thus in the highly non-linear regime. In general, numerical methods (see next chapter) have to be used to accurately simulate their formation and structure. For some simplified cases with high degrees of symmetry, analytic solutions can be found however, providing useful insights to non-linear structure formation.

[5] However, it has been shown that these "small scale structure tensions" can also be alleviated within the ΛCDM framework if baryonic processes such as stellar feedback are modeled in more detail [53].

1.4.1 Spherical and ellipsoidal collapse models

The simplest model assumes a spherical density peak of radius r with constant overdensity δ on a homogeneous background density $\bar{\rho}$. Due to the spherical symmetry, the problem is fully parametrized by the evolution of the radius $r(t)$. Assuming an EdS universe ($\bar{\rho} = \bar{\rho}_m = \rho_c$), we can use the conservation of energy of the outermost shell:

$$\mathcal{E} = \frac{1}{2}\dot{r}^2 - \frac{GM}{r} = \frac{1}{2}\left(\dot{r}^2 - \frac{8\pi G\rho}{3}\right), \tag{1.85}$$

which we can rewrite as

$$\frac{\dot{r}^2}{r^2} = \frac{8\pi G}{3}\rho - \frac{k}{r^2}, \tag{1.86}$$

where we defined $k = -2\mathcal{E}$. This equation corresponds to the Friedman equation of a universe with constant curvature, cf. eq. (1.15). The curvature of this "mini-universe" is determined by the energy $\mathcal{E}$. Overdense and underdense spherical regions thus evolve according to the Friedman equations for a closed or an open universe respectively. Overdense perturbations will slowly decouple from the expanding homogeneous background until the *turnaround time*, after which they collapse. The collapse of a perturbation will eventually halt when the patch reaches virial equilibrium, forming a DM halo. The radius and density evolution of the spherical collapse model is visualized in fig. 1.5.

An analytic derivation of the key results from the spherical collapse model can be found in appendix A.2. Comparing the density of the perturbation $\bar{\rho}(1+\delta)$ with the background density $\bar{\rho}$, we find that at the time of turnaround, $\delta_{\rm ta} \simeq 4.55$, and at the time of virialization, $\delta_{\rm vir} \simeq 177$. These non-linear densities can be compared to the densities predicted by linear theory at the turnaround ($\delta_{\rm TA}^{\rm lin} \simeq 1.06$) and at virialization ($\delta_c = \delta_{\rm vir}^{\rm lin} \simeq 1.686$). We will use these thresholds in the next section to predict where virialized structures have formed using linear perturbation theory only.

As a simple, non-spherical extension of this model, one can consider the collapse of a homogeneous ellipsoid with comoving principal axes $\boldsymbol{X}$ (e.g. [166, 333, 43]). The principle axes obey the equation of motion

$$\frac{\mathrm{d}\boldsymbol{V}}{\mathrm{d}t} = -\frac{1}{a}\nabla\Phi(\boldsymbol{X}), \tag{1.87}$$

where $\boldsymbol{V}$ is the peculiar velocity at the ellipsoid boundary and Φ the gravitational potential perturbation, which we can separate into a potential arising from the interior of the ellipsoid, and an external contribution, i.e. $\Phi = \Phi_{\rm int} + \Phi_{\rm ext}$. To describe the external potential in the linear regime, we can assume that the ellipsoid evolves from a Lagrangian sphere with radius $\boldsymbol{R}_0$[6]. We can then use the ZA (cf. section 1.2.4) to describe the collapse and deformation of this sphere under the influence of the gravitational tidal field, i.e. $X_i(t) = \boldsymbol{R}_0(1 - \lambda_i D_+(t))$, where λ_i are the eigenvalues of the deformation tensor $\nabla\nabla\Phi_i/(4\pi G\bar{\rho}a^3)$. In the linear regime, the external

[6]The approximation of initially spherical perturbations has been shown to predict inaccurate collapse times (e.g. [207], where also an extended ellipsoid model accounting for non-spherical proto-halo patches is presented). We will measure the shapes of proto-halos in chapter 5 where we find that especially low mass halos tend to originate from elliptic Lagrangian volumes.

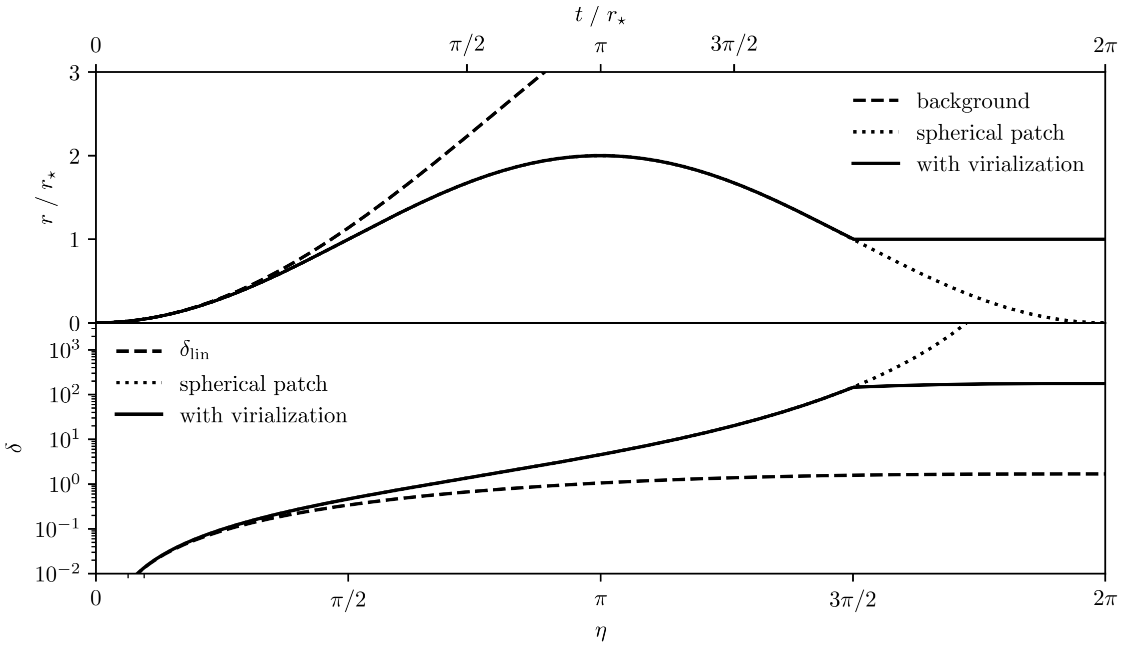

Figure 1.5: Collapse of a spherical perturbation with radius r as a function of conformal time η, with $t = r_\star(\eta - \sin\eta)$ and $r_\star = GM$, where M is the total mass of the patch. The patch grows until the turnaround time at $\eta = \pi$, after which it contracts until it virializes at around $\eta = 3\pi/2$ to $\eta = 2\pi$ due to imperfections in the symmetry. The overdensity at virialization is $\delta \simeq 177$, whereas the linear approximation would only predict $\delta_c \simeq 1.686$.

potential $\Phi_{l,\mathrm{ext}}$ can then be written as [221]

$$\Phi_{l,\mathrm{ext}}(\boldsymbol{x}) = 2\pi G\bar{\rho}_\mathrm{m}a^2 \sum_{j=1}^{3} \left(\lambda_j - \frac{\delta_\mathrm{init}}{3}\right) D_+(t)x_j^2, \tag{1.88}$$

where $\delta_\mathrm{init} = \lambda_1 + \lambda_2 + \lambda_3$ is the initial overdensity of the ellipsoid. We can assume that $\Phi_\mathrm{ext} = \Phi_{l,\mathrm{ext}}$ during the entire collapse of the ellipsoid, since the internal potential will dominate during the non-linear regime and hence any approximation of the external field is irrelevant.

The internal potential can be derived from the Poisson equation, resulting in (e.g. [62])

$$\Phi_\mathrm{int}(\boldsymbol{x}) = \pi G a^2 \bar{\rho}_\mathrm{m}\delta \sum_{i=1}^{3} \alpha_i x_i^2, \tag{1.89}$$

with the coefficients

$$\alpha_i = X_1 X_2 X_3 \int_{\mathbb{R}_+} \mathrm{d}y \left(X_i^2 + y\right)^{-1} \prod_{j=1}^{3} \left(X_j^2 + y\right)^{-1/2}. \tag{1.90}$$

Combining the potentials and using eq. (1.87), the dynamics of the principle axes can be written as [221]

$$\frac{\mathrm{d}^2 X_j}{\mathrm{d}t^2} + \frac{2\dot{a}}{a}\frac{\mathrm{d}X_j}{\mathrm{d}t} = -4\pi G\bar{\rho}_{\mathrm{m}} X_j \left[\frac{1}{2}\alpha_j \delta + D_+(t)\left(\lambda_j - \frac{\delta_{\mathrm{init}}}{3}\right)\right]. \tag{1.91}$$

This equation is valid until the shortest axis collapses. To extend the model, a common practice is to "freeze" the axes once they reach a radius corresponding to the virialized radius of a spherical perturbation with the same mass. The ellipsoid model is thus fully specified by the eigenvalues of the gravitational tidal field λ_i, or alternatively by the initial overdensity δ_{init} and the ellipticity and prolateness parameters

$$e = \frac{\lambda_1 - \lambda_3}{2\sum \lambda_i} \qquad p = \frac{\lambda_1 + \lambda_3 - 2\lambda_2}{2\sum \lambda_i}. \tag{1.92}$$

The ellipticity $e \in [0, 0.5]$ describes the overall deviation from spherical symmetry ($e = 0$), whereas p differentiates between an oblate ($p < 0$) and prolate ($p > 0$) symmetry. Comparing the collapse time of an ellipsoid with the collapse time of an equal sized spherical perturbation, one finds that in the ellipsoidal model, the collapse along the shortest axis occurs earlier [332, 287], and the collapse of the last axis later [289].

The ellipticity and prolateness of the tidal field depends on the local overdensity. Using eq. (1.92), one can derive [221]

$$\mathcal{P}(e, p|\delta_{\mathrm{init}}) \propto e(e^2 - p^2)\exp\left[-\frac{5\delta_{\mathrm{init}}^2}{2\sigma^2}(3e^2 + p^2)\right], \tag{1.93}$$

where $\sigma^2 = \langle\delta^2\rangle$ is the variance of the overdensity field. In fig. 1.6, we show the distribution for some selected values of $\delta_{\mathrm{init}}/\sigma$. The distributions peak at $p = 0$, and regions with a larger overdensity tend to have a more spherical tidal tensor.

1.4.2 Density peaks

The spherical and ellipsoidal collapse models describe the formation of a gravitationally bound halo of mass M through the collapse of a perturbation of volume $V = M/\bar{\rho}$ in the initial density field. In *peak theory*, it is assumed that this region corresponds to a peak of the density field smoothed on the scale M. It has been shown that this assumption is reasonable for a large fraction ($\sim 70\%$) of halos, with "peakless" halos predominantly emerging from highly clustered regions under the influence of strong tidal fields [206]. Nevertheless, studying the density peaks of the initial density field can provide useful insight into number densities, the spatial distribution, and the primordial shapes of halos.

In the following, we will consider the smoothed overdensity field $\delta_R(\boldsymbol{x}) = \int \mathrm{d}^3\boldsymbol{x}'\,\delta(\boldsymbol{x}')W_R(\boldsymbol{x}+\boldsymbol{x}')$, where W_R is the smoothing kernel of scale R. A peak $\boldsymbol{x}_P$ of this field is characterized by $\nabla\delta_R(\boldsymbol{x}_P) = 0$ and a negative definite Hessian

$$H_{ij}(\boldsymbol{x}) = \frac{\partial^2 \delta_R(\boldsymbol{x})}{\partial x_i \partial x_j}, \tag{1.94}$$

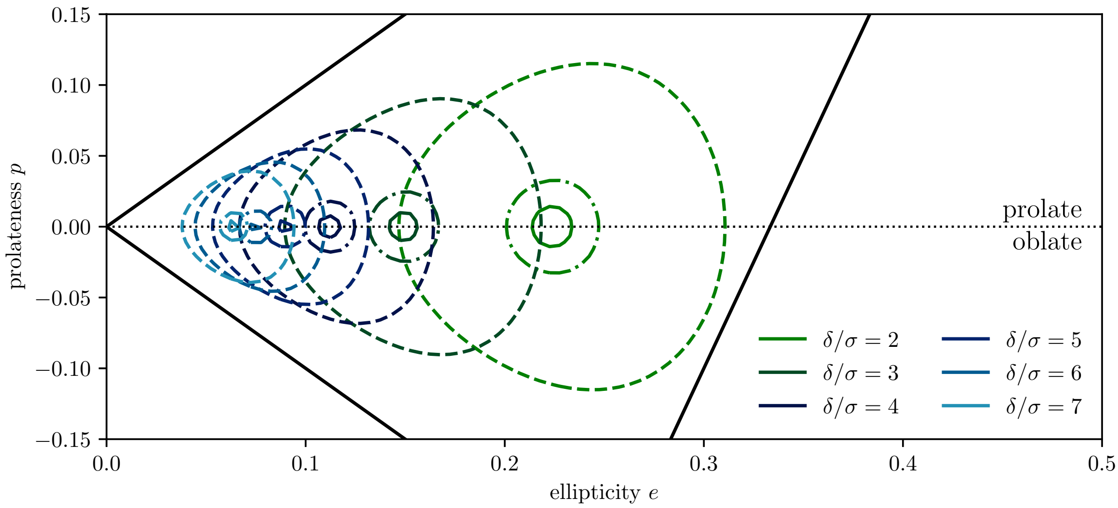

Figure 1.6: The ellipticity – prolateness probability distribution of the tidal field at $\delta_{\mathrm{init}}/\sigma$. Note that by construction (cf. eq. (1.101)), the ellipticity e is constrained to the interval $[0, 0.5]$ and the prolateness p to $[-e, e]$ for $e \leq 0.25$ and $[-1 + 3e, e]$ for $e > 0.25$. We outline this validity triangle with black lines.

i.e. $\Lambda_i > 0\ \forall i$, where $\Lambda_1 \geq \Lambda_2 \geq \Lambda_3$ are the eigenvalues of $-H_{ij}$. In the neighborhood of a density peak, the overdensity can be estimated as

$$\delta_R(\boldsymbol{x} - \boldsymbol{x}_P) \simeq \delta(\boldsymbol{x}_P) + \frac{1}{2} H_{ij} (\boldsymbol{x} - \boldsymbol{x}_P)_i (\boldsymbol{x} - \boldsymbol{x}_P)_j \tag{1.95}$$

$$\simeq \delta(\boldsymbol{x}_P) - \frac{1}{2} \Lambda_i (\boldsymbol{x} - \boldsymbol{x}_P)_i^2, \tag{1.96}$$

where in the last step we have assumed that the coordinate system x_i is aligned with the eigenframe of H_{ij}.

For the following discussion, it is useful to introduce the spectral moments of the density fields,

$$\sigma_j^2(R) = \frac{1}{2\pi^2} \int \mathrm{d}k\ k^2 P(k) k^{2j} \tilde{W}_R(k)^2, \tag{1.97}$$

where $P(k)$ is the linear power spectrum extrapolated to $z = 0$. Note that for $j = 0, 1$, and 2, this quantity corresponds to $\sigma_0^2(R) = \langle \delta_R^2 \rangle$, $\sigma_1^2(R) = \langle (\nabla \delta_R)^2 \rangle$, and $\sigma_2^2(R) = \langle (\nabla^2 \delta_R)^2 \rangle$, which can be seen by substituting $P(k)$ according to eq. (1.72).

Furthermore, we can characterize a density peak by its *peak height* $\nu = \delta_R / \sigma_0$. It is then possible to estimate the number density of peaks of a certain height $\mathcal{N}_{\mathrm{pk}}(\nu)\,\mathrm{d}\nu$ of any Gaussian random field. Since the derivation and full expression are rather lengthy and tedious, we refer to Bardeen et al. [20] for a full description. For high peaks where $\nu \gg 1$, the (comoving) number density can be approximated as

$$\mathcal{N}_{\mathrm{pk}}(\nu)\ \mathrm{d}\nu = \frac{\left(\sigma_2^2/(3\sigma_0^2)\right)^{3/2}}{(2\pi)^2} \left(\nu^3 - 3\nu\right) e^{-\nu^2/2} \mathrm{d}\nu. \tag{1.98}$$

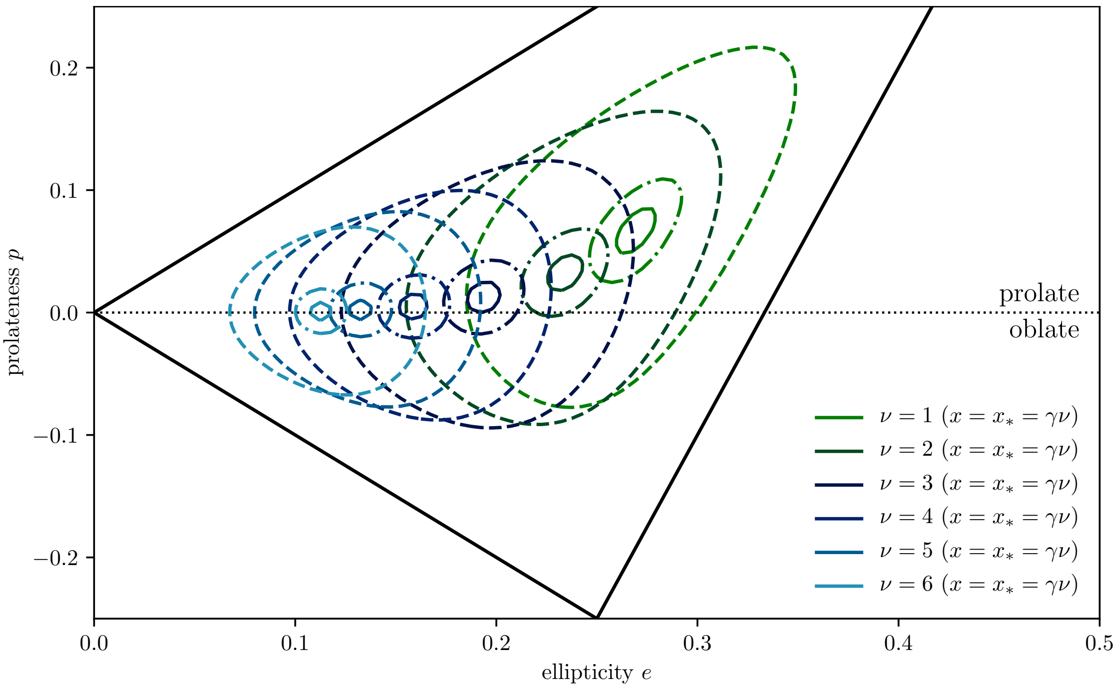

Figure 1.7: The ellipticity – prolateness probability distribution of the peak shape at fixed peak curvature x, where x is set at the characteristic scale x_* for a given ν, i.e. $x = x_* = \gamma\nu$, with $\gamma = \sigma_1^2/(\sigma_0\sigma_2) = 1.58^{-1}$, corresponding to the values chosen in [20]. The contours include 50, 5 and 1% of the distribution. Note that by construction (cf. eq. (1.101)), the ellipticity e is constrained to the interval $[0, 0.5]$ and the prolateness p to $[-e, e]$ for $e \leq 0.25$ and $[-1+3e, e]$ for $e > 0.25$. We outline this validity triangle with black lines.

Note that the shape of this distribution is (up to a normalization) independent of the power spectrum. The total comoving number density of peaks of arbitrary height, i.e. $n_{\rm pk} = \int_{\mathbb{R}} \mathrm{d}\nu\, \mathcal{N}_{\rm pk}(\nu)$, can be calculated analytically [20]:

$$n_{\rm pk} = \frac{29 - 6\sqrt{6}}{5^{3/2} 2 (2\pi)^2 R_*^3} \simeq 0.016 R_*^{-3}, \tag{1.99}$$

where $R_* = \sqrt{3}\, \sigma_1/\sigma_2$.

In addition to the number density, one can also derive clustering statistics of peaks with given peak height thresholds [20]. By using the ZA to displace the peaks according to the local gravitational field, one can then derive the correlation function of evolved peaks, which correspond to halos in the peak-theory picture (e.g. [211]).

Another interesting property of peaks are the shapes of the overdensity field surrounding it. We can estimate the isodensity surface $\delta_R(\boldsymbol{x}) = c$ using the second order expansion of δ_R around $\boldsymbol{x}_P$ from eq. (1.96). The isodensity contour is then given by an ellipsoid with semi-axes a_i defined by

$$a_i^2 = \frac{2(\delta_R(\boldsymbol{x}_P) - c)}{\Lambda_i}. \tag{1.100}$$

Similar to the characteristics of the tidal field (cf. eq. (1.92)), we can define the ellipticity and prolateness of the triaxial ellipsoid by

$$e = \frac{\Lambda_1 - \Lambda_3}{2\sum \Lambda_i} \qquad p = \frac{\Lambda_1 + \Lambda_3 - 2\Lambda_2}{2\sum \Lambda_i}. \tag{1.101}$$

The probability distribution of these shape parameters under the constraint of the peak height ν and peak curvature $x = \sum \Lambda_i/\sigma_2$, i.e. $\mathcal{P}(e, p|\nu, x)$, can also be computed analytically for a Gaussian random field [20]. It can be shown that the distribution depends only on x. The peak curvature x however will generally increase for larger peak heights[7]. Figure 1.7 shows some examples of the ellipticity-prolateness probability distribution at a fixed value of x. The larger x (and therefore the higher the peak), the more spherical ($e \to 0$) the peak becomes. Peaks of lower heights tend to be more elliptical, with a higher probability of positive prolateness ($p > 0$). Associating these peak-patches to regions that will later collapse to halos, we therefore expect that more massive halos (larger peak-heights) will form from more spherical regions in the initial overdensity field, whereas less massive halos tend to originate from more elliptical regions. We will measure the shapes of proto-halos in chapter 5.

1.4.3 Halo abundance

We will now derive an estimate of the abundance of collapsed objects, the halo mass function (HMF), following the prescription by Press and Schechter (PS) [264]. The critical assumption that PS made is that, even if the field is non-linear on small-scales, linear theory is still able to predict the amplitude of long-scale modes, requiring that the large-scale power exceeds the power generated via non-linear coupling of small-scale modes [335, 242].

Given an overdensity field δ_M smoothed on the mass scale M, we can identify positions $\boldsymbol{x}$ at which the overdensity exceeds the critical density discussed in the previous section, i.e. where $\delta_M \geq \delta_c$. The argument of PS says that these points will be contained in a halo of mass $M_H \geq M$. Since δ_M is a Gaussian field with variance $\sigma^2(M)$ given eq. (1.80), we can compute the probability of δ_M exceeding δ_c by

$$\mathcal{P}(\delta_M > \delta_c) = \frac{1}{\sqrt{2\pi}\sigma(M)} \int_{\delta_c}^{\infty} \mathrm{d}\delta\ \exp\left[-\frac{\delta^2}{2\sigma^2(M)}\right] = \frac{1}{2}\left[1 - \mathrm{erf}\left(\frac{\nu}{\sqrt{2}}\right)\right], \tag{1.102}$$

where $\nu = \delta_c/\sigma(M)$ is the peak-height defined in the last section and $\mathrm{erf}(x) = 2\pi^{-1/2}\int_0^x \mathrm{d}y\, e^{-y^2}$. Since according to the cosmological principle $\sigma(M) \to 0$ for $R \to \infty$, we can always find a smoothing scale M' at which $\delta_{M'} = \delta_c$ if $\delta_M > \delta_c$. Arguing that half of the mass that will eventually be accreted is unaccounted for ($\delta < 0$), PS introduced a “fudge”-factor by multiplying the probability by 2, providing a better fit to observations. This probability is then related to

[7] The characteristic scale is $x_* = \nu\sigma_1^2/(\sigma_2\sigma_0)$. Analytic formulae of the conditional probability distributions $\mathcal{P}(e, p|x)$ and $\mathcal{P}(x|\nu)$ can be found in [20] and [221].

the number density of halos with mass $M_H \in [M, M + \mathrm{d}M]$ per unit comoving volume by $(\mathrm{d}n/\mathrm{d}M)\mathrm{d}M = \bar{\rho}/M\ (\mathrm{d}\mathcal{P}/\mathrm{d}M)\mathrm{d}M$, which we can write as

$$\begin{aligned}\frac{\mathrm{d}n}{\mathrm{d}M}\,\mathrm{d}M &= -2\frac{\bar{\rho}}{M}\left(\frac{\mathrm{d}\mathcal{P}(\delta_M > \delta_c)}{\mathrm{d}\sigma(M)}\right)\left(\frac{\mathrm{d}\sigma(M)}{\mathrm{d}M}\right)\,\mathrm{d}M \\ &= -\sqrt{\frac{2}{\pi}}\frac{\bar{\rho}}{M\sigma(M)}\left(\frac{\mathrm{d}\sigma(M)}{\mathrm{d}M}\right)\nu e^{-\nu^2/2}\,\mathrm{d}M.\end{aligned} \tag{1.103}$$

This function is known as the *PS mass function* [264], and given its simplicity, it is able to describe results from N-body simulations to a surprising degree (cf. fig. 1.8). However, the derivation contains strong simplifications (e.g. spherical symmetry and negligence of peaks-within-peaks, see e.g. [224]), a somewhat arbitrary fudge-factor of 2, and the comparison with simulations is still far from perfect. There has been substantial research into dealing with these caveats (see e.g. [221] for an overview).

The PS mass function can be derived in a more thorough way with the *excursion set* formalism, which is sometimes also referred to as the *extended PS formalism* [42]. In this theory, the fraction of matter in gravitationally bound objects of mass M is estimated from the first-crossing distribution of Markovian random walk trajectories (i.e. estimating the probability of the random walk exceeding a threshold δ_c) when decreasing the filtering scale of the overdensity field (see e.g. [221]). The theory naturally produces the factor 2 that had to be included with an ad-hoc argument in the PS derivation. Furthermore, one can replace the critical threshold from the spherical collapse model with the more general and mass dependant threshold of the ellipsoidal model to account for the triaxial nature of gravitational collapse [289]. Since lower mass halos are generally influenced by more elliptic tidal fields (cf. fig. 1.6), the collapse time is longer and thus the required collapse threshold higher, reducing the number of expected low mass halos (cf. the HMF comparison in fig. 1.8).

A further model to predict the locations of halo formation in the initial conditions is the *peak-patch* model [43], which combines the theory of density peaks discussed in the previous section and the excursion set formalism (also see [303] for a recent implementation to create mock halo catalogs). In addition to the purely theoretical HMF, there is a large variety of fitting formulas calibrated from numerical simulations available (e.g. Sheth & Tormen 1999 [288], Jenkins et al. 2001 [170], Warren et al. 2006 [323], Tinker et al. 2008 and 2010 [314, 313], etc.). Nevertheless, the PS formalism still provides useful insight into hierarchical structure formation. From the exponential cutoff in eq. (1.103), we can see that halos can only form in significant numbers if $\nu > 1 \Leftrightarrow \sigma(M) > \delta_c$, defining the characteristic non-linear scale

$$\sigma(M_{\mathrm{NL}})D_+(t) = \delta_c. \tag{1.104}$$

1.5 Properties of DM Halos

The exact definition of where to put the boundary of a halo, and thus which mass and radius it will have, is a disputed topic and various conventions are being used. A common way to define the halo edge is by using a spherical overdensity criterion, either with respect to the background density or to the critical density of the universe. The mass and radius of the sphere where this

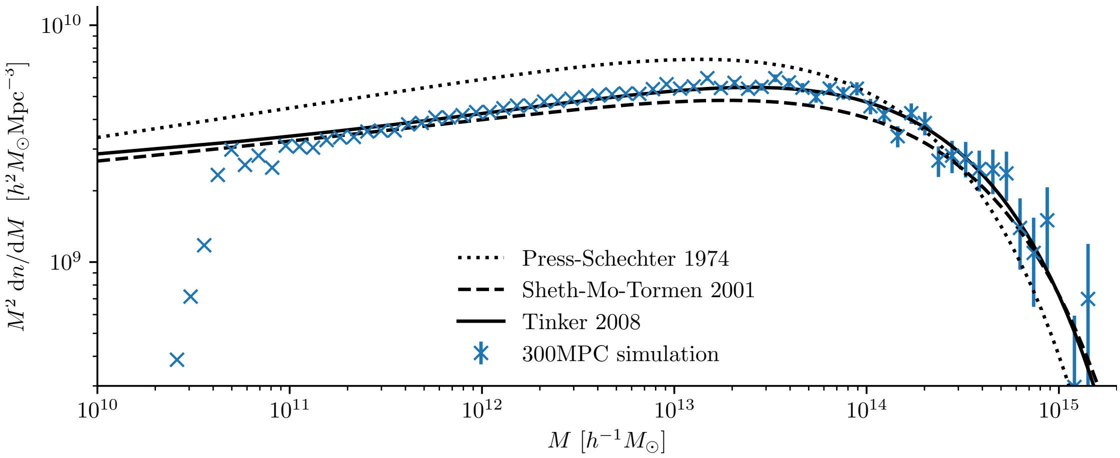

Figure 1.8: HMF measured from the 300MPC simulation (cf. appendix A.3) in comparison with the theoretical predictions by the spherical collapse model by Press and Schechter [264], the ellipsoidal collapse model by Sheth et al. 2001 [289], and the fitting function by Tinker et al. 2008 [314]. The HMF is multiplied by M^2 for visualization purposes to compress the dynamic range. At masses below $10^{11} h^{-1} M_\odot$, the halos in the simulation are no longer well resolved, causing the measured HMF to drop. At high masses, only few halos exist in the simulation volume, increasing the Poisson noise.

critical overdensity Δ is reached, is then denoted by $M_{\Delta b}$ and $R_{\Delta b}$ or $M_{\Delta c}$ and $R_{\Delta c}$ respectively. The most common value for Δ is 200 (close to the virial overdensity from the spherical collapse model, cf. section 1.4). However, in research fields interested in the inner structure of the halo, larger thresholds such as $\Delta = 500$ or $\Delta = 2500$ are being used (e.g. for scaling relations of different galaxy cluster properties).

Early simulations showed that the density distribution within the halos do not follow a uniform power law, but instead the logarithmic slope changes gradually from -1 near the center[8] to -3 at large radii, with remarkable similarity between a large range of halos [231]. The density profiles have found to be well fitted by a two-parameter formula, known as the NFW profile:

$$\rho(r) = \frac{\rho_0}{(r/r_s)(1 + (r/r_s)^2)}, \tag{1.105}$$

where ρ_0 is the characteristic density and r_s is the scale radius indicating where the slope is roughly -2. The ratio between the halo radius and the scale radius determines the concentration of the halo, i.e. $c_{\Delta(b/c)} = R_{\Delta(b/c)}/r_s$. The concentration parameter has been shown to decrease with increasing halo mass, and to increase with the age of the halo and the time since the last major merger event. The universality of the NFW profile is thought to be established by the early formation process of the halo with frequent merger events [221]. These establish the inner

[8] Rotation curve measurements from some galaxies suggest a flat inner density profile incompatible with the numerical predictions of the ΛCDM model. This so-called *cusp–core* tension might arise from unaccounted baryonic physics [53].

structure of the halo and thus set r_s, whereas late time accretion increases the mass and radius of the halo without affecting the core of the halo and therefore leaving r_s roughly fixed and increasing the concentration over time.

With the availability of higher resolution simulations, deviations from the NFW profile were found [307] and the use of a three parameter formula, known as the Einasto profile, was proposed to account for these [230]:

$$\rho(r) = \rho_0 \exp\left(-\frac{2}{\alpha}\left[\left(\frac{r}{r_s}\right)^{\alpha} - 1\right]\right). \tag{1.106}$$

The shape parameter α determines how quickly the profile steepens towards the outskirts, and generally increases with mass but has a wide distribution [115].

Due to the anisotropic nature of the collapse, halos are not expected to follow the idealized spherical picture described so far, but rather have elliptical shapes. Numerical simulations show that massive halos and halos at high redshifts tend to be more aspherical [5], and halos that have recently experienced a major merger have a tendency to be oblate. The halo shapes are correlated over large distances and tend to be aligned with the large scale environment [19, 156]. This phenomenon is known as *intrinsic alignment* [149, 317] and has to be accounted for in studies measuring the correlated shape distortion of background galaxies from the foreground matter distribution.

Halos are kept in equilibrium by pressure support from velocity dispersion that can be split in a radial and tangential component ($\sigma_r^2(r)$ and $\sigma_t^2(r)$ respectively). The distribution between the two components is parametrized by the anisotropy parameter

$$\beta(r) = 1 - \frac{\sigma_t^2}{2\sigma_r^2}, \tag{1.107}$$

hence $\beta = 1$ corresponds to a purely radial, $\beta = \infty$ to a purely tangential, and $\beta = 0$ to an isotropic system. In simulations, typical dark matter halos appear to have more isotropic velocity dispersion in the inner regions and radially biased anisotropy at larger radii [107].

In the linear collapse regime, halos can acquire angular momentum due to the misalignment between tidal forces and the inertia tensor of the proto-halo [161, 243]. This phenomenon is described in the *tidal torque theory* (TTT, [331]). This initial angular momentum may, however, be significantly altered during the non-linear evolution and during merger events. The amount of coherent rotation with respect to random motion in a halo can be expressed as the dimensionless (Peebles) spin parameter [243]

$$\lambda_P = \frac{J\sqrt{|E|}}{GM^{5/2}}, \tag{1.108}$$

where J is the magnitude of the angular momentum, E the total energy, and M the halo mass. The total energy is a hard to measure parameter in both observations and simulations. Therefore, an alternative definition of the spin parameter exists, the Bullock spin parameter [52], which can be derived from λ_P under the assumption of an isothermal density profile:

$$\lambda_B = \frac{J}{\sqrt{2}MRv_c} = \frac{J}{\sqrt{2GRM^3}}, \tag{1.109}$$

where $v_c = \sqrt{GM/R}$ is the virial circular velocity. Simulations show that the angular momentum vector tends to be aligned with the minor axis of the ellipsoid describing the halo [19]. There is also a large environmental effect on the orientation of the angular momentum: low mass halos prefer to spin along the filament or the wall they are embedded in, whereas more massive halos have a tendency to rotate perpendicular to their structure [132, 198].

Due to the hierarchical growth of halos in the CDM model, a large fraction of mass is accreted via mergers. After a merger event, the lower mass halo becomes a subhalo orbiting in the potential of its host. Strong tidal forces and dynamic friction strip away weakly bound mass of the subhalo and whether a substructure survives or is completely disrupted within the host halo depends on the orbital parameters, the relative mass, and its concentration parameter. High resolution simulations show that a large fraction of the halo mass remains in the form of substructure down to the resolution scale (e.g. [124]). Furthermore, it has recently been shown that N-body simulations suffer from significant overmerging and therefore at least some of the observed disruption is artificially induced by discreteness effects [48]. The fact that we are unable to observe this rich substructure in our galaxy and the neighboring galaxies (the *missing satellites problem*) is expected due to baryonic effects [53], e.g. lower density cores of medium sized satellites from stellar feedback and interactions such as tidal and ram pressure stripping between the satellites and the host galaxies.

CHAPTER 2

Cosmological Simulations

In the previous chapter, we have shown how small perturbations with $\delta \ll 1$ can be treated analytically in the linear approximation. However, as perturbations grow and $\delta \sim 1$, the predictive power of these solutions decreases. Higher order approximations (such as n-loop order approximations [38] and renormalized perturbation theory [70]) only converge slowly, and in general a full non-linear treatment using numerical simulations is needed. While dark matter can assumed to be collisionless, and thus be treated by conventional collisionless N-body methods, baryonic physics is more complex and requires the hydrodynamic equations to be solved as well as the modeling of processes below the resolution of simulations, such as gas cooling, star formation, metallicity enrichment, feedback mechanisms from supernovae and black holes, and interactions between ionized matter and magnetic fields (see e.g. [295]).

This chapter provides a brief overview of numerical methods used in a cosmological context. We discuss the collisionless dynamics solved in N-body simulations and how initial conditions are set up (section 2.1), how structures in N-body simulations are identified (section 2.2), and how the Lagrangian information can be used to reconstruct the phase-space distribution from the N-body tracers (section 2.3). The simulations that have been performed for this thesis and analyzed in the subsequent chapters are described in appendix A.3.

2.1 N-body Methods for Collisionless Dynamics

The state of a collisionless system is captured by the phase-space distribution function $f(\boldsymbol{x}, \boldsymbol{p}, t)$, and evolves according to the Vlasov-Poisson system of equations (cf. eqs. (1.35) and (1.36)). Solving this partial differential equation with an Eulerian scheme directly in seven dimensions is extremely difficult due to the number of dimensions, the necessary resolution because of the strong clustering of matter at late times, and the complex multistreaming distribution of cold dark matter in the non-linear regime. Even with recent progress in solving the system in the full six dimensional phase space (e.g. [342, 308, 78]), memory requirements still limit the usability of these solvers for large scale simulations needed in cosmology.

The other method of solving the equations is by sampling the phase-space distribution by discrete particles. These N particles trace the continuous phase-space function, and since $\mathrm{D}f/\mathrm{D}t = 0$ along the flow, the particle masses are conserved as well. The flow (the formal solution of the Vlasov-Poisson system) is given in the form of *characteristics*: a set of curves in 6+1 dimensional space which fill the entire volume but do not intersect each other. Their trajectories $(\boldsymbol{x}, \boldsymbol{p}, t)(s)$

are given by the differential equations

$$\frac{\mathrm{d}\boldsymbol{x}}{\mathrm{d}s} = \frac{\boldsymbol{p}(s)}{m} \qquad\qquad \frac{\mathrm{d}\boldsymbol{p}}{\mathrm{d}s} = -m\nabla\Phi(\boldsymbol{x}(s), s). \tag{2.1}$$

Using the scale factor a as the time variable, we can rewrite the evolution as

$$\frac{\mathrm{d}\boldsymbol{x}}{\mathrm{d}a} = \frac{\boldsymbol{p}}{ma^3 H} \qquad\qquad \frac{\mathrm{d}\boldsymbol{p}}{\mathrm{d}a} = -m\frac{\nabla\Phi}{aH}. \tag{2.2}$$

The N particles that we use to sample the phase-space follow these trajectories. The accuracy of this method, thus, naturally depends on the resolution parameter N. The exact sampling of the phase space depends on our requirements: if we want to simulate a large volume with uniform accuracy, we will uniformly sample the phase-space with equal mass particles. However, if we are interested in a particular region, we can increase the resolution in that area by sampling with a larger number of low-mass particles and cover the rest of the volume with a few high-mass particles. In section 2.1.3, we will discuss the setup of the initial simulation state in more detail.

Going back to eq. (2.2), we find that the numerical integration of the particle trajectories consists of two parts: a gravity step in which forces from the particle positions are computed, and a time integration step to update the particle positions and momenta given the force field. We will discuss these two parts in the following.

2.1.1 Time integration

The N-body system is a Hamiltonian system; for each particle we can write the phase-space coordinates as $\boldsymbol{w} = (\boldsymbol{q}, \boldsymbol{p})$ and its Hamiltonian as $\mathcal{H}(\boldsymbol{q}, \boldsymbol{p}) = \boldsymbol{p}^2/(2ma^2) + m\Phi(\boldsymbol{q})/(2a)$ [74]. The evolution of the system is then given by Hamilton's equations which we write as

$$\dot{\boldsymbol{w}} = \mathrm{D}_{\mathcal{H}}(\boldsymbol{w}), \tag{2.3}$$

where $\mathrm{D}_{\mathcal{H}} = \{\cdot, \mathcal{H}\}$ is the Liouville operator acting on $\boldsymbol{w}$ via the Poisson bracket $\{A, B\} = \partial_{\boldsymbol{x}} A\, \partial_{\boldsymbol{p}} B - \partial_{\boldsymbol{x}} B\, \partial_{\boldsymbol{p}} A$. The formal solution of this equation can be written as a canonical transformation

$$\boldsymbol{w}(t + \Delta t) = e^{\Delta t \mathrm{D}_{\mathcal{H}}} \boldsymbol{w}(t), \tag{2.4}$$

where we can think of the operator $e^{\Delta t \mathrm{D}_{\mathcal{H}}}$ as a symplectic map from time t to $t + \Delta t$ preserving the phase-space volume. Any numerical integrator should thus also respect the symplectic structure to produce stable and accurate results.

There is no general simple solution for eq. (2.3). We can, however, use the fact that the Hamiltonian for the N-body problem is separable in a kinetic and potential part by $\mathcal{H}(\boldsymbol{q}, \boldsymbol{p}) = \mathcal{T}(\boldsymbol{p}) + \mathcal{V}(\boldsymbol{q})$. We can thus split the symplectic map by

$$e^{\Delta t \mathrm{D}_{\mathcal{H}}} \simeq e^{\Delta t \mathrm{D}_{\mathcal{V}}} e^{\Delta t \mathrm{D}_{\mathcal{T}}}. \tag{2.5}$$

Note that this is only an approximation since $[\mathrm{D}_{\mathcal{T}}, \mathrm{D}_{\mathcal{V}}] \neq 0$, hence, using the Baker-Campbell-Hausdorff identity, the error is of quadratic order: $[\Delta t \mathrm{D}_{\mathcal{T}}, \Delta t \mathrm{D}_{\mathcal{V}}] \propto (\Delta t)^2$. The new operators, also known as the *drift* and *kick* operators, have the exact solutions[1]

$$e^{\Delta t \mathrm{D}_{\mathcal{T}}} \begin{pmatrix} \boldsymbol{x} \\ \boldsymbol{p} \end{pmatrix} = \begin{pmatrix} \boldsymbol{x} + (ma^{-2})\Delta t\, \boldsymbol{p} \\ \boldsymbol{p} \end{pmatrix} \tag{2.6}$$

$$e^{\Delta t \mathrm{D}_{\mathcal{V}}} \begin{pmatrix} \boldsymbol{x} \\ \boldsymbol{p} \end{pmatrix} = \begin{pmatrix} \boldsymbol{x} \\ \boldsymbol{p} - (ma^{-1})\Delta t\, \nabla\Phi \end{pmatrix}. \tag{2.7}$$

The time integration scheme in eq. (2.5) is also known as the symplectic Euler scheme and is accurate to first order in Δ_t. The accuracy can be improved to order $(\Delta t)^n$ by combining multiple kick and drift steps

$$e^{\Delta t \mathrm{D}_{\mathcal{H}} + \mathcal{O}(\Delta_t^{n+1})} = \prod_i^N e^{a_i \Delta t \mathrm{D}_{\mathcal{V}}} e^{b_i \Delta t \mathrm{D}_{\mathcal{T}}}, \tag{2.8}$$

where the coefficients a_i and b_i fullfil $\sum_i a_i = \sum_i b_i = 1$, and have to be chosen such that the required accuracy is achieved. This can be done by analyzing the Baker-Campbell-Hausdorff identity and requiring terms of lower order to vanish (see e.g. [105] for a fourth order integrator and [341] 6th and 8th order integrators).

The most common scheme that is used for collisionless N-body simulations is the kick-drift-kick leap-frog integrator, which is the second order scheme obtained by setting the coefficients to $a_0 = a_1 = 0.5, b_1 = 1, b_2 = 0$:

$$e^{\Delta t \mathrm{D}_{\mathcal{H}} + \mathrm{D}_{\mathcal{H}_{\mathrm{err}}}} = e^{\frac{1}{2}\Delta t \mathrm{D}_{\mathcal{V}}} e^{\Delta t \mathrm{D}_{\mathcal{T}}} e^{\frac{1}{2}\Delta t \mathrm{D}_{\mathcal{V}}}. \tag{2.9}$$

In theory, the symplectic drift-kick-drift integrator could also be used with $a_0 = 0, a_1 = 1, b_1 = b_2 = 0.5$. However, it has been shown that the error in this method grows faster than in the kick-drift-kick variant if variable timesteps are being used [300]. Higher order schemes are rarely used for cosmological N-body simulations, as the particles are collisionless and close two-body encounters where a higher-order scheme would be beneficial, are avoided by force softening (see below).

Adaptive timesteps

In cosmological simulations, gravitational forces cover a large dynamic range. Integrating short-range interactions within high density regions, such as galaxies and clusters, require smaller timesteps than the long range gravitational field of the large scale structure. Unfortunately, varying Δt in space and time generally breaks the symplectic nature of the integrator. By splitting the potential into a long-range and a short-range potential $\mathcal{V}_{\mathrm{lr}}$ and $\mathcal{V}_{\mathrm{sr}}$ however, one can construct a symplectic map by [300]

$$e^{\frac{1}{2}\Delta t \mathrm{D}_{\mathcal{V}_{\mathrm{lr}}}} \left(e^{\frac{1}{2m}\Delta t \mathrm{D}_{\mathcal{V}_{\mathrm{sr}}}} e^{\frac{1}{m}\Delta t \mathrm{D}_{\mathcal{T}}} e^{\frac{1}{2m}\Delta t \mathrm{D}_{\mathcal{V}_{\mathrm{sr}}}} \right)^m e^{\frac{1}{2}\Delta t \mathrm{D}_{\mathcal{V}_{\mathrm{lr}}}}, \tag{2.10}$$

which corresponds to m short-range kick-drift-kick leap-frogs before updating the long-range potential. This method naturally works together with the hybrid force calculations discussed in section 2.1.2.

[1] Note that if the integration time is long compared to the expansion of the universe, we have to replace $\Delta t/a$ and $\Delta t/a^2$ by $\int_t^{t+\Delta t} \mathrm{d}t\, a(t)^{-1}$ and $\int_t^{t+\Delta t} \mathrm{d}t\, a(t)^{-2}$ respectively.

A common criterion to determine the time-step of an individual particle is given by $\Delta t_i = \eta\sqrt{\epsilon/|\boldsymbol{a}_i|}$, where $\boldsymbol{a}_i$ is the acceleration of the particle, ϵ the force softening (see below) and η an accuracy parameter (e.g. [300, 74]). This rule has been shown to produce robust results (see [263] for a comparison of different criterions).

2.1.2 Force calculation

Cosmological simulations only cover a limited volume of the entire Universe. In order to implement isotropy and homogeneity on large scales, one can apply periodic boundary conditions to the simulated box. Assuming a cubic volume of size L, the potential then becomes [74]

$$\Phi(\boldsymbol{x}, t) = -G \sum_{\boldsymbol{n}} \int \mathrm{d}^3\boldsymbol{p}\, \mathrm{d}^3\boldsymbol{x}' \, \frac{f(\boldsymbol{x}' + \boldsymbol{n}L, \boldsymbol{p}, t)}{|\boldsymbol{x} - \boldsymbol{x}' - \boldsymbol{n}L|}, \tag{2.11}$$

where $\boldsymbol{n} = (i, j, k)$ represents the box replica shifted by the distance $\boldsymbol{n}L$. The periodic sum can be approximated using Ewald's method [98]. If Fourier methods are used to compute the forces, periodicity is naturally provided.

Naively evaluating the phase-space moment in eq. (2.11) from the particle distribution results in equations of motions of a collisional system, which allows for two-body encounters with diverging forces. However, the dark matter particles in cosmological N-body simulations are tracers of the continuous dark matter phase space distribution rather than actual particles; hence, such short-range interactions would not be physical. This problem can be alleviated by introducing force-softening, with the goal of estimating a smooth density distribution from the particle data. We can replace the Dirac-δ peaks by kernels characterized by the softening length ϵ such that we can write the density as [76]

$$\tilde{\rho}(\boldsymbol{x}) = \sum_{i}^{N} \frac{m_i}{\epsilon^3} W(|\boldsymbol{x} - \boldsymbol{x_i}|/\epsilon_i). \tag{2.12}$$

Commonly used kernels are the Plummer sphere [257]

$$W(r) = \frac{3}{4\pi\left(1 + r^2\right)^{5/2}}, \tag{2.13}$$

and the cubic spline kernel first applied to solve SPH problems [226]

$$W(r) = \frac{1}{4\pi\epsilon^3} \begin{cases} 4 - 6r^2 + 3r^3 & r < 1 \\ (2 - r)^3 & 1 \leq r < 2 \\ 0 & r \geq 2. \end{cases} \tag{2.14}$$

It has been shown that the spline kernels produce more accurate forces than the Plummer sphere (see [76] for a comparison of the performance of various kernels.)

Lower bounds on the softening length ϵ can be found by limiting typical deflection angles in close encounters [333], and by requiring that two-body forces do not exceed the typical mean-field strength [263]. For a virialized system of mass M and radius R, one finds $\epsilon > \epsilon_{\text{min}} \sim$

$R/\sqrt{N}$, where $N = M/m$ is the number of particles. Choosing a large softening length will allow for larger timesteps and thus decrease the total number of force computations required. However, with increasing softening length, the effective resolution of the simulation is reduced. A good choice of ϵ thus has to balance these two opposing effects. Analyzing the convergence of halos in cosmological simulations, Power et al. [263] suggest $\epsilon \sim 4\epsilon_{\mathrm{min}}$. This proposal has been widely adopted for many zoom simulations (cf. section 2.1.3), such as the Phoenix [114], AGORA [178], and Auriga [122] simulations. For uniform mass resolution simulations that are not targeted on a specific halo, the softening length is usually set to be a fraction of the mean particle separation, with suggested values ranging from 1/120 [181], $1/60$ [208], to 1/10 [179]. For our simulations (cf. appendix A.3), we adopt the commonly used factor 1/50.

Direct force computation

Computing the forces by pairwise summation is of order $\mathcal{O}(N^2)$, where N is the total number of particles. For large N, this becomes computationally too expensive and better scaling methods such as the ones discussed below have to be used. However, for small simulations and short range force calculations on optimized hardware (cf. section 2.1.2), the small overhead of this simple method may actually result in an overall faster computation.

Tree codes and fast multipole methods

Tree codes and fast multipole methods approximate eq. (2.11) by splitting the volume into distinct groups for which the force contributions can be evaluated by a single expression if certain requirements are met. This reduces the complexity by not having to iterate over all individual particles.

Tree codes [23] split the volume into a hierarchical spatial tree such as cubic oct-trees or binary KD-trees. Each node is split until the leaf nodes contain fewer than n_{max} particles. In a preparatory step, the multipole expansions have to be computed for each node recursively. Forces can then be computed by "walking" through the tree, starting by the top node: if the multipole expansion of the node provides an accurate enough force estimate (i.e. if the node is small and distant enough, expressed as the opening angle), the walk along this specific branch of the tree is stopped and the force estimate used. Otherwise, the node is "opened" and the algorithm progresses by analyzing each of the children. The number of force computations for each particle scales with the depth of the tree ($\sim \log N$) and tree algorithms are thus of order $\mathcal{O}(N \log N)$. A specific tree method is characterized by the maximum order of multipole expansion, the opening criterion, and the spatial grouping algorithm. The widely used GADGET2 code [300] for example uses an oct-tree with only monopole moments (total masses), which, when expressed with respect to the center of mass, have vanishing dipoles and are thus first order accurate [74]. During the force evaluation, the parent node is opened if the estimated truncation error is larger than a relative threshold of the total force in the last time-step.

In addition to the particle-node interactions of the tree-code, fast multipole methods also consider node-node interactions by approximating the potential or force "landscape" within a node by a multipole expansion [123, 75]. This allows to lower the scaling of the force computation to

$\mathcal{O}(N)$, providing a very efficient method for high particle number simulations (e.g. PKDGRAV3 [262]).

Particle-Mesh methods

Instead of solving Poisson equation by direct summation or tree approximations, one can solve the differential equations on a regularly spaced grid and with the help of Fast Fourier Transforms (FFT). These schemes are called *particle-mesh* (PM) methods and are $\mathcal{O}(N_{\mathrm{grid}} \log N_{\mathrm{grid}})$ for the FFT and $\mathcal{O}(N)$ for the mass assignment and the force interpolation. Gravitational softening is implicitly applied on the length scale of the cell size. To compute the forces, we note that in Fourier space, the potential is given by

$$\hat{\Phi}(\boldsymbol{k}) = \frac{4\pi G\bar{\rho}}{|k|^2}\hat{\delta}(\boldsymbol{k}). \tag{2.15}$$

The force field can then be calculated by multiplying $\hat{\Phi}$ with $-i\boldsymbol{k}$ and applying an inverse Fourier transform or alternatively by transforming the potential back to real space first and then using a finite difference scheme [300]. We can then interpolate the forces from the grid to the particle positions. This method requires the computation of the overdensity field δ on the grid from the particle positions. There are different mass assignment methods depending on the shape that we assign to the particles [154]. The most common methods are the nearest grid-point (NGP), cloud-in-cell (CIC), and triangular-shaped-clouds (TSC) scheme with the one dimensional shape functions

$$S_{\mathrm{NGP}}(x) = \frac{1}{\Delta x}\delta_D(x) \tag{2.16}$$

$$S_{\mathrm{CIC}}(x) = \frac{1}{\Delta x}\begin{cases} 1 & |x| \leq \frac{\Delta x}{2} \\ 0 & \text{otherwise} \end{cases} \tag{2.17}$$

$$S_{\mathrm{TSC}}(x) = \frac{1}{\Delta x}\begin{cases} 1 - \frac{x}{\Delta x} & |x| \leq \frac{\Delta x}{2} \\ 0 & \text{otherwise} \end{cases} , \tag{2.18}$$

where Δx is the size of a cell. The three-dimensional shape function is just the product $S_{3\mathrm{d}}(\boldsymbol{x}) = \prod_i S(x_i)$. A cell that is offset by $\boldsymbol{x}$ from the particle is thus assigned the weight $w_{3\mathrm{d}}(\boldsymbol{x}) = \prod_i w(x_i)$, with the one-dimensional assignment functions given by

$$w_{\mathrm{NGP}}(x) = \begin{cases} 1 & |x| \leq \frac{\Delta x}{2} \\ 0 & \text{otherwise} \end{cases} \tag{2.19}$$

$$w_{\mathrm{CIC}}(x) = \begin{cases} 1 - \frac{|x|}{\Delta x} & |x| \leq \Delta x \\ 0 & \text{otherwise} \end{cases} \tag{2.20}$$

$$w_{\mathrm{TSC}}(x) = \begin{cases} \frac{3}{4} - \left(\frac{|x|}{\Delta x}\right)^2 & |x| \leq \frac{\Delta x}{2} \\ \frac{1}{2}\left(\frac{3}{2} - \frac{|x|}{\Delta x}\right)^2 & \frac{\Delta x}{2} \leq |x| \leq \frac{3\Delta x}{2} \\ 0 & \text{otherwise} . \end{cases} . \tag{2.21}$$

The total density assigned to the cell at position $\boldsymbol{x}_c$ by all particles is given by the convolution

$$\rho(\boldsymbol{x}_\mathrm{c}) = \frac{m}{(\Delta_x)^3} \int \mathrm{d}^3\boldsymbol{x}' n(\boldsymbol{x}') w(\boldsymbol{x}_\mathrm{c} - \boldsymbol{x}'). \tag{2.22}$$

The artificial smoothing introduced by the grid projection needs to be deconvolved in Fourier space by dividing with the Fourier transform of the assignment function, which is given by [173]

$$\hat{w}(\boldsymbol{k}) = \prod_i \mathrm{sinc}^n \left(\frac{k_i L}{2N} \right), \tag{2.23}$$

where $n = 1$ for NGP, $n = 2$ for CIC, and $n = 3$ for TSC. Since the force field is calculated on the grid and forces have to be interpolated back to the particle position using the same scheme, this correction has to be applied twice [300].

As an alternative to solving the Poisson equation on the grid with Fourier transforms, relaxation methods such as Gauss-Seidel iterations can be used to invert the finite-difference matrix equation. The convergence rate can be drastically improved by using a hierarchy of coarser discretizations for which relaxation occurs faster, and propagating the results along the hierarchy [49, 326]. One can show that with appropriate relaxation methods, a scaling of $\mathcal{O}(N_\mathrm{grid})$ can be achieved [316]. Additionally, multigrid methods allow for non-uniform grids adapted to the local particle density (similar to tree and fast multipole methods), and require only a small boundary layer from the neighboring processors, reducing the communication overhead in massively parallel setups [125].

Hybrid methods

Each of the methods discussed above have advantages and disadvantages which may be compensated by using a combination of methods. The FFT PM solver for example automatically accounts for periodic boundary conditions, lacks however in spatial resolution on small-scales. Thus, a long-range solver using FFTs is often combined with direct summation (*P^3M* [93]) or tree codes (*TreePM* [338, 40]). In multigrid PM methods, FFTs can be used on the coarsest grid to implement periodic boundary conditions [188].

The optimal combination of methods also depends on the hardware architecture. Although TreePM has a better scaling relation than direct summation, it comes with a larger computational overhead and more complex data structures. The more compute-intensive but straight-forward particle-particle computation has been found to perform faster for local short-range computations on accelerated hardware (e.g. GPUs), whereas TreePM is preferred if only CPUs are available [131].

2.1.3 Initial Conditions for Cosmological Simulations

The N-body simulation has to be initialized with a random realization of the perturbation field at the starting redshift, the *initial conditions* (ICs). Note that the initial redshift has to be chosen high enough so that the perturbations on the sampled scales are still in the linear regime, but it also has to be well in the matter-dominated era to be suitable for an N-body simulation. The

Gaussian random field can be generated in Fourier space from the power spectrum defined in eq. (1.77) and the probability distribution of the real and imaginary components of $\delta(\boldsymbol{k}, z_{\mathrm{start}})$ given by eq. (1.76). However, this naïve sampling in Fourier space introduces a significant error in the real-space statistical properties due to the finite box size [247, 291]. Better results are thus obtained by sampling a white noise field $\mu(\boldsymbol{x}_{ijk})$ and the discretized correlation function in real-space $\xi(|\boldsymbol{x}_{ijk}|)$, and by performing a convolution, i.e. [133]

$$\delta(\boldsymbol{x}) = \xi(|\boldsymbol{x}|) * \mu(\boldsymbol{x}). \tag{2.24}$$

Even though the sampling is done in real space, the convolution can still be performed in Fourier space using FFTs.

Once the linear perturbation field has been generated, the simulation particles have to be sampled so that the constraints given by the density field are obeyed. We can use the Lagrangian perturbation theory discussed in section 1.2.4 to compute the displacement and velocity fields for particles at Lagrangian coordinates $\boldsymbol{q}$. These Lagrangian coordinates are usually chosen on a regular grid, however other possibilities exist, such as glass-like initial conditions, where particles are first placed randomly, and the system is evolved backwards until it reaches a quasi-equilibrium, creating a Lagrangian point-set without preferred directions [332, 322]. Further methods for Lagrangian particle distributions include quaquaversal tiling (Q-SET) [142] and capacity constrained Voronoi tessellation (CCVT) [197].

To compute the velocity and displacement fields in the ZA or higher order Lagrangian perturbation theory from these initial Lagrangian particle distributions, Poisson's equation and gradients have to be computed (cf. eq. (1.66)), either in Fourier space or using a finite difference scheme (cf. [133]).

Zoom initial conditions

Cosmological simulations span an enormous range of scales, from the LSS on sizes up to gigaparsecs down to individual galaxies and their substructures on scales ranging from several parsecs to kiloparsecs. The computational cost of computing and storing the full dynamic range in the entire simulated volume sets a limit on the upper and lower scales that can be simulated in a single run. A popular approach to circumvent this limitation is the so-called *multi-mass* or *zoom* technique, in which the immediate region around the object of interest is simulated with a highly increased resolution compared to its surrounding large scale environment. This allows capturing both the influences of the cosmic environment from fluctuations on scales equal and larger than the object as well as small scale fluctuations affecting the structure of the object directly.

To set up such a zoom simulation, the Lagrangian volume that collapses to the object of interest at later times has to be known, requiring to run a full (i.e. uniform mass) simulation first and tracing back the particles to their initial position. We will discuss the process to set up zoom simulations in detail in chapter 4, and we will study the Lagrangian volumes from which halos form, the emphproto-halos, in chapter 5.

One usually abstracts the shape of the Lagrangian volume spanned by the traced-back particles to a more regular and convex description, which corrects to some degree for potentially irregular shapes due to the limited number of tracer particles. Common Lagrangian volume descriptors include minimum bounding rectangular boxes, rotated rectangular boxes, minimum bounding ellipsoids, and convex hulls (cf. [239]). Once the Lagrangian proto-halo region is determined, it can be sampled in a higher resolution than the remaining box. There are two common approaches to do this multi-mass sampling: either, the initial conditions can be generated at high resolution for the entire box and subsequently degraded outside the target region, or, small-scale perturbations can be added to the coarse resolution withing the zoom region [36, 133]. Typically, one uses the second approach, as the memory requirements for the first method quickly become unfeasible. Special care needs to be taken to guarantee continuity and differentiability across coarse-fine boundaries, and to assure that the refined grid adheres to the Fourier modes of the coarse grid, see [133] for a detailed description. A widely used multi-scale IC generator is MUSIC [133], which we will also be using to set up the simulations used in this thesis, and which forms the foundation of the *online cosmological initial conditions for zoom simulations* (COSMICWEB) project, which we will present in chapter 4.

2.2 Analysis of Structures in Simulations

An important post-processing task is the identification of different structures that formed during the gravitational collapse, as they provide the connection between the models of structure formation and actual observations and give insight into environmental dependent evolution of galaxies and halos. Therefore, various methods and tools were developed to map the phase-space distribution traced by the N-body particles to gravitationally bound objects and identify their distribution in a larger environmental context given by the cosmic web (cf. section 1.2.4).

2.2.1 Identifying gravitationally bound objects

Extracting halo catalogs from numerical simulations has a wide range of applications in cosmology. To constrain cosmological parameters, the observed LSS has to be compared with the theoretical abundance and clustering found in N-body simulations, requiring a consistent identification of gravitationally bound structures. Knowing the formation history and structure of halos, *semi-analytic models* can be applied to study the formation of galaxies and to generate mock catalogs. The abundance of substructure found in simulations can also be directly compared with observations and is important for accurate modeling of gravitational lensing (cf. e.g. [180, 7, 210].

The standard, most basic techniques that are being used for halo-finding are the *spherical overdensity* method (SO, [264, 190]) and the *friends-of-friends* algorithm (FoF, [72]). In the SO method, spheres are expanded around local density peaks until the mean density falls below a certain threshold (cf. section 1.5). The method proceeds iteratively, starting from the densest location in the simulation and removing all particles within an identified halo from the list of potential density peaks. However, it assumes that halos are spherical which might not correspond to the true shape of the gravitationally bound volume.

FoF algorithms are based on the simple concept that particles belong to the same group if they lie within some linking length b, expressed as a multiple of the mean particle separation. In this way, a group is roughly characterized by an isodensity contour $\rho \propto b^{-3}$. The commonly used linking length $b = 0.2$ corresponds approximately to $\rho \sim 60\bar{\rho}$. For a spherical halo with an isothermal profile $\rho(r) \propto r^{-2}$, this linking length implies a mean overdensity of 180, close to the virialized density threshold predicted by the spherical collapse model[2] [108, 190] (cf. section 1.4). The advantage of FoF algorithms is the absence of any shape assumptions and the simple numerical implementation via equivalence classes. HMF obtained with this method show a nearly universal and redshift independent behavior [170, 271]. However, the algorithm can cause spurious linking of neighboring halos in high density environments [121].

The SO and FoF methods work well for finding isolated halos, struggle however in dense environments and identifying subhalos orbiting around larger host halos. Various codes were thus developed to deal with these issues, by using additional information such as the complete 6D phase-space distribution [96, 30], Lagrangian information [99], and the time evolution [141]. A comprehensive comparison of different contemporary halo and subhalo finders can be found in the series of papers from the *halo finder comparison project* [182, 238, 183].

Halos can be tracked through the evolving simulation by following the constituting particles, assigning each halo a *descendant* halo in the next snapshot. We can then order the halos both in space and in time, building a *substructure* and *merger* tree. For the substructure tree, halos within the radius of a more massive halo, the *host* halo, can be assigned as its subhalos. In theory, this hierarchy can span over multiple levels, i.e. subhalos of subhalos, etc. In the time hierarchy, two or more halos may share a common descendant halo, or a previously *free* halo may become a subhalo in the next snapshot, both representing a merger event. T he merger can be classified by the mass ratio of the merging halos, with a major merger commonly referring to a ratio threshold of 1:3 (e.g. [73, 117]) or 1:4 (e.g. [176, 268]). By following the most massive progenitor halos back in time, one can extract the *main progenitor* branch.

2.2.2 Identifying components of the cosmic web

The anisotropic nature of gravitational collapse leads to the formation of a multi-scale network of walls, filaments and halos, the cosmic web, surrounding near-empty voids (cf. section 1.2.4, and also [329]). These patterns are also present in the distribution of observed galaxies (e.g. from the Sloan Digital Sky Survey SDSS [311]).

Understanding and analyzing the structure of the cosmic web is important for multiple reasons. The cosmic web defines the large-scale environment of forming halos and galaxies and the location of such objects in the cosmic web may thus influence their evolution and appearance today. A classic example of such an environmental effect is the origin of halo spin due to misalignments between the inertia tensor of the forming halo and the tidal field exerted by the environment [88, 331, 250, 203]. The topology of the cosmic web was also shown to have a strong impact on star formation activity of forming galaxies that can accrete cold gas efficiently through connected filaments at high redshifts (e.g. [77, 10]). The geometry of the cosmic web can also be used directly as a cosmological probe: the analysis of the distribution and morphology of voids for example can be used to gain insight into dark energy (e.g. [241, 327, 253]).

[2] Studies using percolation theory show that the isodensity contour does not correspond to a single density value, but to a range of values which for $b = 0.2$ is close to $81\bar{\rho}$ [227]. Furthermore, if only FoF is used, the mean halo density is sensitive to the halo profile, the substructure, and the mass resolution [323, 227].

Extracting the geometry and identifying the different components of the cosmic web is therefore an important task in the analysis of cosmological simulations. Similar to the different conventions and techniques used to identify halos, there are various different methods and codes to classify the cosmic web (also see the comparison papers by Colberg et al. [65] and by Libeskind et al. [199]). The main methods can be classified in roughly three categories:

- **Hessian based models** use the local geometric information in the Hessian of the tidal field or the velocity shear field. The tidal field causing the anisotropic collapse retains its anisotropic properties on large scales and thus its eigenvalue signatures can be used to classify the cosmic web (the so-called T-web classification, [43, 132, 138, 104]). The large scale velocity field is directly related to the tidal field in the linear regime (see section 1.2.4) and thus its shear contains the same geometric information (V-web classification, [155, 198]). The morphology of the density field can also directly be used (e.g. [13]). To capture the multi-scale nature of the cosmic web, the fields can be smoothed on a range of scales to identify components embedded in larger structures [61].

- **Topological methods** assign the cosmic web components to distinct large-scale topological properties of the studied field. By using a watershed technique on the density field for example, voids can be identified, and walls assigned to the two-dimensional structures separating them, filaments to the one-dimensional wall intersections, and nodes to the connections of filaments [255, 233, 12, 16]. This concept can be further developed using the mathematical concept of discrete Morse theory, allowing for a sophisticated segmentation of the volume [298].

- Finally, **phase-space** or **Lagrangian methods** use the folding of the dark matter sheet (cf. next section) to detect the axes along which gravitational collapse has already occurred and how far this collapse has proceeded. The *MultiStream Web Analysis* (MSWA) method by Shandarin et al. [285] (also see [269]) uses the phase-space tessellation method described in the next section to count the number of overlapping dark matter sheets at a given coordinate (i.e. the number of shell-crossings). These sheet numbers are then heuristically assigned to the cosmic web environments: voids: $n_{\text{stream}} = 1$, walls: $3 \leq n_{\text{stream}} < 17$, filaments: $17 \leq n_{\text{stream}} < 90$ and halos: $n_{\text{stream}} \geq 90$. The ORIGAMI [99] code finds the individual axes along which the Lagrangian particle ordering is inverted and thus shell-crossing has occurred. The number of these axes is then directly related to voids (0), walls (1), filaments (2) and halos (3).

In chapter 3 we will discuss how the velocity dispersion emerging during collapse and measured on the phase-space sheet can be used to identify the components of the cosmic web from a dynamical point of view.

2.3 Reconstruction of the Dark Matter Phase-Space Sheet

In section 2.1, we described how one can sample particles from the phase-space distribution to simulate the dynamics of DM. We treated them as point-like objects with a softening to achieve a collisionless behavior. The sampled particles are however merely a numerical tool rather than

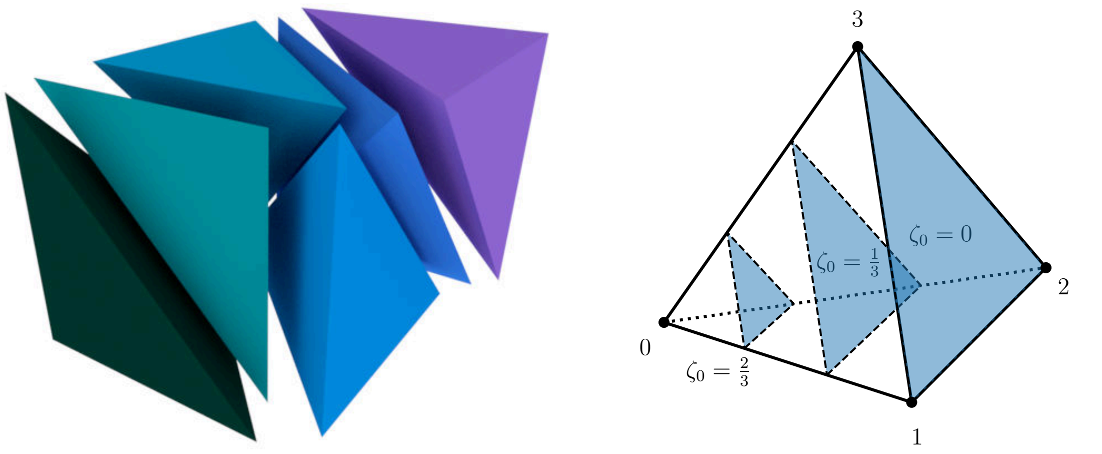

Figure 2.1: **Left**: one possibility of the decomposition of the unit cube in six equal-volume tetrahedra. **Right**: illustration of tetrahedral coordinates $\boldsymbol{\zeta} = (\zeta_0, \zeta_1, \zeta_2, \zeta_3)$ for which each ζ_i is 0 at vertex i and grows to 1 at the opposite face. A point within the tetrahedron can be described by $\zeta_i \in [0, 1]$ and the constraint $\sum_i \zeta_i = 1$.

physical entities. Nevertheless, we can use their nature as tracers of phase-space to reconstruct the underlying continuous distribution. This approach has been successfully demonstrated by Abel et al. 2002 [1] and Shandarin et al. 2012 [285], and applied to study the large scale velocity fields [139] and emergence of velocity dispersion [51] (chapter 3), to improve lensing maps extracted from N-body simulations [9], and to reduce discreteness artifacts in the force computation of numerical simulations [136, 134].

This section contains an overview of Lagrangian phase-space tessellation techniques, and in particular we review the tetrahedral tessellation technique used in [1, 139] and Buehlmann & Hahn 2019 [51] (adapted in chapter 3).

2.3.1 Tessellation of the phase-space submanifold

At early times, the CDM displacement and velocity fields are well-described by the ZA (cf. section 1.2.4). The map $\boldsymbol{q} \rightarrow (\boldsymbol{x}, \boldsymbol{v})$ thus describes a three-dimensional manifold embedded in the six-dimensional phase-space (assuming a perfectly cold fluid, which is a reasonable assumption for CDM). The N-body particles sampled with the ZA are tracers of this submanifold and can be thought of as vertices of phase-space volume elements. These volume elements are particularly simple if a cubic lattice is chosen for sampling the Lagrangian coordinates (cf. section 2.1.3).

For the tetrahedral tessellation technique, we can further split each of the Lagrangian cubes into three-dimensional simplices (tetrahedra). This decomposition is, however, not unique. The minimum tessellation with the minimum number of five tetrahedra was for example being used in [285]. For the discussion in this section and the analysis in chapter 3, we use the equal-volume segmentation shown in fig. 2.1. Note that this decomposition is not isotropic and if anisotropic artifacts are a concern, results need to be averaged over 12 separate tessellations with rotated decompositions.

If we keep track of the particles belonging to each volume element (e.g. by using particle ids), we can reconstruct this tessellation at any later time. Due to Liouville's theorem, each element, although deformed, will still carry the same mass. As a simple density estimate, we can assume a constant stream density inversely proportional to the volume across the tetrahedron (a *piece-wise constant* approximation). The density at any position $\boldsymbol{x}$ is then the sum of the stream densities of all intersecting tetrahedra at that point. This approximation is illustrated in fig. 2.3 (panel C), for a two-dimensional example. The 3x3 particles span 4 unit squares in Lagrangian space, that can each be divided into two triangles in two different ways (solid and dashed lines). For panel C, we only use the solid triangulation; however, a better approximation can be obtained if one averages over both triangulations.

2.3.2 Interpolation on Tetrahedra

Instead of using a piece-wise constant approximation, we can linearly interpolate any function on the tetrahedron if we know its values at the vertices. For that purpose, we can use natural tetrahedral coordinates $\boldsymbol{\zeta} = (\zeta_0, \zeta_1, \zeta_2, \zeta_3)$ illustrated in fig. 2.1. One can easily check that $\sum_i \zeta_i = 1$. To convert tetrahedral coordinates to spatial coordinates, we can use the linear transformation

$$\begin{bmatrix} 1 \\ x \\ y \\ z \end{bmatrix} = \begin{bmatrix} 1 & 1 & 1 & 1 \\ x_1 & x_2 & x_3 & x_4 \\ y_1 & y_2 & y_3 & y_4 \\ z_1 & z_2 & z_3 & z_4 \end{bmatrix} \cdot \boldsymbol{\zeta}^T \equiv \boldsymbol{J} \cdot \boldsymbol{\zeta}^T. \tag{2.25}$$

The volume of the tetrahedron can then be computed as[3] $6V = |\det \boldsymbol{J}|$. As long as $V \neq 0$, the map $\boldsymbol{\zeta} \to \boldsymbol{x}$ is invertible, and we can easily find the tetrahedral coordinates for a position $\boldsymbol{x}$.

Any function f with known values at the vertices $f(\boldsymbol{x}_i) = f_i$ can be linearly interpolated in tetrahedral coordinates as

$$f(\boldsymbol{\zeta}(\boldsymbol{x})) = \sum_i f_i \, \zeta_i(\boldsymbol{x}). \tag{2.26}$$

The derivative of f can be obtained via the chain rule

$$\begin{aligned} \frac{\partial f}{\partial x_i} &= \sum_j \frac{\partial f}{\partial \zeta_j} \frac{\partial \zeta_j}{\partial x_i} = \sum_j \left(\boldsymbol{J}^{-1}\right)_{(i+1)j} \frac{\partial f}{\partial \zeta_j} \\ &\approx \sum_j \left(\boldsymbol{J}^{-1}\right)_{(i+1)j} f_j, \end{aligned} \tag{2.27}$$

where we used the linear approximation of f from the previous equation. Note that the derivatives only exists if $V \neq 0$ and that the approximation is only accurate to first order.

[3] We use the absolute value of the determinant since the sign changes when the vertex order is reversed (e.g. during shell-crossing).

We can estimate the stream-density at the vertices by

$$\rho(\boldsymbol{q}_i) = \left(\frac{\sum_{i=1}^{N} m_i V_i}{N} \right)^{-1}, \tag{2.28}$$

where N is the number of tetrahedra (each with volume V_i and mass m_i respectively) sharing the vertex. Since we know the velocities at the vertices $\boldsymbol{q}_i$ from the particle data, we can easily interpolate densities, velocities, and derivatives thereof across the tetrahedron.

2.3.3 Projections of the dark matter sheet

To evaluate the spatial properties of a function $f(\boldsymbol{q})$ interpolated on the phase-space tessellation, we need to project the DM sheet to Eulerian space. At each point $\boldsymbol{x}$, the projection $\langle f \rangle(\boldsymbol{x})$ (cf. eq. (1.38)) can be obtained by taking the density-weighted average over all intersecting tetrahedra, i.e.

$$\langle f \rangle(\boldsymbol{x}) = \frac{\sum_k \rho_k(\boldsymbol{x}) f_k(\boldsymbol{x})}{\sum_k \rho_k(\boldsymbol{x})}, \tag{2.29}$$

where $\rho_k(\boldsymbol{x})$ and $f_k(\boldsymbol{x})$ are interpolated from their values at the vertices of the tetrahedra T_k. We can use this formula to estimate the mean velocity $\langle \boldsymbol{v} \rangle(\boldsymbol{x})$, the velocity dispersion (cf. eq. (1.39))

$$\sigma_{ij}^2(\boldsymbol{x}) = \langle v_i v_j \rangle(\boldsymbol{x}) - \langle v_i \rangle(\boldsymbol{x}) \langle v_j \rangle(\boldsymbol{x}), \tag{2.30}$$

and any higher order moment of the phase-space distribution function.

Panel (D) of fig. 2.3 shows the density estimate using the interpolated triangulation technique. Unlike panel (C), the result is also averaged over both triangularization possibilities. Thanks to the interpolation, the estimated density is continuous across the triangle edges, except at the transitions between the single- and multistreaming regime. However, caustics at these interfaces cannot be captured by the tetrahedral decomposition (unless the volume becomes zero). To capture the caustics, higher order interpolations have to be used, which we will discuss next.

2.3.4 Higher order interpolation on cubes

The interpolation technique described above is a linear piece-wise interpolation on a tetrahedral segmentation. Higher order interpolations can be achieved by considering larger Lagrangian volume elements with more tracer particles. In particular, Hahn & Angulo 2016 [134] used 3-variate polynomials on cubic volume elements to interpolate the mapping $\boldsymbol{q} \to \boldsymbol{x}$. Combining three polynomials of order n along each dimension, we can write a 3-variate polynomial as

$$\pi(k)(\boldsymbol{q}) = \sum_{i,j,k=0}^{n} a_{ijk} q_0^i q_1^j q_2^k. \tag{2.31}$$

Note that the multivariate polynomial itself has order $3n$, and thus can have multiple roots even for $n = 1$; for $n > 1$, the map can only be inverted numerically. The polynomial has n^3 degrees of freedom, and therefore, a Lagrangian cube with side length n has to be chosen to compute the coefficients. By writing the Lagrangian coordinate combinations in a vector $\boldsymbol{Q}$ defined as

$$\boldsymbol{Q} = \Big(1, q_3, q_3^2 \ldots, \underbrace{q_1^i q_2^j q_3^k}_{Q_{n^2 i+nj+k}}, \ldots, q_1^n q_2^n q_3^n\Big), \tag{2.32}$$

we can write the map $\boldsymbol{q} \to \boldsymbol{x}$ as

$$\boldsymbol{x} = A\boldsymbol{Q}. \tag{2.33}$$

The coefficients of the matrix A with shape $(3, n^3)$ can be determined from the coordinates at each of the n^3 vertices. Defining the coordinate matrices $\mathcal{Q} = (\boldsymbol{Q}_1, \ldots, \boldsymbol{Q}_{n^3})$ and $\mathcal{X} = (\boldsymbol{x}_1, \ldots, \boldsymbol{x}_{n^3})$, we can compute A as

$$A = \mathcal{X}\mathcal{Q}^{-1}. \tag{2.34}$$

Note that if the Lagrangian points are on a regular grid, $\mathcal{Q}^{-1}$ has only to be computed once per given interpolation order.

Unlike the tetrahedral decomposition discussed previously, it is difficult to invert the map due to the non-linear terms. Therefore, it is less feasible to project the dark matter sheet point-wise for the higher-order interpolations. However, we can use the interpolation to sample additional "particles" to refine the resolution. These particles can then be used, for example, to estimate the density via CIC or TSC (cf. section 2.1.2) with lower Poisson noise, increasing the force accuracy, especially in low density regions [134].

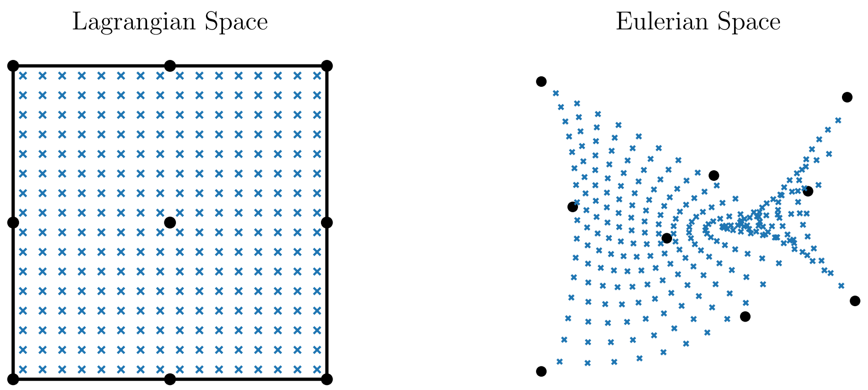

Figure 2.2: Refinement of the particle sampling in a Lagrangian cube using a bivariate polynomial that was fit to 9 N-body particles (black). The refinement particles (blue) are sampled on a regular grid in Lagrangian space.

Figure 2.2 illustrates the sampling of additional high resolution particles with uniform spacing on the Lagrangian cube and the interpolated mapping to Eulerian space. If the refinement grid has the resolution n_f, each new particle will have mass $m_f = (n/n_f)^3 m$, where m is the N-body particle mass. By writing the Lagrangian coordinates of the refined particles as the matrix $\mathcal{Q}_f$ similar to $\mathcal{Q}$, their mapped Eulerian coordinates can be calculated by

$$\mathcal{X}_f = A\mathcal{Q}_f = \mathcal{X}\mathcal{Q}^{-1}\mathcal{Q}_f. \tag{2.35}$$

Note that if the same refinement grid is used across the simulation, $Q^{-1}Q_f$ has to be computed only once, and the new particles can easily be sampled by a single matrix multiplication for each Lagrangian volume element. The linear and second order interpolation of the mapping of a two-dimensional Lagrangian square in comparison with the triangulation is shown in fig. 2.3.

An alternative method to subsample the Lagrangian space is by using Fourier techniques on the displacement field $\boldsymbol{\psi}(\boldsymbol{q}) = \boldsymbol{x}(\boldsymbol{q}) - \boldsymbol{q}$, i.e. trigonometric interpolation. In theory, one could use the Fourier transform $\tilde{\boldsymbol{\psi}}$ of the full field and add additional modes $\boldsymbol{k}$ above the Nyquist frequency set to 0. Doubling the Fourier modes along each axis by zero-padding the new modes and transforming the displacement back to real-space, would therefore smoothly increase the particle resolution by 2^3. However, for reasonably high-resolution simulations, this method will quickly reach the memory limits of common computer systems. It can however also be applied to subsets of Lagrangian space, if the volume is sufficiency padded to account for the non-periodic boundaries.

Furthermore, we can apply the tetrahedral decomposition and projection method discussed previously to the subsampled particles in order to combine the advantages of both methods: higher order, smooth interpolations and point-wise evaluation of the densities, velocities and moments thereof. Figure 2.5 shows a comparison of the densities and velocities obtained with the tetrahedral tessellation method once directly applied to the particles, and once on a subsampled set of particles using the third order polynomial method with $m = 2$ (i.e. $2^{2\cdot 3} = 64$ times the number of tetrahedra). We can clearly see that especially in low-density regions, the density estimate becomes less "edgy" and caustics become better visible.

In addition, we also measured the velocities of the streams along two lines, one through what appears to be a wall or filament, and one directly through the halo at the center of the shown slice. Along the first line, we can see the phase-space spirals discussed in fig. 1.3 (note that due to the projection on the x, y and z axis, the spirals seem to intersect each other). Adding the particle subsampling, the curves become significantly smoother. For the cut through the halo, the number of overlapping streams becomes so high that individual streams can no longer be distinguished ($\sim$ 600 streams). We therefore also show a velocity histogram at the halo center, showing a Gaussian-like distribution of velocities. Note that the true velocity distribution function is still a sum of Dirac-delta functions, and the approach to a Maxwell-Boltzmann distribution through (chaotic) mixing is only approximate (cf. e.g. [143, 213]).

As a final remark, it is worth emphasizing that the tessellation and interpolation methods described in this section do not "create" new information, i.e. the simulation and any result drawn from it is still limited by the particle resolution. The methods help, however, to lower the shot-noise from the limited number of sampling points in phase-space, and allow for point-wise measurements of densities, velocities, and moments of the phase-space distribution that would not be possible by using the N-body particles only.

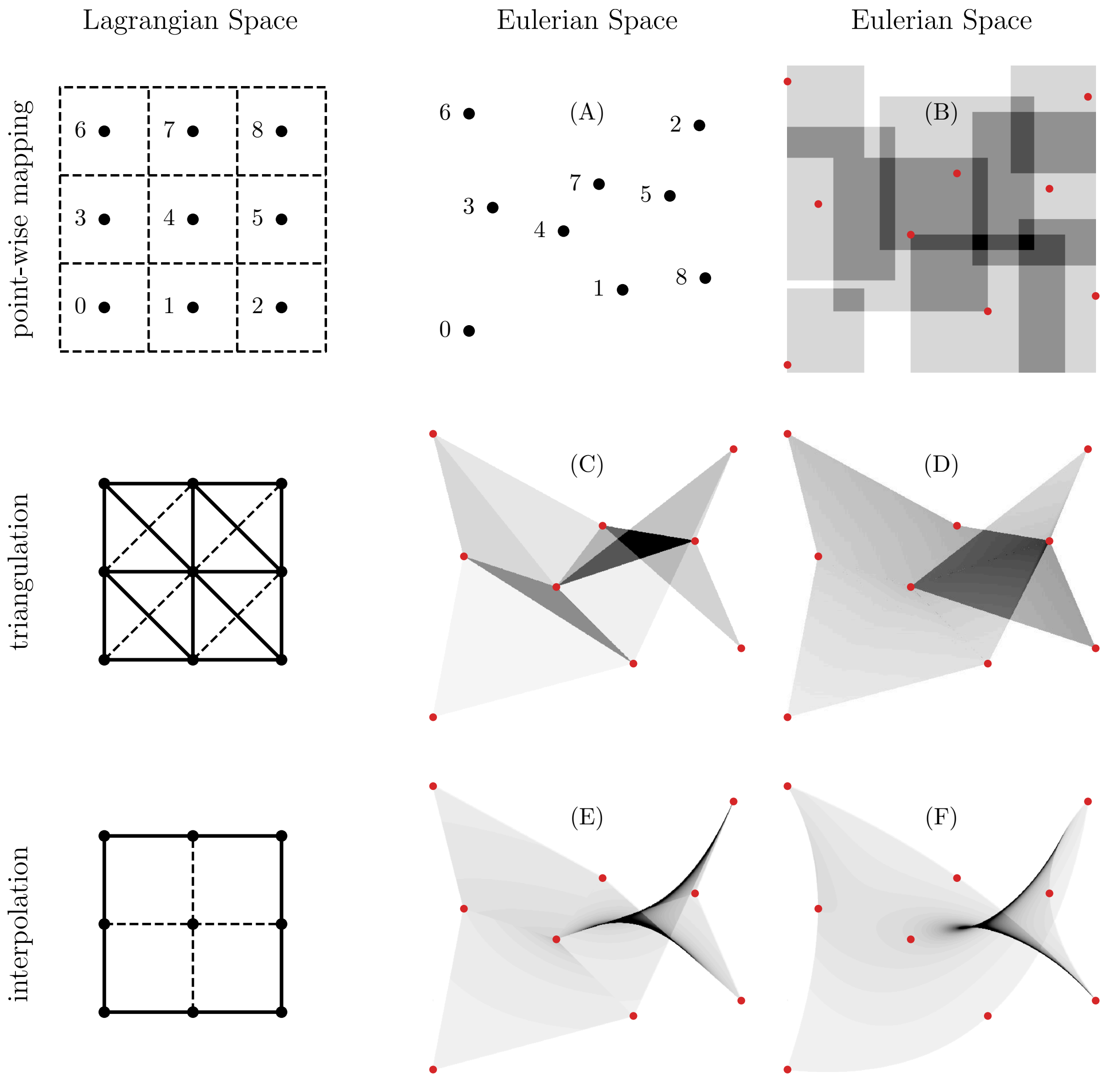

Figure 2.3: Illustrations of different methods to map Lagrangian space (left column) to Eulerian space (right columns). Nine particles that were initially on a regular 3x3 grid are mapped to Eulerian space (A) where particles 2 and 8 have flipped their position. Instead of treating the particles as point-like objects, we can assign a square volume to them (B), similar to the partition in Lagrangian space. The regular grid in Lagrangian space can be tessellated into equal-area, two-dimensional simplices (triangles) which can be reconstructed from their vertices in Eulerian space. This triangulation is, however, not unique, and in two dimensions two possibilities exist. (C) shows the density estimation from a single triangulation if for each triangle a constant density inversely proportional to its volume is assumed. This estimation can be improved by averaging over both triangulations and linearly interpolating the density across the triangles from the value estimated at the corners (D). The distribution can also be interpolated by fitting a multivariate polynomial across a Lagrangian square. (E) shows the combination of linear interpolations on four 1x1 squares and (F) of one 2nd order interpolation on the full 2x2 square.

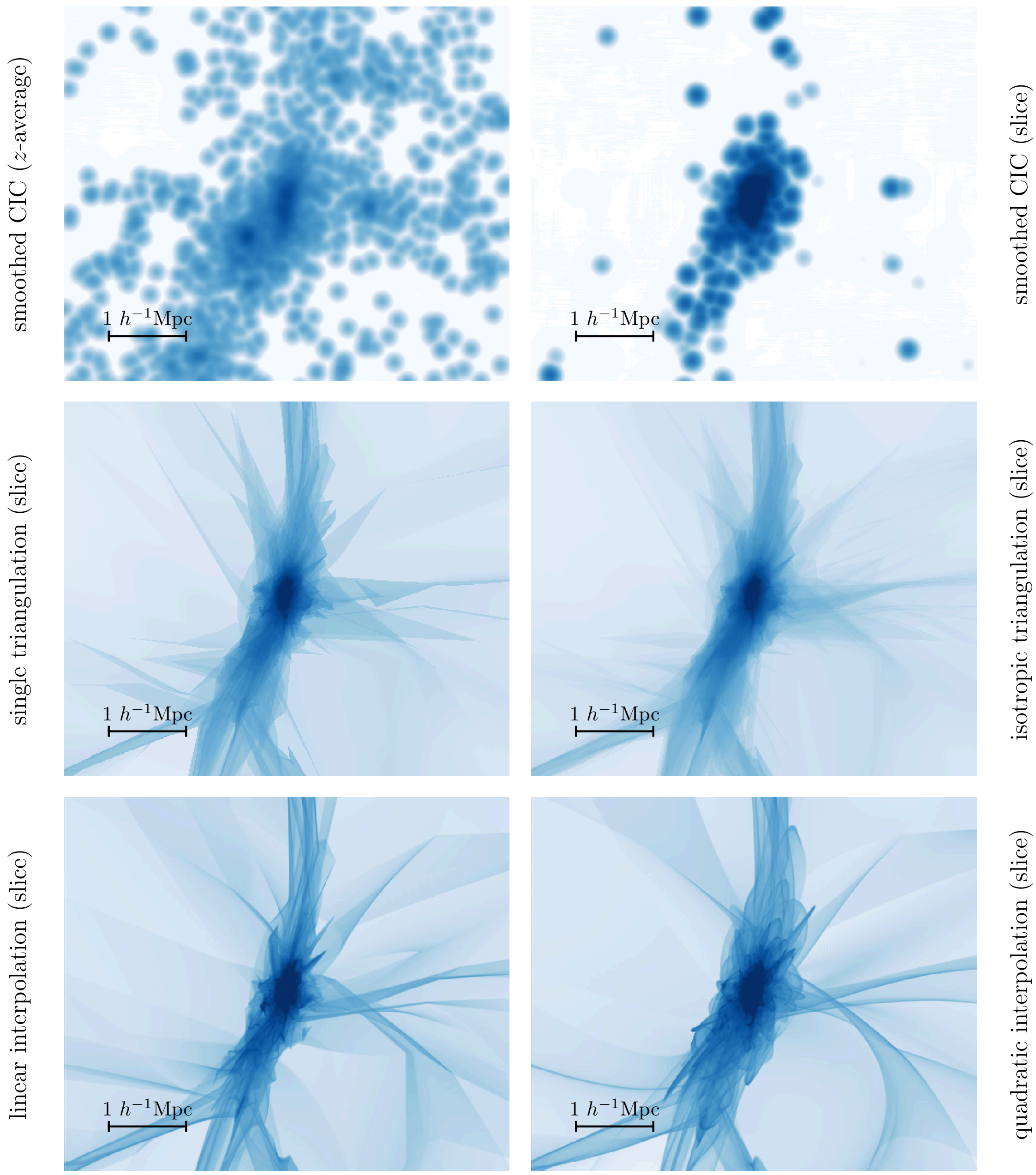

Figure 2.4: Illustration of density estimates with CIC and with dark matter sheet tessellation methods. The images are centered on an isolated halo[1] with $M_{200c} \sim 1.9 \times 10^{13}\ h^{-1} M_{\odot}$ from the low resolution 300MPC_lowres simulation. **Top**: smoothed CIC deposition (Gaussian kernel with $\sigma \sim 50\ h^{-1}$kpc) projected along the z-axis (left) and sliced along the center (right). **Middle**: interpolation on a single tetrahedral decomposition and average over all possible decompositions. **Bottom**: CIC decomposition of a large number of additionally sampled particles using the linear and quadratic polynomial interpolation.

[1] The halo on COSMICWEB: https://cosmicweb.oca.eu/simulation/300MPC_lowres/halo/23802097

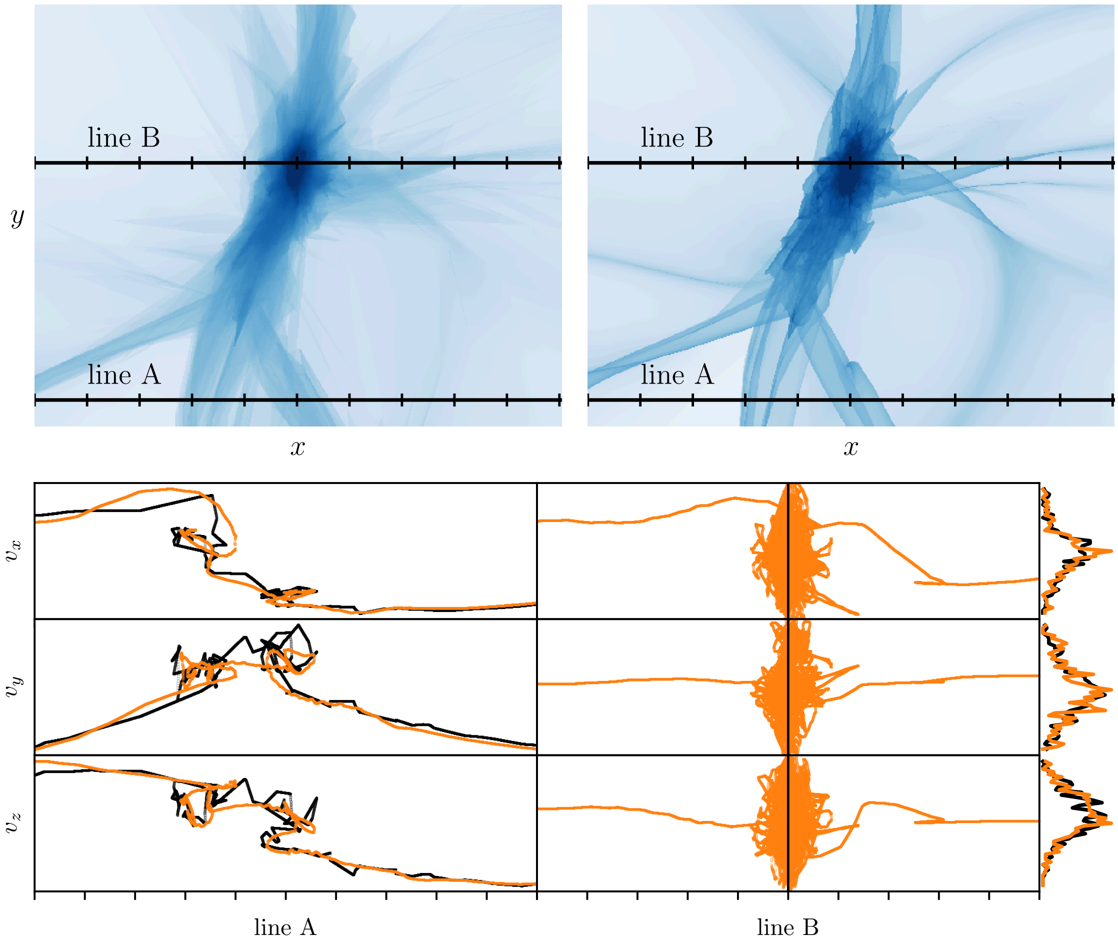

Figure 2.5: **Top:** illustration of the density estimates with the tetrahedral decomposition (averaged over all possible tessellations) using the N-body particles (left) and on subsampled particles using the polynomial interpolation with $n = 3$ and $m = 2$ (right). **Bottom:** Velocity distribution along two lines shown on the density slices. Black lines show the velocities obtained from particles directly, orange from the subsampled particles. For line B, we only show the subsampled result, and in addition the velocity histogram at the halo center (indicated by the black vertical line).

CHAPTER 3

The Large Scale Velocity Dispersion in the Cosmic Web

This chapter has been adapted from Buehlmann & Hahn [51] and supplemented with additional results.

In the previous chapters, we saw how gravitational collapse in a cosmological context produces an intricate cosmic web of voids, walls, filaments, and nodes. The anisotropic nature of this collisionless collapse leads to the emergence of an anisotropic velocity dispersion, or stress, absorbing most of the kinetic energy after shell-crossing. In this chapter, we measure this large-scale velocity dispersion tensor σ_{ij}^2 in N-body simulations using the phase-space tessellation technique discussed in section 2.3.

In the CDM paradigm of cosmological structure formation, the VDF of dark matter particles is well approximated by the cold limit, in which they occupy only a three-dimensional hypersurface in the six-dimensional phase-space: the Lagrangian submanifold. This submanifold can be parameterized by the Lagrangian coordinate $\boldsymbol{q} \in \mathbb{R}^3$, so that the phase-space distribution function can be written as

$$f_{\mathrm{CDM}}(\boldsymbol{x}, \boldsymbol{v}, t) = \int \mathrm{d}^3\boldsymbol{q}\, \delta_D\left(\boldsymbol{x} - \boldsymbol{x}(\boldsymbol{q}, t)\right)\, \delta_D\left(\boldsymbol{v} - \boldsymbol{v}(\boldsymbol{q}, t)\right), \tag{3.1}$$

where $\boldsymbol{x}(\boldsymbol{q}, t)$ and $\boldsymbol{v}(\boldsymbol{q}, t)$ are the momentary position and velocity associated with $\boldsymbol{q}$ at time t. At the earliest times, the submanifold coincides with three-dimensional space, but metric perturbations cause it to deform increasingly due to the growth of velocity perturbations reinforced non-linearly by self-gravity, leading to shell-crossing at later times and resulting in multivalued velocities.

The monokinetic regime is given by those regions where there is a single solution so that the VDF is a Dirac δ-distribution (which is the zero-temperature limit of a Gaussian velocity distribution). Its evolution is fully described by the continuity and the Euler equation (cf. section 1.2.3). Only after shell-crossing, when the VDF becomes a discrete sum over δ-distributions, the second and all higher order cumulants emerge, so that an infinite hierarchy of fluid equations would have to be solved in the absence of collisions or other efficient relaxation processes suppressing the higher order cumulants. It is only on the smallest scales, i.e. inside halos that are not dominated by recent accretion, that efficient (chaotic) mixing lets the velocity distribution approach a VDF relatively close to a Maxwell-Boltzmann distribution (cf. for example [143, 213]).

In three dimensions, the emergence of the second and higher order cumulants happens only in those subspaces in which shell-crossing occurred due to the triaxial nature of the gravitational collapse. This anisotropic collapse should thus be reflected, at least on larger scales, in the second moment of the local VDF, which is the velocity dispersion tensor. We focus on this particular aspect in this chapter by asking: *(1) how does the anisotropic triaxial collapse of structure lead to an anisotropic velocity dispersion on large scales*, and, *(2) to what degree is the anisotropic nature retained even in the presence of small-scale perturbations that will drive a gradual isotropization in the deeply non-linear regime*. Studying the large-scale VDF is important for both our general understanding of cosmic structure formation and in particular for the implications on redshift-space distortions, since the three-dimensional positions of galaxies are always a sum of their positions and their line-of-sight velocities.

The structure of this chapter is as follows. First, in section 3.1, we discuss how gravitational collapse and the formation of the cosmic web lead to the emergence of velocity dispersion in the originally perfectly cold universe. Then, in section 3.2, we provide a brief summary of the N-body simulations and the tessellation method that we use to measure the velocity dispersion tensor field, with more details in appendix A.3. In the ensuing sections, we present our results on the measurement of the velocity dispersion field. We start in section 3.3 with an analysis of the magnitude, including the evolution, density relations, and two-point correlations. In section 3.4, we evaluate the anisotropy of the velocity dispersion tensor, derive a natural and parameterless cosmic-web identification method, and study the density dependence and time evolution of the detected cosmic web environments. We investigate the orientation of the dispersion field in the cosmic web in section 3.5 and compare the DM velocity dispersion with the temperature of gas in collapsed structures measured from a two-component simulation including baryons. Finally, we summarize our findings in section 3.7, and give an outlook on future projects in section 3.8.

3.1 The emergence of velocity dispersion from shell-crossing

In section 1.2.4, we have discussed how at early times (or on large scales), the dynamics of CDM can be described by the ZA. At the earliest times, the map from Lagrangian to Eulerian space is bijective, and therefore the velocity field $\boldsymbol{v}(\boldsymbol{x})$ is single valued at every point in space. However, as time evolves, the dark matter fluid accelerates towards potential wells and the initial perturbations grow according to the growth function $D_+(t)$ until the dark matter sheet undergoes shell-crossing and enters the multistreaming regime. Since perturbations, and therefore the force fields, generally do not possess spatial symmetries, the collapse is anisotropic and happens at different rates along different axes. The principal axes of collapse correspond to the eigenvectors of the tidal field $T_{ij} = \partial^2\phi/\partial q_i \partial q_j$.

Since dark matter in the standard CDM paradigm is collisionless, there is no rapid process that drives the multistreaming regions towards an isotropic Maxwell-Boltzmann distribution and thus an infinite hierarchy of moments of the Vlasov equation would need to be considered in an accurate analytic model (cf. section 1.2.3). Once the perturbation is in the multistreaming regime, the velocity dispersion tensor[1] is defined as the variance of the velocities of the various

[1] Note that in some literature, σ_{ij} is also used to denote the velocity shear tensor $\Sigma_{ij} = \left(\partial \mathbf{v}_i/\partial \mathbf{x}_j + \partial \mathbf{v}_j/\partial \mathbf{x}_i\right)/2$ (e.g. [245]) and should not be confused with the velocity dispersion tensor defined here.

streams at a given point (cf. eq. (1.42)), weighted by their respective local density on each stream,

$$\sigma_{ij}^2(\boldsymbol{x}) = \left\langle v_i(\boldsymbol{x}) v_j(\boldsymbol{x}) \right\rangle - \left\langle v_i(\boldsymbol{x}) \right\rangle \left\langle v_j(\boldsymbol{x}) \right\rangle, \tag{3.2}$$

where stream averaging is defined as

$$\langle f(\boldsymbol{x}) \rangle = \frac{\sum_k \rho^{(k)}(\boldsymbol{x}) f^{(k)}(\boldsymbol{x})}{\sum_k \rho^{(k)}(\boldsymbol{x})}. \tag{3.3}$$

Here, the index k runs over the intersections of the dark matter sheet with position. We will now take a closer look at the evolution of the velocity dispersion as it emerges along the first axis of collapse and how the collapse along the subsequent axes are imprinted in σ_{ij}^2.

3.1.1 From one-dimensional collapse to the cosmic web

To get an intuitive understanding of the velocity dispersion immediately after collapse, we will first look at a simplified model of a perturbation with a single mode k in one dimension (a plane wave), $\phi(q) = A\cos(kq)$ with amplitude A. In the ZA, which in 1D is exact before shell-crossing, we can write

$$x(q,a) = q - D_+(a) A k \sin(kq) \qquad\qquad u(q,a) = -\dot{D}_+(a) A k \sin(kq). \tag{3.4}$$

The mapping $q \leftrightarrow x$ is unique for $D_+(a) < D_+(a_\times)$, where shell-crossing occurs at $a_\times$. This time is defined by $D_+(a_\times) \equiv A^{-1}k^{-2}$, at which time the spatial derivative at $q = 0$ vanishes and the wave collapses. In fig. 1.3 we illustrate the phase-space configuration of the plane wave before and shortly after collapse, and at twice the collapse time $a = 2a_\times$. While the ZA is still able to model the dark matter sheet in the first snapshot, it deviates strongly at later times and especially overestimates the width of the collapsed region.

The Eulerian density shows the characteristic caustics at the border of the collapsed region where $\partial x/\partial q$ vanishes. In the ZA, these outer caustics are captured (albeit at the wrong locations), whereas the density peaks from subsequent shell-crossings at later times cannot be recovered. The velocity dispersion, zero in the monokinetic regime, rises strongly towards the inside of the collapsed region. Since the ZA does not capture subsequent shell-crossings due to secondary infall, it cannot correctly predict the long-term evolution of the velocity dispersion. In the full non-linear solution, the central density increases together with the velocity dispersion, keeping the two in a dynamical equilibrium that cannot be described in the ZA. Nevertheless, the ZA provides a first estimate of the velocity dispersion immediately after shell-crossing. In appendix A.4 we derive an analytic solution for the lowest order polynomial expansion of a plane wave still leading to collapse and show that, within the range of scales captured by our simulations, we expect the velocity dispersion measured shortly after collapse to increase with the scale of the perturbation.

In three dynamical dimensions, collapse can proceed along a second and a third axis, first producing filaments, and finally halos through shell-crossing from the multi-dimensional flow field (cf. [18, 17, 150, 100] for detailed discussions of the emergence of caustic singularities during anisotropic gravitational collapse and the nature of the multistreaming regions). The number of collapsed axes and their directions is directly imprinted in the velocity dispersion tensor, as velocity dispersion is nonzero only along the dimensions that have already collapsed. Studying the eigenvalues and eigenvectors of σ^2_{ij} thus allows us to measure the advancement in structure formation and to identify the different components of the cosmic web. Since σ^2_{ij} is a symmetric, positive semidefinite tensor, its associated eigenvalues λ_i are real and positive or zero. In theory, an eigenvalue of zero corresponds to an un-collapsed dimension along which no velocity dispersion has been generated. In this sense, a void has three zero eigenvalues, a pancake two, a filament one, and for a node all eigenvalues are different from zero. Naturally, due to finite numerical resolution and in a universe generated from random fluctuations on a multitude of scales, we will hardly find exactly vanishing eigenvalues. We discuss a natural way of separating the different regimes depending on the relative strengths of the eigenvalues in section 3.4.

3.2 Measuring large-scale velocity dispersion in N-body simulations

To measure and analyse the properties of the dark matter velocity dispersion in the non-linear regime, we rely on numerical simulations. For this purpose, we have performed a set of cosmological N-body simulations using the tree-PM code GADGET-2 [300], with initial conditions generated at redshift $z = 99$ using MUSIC [133]. The detailed parameters for each simulation are described in appendix A.3.

The set comprises three pairs of a high and low resolution simulation (with 1024^3 and 512^3 particles) of a 300 h^{-1}Mpc box that have been initialized with the an identical random seed and cosmological parameters consistent with the Planck (2015) results [67]. For two pairs (labelled 300WDM1 and 300WDM2), we filter out the small-scale structure in the initial condition, whereas for the 300CDM pair we use the full spectrum. To truncate the initial power spectrum, we use the WDM model discussed in section 1.3.2 with thermal relic DM particle masses of 250eV (300WDM2) and 500eV (300WDM1), leading to truncation scales $\alpha = 250h^{-1}$kpc and $\alpha = 113h^{-1}$kpc respectively. These scales correspond to half-mode masses of $M^{\rm hm}_{\rm WDM} = 2.2 \times 10^{12} h^{-1}{\rm M}_\odot$ and $M^{\rm hm}_{\rm WDM2} = 2.2 \times 10^{11} h^{-1}{\rm M}_\odot$. The scales that we are using are of course incompatible with observations, but instead were tuned to correspond to roughly the non-linear scale M_* at $z = 0$, as well as to an approximately ten times smaller scale. We use the same amplitude for the power spectrum in the WDM initial conditions as the one derived from σ_8 in the CDM case, so that perturbations on large scales have identical amplitudes. Together with equivalent random seeds, all simulations have the same large-scale structure, up to some small back-reaction from small scales which are not present in the WDM runs.

Additionally, for the comparison of the velocity dispersion with the gas temperature in section 3.6, we have run a DM-only and a hydrodynamic simulation of a 150 h^{-1}Mpc box, labelled 150CDM and 150CDM_H respectively. Both simulations use the same random noise field, allowing a direct comparison. The hydrodynamic simulation was run with the adaptive-refinement mesh code RAMSES [312], with an initial resolution of 2^{10} and a density dependent refinement criterion to a maximal resolution of 2^{13}. Since we mainly focus on the isotropization of the gas velocity dispersion and shock heating during collapse, additional features such as gas cooling, heating from the UV background, and subgrid modeling of baryonic physics have been turned off.

To determine the DM velocity dispersion at any given point $\boldsymbol{x}$, we reconstruct the fine-grained phase-space distribution of dark matter using the tessellation method with the tetrahedral decomposition described in section 2.3 (also see [1, 285]). More precisely, we use the equal volume decomposition depicted in fig. 2.1. From this decomposition, we can measure the moments of the velocity field at a given point $\boldsymbol{x}$ in configuration space according to eq. (2.29). The velocity dispersion tensor field, i.e. the variance of the velocities of the tetrahedra intersecting that point, can thus be written as:

$$\sigma_{ij}^2(\boldsymbol{x}) = \frac{\sum_k \rho^{(k)} v_i^{(k)} v_j^{(k)}}{\sum_k \rho^{(k)}} - \frac{\sum_k \rho^{(k)} v_i^{(k)}}{\sum_k \rho^{(k)}} \frac{\sum_k \rho^{(k)} v_j^{(k)}}{\sum_k \rho^{(k)}}. \tag{3.5}$$

The fields $\rho^{(k)}$ and $v_i^{(k)}$ are interpolated linearly on the tetrahedra to the evaluation point using the values at the vertices. For our statistical result, we use the entire volume of the 300 h^{-1}Mpc boxes and compute the velocity dispersion on a 1024^3 and 512^3 grid. For the visualizations, we use a finer grid of sampling points around a $M_{200\mathrm{c}} = 8.9 \times 10^{13}\ h^{-1}\mathrm{M}_\odot$ halo.

3.3 Magnitude of the large-scale velocity dispersion

We start our analysis by measuring the strength of the local velocity dispersion. A natural quantity of the velocity dispersion magnitude is the trace of σ_{ij}^2, which measures the sum of the dispersion along its main axes, $\mathrm{tr}(\sigma_{ij}^2) = \sum_i \lambda_i$, and essentially corresponds to the effective temperature of the dark matter due to gravitational collapse. We will first look at some visualizations of $\mathrm{tr}(\sigma_{ij}^2)$ in our simulations and then look more closely at its local density dependence and its evolution over time. We then measure the autocorrelation as well as cross correlations with the overdensity and velocity divergence.

3.3.1 Visual impression

To give a visual impression of the cosmic velocity dispersion field and its spatial properties, we will first focus on the surroundings of a halo with mass $M_{200\mathrm{c}} \sim 8.9 \times 10^{13}\ h^{-1}\mathrm{M}_\odot$. We compute the velocity and density fields from the tessellation of the dark matter sheet at points located on a uniform 512^3 grid within a 18 h^{-1}Mpc box centred at the halo. The halo we chose is massive enough to exist in all simulations. As can be seen from the density in the multistreaming regions shown in the top row of fig. 3.1, the halo is embedded in the intersection of large walls with several other massive halos close-by. In the WDM simulations, low density walls and higher density filaments at the wall intersections are clearly visible. The highest density is reached in the central halo. Shifting the suppression scale for small-scale fluctuations towards lower masses extends the multistreaming web in previously uncollapsed regions and adds additional perturbations within the existing walls and filaments. Most notably, filaments begin to appear in walls, and nodes in filaments. We will define cleanly what we mean by *walls*, *filaments* and *nodes* in section 3.4.

The second and fourth rows of fig. 3.1 illustrate the velocity dispersion amplitude in the three simulations. Starting from the 300WDM1 simulation, we can clearly see walls separating large

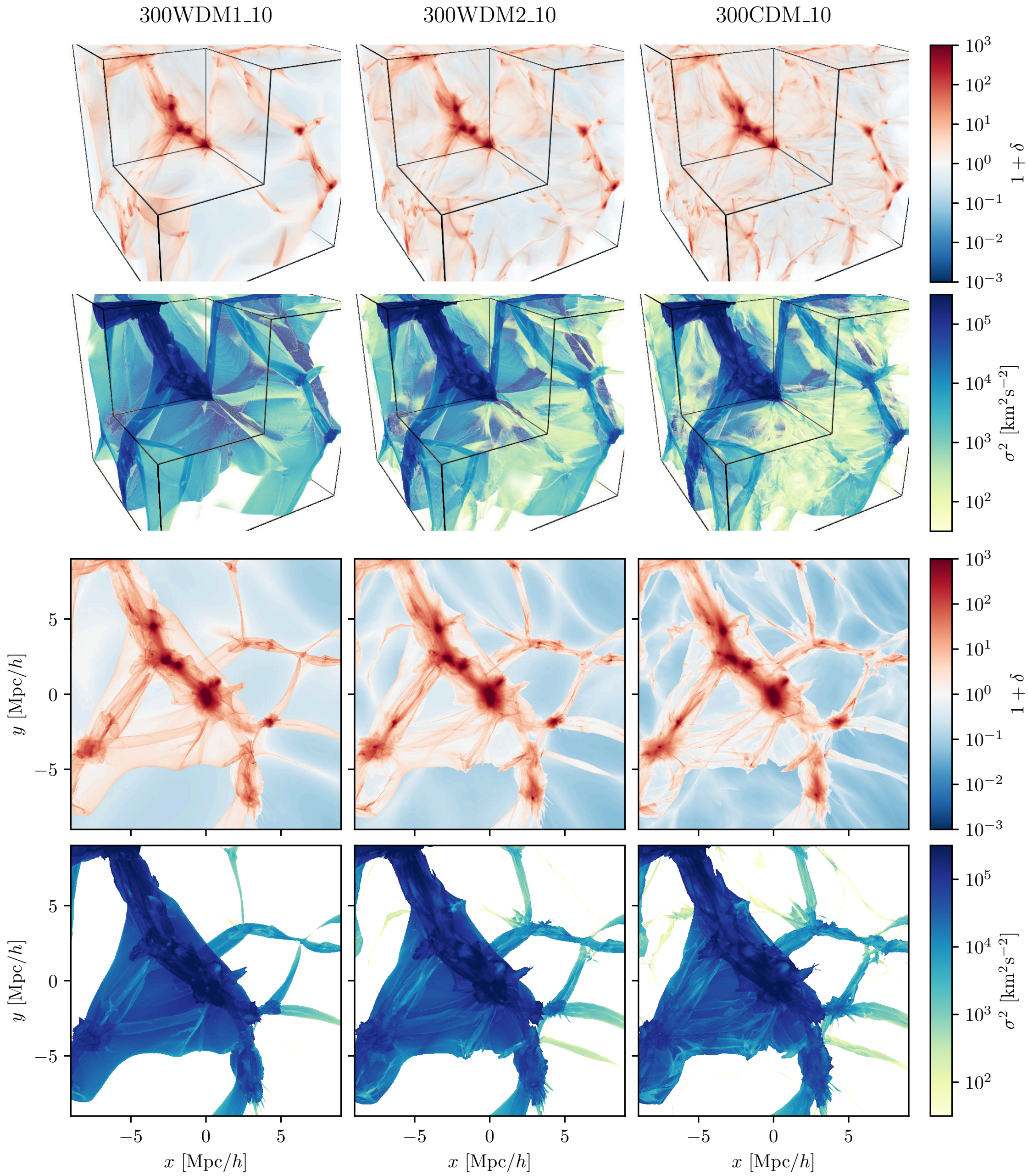

Figure 3.1: Visualization of the normalized density in the multistreaming regions (first and third row) and the amplitude of the velocity dispersion $tr(\sigma_{ij}^2)$ (second and fourth rows) for a 18 h^{-1}Mpc box around a $M_{200c} = 8.9 \times 10^{13}\ h^{-1}\mathrm{M}_\odot$ halo.

volumes with no velocity dispersion. These regions, the cosmic voids, have not collapsed and are thus still in the monokinetic single-stream regime. Among the wall regions, the velocity dispersion increases with the size and thickness of the structures. This is consistent with our one-dimensional collapse model presented in appendix A.4, predicting that larger-scale perturbations also have higher velocity dispersion after collapse and result in wider collapsed regions. In the centre of the cross sections of the large walls, we can see additional finer structures with lower velocity dispersion. These structures originate from the secondary collapse in a direction perpendicular to the wall, causing enhanced densities and suppressed velocity dispersion due to the higher weight of the inner streams (cf. fig. 1.3 at $a = 2.0a_\times$).

The major structures remain remarkably similar in all simulations with only little change in the strength of the velocity dispersion. Decreasing and removing the suppression of small-scale perturbations in the initial conditions naturally adds multistreaming structures in the voids (cf. [306] for a detailed discussion of this aspect). These fine structures are small in size and width, and have relatively low velocity dispersion. The additional small-scale structures within existing collapsed regions have a relatively small effect on the measured velocity dispersion as it is dominated by the large-scale modes. We will further discuss and quantify the influence of small perturbations in section 3.5.

3.3.2 Density correlation of the velocity dispersion

To further investigate the relationship between density and velocity dispersion, we compute $\mathrm{tr}(\sigma_{ij}^2)$ on the full box and plot its distribution with respect to the density (TESS) measured in the multistreaming regions (remember that the velocity dispersion vanishes exactly in single stream regions). The results are plotted in fig. 3.2. The shaded regions show the 100%, 99%, 90%, 50%, and the peak 5% contours and the black lines the median and the 95% interval of the distribution at a specific density $1 + \delta$. Additionally, we include the results from the lower resolution simulation to test for convergence. We find consistent results at high densities but deviations especially for the CDM simulation in low density environments, where the lower resolution simulation fails to capture the collapsed small-scale fluctuations with low velocity dispersion and low densities.

We find that above a density of $\delta \sim 4$ in the 300WDM1 realization and $\delta \sim 1$ in the 300CDM simulation, the velocity dispersion is positively correlated with density, with roughly $\mathrm{tr}(\sigma_{ij}^2) \propto (1 + \delta)^\alpha$ and $\alpha \sim 0.5 - 1$. The correlation is stronger in the 300CDM simulation due to the additional low density, low velocity dispersion regions which do not exist when small-scale fluctuations are suppressed. At low densities, this trend is reversed and the velocity dispersion increases towards the few collapsed regions below mean density. This is most likely due to the collapsed regions with the lowest densities – walls or pancakes – but which still have high velocity dispersion if they originate from a large-scale mode, as can be seen from the visualizations.

The volume distributions of the multistreaming regions peak at $\delta \sim 1 - 3$ and $\mathrm{tr}(\sigma_{ij}^2) \sim 10^3 - 10^4$, depending on the truncation scale of the small-scale structure (higher densities and higher velocity dispersion in the truncated simulations). The presence of small-scale fluctuations in the 300WDM2 and 300CDM simulations does not affect the distribution at the high end of the velocity dispersion distribution, but adds structures with low velocity dispersion and low to medium ($\delta \sim 10$) density. This is consistent with the observation of added small-scale structure

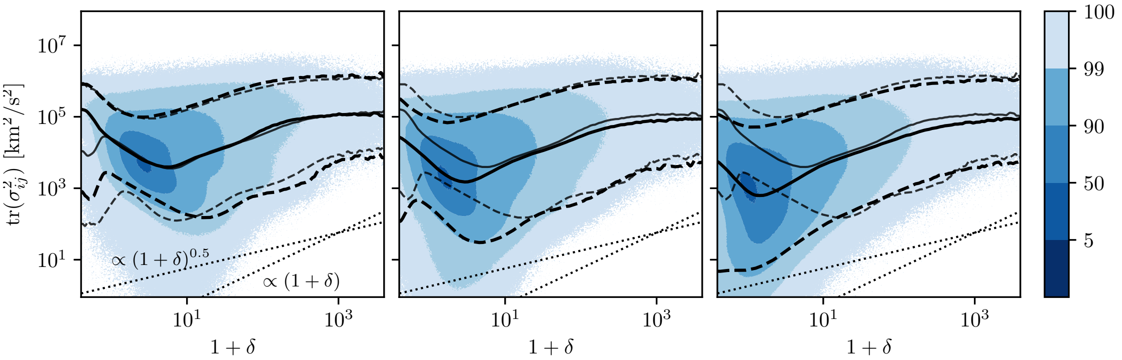

Figure 3.2: Distribution of the velocity dispersion amplitude $tr(\sigma_{ij}^2)$ and density (TESS) measured in the complete simulations, with the shaded areas indicating the 100%, 99%, 90%, 50%, and the peak 5% contours of the distribution. The black lines show the median (solid) and the 95% interval for the distribution at a fixed density $1+\delta$. In addition, we show the intervals obtained from the lower resolution simulations in lighter colors. The bottom dotted lines indicate a $(1+\delta)$ and $(1+\delta)^{0.5}$ slope as comparison.

with low velocity dispersion in previously uncollapsed regions, but persistently high velocity dispersion within the large-scale structures.

3.3.3 Two-point statistics of the cosmic velocity dispersion

As one can see from the 3d-visualizations in fig. 3.1, and later in fig. 3.5 and fig. 3.6, the velocity dispersion is spatially correlated, both in amplitude and in direction. First, we will focus on amplitude auto- and cross-correlations and will focus on directional correlations below in section 3.4. Since the velocity dispersion vanishes in single-stream regions, the field is not defined everywhere in space, hence the resulting two-point statistics will also include a strong signal of the size and shape of multistreaming regions.

To analyse the spatial clustering of the velocity dispersion, it is useful to measure its autocorrelation and cross-correlation with the density field in Fourier space. The density and velocity dispersion power spectra and the corresponding cross-spectrum are given by

$$\left\langle \delta(\boldsymbol{k})\delta(\boldsymbol{k}')^* \right\rangle = P_{\delta\delta}(k)\ \delta_D(\boldsymbol{k}-\boldsymbol{k}') \tag{3.6}$$
$$\left\langle \sigma^2(\boldsymbol{k})\sigma^2(\boldsymbol{k}')^* \right\rangle = P_{\sigma^2\sigma^2}(k)\ \delta_D(\boldsymbol{k}-\boldsymbol{k}') \tag{3.7}$$
$$\left\langle \delta(\boldsymbol{k})\sigma^2(\boldsymbol{k}')^* \right\rangle = P_{\delta\sigma^2}(k)\ \delta_D(\boldsymbol{k}-\boldsymbol{k}'), \tag{3.8}$$

with $\sigma^2 = \mathrm{tr}(\sigma_{ij}^2)$. We deconvolve the density field (CIC) with the CIC assignment kernel $W_{\mathrm{CIC}}(\boldsymbol{k}) = \prod_i \mathrm{sinc}^2(k_i/2k_{\mathrm{Ny}})$, to correct for the smoothing effect of the mass assignment scheme close to the Nyquist wave number $k_{\mathrm{Ny}} = N\pi/L$, and de-alias the measured density power spectrum by interlacing the original field with a grid shifted by half a cell size in all directions (cf. [283]).

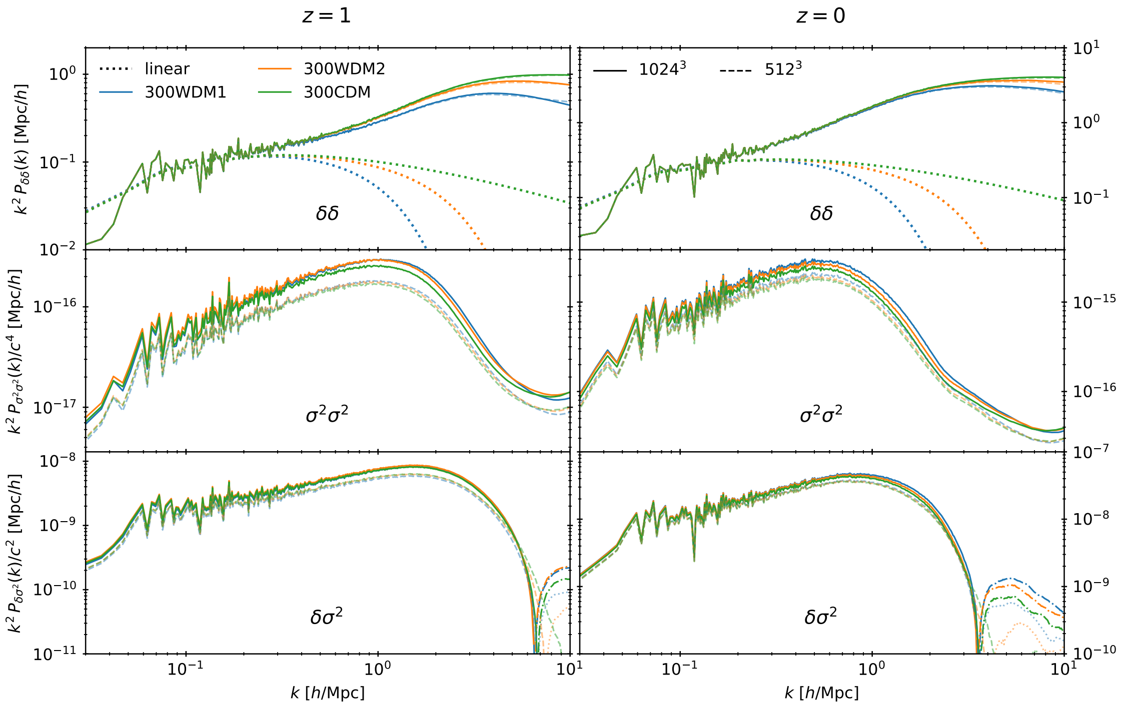

Figure 3.3: Power spectra of the density (top), velocity dispersion $\sigma^2 = \mathrm{tr}(\sigma_{ij}^2)$ (middle) and cross correlation (bottom) at redshift 1 and 0. Dashed lines show the lower resolution realizations and negative values in the case of the cross-spectrum at large k are indicated with dash-dotted and dotted lines.

Figure 3.3 shows the measured power spectra at redshift $z = 1$ and $z = 0$ for the three simulations. Starting from the top, we notice that at both redshifts the matter power spectrum is enhanced at small scales compared to the linear power spectrum due to the non-linear growth of structures. As expected from the set-up of the simulations, the amount of small-scale clustering is dependent on the truncation scale of the initial power spectrum. A comparison between the low and high resolution simulations shows that the results are well converged.

For the velocity dispersion power spectrum, the situation is somewhat different: even at the largest scales, we find a measurable offset of $\sim$ 20% in amplitude between the 300WDM1, 300WDM2 and 300CDM simulations. A comparison with the lower resolution simulations shows that none of the measurements are perfectly converged. This lack of fast convergence is very reminiscent of the convergence properties of the vorticity power spectrum, where various studies have found that the non-linear scale has to be very well resolved [267, 139]. Just as the vorticity, σ^2_{ij} is only non-zero in multistreaming regions and thus more strongly affected by resolution than those quantities that are non-zero also in the monokinetic regime and thus defined everywhere in space.

Since shell-crossing occurs predominantly in overdense regions, the velocity dispersion is highly correlated with the density field on large scales. On the largest scales, we find that $P_{\sigma^2\sigma^2}(k) \propto k^{-1}$, with a sharp drop on small scales. The same holds for the cross-spectrum, which however becomes negative above $k \sim 6\ h\mathrm{Mpc}^{-1}$ at $z = 1$. The inversion moves towards larger scales at later times, with $k \sim 3.5\ h\mathrm{Mpc}^{-1}$ at $z = 0$. This is a signature of the largest collapsed structures and has also been observed in the density – velocity divergence cross-spectrum [139, 169] and the velocity divergence – velocity dispersion cross-spectrum [169] at similar scales. The transition from correlation to anticorrelation at small scales is of course consistent also with the two-dimensional density-dispersion histograms we presented in the previous section. We note that the scale of anticorrelation between overdensity and velocity dispersion is independent of the type of simulation, and nearly independent of the resolution, indicating further that it originates from the largest collapsed structures. This phenomenon thus plausibly originates from the outer shells of the largest collapsed structures and we therefore expect it to be intimately related to the splash-back radius of galaxy clusters (cf. [119, 228, 212]), which denotes the outer caustic in isotropically collapsed systems (what we will call 'nodes' below).

3.4 The anisotropy of the velocity dispersion tensor

We previously argued that the progression of anisotropic collapse from walls to filaments to nodes should be reflected directly in the tensor σ^2_{ij}, absent of any strong isotropization processes. In this section, we analyze the anisotropy of the velocity dispersion using the anisotropic coefficients c_l, c_p, and c_s which are widely used in neuro-sciences for diffusion tensor imaging (e.g. [4, 251]). These allow us to visualize the anisotropy of σ^2_{ij} and provide a natural segmentation of the cosmic web. We then analyse the mass and volume fractions of the identified environments, measure their density distribution, and compare our results with other cosmic web finders. Following the N-body particles across multiple snapshots, we trace the mass build-up of the environments through time and measure the evolution of the mass and volume fractions.

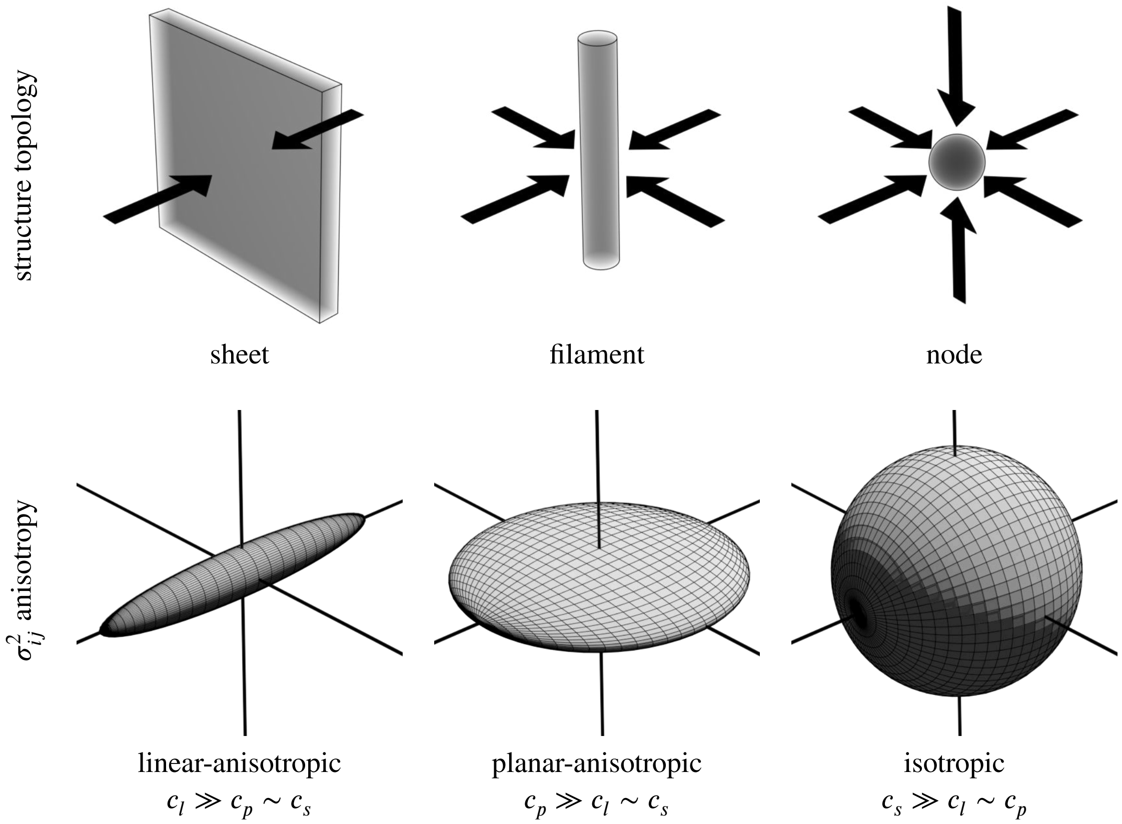

Figure 3.4: Illustration of collapsed axes in sheets, filaments, and nodes and the corresponding shape of the velocity dispersion tensor. Velocity dispersion emerges along the direction of the collapsed axes and thus the different cosmic web environments can be differentiated by the number of significant axes of σ_{ij}^2 which can be measured by the anisotropic coefficients c_l, c_p, and c_s, further described in the main text.

3.4.1 Classification of the cosmic web

In an idealized setting we would expect that uncollapsed and collapsed axes should correspond to vanishing and non-zero eigenvalues of the velocity dispersion tensor respectively. Naturally, an exact vanishing of eigenvalues is unlikely in a numerical setting, and due to overlapping perturbations on various scales. We therefore derive three dimensionless quantities from the eigenvalues $\lambda_1 > \lambda_2 > \lambda_3 \geq 0$ of σ^2_{ij} which capture the relative strengths of the collapsed dimensions (reflecting thus dominantly one-, two-, or three-dimensional collapse):

1. the linear anisotropy $c_l = (\lambda_1 - \lambda_2)/(\sum \lambda_i)$,
2. the planar anisotropy $c_p = 2(\lambda_2 - \lambda_3)/(\sum \lambda_i)$, and
3. the spherical anisotropy (or isotropy) $c_s = 3\lambda_3/(\sum \lambda_i)$.

Note that by construction $c_l + c_p + c_s = 1$, and hence these quantities parametrize a *barycentric space* with three extrema ($c_s = 1$: fully symmetric, $c_p = 1$: symmetric along two axes, and zero along the third, $c_l = 1$: dispersion only along one axis) and can be represented in a ternary diagram, as shown in fig. 3.5. We can divide this diagram into three parts depending on the dominant parameter and decide if a region is either

1. linear-anisotropic $\Leftrightarrow$ c_l is dominant $\Leftrightarrow$ 'wall'-like,
2. planar-anisotropic $\Leftrightarrow$ c_p is dominant $\Leftrightarrow$ 'filament'-like,
3. isotropic $\Leftrightarrow$ c_s is dominant $\Leftrightarrow$ 'halo'-like.

For a more sophisticated classification of the cosmic web, one might consider different segmentations of the anisotropy triangle, for example, by classifying filaments as regions which have a planar anisotropy larger than a small threshold, above which one assumes that collapse along the second axis has started. An analogous argument can be made for the isotropic component and nodes. We leave the investigation of these advanced classifications for a later study and define walls, filaments, and nodes depending on the dominant anisotropic parameter which avoids the introduction of additional parameters. Note that the multi-scale nature of the cosmic web means that filaments can be embedded in walls and nodes in filaments. Since this method uniquely identifies the environment at a specific point in space by its dominant anisotropic parameter, it does not resolve this hierarchical structure and the classification depends on the amount of small-scale perturbations. To identify the cosmic web on various scales, additional smoothing steps (either by suppressing small-scale fluctuations in the initial conditions or by post-processing) are required.

We compute the anisotropy parameters for each volume cell in the multistreaming region and show the resulting volume and mass distribution in fig. 3.7 for the 300WDM1_10, 300WDM2_10 and 300CDM_10 simulations. The largest part of the volume in all simulations has a highly linear-anisotropic velocity dispersion and hence is in wall-like structures. This is more pronounced in the WDM1 case, where 83% of the multistreaming volume has a planar anisotropy coefficient smaller than 0.25 and only a small fraction ($\sim$ 3%) has an isotropic coefficient larger than 0.25. In the CDM simulation, a larger fraction of the collapsed volume is isotropized, with

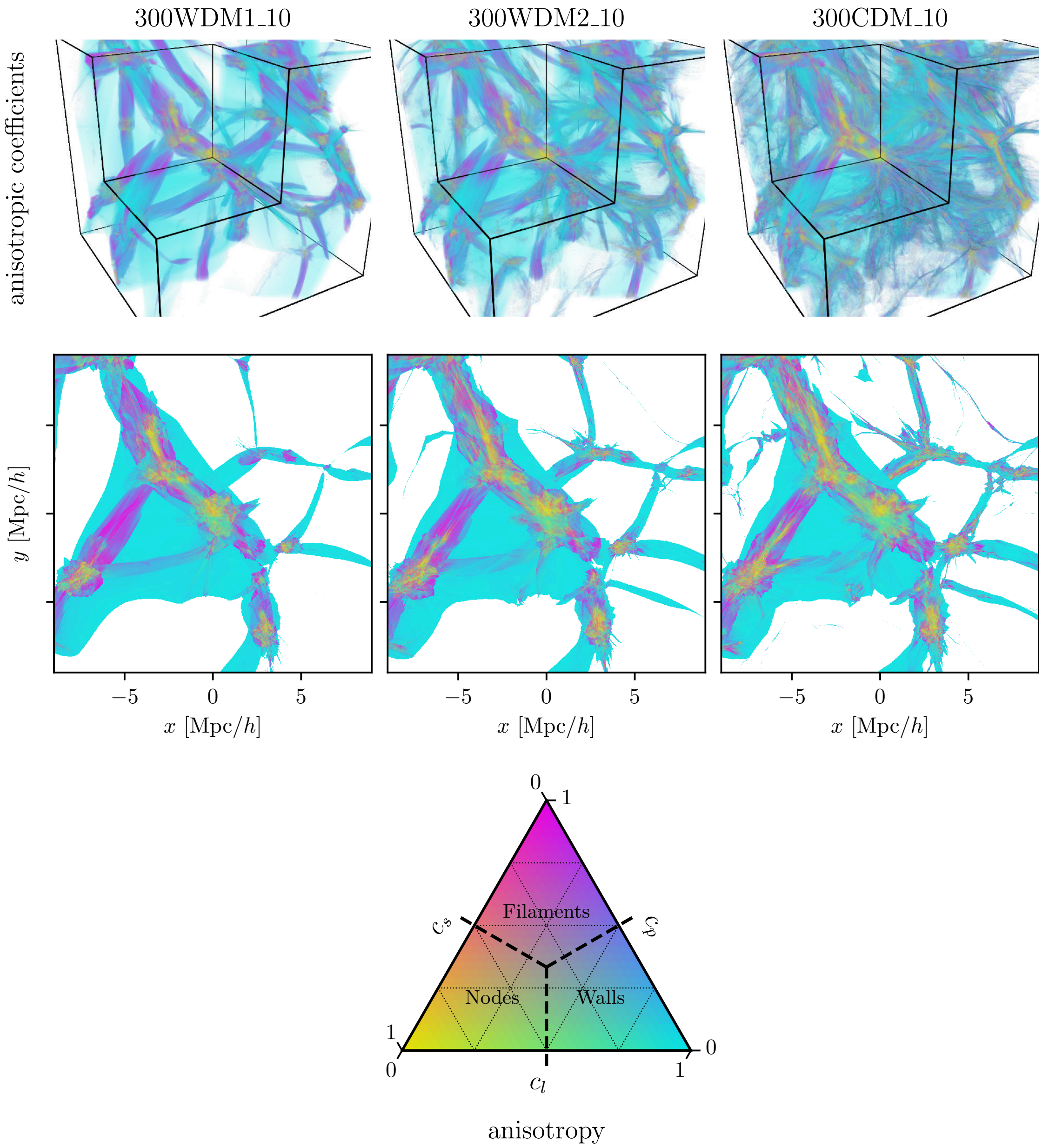

Figure 3.5: The anisotropy coefficients c_l, c_p, and c_s for a $\sim 18\ h^{-1}$Mpc box around a halo for the 300WDM1_10 (left), 300WDM2_10 (middle), and 300CDM_10 (right) simulation. The anisotropy is color-coded according to the ternary diagram, with linear, planar, and symmetric dominant regions in cyan, magenta, and yellow respectively.

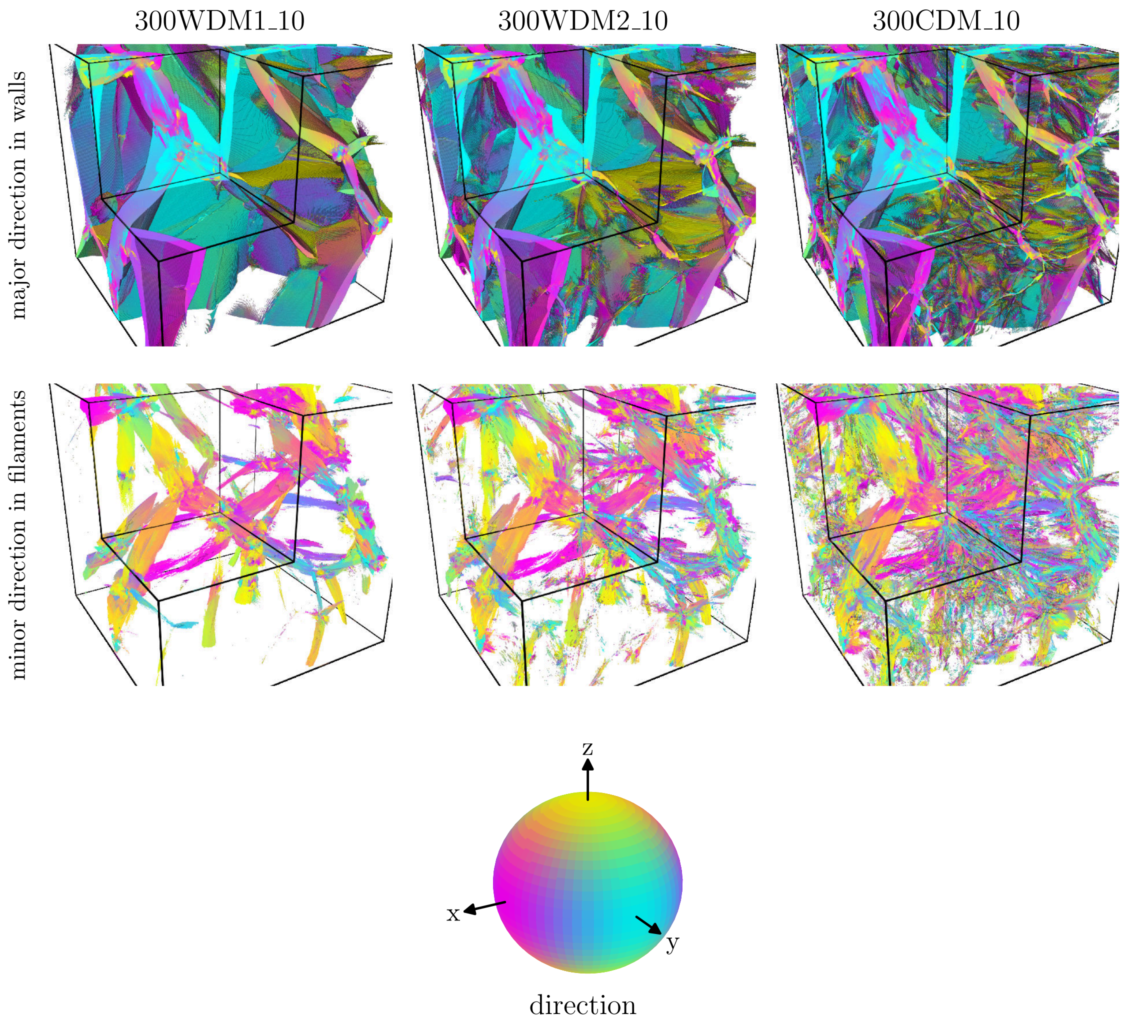

Figure 3.6: Direction of the major eigenvector of σ_{ij}^2 within wall-like regions and the minor eigenvector within filament-like regions. The characteristic directions are color-coded according to the unit sphere and they are perpendicularly aligned within wall-like regions and parallel to the extent of filaments.

26% of the volume having $c_p > 0.25$ and 10% having $c_s > 0.25$. Interestingly, we can see that the large volume fraction with vanishing spherical anisotropy in the 300WDM1 realization moves away from the $c_s = 0$ line and becomes more isotropized by the small-scale perturbations in the 300CDM simulation.

Looking at the mass-weighted distribution, we find a second peak at large c_s originating from high density regions which are predominantly located in fully collapsed structures (cf. fig. 3.8). From the 300WDM1 (300CDM) simulations, we find 17% (26%) of the collapsed mass being in regions with a planar coefficient larger than 0.25 and 42% (60%) in regions with an isotropic coefficient larger than 0.25. The results for the 300WDM2_10 simulation are located between the other two simulations.

	Simulation	uncollapsed %	walls %	filaments %	nodes %
volume	300WDM1	95 (95)	4.9 (4.5)	0.5 (0.4)	0.1 (0.1)
	300WDM2	92 (93)	7.4 (6.3)	0.7 (0.7)	0.2 (0.2)
	300CDM	89 (91)	9.6 (7.4)	1.2 (1.0)	0.4 (0.3)
mass	300WDM1	41 (48)	33 (31)	11 (9)	16 (13)
	300WDM2	*30 (40)*	35 (33)	10 (10)	*24 (17)*
	300CDM	*24 (37)*	36 (34)	11 (10)	*30 (19)*
		$\bar{\delta}$	$\bar{\delta}$	$\bar{\delta}$	$\bar{\delta}$
density	300WDM1	-0.6 (-0.5)	5.7 (5.9)	22 (21)	*204 (125)*
	300WDM2	-0.7 (-0.6)	3.8 (4.3)	14 (13)	*115 (78)*
	300CDM	-0.7 (-0.6)	2.7 (3.6)	8 (9)	69 (63)

Table 3.1: **Top:** mass and volume fractions in the single- and multistreaming regions. The multistreaming regions are split by the dominant anisotropy parameter into *linear* (wall-like), *planar* (filament-like), and *isotropic* (node-like) environments. The percentages are computed from the 1024^3 particle realizations using the tessellation density estimate, with the CIC densities showing consistent results. **Bottom:** mean density of the individual environments. Values from the 512^3 simulations are given in parentheses for comparison and highlighted in italic if they show a strong discrepancy.

In table 3.1 we list the volume and mass fractions of the c_p, c_l, c_s dominant and of the single-stream regions for the different simulations, including the lower resolution simulations to check for convergence. We note that convergence of the results in the CDM limit is generally a non-trivial question since in the perfectly cold limit, virtually all structure on the investigated scales should be in halos (cf. [306]). This can be seen from the CDM volume and mass fraction in node-like regions that is larger in the higher resolution simulation.

The fraction of volume and mass in multistreaming regions increases with colder simulations, consistent with the additional small-scale structures observed in fig. 3.1. The uncollapsed single-stream regions remain the dominant fraction of the volume, whereas most mass can be found in collapsed regions. Each of the three multistreaming regions gains volume by adding small-scale structures, but only the mass fraction in node-like regions increases significantly, while that in

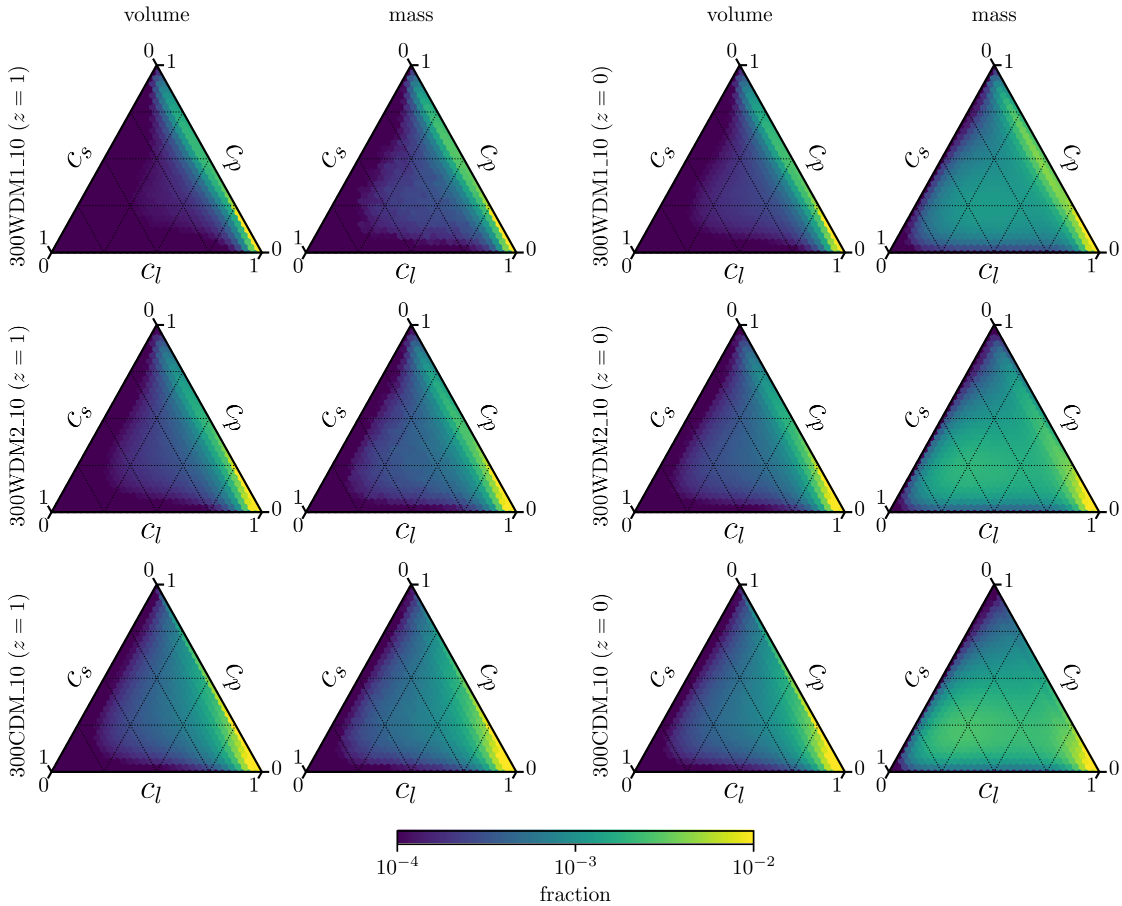

Figure 3.7: Distribution of volume and mass in multistreaming regions according to the anisotropic coefficients c_l, c_p, and c_s at redshifts $z = 1$ and $z = 0$. In most of the volume, the velocity dispersion is linear-anisotropic, with some fraction being between linear- and planar-anisotropic. The mass weighted distribution is bimodal with a second peak at high isotropy due to the contribution of the high density regions.

walls and filaments remain roughly constant.

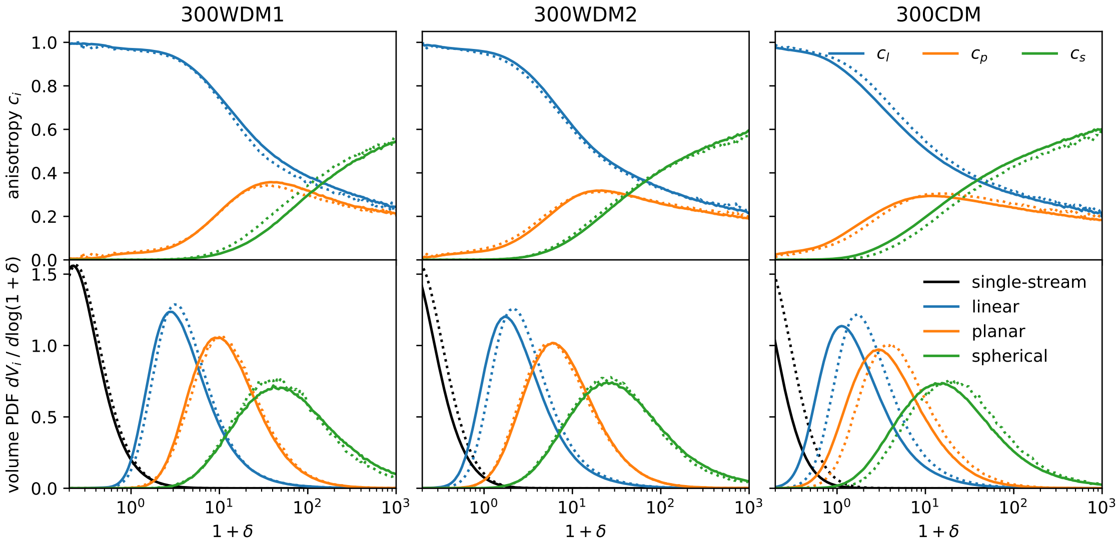

Figure 3.8: **Top:** Average value of the anisotropy coefficients depending on the local density (TESS) for the 300WDM1 (left), 300WDM2 (middle), and 300CDM (right) simulations at high (solid) and low (dotted) resolutions. **Bottom:** Relative distribution of regions with predominately linear anisotropy (walls), planar anisotropy (filaments), and spherical anisotropy (nodes) depending on the local density. We also include the single-stream distribution that falls within the shown density range.

To further investigate the density dependence of the anisotropic parameters, we measure their mean value as a function of the local density (TESS) $\delta(\boldsymbol{x}) + 1$. The results are shown in the top panels of fig. 3.8 and a comparison with the low resolution simulation (dotted) shows that they are fairly well converged in the simulations with truncated small-scale perturbations. In collapsed regions close to the mean density, the linear anisotropy parameter is strongest, whereas high-density regions have a predominantly isotropic velocity distribution. The planar anisotropic coefficient peaks around $\delta \sim 10$ in the CDM case and $\delta \sim 30$ in the WDM1 simulation, and decreases for both smaller and higher overdensities. The simulations differ mainly in the low density regime, which is almost purely linearly anisotropic in the 300WDM1 simulation, but has a small planar anisotropic contribution in the 300CDM simulation. Overall, small-scale perturbations lower the density threshold at which shell-crossing along the second and third axes can occur, and thus at which the planar anisotropy and isotropy become measurable. In the 300CDM simulation, this threshold remains unresolved due to initial density fluctuations at arbitrarily small scales.

Labelling each cell by its dominant anisotropic parameter, we can examine the density distribution of linear-, planar-, and spherical-anisotropic multistreaming regions (walls, filaments and nodes). The results are shown in the lower panel of fig. 3.8 and the mean density of each environment can be found in table 3.1. In agreement with the measured mean anisotropic coefficients, wall-like regions are predominantly in low density environments, followed by filament-like and node-like regions (this hierarchy also directly follows from the study of the initial shear tensor by calculating the probability of the eigenvalue signatures depending on the local overdensity, cf. [258]). In the 300WDM_10 simulation, the distributions peak at $\delta \sim 3$, $\delta \sim 10$, and $\delta \sim 50$ respectively. In the case of the colder simulation, the distributions shift towards lower densities due to the additional small-scale perturbations ($\delta \sim 1$, $\delta \sim 3$, and $\delta \sim 20$ respectively, for the 300CDM_10 simulation). A comparison to the low resolution simulation (dotted) shows qualitatively consistent results for both WDM simulations but a shift towards higher densities in the 300CDM_9 simulation due to the unresolved small-scale structure.

3.4.2 Comparison of cosmic web environments detected by different finders

Previous studies on volume and mass fractions in the cosmic web have found a wide range of values (a recent comparison can be found in [199], with some results included in the comparison table 3.2]). These sometimes large discrepancies are the result of fundamentally different classification criteria, which complicate the comparison of our results.

Most closely related to our method are the cosmic web finders MSWA [285] and ORIGAMI [99] (cf. section 2.2.2), which also exploit the Lagrangian to Eulerian coordinate mapping. Since we use the same single-stream definition as MSWA, our mass and volume fractions for cosmic voids are comparable. We note that the reported void volume fractions using this technique are consistently $\sim 90\%$, but the mass fractions vary strongly (23% by [285], 32% by [269] and 56% by [199]). The void volume fraction reported in Libeskind et al. [199] for ORIGAMI is lower (70%), with a larger volume fraction classified as nodes (7.4%) and filaments (6.4%). The mass is equally more attributed to nodes (50%), but less to walls (14%).

Compared to further methods, we find our volume and especially mass fraction of filament-like regions to be towards the lower end of the wide range of reported values. Results for the mass fraction using stream number thresholds range from 10%-20%, with other methods assigning up to 50% (NEXUS+ [60]) and 60% (DisPerSE [298, 199]) of the total mass to filaments. On the other hand, the total mass fraction of wall-like regions is at the upper level of previous studies (13%-33%), with our results being comparable to Shandarin et al. [285].

To compare the density dependence of the environments detected by the different cosmic web finders, we use the public data from the cosmic web comparison paper by Libeskind et al. [199], which includes an N-body simulation[2] snapshot at $z = 0$ and the classification of the cosmic web environments on a 100^3 grid. The public data includes various classification techniques and we refer the reader to [199] for further information and references.

To increase the comparability of the results, we compute the volume averaged density field using the DTFE code [278, 328, 59] on the same 100^3 grid for the provided snapshot as well as on a 256^3 grid for the 300CDM_512 simulation at $z = 0$. Figure 3.9 shows the measured density distribution of each environment. Note that not all classifiers detect every environment and hence some lines are missing from some of the panels. Additionally, we compute the volume and mass fractions of each environment and its mean density. The values are listed in table 3.2.

Overall, the cosmic web environments detected via the velocity dispersion anisotropy discussed in this paper are consistent with the range of density distributions and mass and volume fractions from existing methods. As already reported in [199], the measured quantities of the

[2] Simulation parameters: 200 h^{-1}Mpc box, 512^3 particles with ΛCDM cosmology and [67] parameters

Method	volume fraction				mass fraction				mean density			
	uncollapsed %	walls %	filaments %	nodes %	uncollapsed %	walls %	filaments %	nodes %	uncollapsed $\bar{\delta}$	walls $\bar{\delta}$	filaments $\bar{\delta}$	nodes $\bar{\delta}$
Bisous	–	–	12.1	–	–	–	31.0	–	–	–	2.6	–
CLASSIC	70.3	23.8	5.3	0.6	31.1	32.2	23.4	13.3	0.4	1.4	4.4	21.1
DisPerse	38.8	37.3	23.9	–	12.5	25.2	62.3	–	0.3	0.7	2.6	–
MMF-2	73.3	19.0	7.8	–	47.9	19.8	32.3	–	0.7	1.0	4.2	–
MSWA	90.3	8.8	0.7	0.1	49.5	27.9	13.0	9.6	0.5	3.1	17.7	84.5
NEXUS	65.7	22.8	11.3	0.1	14.7	21.5	52.8	11.0	0.2	0.9	4.7	95.0
ORIGAMI	73.8	12.3	6.4	7.5	19.5	11.5	11.9	57.1	0.3	0.9	1.9	7.6
Spineweb	33.2	30.7	36.1	–	14.7	22.5	62.8	–	0.4	0.7	1.7	–
T-WEB	42.5	41.3	14.9	1.3	13.3	31.3	37.6	17.8	0.3	0.8	2.5	14.0
V-WEB	78.7	18.1	3.0	0.2	39.2	32.5	20.3	8.1	0.5	1.8	6.9	35.4
σ^2_{ij} anisotropy	91.3	7.4	1.0	0.3	51.1	30.4	8.2	10.3	0.6	4.1	8.0	34.5

Table 3.2: Mass and volume fractions and the mean density of the cosmic web environments. The comparison data has been obtained from the data published together with the cosmic web comparison paper by [199]. The data from the velocity dispersion anisotropy classification described in this paper has been computed from the 300CDM_512 simulation. Since we are using the DTFE density estimation for comparability, the mass fractions and mean densities reported for the 300CDM_512 simulation show a small deviation from the data in table 3.1.

cosmic web regions highly depend on the applied definition. The mass and volume fractions measured in this paper agree best with MSWA method as we have already noted above. However, filaments and nodes extend to lower densities than the ones identified with MSWA and their density distributions are more similar to the environments identified with V-web [155], MMF-2 (filaments only [10]), CLASSIC (see [199] for method and further references) and T-web [132, 104].

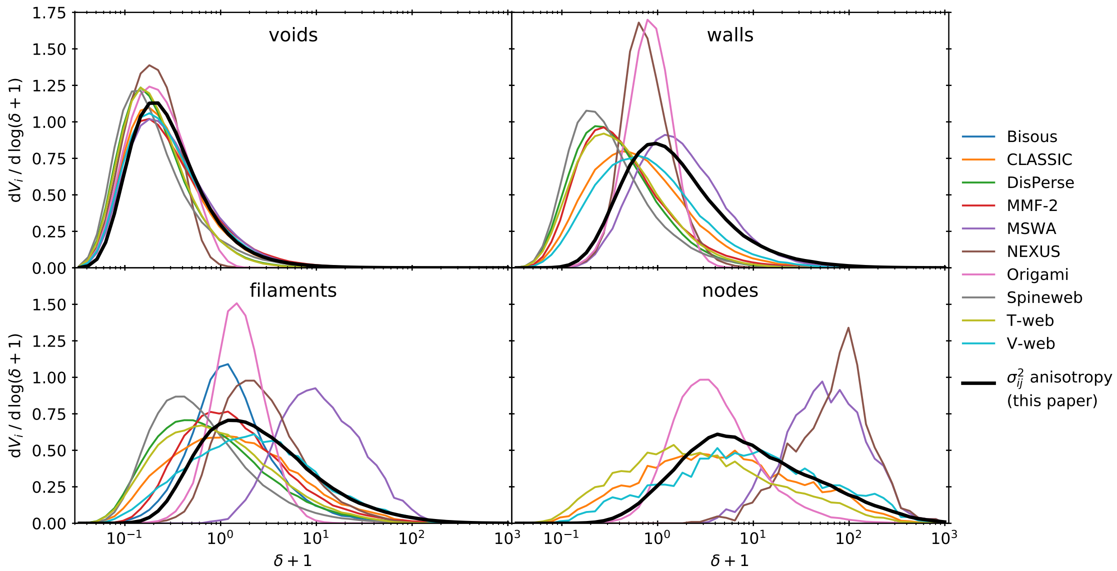

Figure 3.9: Comparison of the density contrast $1+\delta$ distribution (normalized) of the cosmic web environments found by different cosmic web finders (note that not all environments are classified by every finder). The comparison data has been obtained from the data published together with the cosmic web comparison paper by [199] containing more details about the individual classifiers.

3.4.3 Evolution of mass and volume fractions of structures over cosmic time

Most of our results above have been obtained at $z = 0$. In order to complement this momentary picture at late time, we investigate in this subsection the evolution of the collapsed regions of the respective morphologies over cosmic time.

From the theory of anisotropic collapse, we expect the first multistreaming regions to have linear-anisotropic velocity dispersion. Planar-anisotropic and isotropic velocity dispersion emerge at a later stage when the wall-like structures collapse along the second and third axes. As the collapse time depends on the amplitude and scale of the perturbation (cf. appendix A.4), more single-streaming volume will continuously enter the linear-anisotropic regime and collapse further. In fig. 3.10, we measure the volume and mass fraction that has collapsed at different times during our simulation. As the perturbations with the highest overdensities enter the multistreaming regime first, a significant fraction of the total mass can be found in collapsed regions before the same fraction of volume has collapsed. The multistreaming mass fraction remains larger than

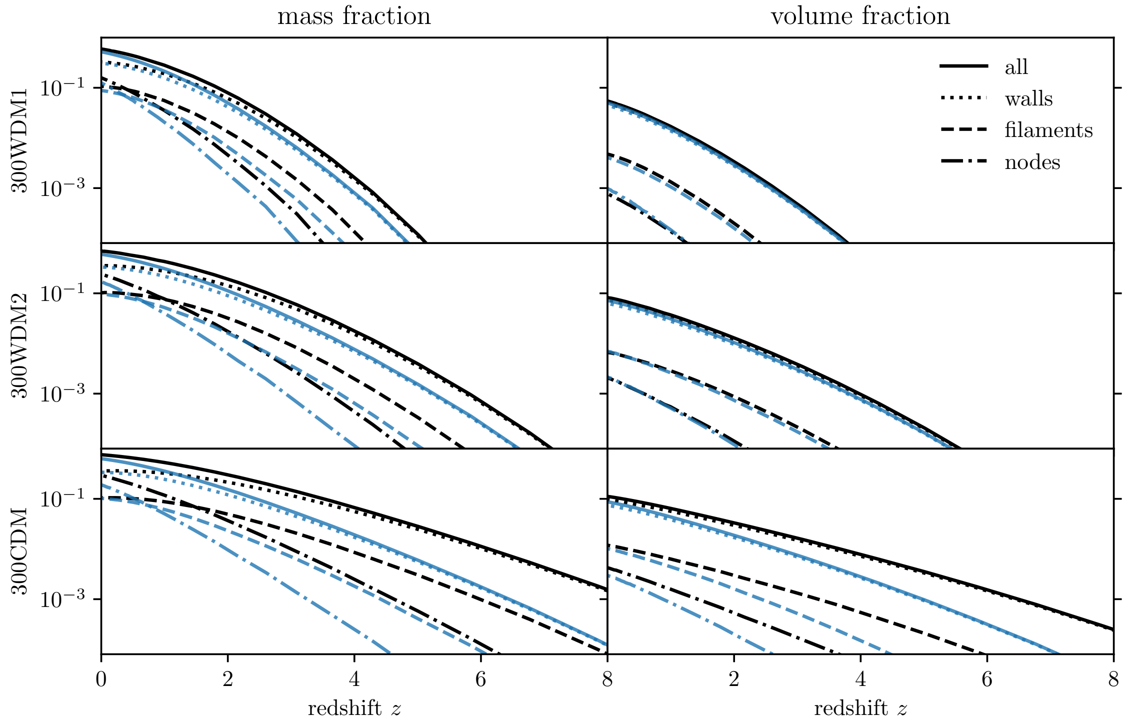

Figure 3.10: Evolution of the fraction of the mass (left) and volume (right) that has collapsed (solid lines) and the subdivision according to the anisotropic shape of the velocity dispersion tensor (dotted and dashed lines) for the CDM and WDM simulations (rows). To check for convergence, we include the results for the low resolution simulations (blue). The cell densities have been obtained by the CIC algorithm.

the volume fraction throughout the simulation. We find that the first multistreaming regions occur at later times in the WDM simulation, consistent with the slower collapse of larger scales. The truncated initial power spectrum leads to an overall lower fraction of multistreaming volume and mass at any time during the entire simulation. We notice that as expected, the first collapsed structures have linear-anisotropic velocity dispersion, before a significant fraction of mass and volume becomes planar and spherically isotropic. Comparing the high and low resolution results we notice that even for the 300WDM1 and 300WDM2 simulations, the mass fractions at high redshifts depend on the resolution. This discrepancy becomes naturally larger in the case of the 300CDM simulation, as new small-scale perturbations are added when the resolution of the simulation is increased. Since these small fluctuations are the first to collapse, the difference becomes particularly evident at early times.

In order to better understand the evolution of the environments, we follow the dark matter particles that reside in the various environments at $z = 0$ back in time. At each earlier snapshot we compute the relative mass fractions of the environments. The results up to $z = 5$ are shown in fig. 3.11. Starting from the single-stream regions, we find that their progenitors were mostly single-stream regions. Wall-like regions mainly feed from single-stream regions, with a small fraction passing through cells with planar or spherical anisotropy. As predicted by the anisotropic collapse model, walls collapse to filaments, hence the progenitors of filament-like regions were mainly in wall-like regions. For the node-like regions however, we find that many of their constituent particles appear to collapse directly from wall-like regions. Given the relatively low time and space resolution we have around halos, this aspect should be investigated more closely in future work.

Among the progenitors of each environment, we find a small fraction of particles that have changed environment in the opposite way than predicted by the theory of anisotropic collapse. This fraction is larger in the colder simulations, with up to 20% of the void progenitors passing through multistreaming cells and 25% of the filament progenitors coming from node-like regions. This is most likely due to the finite resolution of the rasterization grid. If the cell encloses multiple environments (either due to the small size of the collapsed region in CDM, or at a boundary), a particle still in a lower level in the collapse hierarchy might be attributed to a higher level environment dominating the cell (e.g. a void particle assigned to a wall-cell). This issue could be avoided by evaluating the tessellation directly at the particle positions.

The scale of the WDM cut-off does not change the qualitative results of mass flowing from the single-stream regime to wall-, filament- and finally node-like structures. However, the fraction of mass flowing in the opposite direction increases with the amount of small-scale structure, further indicating that this is an effect of the rasterization cell size. Changing the resolution of the simulation does not alter the mass fractions of the progenitors significantly. However, since the measured collapsed mass fraction at a given time is lower at lower resolutions if the perturbations are not fully captured (see discussion above), the mass transport from one environment to the next is also delayed. This is especially evident for the 300WDM2 and 300CDM simulations as well as the node-like environments in the 300WDM1 case.

This so-called *mass transport* across the cosmic web has been studied in detail e.g. by Cautun et al. [60] using the NEXUS+ algorithm. Qualitatively, these authors reported similar trends in mass flowing from voids to walls to filaments and finally to halos, including significant reverse

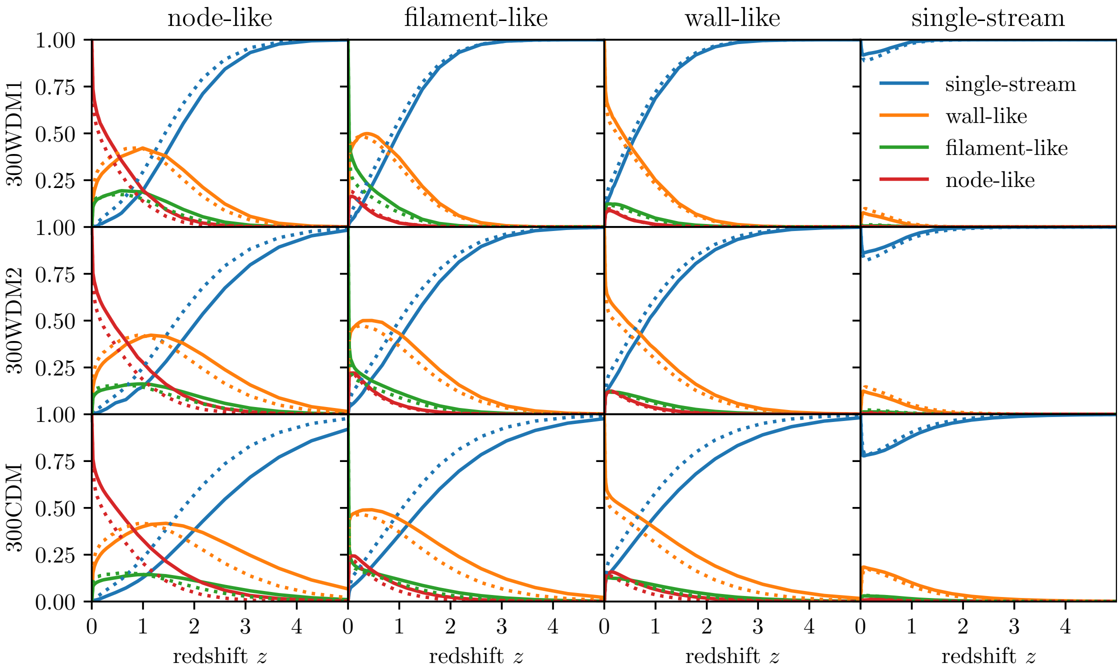

Figure 3.11: Environmental origin of the mass in node-like (first column), filament-like (second column), wall-like (third column) and single-stream (right column) environments at $z = 0$ for the three different dark matter variants (rows). We show the mass fractions by environment at redshift z that are in the target environment at redshift $z = 0$. The results from the xDM_10 simulations are plotted with solid and their lower resolution xDM_9 counterparts with dotted lines.

flows which they attributed to incorrect identification of environments in underdense regions. Their results differ in the timescale of matter transport through the environments, with collapsed environments being overall more "stable" between $z = 2$ and today, whereas we find large mass fractions in uncollapsed regions. This is most likely tied to the unconverged collapsed mass fraction in cold simulations discussed above. Furthermore, they observe a filamentary mass fraction of ~80% as the progenitors of nodes, whereas in our measurements only ~20% of the node mass has previously been in filaments. This most likely is connected to our overall lower filamentary mass fractions and using a different segmentation of the anisotropy triangle will most likely lower the discrepancies.

3.5 Orientation of the cosmic velocity dispersion

In the previous section, we have measured the anisotropy of the velocity dispersion field. The characteristic direction of the anisotropy, i.e. the main axis of the tensor field in wall-like structures and the minor axis in filament-like structures, contains additional information on the axes of collapse. In fig. 3.6, we visualize the directions in walls (middle) and filaments (bottom) in the 18 h^{-1}Mpc cube using the direction-color encoding shown in the colored unit sphere. For wall-like structures the main axis of the velocity dispersion is perpendicular to the structure itself, whereas in filament-like structures the minor axis is parallel to the filament as expected from the collapse history of these regions. We can already see by eye that the characteristic directions are consistent over large distances across an entire segment of the cosmic web. This remains true for large structures even in the CDM simulation where the visualizations become however somewhat cluttered by small-scale structures. This long range consistency of the velocity dispersion tensor could be used in principle to further dissect the volume by unambiguously identifying individual walls and filaments. In this section, we will first measure the typical extent of the alignment using a marked correlation function and measure its deviations induced by small-scale perturbations. In the second part, we compare the orientation of the velocity dispersion field with the tidal force tensor which has also been used for classifying the cosmic web and which is tightly related to the velocity dispersion.

3.5.1 Alignment of the velocity dispersion tensor

Since filaments and walls are to first order not spatially curved, we expect the characteristic directions of the velocity dispersion field to be consistent over their typical sizes. To quantify this alignment as a function of distance, we use so-called marked correlation functions. They extend the classical correlation function framework (cf. [245]) to study the spatial clustering of (usually scalar) properties of objects, so-called *marks* [304, 305]. These marked correlation functions have already been successfully applied to study the clustering of galaxy properties (e.g. [31, 290, 293, 292]), the self-alignment and tidal field alignment of cosmic voids [256], and have more recently been suggested as a tool to constrain modified gravity models [330].

The commonly used marked correlation function [290] is defined as the ratio of the weighted to the unweighted correlation function,

$$\mathcal{M}(r) = \frac{1 + W(r)}{1 + \xi(r)} \approx \frac{WW}{DD}, \tag{3.9}$$

where $1 + W(r) = \sum_{ij} m(\boldsymbol{x}_i, \boldsymbol{x}_j)/\bar{m}$ is the sum over all objects i, j at separation r weighted by the mark function $m(\boldsymbol{x}_i, \boldsymbol{x}_j)$, which for scalar marks usually is its product, i.e. $m(\boldsymbol{x}_i, \boldsymbol{x}_j) = m_i m_j$. Analogous to the unweighted correlation function, the approximation WW/DD (the ratio of the weighted to the unweighted pair counts) can be used to efficiently estimate the marked correlation function. If the marks are uncorrelated, $\mathcal{M}(r) = 1$. Correlated and anticorrelated marks manifest themselves as larger and smaller values respectively.

For our measurement, the marks are the velocity dispersion tensors (or more precisely its eigenvectors) defined in every volume cell, which we have to reduce to a scalar quantity in the mark function (cf. [31]). We use the angle θ between the major or minor eigenvectors $\boldsymbol{e}$ of σ^2_{ij} at the volume elements located at $\boldsymbol{x}_1$ and $\boldsymbol{x}_2$ and since the eigenvectors are invariant under sign inversion, we define $m(\boldsymbol{x}_i, \boldsymbol{x}_j) = (\boldsymbol{e}(\boldsymbol{x}_1) \cdot \boldsymbol{e}(\boldsymbol{x}_2))^2 = \cos(\theta)^2$. Together with our grid-based data, this definition allows us to efficiently compute $\mathcal{M}(r)$ in Fourier space using

$$\mathcal{F}(WW)(\boldsymbol{k}) = \frac{1}{\bar{m}} \int d^3\boldsymbol{r} \exp(i\boldsymbol{k}\boldsymbol{r}) \int d^3\boldsymbol{r}_1 \left(e_i(\boldsymbol{r} + \boldsymbol{r}_1) e^i(\boldsymbol{r}_1)\right)^2 \tag{3.10}$$

$$= \frac{1}{\bar{m}} \mathcal{F}(e_i e_j)(\boldsymbol{k}) \cdot \mathcal{F}(e^i e^j)(-\boldsymbol{k}), \tag{3.11}$$

with summation over $i, j = 1, 2, 3$.

We are primarily interested in the excess of alignment compared to a random distribution of the eigenvectors. To measure this excess, we compute $\mathcal{M}_{\text{rand}}(r)$ over five permutations of the velocity dispersion tensor field. Comparing $\mathcal{M}(r)$ with the variance of $\mathcal{M}_{\text{rand}}(r)$ allows us to quantify the significance of our results. The results for the alignments of the major (minor) eigenvectors of σ^2_{ij} in the wall-like (filament-like) collapsed regions are shown in fig. 3.12. On small scales, the characteristic directions for both wall-like and filament-like structures are highly correlated, which is consistent with our expectation based on the spatial coherence of the tensors shown qualitatively in fig. 3.6. The alignment decays with increasing distance and disappears for scales larger than $\sim 30\ h^{-1}$Mpc which corresponds roughly to the typical extent of large walls and filaments found in simulations [60] and observations (e.g. [44]). The alignment of the major eigenvector field in wall-like structures is generally stronger than the alignment of the minor eigenvector field in filament-like regions, indicating that the orientation of the velocity dispersion field is more consistent in the early stages of collapse (along walls) than in regions that have evolved further in the collapse hierarchy (along filaments).

Going from the WDM to the CDM simulation, the alignment correlations remain highly significant but decrease at all scales as expected. Small-scale initial perturbations on the one hand create additional collapsed structures in previously uncollapsed regions, and on the other hand isotropize the smooth large-scale structures by causing them to fragment into smaller filaments and halos. In order to measure this “isotropization” we compare the mark correlation function measured on the wall-like and filament-like support of the 300WDM1_10 simulation between the CDM and WDM1 realizations. The result is shown in the lower panel of fig. 3.12. On short

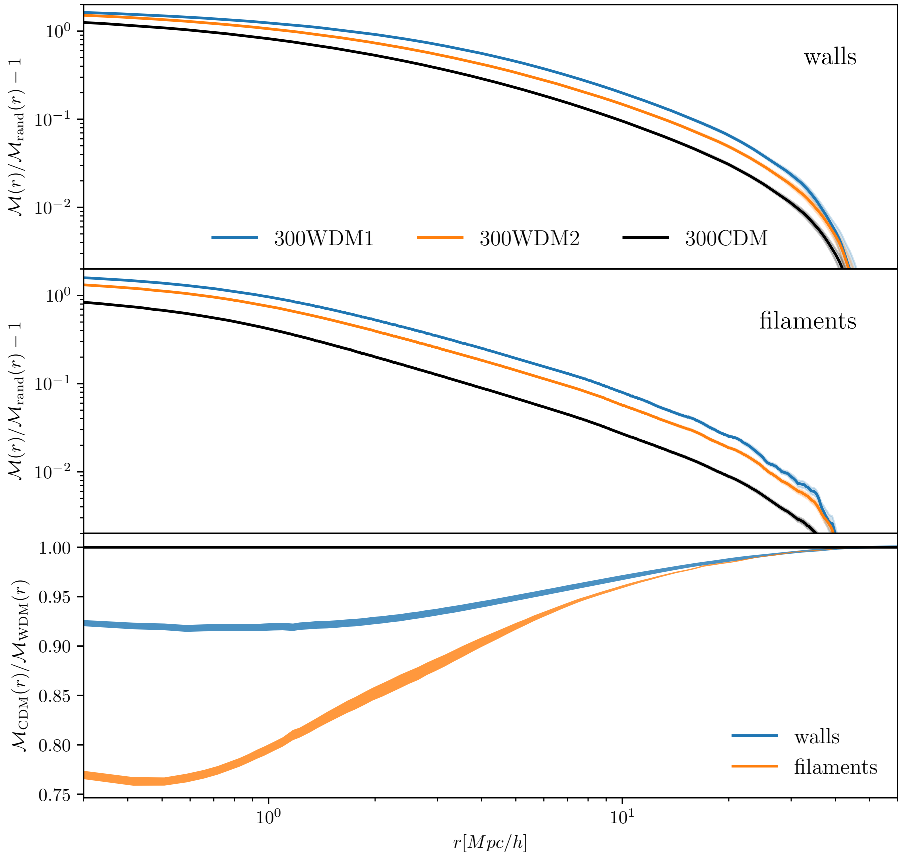

Figure 3.12: Relative strength of the marked correlation function (eq. (3.10)) measuring the velocity dispersion alignment over the distance r compared to a random field. We show the alignment of the major eigenvector field in wall-like structures (top) and minor eigenvector field in filament-like regions (middle) for the different simulations. Bottom: Relative strength of the marked correlation function in 300CDM_10 compared to 300WDM1_10, measured on the regions that are classified as walls and filaments in the 300WDM1_10 simulation.

separations the marked correlation function in the 300CDM simulation is 8% lower in wall-like regions and 25% lower in filament-like regions. As the marked correlation approaches the random distribution on larger scales, the difference between the simulations vanishes.

Another way of locally quantifying the influence of small-scale structures on the large-scale walls and filaments is to compare the strength of the velocity dispersion along and perpendicular to the structure and how it changes by adding perturbations. For this we define the angle between the two velocity dispersion components as $\tan(\alpha) = \sigma^2_{\parallel}/\sigma^2_{\perp}$, where the orientation is defined by the eigenvectors of σ^2_{ij} in the WDM1 simulation. To compute the parallel and perpendicular components, we transform $\sigma^2_{ij,\mathrm{xDM}}$ to the eigenframe of $\sigma^2_{ij,\mathrm{WDM1}}$ and use its diagonal components.

In fig. 3.13 we compare the point-wise differences in amplitude and alignment angle between the 300WDM1 simulation and the 300WDM2 and 300CDM simulations respectively for wall-like and filament-like regions. Since the amplitude of the velocity dispersion is connected to the scale of the structure (cf. section 3.3), we plot the distributions as a function of $\mathrm{tr}(\sigma^2_{ij})$ to check for additional biases. We find that the velocity dispersion in regions with low amplitude in 300WDM1 is generally enhanced in both filaments and walls, but less affected by the small-scale structure if the velocity dispersion is already large. Overall, both the amplitude of σ^2_{ij} and the alignment are highly consistent in most of the wall-like and filamentary volume.

3.5.2 Correlation with the gravitational tidal field

The Zel'dovich approximation (cf. section 1.2.4) predicts that anisotropic collapse is dictated by the large-scale tidal field tensor

$$T_{ij} = \frac{\partial^2 \phi}{\partial x_i \partial x_j}, \tag{3.12}$$

where ϕ is the gravitational potential. Since the large-scale gravitational potential is constant at linear order, the large-scale tidal field remains correlated with the collapse evolution of the cosmic web. This fact has been used previously to classify the cosmic volume into the void-wall-filament-node morphology [132]. Since in the ZA, the particle velocities before shell-crossing obey $\mathbf{v} \propto \boldsymbol{\nabla}\phi$ (this relation can be extended to the early non-linear regime, see e.g. [63, 64], but the corrections remain small if the velocity field is filtered on sufficiently large-scales), a similar argument implies that before shell-crossing (or smoothed on large-scales), the velocity divergence tensor of the mean velocity field also reflects these cosmic web environments (used in the V-web classification of [155]). After shell-crossing, this inflow pattern gives rise to the anisotropic dispersion that we discuss and quantify in this paper.

We thus want to ask next whether we can recover this expected correlation between the two tensor fields: the tidal field as the dynamic origin of anisotropic collapse, and the large-scale velocity dispersion tensor as the result and signature of anisotropic collapse. We compute the tidal field tensor of the large-scale structure from the smoothed density field measured by the CIC deposition of the dark matter particles. We use a Gaussian kernel with radius $r_s = 1\ h^{-1}$Mpc to filter out small-scales. The qualitative results are not sensitive to r_s and the measured alignment only drops significantly for $r_s < 500\ h^{-1}$kpc and $r_s > 4\ h^{-1}$Mpc. The tidal field can be conveniently derived in Fourier space as $\hat{T}_{ij}(\boldsymbol{k}) = -4\pi G\,(k_i k_j)k^{-2}\,\hat{\rho}_s(\boldsymbol{k})$. We compute the eigenvalue

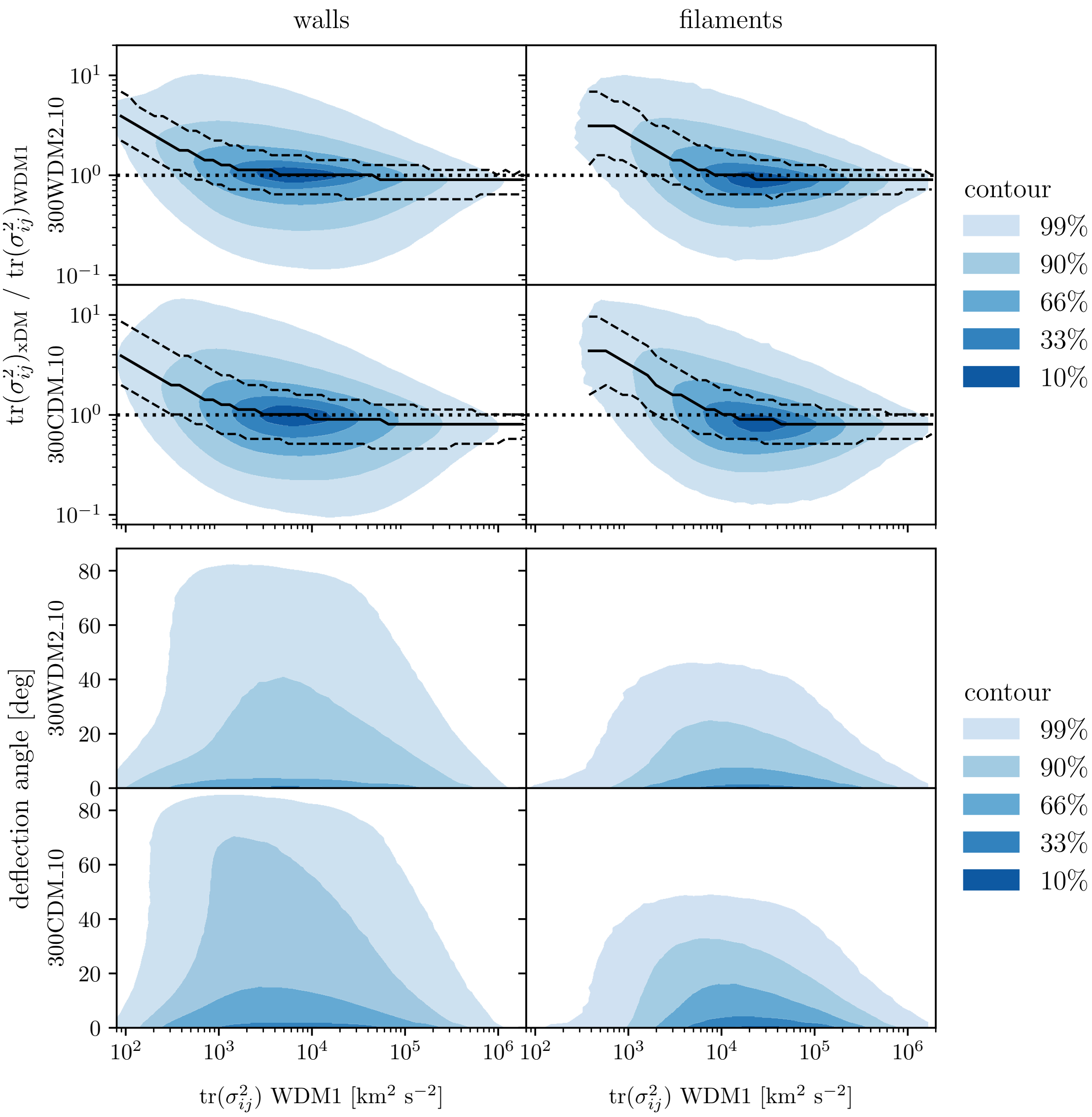

Figure 3.13: Comparison of the velocity dispersion in walls and filaments between the 300WDM1_10 simulation and 300WDM2_10 and 300CDM_10 respectively. **Top**: relative change of the magnitude (trace) of σ^2_{ij} as a function of the WDM1 magnitude. **Bottom**: change of angular alignment of the velocity dispersion defined as the angle spanned by the velocity dispersion along and perpendicular to the wall (filament) $\tan(\alpha) = \sigma^2_{||}/\sigma^2_{\perp}$. The directionality of the structures is defined by their characteristic eigenvector of the velocity dispersion tensor in the 300WDM1_10 simulation. The contour levels include 99%, 90%, 66%, 33% and 10% of the volume elements respectively and the lines show the median and 66% intervals at fixed velocity dispersion amplitude.

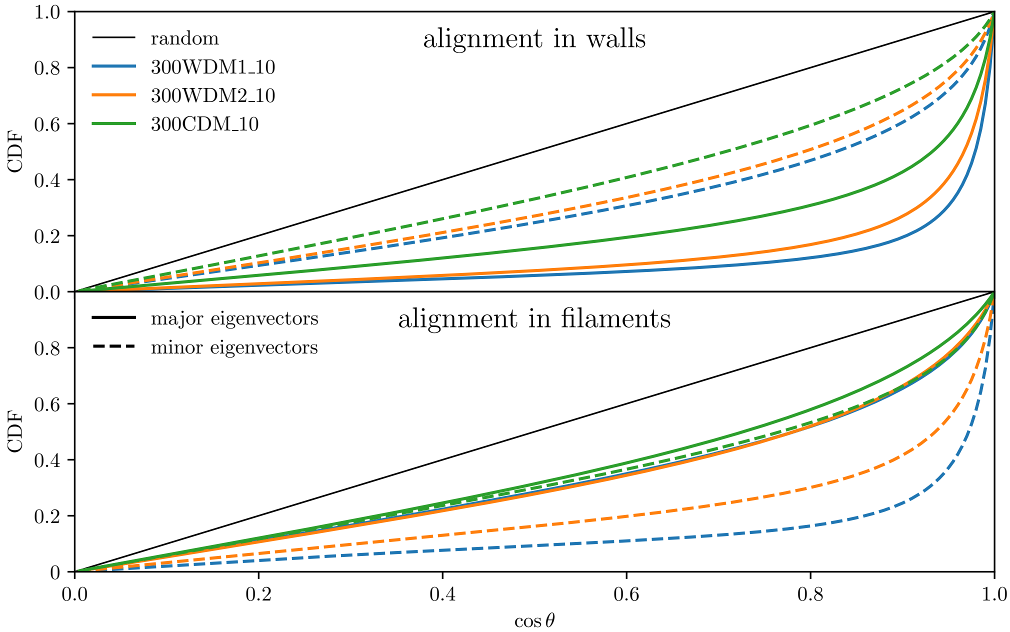

Figure 3.14: Cumulative distribution function of angles between the major (solid) and minor (dashed) eigenvectors of σ^2_{ij} and the tidal field tensor. The tidal field has been computed from the smoothed density field ($l_S = 1\ h^{-1}$Mpc) at redshift $z = 0$. The distributions are plotted separately for the wall-like (top) and filament-like (bottom) regions.

decomposition in each cell to obtain the principal axes of the tidal field and measure the angle θ between its eigenvectors and the eigenvectors of the velocity dispersion tensor.

Figure 3.14 shows the cumulative distribution function (CDF) of the angles between the major-major and minor-minor eigenvectors of the two fields within the wall-like and filament-like regions. For a purely random distribution, $\cos\theta$ is uniformly distributed over $[0, 1]$. We notice a strong positive alignment for both vector fields in all simulations, with the major eigenvectors being stronger aligned in wall-like regions, and minor eigenvectors in filament-like regions. This follows directly from the distinct nature of the major and minor directions in walls and filaments as discussed previously. As expected, the two vector fields have the highest alignment in the 300WDM_10 simulation with 73% (67%) of the major (minor) eigenvectors in wall-like (filament-like) regions deviating by less than 20 degrees from their counterpart. The deviations in the velocity dispersion alignment discussed in the previous section lower this alignment in the colder simulations, especially in filamentary regions that have progressed further in the collapse hierarchy (43% of the major eigenvectors in walls and 33% of the minor eigenvectors in filaments within 20 degrees in the 300CDM_10 simulation). However, the alignments remain highly significant.

3.6 Comparison with the collisional dynamics of an ideal gas

Before we conclude our studies of the velocity dispersion, we take a look at the behavior of baryonic gas during the collapse of a perturbation. For this purpose, we have run a hydrodynamic simulation, allowing us to measure the gas density and temperature in the regions where DM has undergone shell-crossing.

Before we conclude our studies of the velocity dispersion arising from the collapse of cosmic structures, we want to take a look at the dynamics of baryons. They form a collisional ideal gas, and thus behave fundamentally different from the collisionless DM component. Baryons in the intergalactic medium (IGM), in contrast to DM, are also directly detectable for example as absorption features in high redshift spectra of quasars in the form of the Ly-α forest [209, 218]. Until shell-crossing, baryons and DM roughly trace each other[3] (e.g. [8]), but the collisional character of the former leads to local thermodynamic equilibrium and the formation of shocks instead of caustics. The anisotropic velocity dispersion, that captures most of the kinetic energy of the DM sheets after collapse, thus becomes an isotropic velocity dispersion in the baryonic case, where the VDF is described by the Maxwell-Boltzmann distribution. The temperature of the gas in the collapsed region depends on the kinetic energy before collapse, and it is thus reasonable to expect that it will be related to the velocity dispersion of DM.

In this section, we will measure this temperature – DM velocity dispersion relation and investigate the possibility of predicting IGM temperatures from DM-only simulations. For this purpose, we have run a cosmological hydrodynamic simulation following baryons and DM, allowing us to measure the gas density and temperature in the regions where DM has undergone shell-crossing. This hydrodynamic simulation was initialized with the same parameters and random seed as the 150CDM DM-only simulation (cf. section 3.2) and was run with the RAMSES [312] simulation code. Since we are mostly interested in the shock-heating of the ideal gas during gravitational collapse, we disabled the cooling module, the UV background radiation, and other subgrid models. More details on the simulations can be found in appendix A.3.

In fig. 3.15, we show the velocity dispersion magnitude and gas temperature measured on a slice in the 150CDM simulations. We immediately observe that the temperature distribution follows the distribution of DM multistreaming regions. While the baryonic gas is cold in voids (especially since we ignore UV background heating), it is substantially heated in the multistreaming environments, and peaks at the intersections of the cosmic web. These intersections correspond to filaments and nodes, which have undergone collapse along multiple axes, heating the gas to an even larger amount[4]. Unlike the collapsed environments in the DM component which form a relatively fine net-like structure, the gas temperature distribution appears more clumpy, with heated regions extending beyond the DM multistreaming regions. The temperature in these

[3] This is only approximately true, since baryons below the horizon scale are coupled to photons before recombination and thus baryonic perturbations are damped. At later times, the gravitational coupling between DM and baryons will reduce this discrepancy, cf. [339, 8].

[4] Note that we have disabled cooling in the simulation, which would be very efficient in the densest and hottest regions (nodes). Measurements at the high temperature end have thus be treated with caution, and more sophisticated simulations would have to be used to make a predictive statement about the $\mathrm{tr}(\sigma ij^2)$–T relation. The measurements presented here should however be sufficient to demonstrate the effect of isotropization of the velocity dispersion during the gaseous collapse.

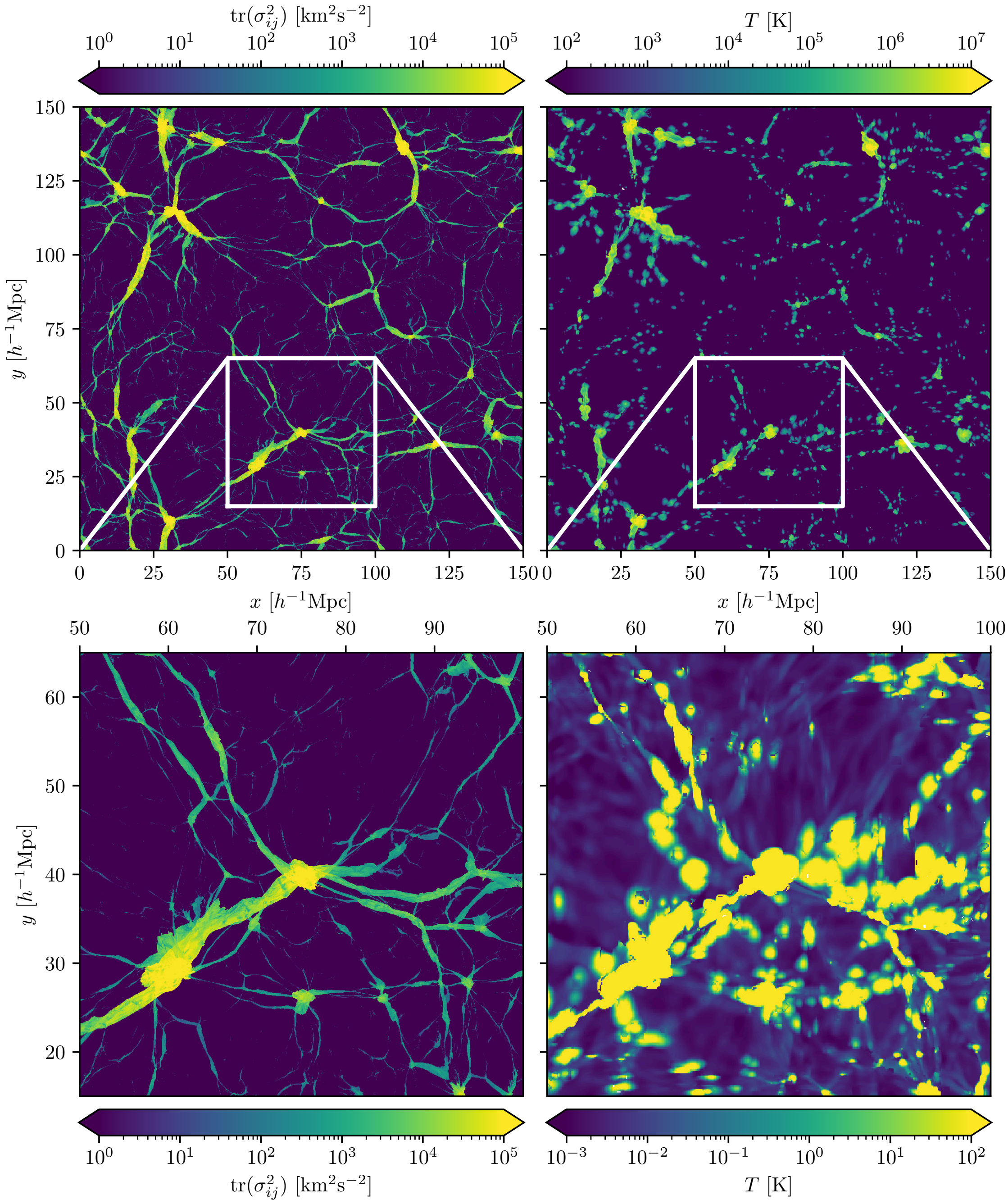

Figure 3.15: Velocity dispersion and the gas temperature, measured on a slice of the 150CDM DM-only ($\mathrm{tr}(\sigma_{ij}^2)$, left panels) and the 150CDM_H hydrodynamic simulation (T, right panels) at $z = 0$. The upper panels show a slice through the entire 150 h^{-1}Mpc box, and a zoomed region of 50 h^{-1}Mpc size is highlighted in the lower panels. Note that the color range is shifted to lower temperatures in the bottom right panel.

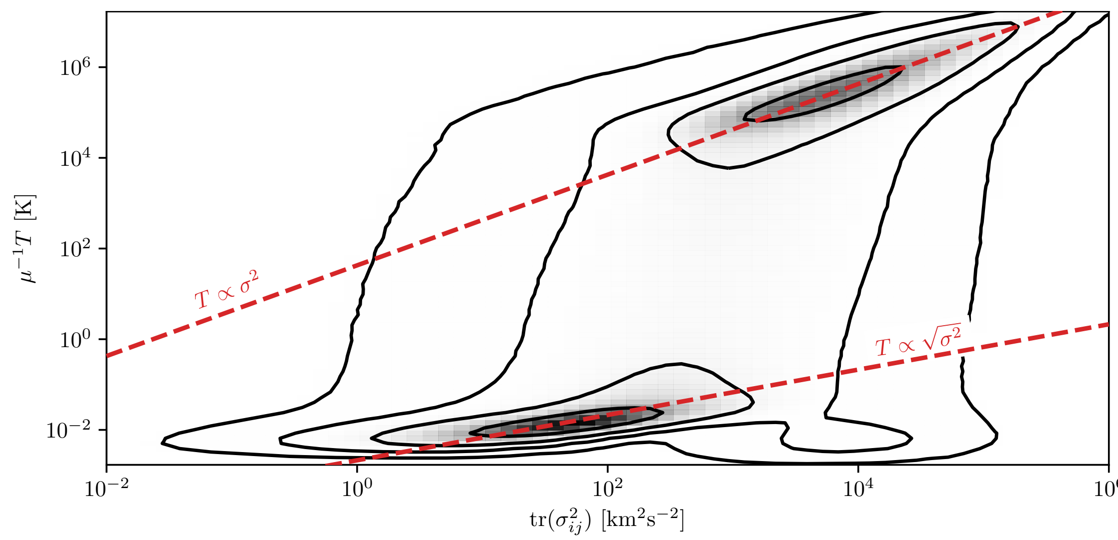

Figure 3.16: Volume-averaged velocity dispersion – gas temperature relation, obtained from the DM phase-space distribution in the 150CDM simulation ($\mathrm{tr}(\sigma_{ij}^2)$) and the gas in the 150CDM_H simulation ($\mu^{-1}T$) at $z = 0$ on a 1024^3 mesh. Contours include 99%, 90%, 50% and 15% of all DM-multistreaming cells. The two clearly-visible, elongated peaks have approximate slopes $T \propto \mathrm{tr}(\sigma_{ij}^2)$ and $T \propto \mathrm{tr}(\sigma_{ij}^2)^{1/2}$.

clumps ranges from 10^5 to 10^7 K, and between these clumps, gas at a much lower temperature ($T \sim 10^{-2}$ [K], but still above the temperature in voids) extends along the walls of the cosmic web. There appear to be two different regimes of the gas temperature, one that has been efficiently heated and one that has been slightly warmed.

To investigate this phenomenon in more detail, we measure the velocity dispersion – temperature relation in the DM multistreaming regions. The result is shown in fig. 3.16, with temperatures normalized by the average molecular weight μ, which depends on the degree of ionization, and therefore temperature and density, of the medium. Generally, the gas temperature correlates with the DM velocity dispersion. However, the distribution is bimodal, with the first peak at very low temperatures and relatively low velocity dispersion and the second peak at high velocity dispersion and temperature. These peaks have an elongated shape, with the first peak rising roughly as $T \propto \mathrm{tr}(\sigma_{ij}^2)^{1/2}$ and the second peak as $T \propto \mathrm{tr}(\sigma_{ij}^2)$. By comparing the temperatures, we can associate these peaks with the two phases that we have previously observed in the illustration.

The very low temperature of the lower peak indicates that these regions have not been shock-heated yet, and indeed, a comparison of the gas density and temperature in fig. 3.17 shows that $T \propto \rho^{\gamma-1}$ with $\gamma \sim 5/3$, corresponding to the adiabatic relation of an ideal gas at fixed entropy. Gas in these regions has thus been merely compressed during the infall process, but no shock has been formed yet. Note that the low temperature of this gas is due to the absence of an ionizing background radiation in our simulation, which would heat the intergalactic medium by photo-ionization to several thousand Kelvin (see e.g. [220, 130, 266]). We can estimate the temperature of the non-shocked, uncompressed gas from the adiabatic expansion: without coupling to the

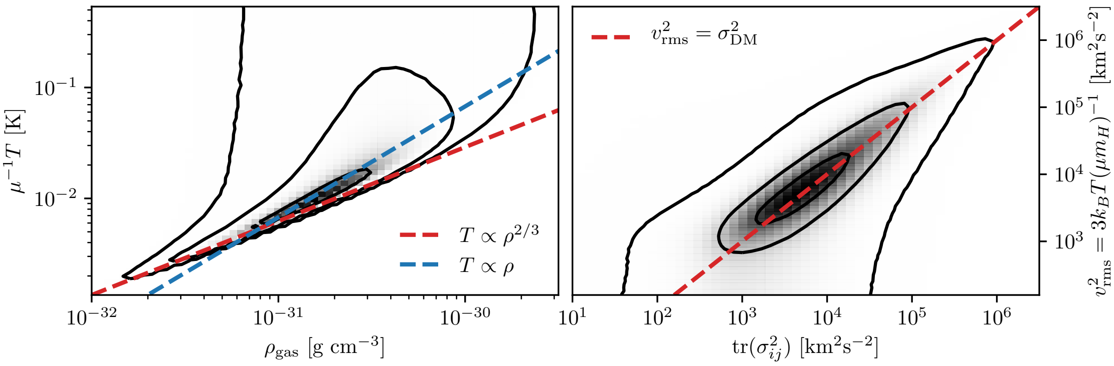

Figure 3.17: **Left:** gas density – gas temperature distribution of the low temperature and low velocity dispersion region from fig. 3.16. **Right:** DM velocity dispersion – hydrogen velocity dispersion (inferred from the temperature) distribution in the high temperature and high velocity dispersion region from fig. 3.16.

photon background, the temperature evolves as $T_{\rm gas} \propto a^{3(\gamma-1)}$, where $\gamma = 5/3$ for an ideal gas. Therefore, $T_{\rm gas}(z=0) \simeq T_{\rm CMB}(1+z_{\rm CMB})^{-1} \simeq 2.5 \times 10^{-3}$ K, agreeing with our measurements.

The prevalence of non-shocked gas in shell-crossed environments may be partially due to small misalignments between the positions of collapsed structures in the GADGET 150CDM simulation and the RAMSES hydrodynamic simulation. Improved results can definitely be obtained by directly using the DM particle positions from the hydrodynamic simulation; we will do so for future projects.

For the remainder of this section, we will focus on the high velocity dispersion – high temperature peak. The internal energy density of an ideal monoatomic gas with 3 degrees of freedom is $\varepsilon = 3nk_{\rm B}T/2 = 3\rho T k_{\rm B}/(2\mu m_{\rm H})$, which is connected to the velocity dispersion of the gas via kinetic theory by $\varepsilon = \rho v_{\rm rms}^2/2$, where $v_{\rm rms} = \left(3\langle v_{\rm 1D}^2\rangle\right)^{1/2}$ is the root-mean-square velocity, with $v_{\rm rms}^2$ corresponding to the velocity dispersion of the gas.

In fig. 3.17, we show the comparison between the trace of the dark matter velocity dispersion and the isotropic velocity dispersion of the baryonic gas. The distribution follows closely a 1:1 relation, with a measured standard deviation of ~ 0.4 dex at fixed tr(σ_{ij}^2). This shows that the anisotropic kinetic energy before the collapse is transformed into an internal energy described by an isotropic temperature during the shock phase of gravitational collapse.

This result is very encouraging as it allow to relate the gas temperature directly to properties of DM. The ability to accurately predict such temperatures in the cosmic web is an important ingredient to model the IGM properties from DM-only simulation. So far, this is commonly done via the density-temperature relation [165, 186, 219] and used in the generation of mock-observations for Ly-α absorption lines in quasar spectra [246, 297].

In order to improve the accuracy of temperature predictions and to better understand the scatter in the DM velocity dispersion – gas temperature relation and the low velocity dispersion peak, more detailed studies will need to be carried out. In particular, better and more realistic hydrodynamical simulations will need to be performed to include cooling, background heating and feedback processes, potentially altering the properties of the gas significantly. Moreover, the influence of the different cosmic web environments needs to be analyzed, since the collapse along the second and third axis will lead to additional shocks. We summarize future plans in section 3.8.

3.7 Conclusions

During the anisotropic gravitational collapse of cosmic structure from cold initial conditions, kinetic energy is absorbed after shell-crossing into velocity dispersion, or stress, and provides the effective pressure that resists gravity in virial equilibrium. Due to the collisionless nature of dark matter, there is no microscopic process that renders this velocity dispersion isotropic so that it must retain some memory of anisotropic collapse in the cosmic web on large scales. On the other hand, the collapse of smaller structures always precedes the collapse of larger structures in the hierarchical structure formation scenario of CDM. One thus expects that smaller scale perturbations always act to increase the isotropy of the dispersion tensor. In order to disentangle this influence of small-scale structures from other non-linear, or even numerical effects, we always considered three simulations that all start from the same random phases. In addition to a vanilla CDM simulation, where the perturbation spectrum is effectively unresolved, we also include two simulations which start from initial conditions with suppressed small-scale fluctuations (exactly like in WDM scenarios).

For these three flavours of simulations, we computed the velocity dispersion tensor directly from the CDM distribution function that we reconstructed using the phase-space sheet tessellation technique ([1, 285], cf. section 2.3), which has previously been shown to yield highly accurate results for velocity fields [139]. We characterize the magnitude of the dispersion tensor through its trace value, and the anisotropic nature through three characteristic dimensionless numbers, the linear, planar and spherical anisotropy (section 3.4). The relative dominance of one over the others of these numbers allows a parameter-free definition of wall-like, filament-like and node-like environments. This is a consequence of the collapse along one, two or three directions, causing large velocity dispersion along precisely those axes. Voids, in contrast, are characterized by the vanishing of the dispersion tensor since, in this picture, they are still simply single-stream regions.

Our main results regarding the one and two-point statistics of the dispersion tensor can be summarized as follows:

1. the amplitude of the velocity dispersion at $z = 0$ is correlated with density in high density regions, and anticorrelated in collapsed regions below a simulation dependent threshold ($\delta < 4$ in the warmest simulation and $\delta < 1$ for the CDM simulation). For $\delta > 0$ we find for the amplitude a scaling $\mathrm{tr}(\sigma^2_{ij}) \propto (1+\delta)^\alpha$ with $\alpha \sim 0.5 - 1$.

2. the anisotropy of σ^2_{ij} is strongly correlated with density, with environments below $\delta \sim 10$ having a strong linear anisotropy and turning isotropic at higher densities.

3. the velocity dispersion power spectrum is proportional to the linear theory density power spectrum on large scales, but decays faster than the non-linear matter spectrum on small scales.

4. the velocity dispersion – density cross-spectrum behaves similarly on large scales but becomes negative above $k \gtrsim 3\ h\mathrm{Mpc}^{-1}$.

5. the velocity dispersion tensor field is spatially correlated not only in magnitude, but also in direction. This correlation extends over the typical size of filaments and walls in the cosmic web and is in agreement with the model of anisotropic collapse causing a consistent alignment of σ_{ij}^2 over a collapsed large scale mode.

6. the velocity dispersion tensor is very well aligned with the large-scale tidal field tensor, which is responsible for the anisotropic collapse on large scales. This implies that large-scale random motions in shell-crossed regions still reflect their origin from anisotropic collapse.

A large amount of studies have been devoted to dissect the cosmic web into distinct components in N-body simulations (e.g. [132, 14, 15, 298, 155, 99] and many more) with a wide variance of results on both the volume and mass occupying the various structures [199]. Typically, these methods require either the introduction of a filter scale (owing to the multi-scale nature of the cosmic web, in which small halos sit inside filaments that sit inside large-scale walls) or some tuning of multi-scale filter parameters. The velocity dispersion tensor allows a parameter free determination of the same environments and is directly motivated by the anisotropy of large-scale gravitational collapse. We can directly confirm previous results that

1. mass predominantly flows from voids to walls to filaments and finally to halos, in agreement with expectations from anisotropic collapse,

2. nodes occupy the densest regions, followed by filaments and walls. The measured mean densities are however highly dependent on the amount of small-scale structure that can be captured by the resolution of the simulation, and generally decrease with increased resolution.

We expect that these results can give important insights into the anisotropic nature of gravitational collapse and the emergence of anisotropic stress in the cosmic web which are of great importance in effective perturbative models of large-scale structure formation and evolution, but also in the modeling of redshift space distortions in cosmological observations. A further interesting future application is to investigate the statistics of the “coldness” of local Hubble flows [175, 11].

Finally, we have compared the DM velocity dispersion with the baryonic gas temperature in a cosmological two-component baryon and DM simulation. For a large fraction of the gas in DM multistreaming environments, we have found a remarkable agreement between the average velocities of particles inferred from the gas temperature and the dark matter velocity dispersion. Multistreaming in DM goes hand-in-hand with shock-heating of the baryonic component. While the DM velocity dispersion is inherently anisotropic after collapse, the collisional nature of baryons leads to isotropic pressure. For a second part of the gas, no shock heating was found, which may be due to misalignments between the simulations and will require further tests in the future. This result, possible only due to accurate, point-wise measurements of the DM velocity dispersion, presents a promising step towards improving predictions of the IGM temperature from DM-only simulations. Being able to accurately predict baryonic densities and temperatures is an important ingredient in the theoretical modeling of absorption lines in the spectra of distant quasars (Ly-α forest) (e.g. [246, 297]). We give an outlook to future projects in the next section and also in chapter 6.

3.8 Outlook

Further work on the large-scale velocity dispersion can be categorized into two classes: improvements on the measurement and analysis technique and applications of the measurements. We will look at these to categories in the following.

3.8.1 Improvements of the velocity dispersion measurement

In order to separate the small-scale structure from the large-scale cosmic web, we were running simulations with a truncated initial power spectrum. It would be advantageous, however, to be able to disentangle the different scales of the cosmic-web as a post-processing of a single simulation with the full initial spectrum (e.g. the 300CDM simulation in our case). This separation of scales has to be achieved by some smoothing operation that preserves the large-scale mapping from Lagrangian space to phase-space. We have experimented with different Lagrangian smoothing kernels, but so far no satisfactory result has been obtained and more research is required.

For the result presented in this chapter, we have only used the single coverage tessellation without the polynomial or Fourier interpolation technique presented in section 2.3. Using a higher order interpolation to refine the particle grid and increase the number of tetrahedra and averaging the measured velocity dispersion over the full set of potential tessellations will improve the results especially in low density areas (cf. fig. 2.5) and may help to better resolve filaments and increase the low filamentary mass fraction measured in section 3.4.1.

In high density areas with a large number of overlapping streams, such as within DM halos, the particle sampling of phase-space is not fine enough to follow the phase-space sheet accurately and therefore the estimated velocity dispersion and densities via the tessellation technique cannot be guaranteed to be accurate. Better results may be obtained by estimating the velocity dispersion directly from the particles in such cases. To allow for a precise measurement over the entire simulation volume, a hybrid method applying the correct technique depending on the local stream count could be considered.

3.8.2 Applications of the velocity dispersion measurement

We have applied the anisotropy of the velocity dispersion tensor to classify the distinct cosmic web components by using the dominant anisotropic component. Different (parametrized) segmentations of the anisotropy diagram (fig. 3.5 could be considered, e.g. by measuring how far the collapse along the second and third axis has proceeded relative to the first axis. An analysis of the anisotropy in different idealized environments could provide some insight into possible classifiers.

Our classification of the cosmic web so far does not exploit the characteristic orientation of the anisotropy in walls and filaments. This directionality could be used to isolate individual segments of the cosmic web. Together with the ability of accessing different scales of the cosmic web that we discussed above, it would be possible to assign halos to specific walls and filaments. This would allow us to study the assembly bias due to the impact of the cosmic web environment on halo and galaxy formation (see e.g. [47, 275, 116]).

The ability to accurately measure the evolution of the cosmic velocity dispersion and higher moments of the dark matter phase-space distribution is also an important ingredient in the development of analytical perturbation theories that extend beyond shell-crossing. The effective sound speed of DM, related to $\sqrt{\mathrm{tr}(\sigma_{ij}^2)}$ in our analysis, is for example an important ingredient in effective field theories of large scale structure (e.g. [27, 56]). Ultimately, any fluid description of DM beyond shell-crossing will have to incorporate the anisotropic stress tensor in some form.

The ability to improve predictions of the IGM temperature beyond the commonly used density – temperature relation entails various interesting further projects, such as improved Ly-α modeling from DM-only simulations as we have already discussed in section 3.6. However, more studies of the DM velocity dispersion – gas temperature relation are required, e.g. using more realistic hydrodynamical simulations, measurements of the correlation in different cosmic web environments, and understanding the origin of the observed scatter.

Inferring properties of the baryonic matter from DM-only simulations is a natural field of application for machine learning techniques and generative methods. This has already been successfully demonstrated for example for mock Sunyaev-Zel'dovich observations [315], mapping the DM density to baryonic gas pressure. Applying such methods to predict gas densities and temperatures from DM densities and velocity dispersions presents a promising avenue to develop this project further.

CHAPTER 4

COSMICWEB: Online Cosmological Initial Conditions for Zoom Simulations

Part of this chapter will be submitted to "Computational Astrophysics and Cosmology" for publication as a refereed article.

Zoom simulations, which we have briefly mentioned in section 2.1.3, provide a powerful tool for studies in galaxy formation and evolution, by covering a large range of scales while focusing the computational resources on a specific object of interest. This technique allows us to resolve the internal structure of the target object at higher resolutions and therefore model baryonic physics on smaller scales, with recipes motivated by more local physics.

Zoom simulations have been successfully used to study a large range of gravitationally bound objects ranging from the first galaxies to massive galaxy clusters, with a variety of different simulation codes and subgrid models. Recent projects using cosmological zoom simulations include for example the AGORA simulation comparison project [178], the Auriga project [122] targeting Milky Way mass halos to study disc formations, the FIRE-1 [157] and FIRE-2 [158] simulations exploring feedback processes in galaxy formation, and the RHAPSODY-G [137] and CLUSTER-EAGLE [21] simulations studying massive galaxy clusters. Recent simulation projects study the effects of additional baryonic physics on galaxy and cluster formation, such as magnetic fields [215, 214, 85, 84], anisotropic thermal conduction [91, 174, 22] and cosmic rays [92]. Zoom simulations provide an ideal tool to study these processes in a cosmological context (in contrast to studying isolated objects in idealized simulations). In the future, with the inclusion of further models and improved subgrid recipes that are able to model baryonic processes on a more physical and less phenomenological level, zoom simulations will play an even more important role by allowing to easily compare different models and implementations.

The widely adapted initial conditions generator MUSIC [133] provides a powerful tool to set up zoom simulations: with the capability to output initial conditions in multiple formats for different simulation codes, and the integration of white-noise field generators from other initial condition tools, it allows to i) create the same zoom simulation for different simulation software for code comparisons, and ii) create zoom simulations from existing simulations that were not necessarily run with the same code or set-up with the same initial conditions generator. However, there is currently no platform available to easily find zoom-targets from existing simulations and to create and share zoom initial conditions.

With COSMICWEB, we provide an ecosystem for the community of people running zoom simulations to fill this gap. A uniform web-interface allows to easily find and validate target objects for zoom simulations from existing state-of-the-art simulations as well as new simulations. For the selected targets, a configuration file specifying the simulation parameters as well as the high-resolution zoom region can be downloaded from COSMICWEB or directly with MUSIC to generate the zoom initial conditions for the specified simulation code. The initial conditions can then be cited in articles, talks or on webpages, allowing others to reproduce, compare, and verify scientific results.

This chapter focuses on the design and implementation of the COSMICWEB application. In the next chapter, we will take a closer look at the proto-halo patches that have been computed for the project. The structure of this chapter is as follows: we begin in section 4.1 with a brief overview of the steps involved in the creation of a zoom simulation, how the current situation motivated the development of COSMICWEB, and what the scope the project is. In section 4.2, we discuss the data that will be available at the release of COSMICWEB. Section 4.3 describes the modular design of COSMICWEB and how the different components interact. We take a closer look at the web interface in section 4.4 and the database in section 4.5. We conclude in section 4.6 and briefly describe the state of the project at the time of writing. In section 4.7, we give an outlook on future plans additions to the project.

4.1 Motivation and goals

Setting up zoom simulations requires knowledge of the initial region from which the object of interest originates form, the so-called *proto-halo patch*. For its construction, one needs to first run a lower resolution full-box simulation, in which one then selects an object of interest and traces its constituent particles back to the initial conditions, from where the boundaries of the Lagrangian volume can be determined. Extra care needs to be taken to not contaminate the zoom region with lower mass particles, as these can have a significant effect on properties of the target object; in particular, they may lower the baryon fraction and cause artificial fragmentation of the gas in the halo (e.g. [239]).

The process to set up a zoom simulation is illustrated in fig. 4.1 and contains the following steps:

1. From a given seed for the random number generator and cosmological parameters, generate the initial particle displacements and velocities for a uniformly resolved simulation at a high redshift.

2. Evolve this initial state to today while storing multiple snapshots and tracking the individual particles. This can be done with various N-body simulation codes.

3. In each snapshot, find bound structures and generate a halo catalog. Build a merger tree by tracing halos across time.
   Select halos matching the research requirements for re-simulation.

4. Compute Lagrangian volume by backtracking particles within the traceback-radius R_{tb} to their Lagrangian position. For COSMICWEB, we compute the minimum bounding ellipsoid of the particles to describe the Lagrangian volume.

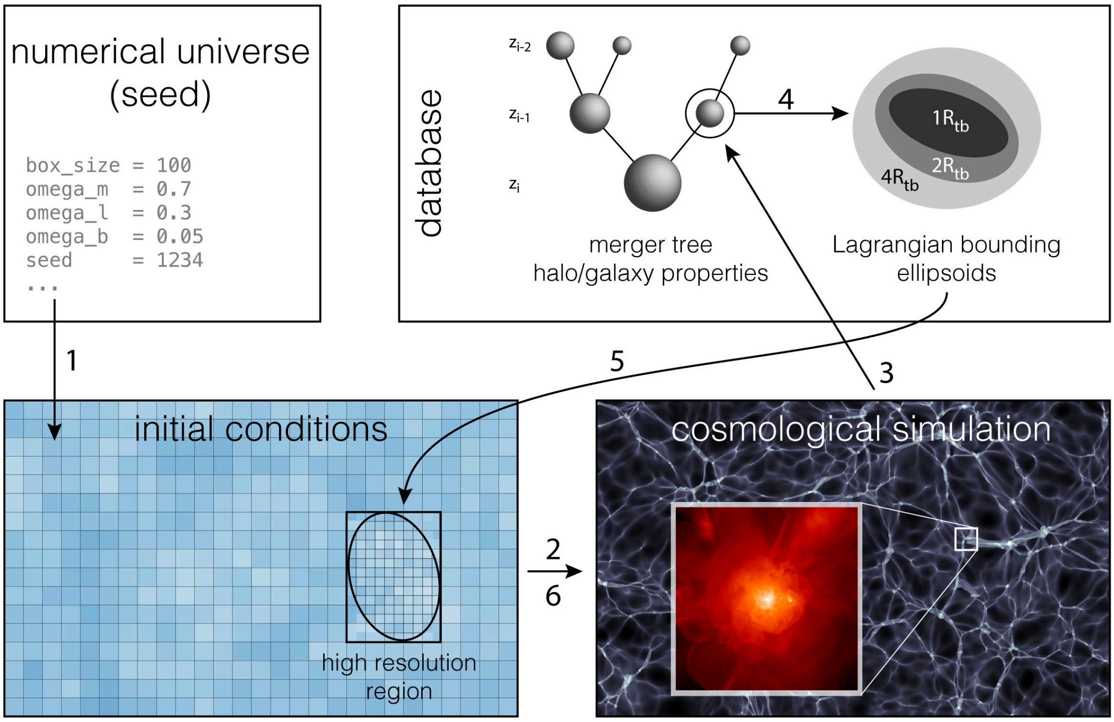

Figure 4.1: Illustration of the steps involved in the creation of a zoom simulation. A full description of the process can be found in the main text. The COSMICWEB database stores halo catalogs, merger trees and the associated Lagrangian proto-halo patches of pre-run simulations and makes them accessible through an intuitive web frontend.

5. Sample this Lagrangian volume in the initial conditions with higher resolution using a multi-scale initial condition generator such as MUSIC [133].

6. Run the zoom simulation with advanced baryonic physics, depending on the project requirements.

The steps 1 to 5 are preparatory steps that so far have to be repeated for every zoom simulation (unless one has access to a suitable pre-run simulation). Large publicly available halo and galaxy catalogs of large simulations exist (e.g. [216, 232, 148]), but they are usually not associated with proto-halo patches. Furthermore, the direct comparison between different simulation codes, baryonic physics prescriptions, and the verification of scientific results is impeded, since the initial conditions used for studies involving zoom simulations are usually not made public or easily accessible.

With COSMICWEB, we address three issues with the current work flow for setting up and running zoom simulations:

- *Finding interesting objects to simulate.* We provide access to the halo catalogs and merger trees of pre-run simulations in which the user can search for halos (and galaxies) at various redshifts matching his research project requirements.

- *Generating zoom initial conditions.* For every halo, we provide multiple proto-halo patches including a different amount of the halo environment. The application combines these patches with the initial conditions of the simulation to generate a MUSIC [133] configuration file that can be used to generate the initial conditions for various simulation codes.

- *Referencing initial conditions.* Users can reference halos and collections of halos that they used in their works, allowing the community to reproduce results and to compare different simulation codes for verification. To reference halos, COSMICWEB generates a tag that can be included in publications and through which the zoom initial conditions can be accessed using the COSMICWEB application or directly downloaded with a script provided with MUSIC.

In the following sections, we discuss the data that is currently available in the COSMICWEB project, and how the aforementioned design goals have been implemented.

4.2 Cosmological simulations, merger trees and proto-halo patches

We will briefly summarize the currently available simulations and the data they contain. This overview presents a snapshot at the time of writing. Further simulations will be made available in the future (see section 4.7 for current plans) and can also be contributed by the community thanks to the modular design (cf. section 4.3).

4.2.1 Simulations

Currently, data from seven DM-only simulations is hosted at the Observatoire de la Côte d'Azur as shown in table 4.1. The simulations span cosmological volumes from $60^3\ h^{-3}\mathrm{Mpc}^3$ to $1\ h^{-3}\mathrm{Gpc}^3$ and mainly use cosmological parameters conforming with the Planck 2015 [67] results. The 150MPC and 300MPC simulations were run both with 1024^3 and 512^3 particle resolutions to allow for comparisons between the catalogs and Lagrangian proto-halo patches, and to test for convergence. Additionally, we include two simulations which have been previously used for zoom simulations: the cosmological volumes of the AGORA comparison project [178] and of the RHAPSODY cluster re-simulation project [336, 337, 137] which is originally based on the Carmen simulation of the LasDamas project [217] (we labeled the simulations as "AGORA" and "RHAPSODY" for the sake of convenience). These simulations use older WMAP 7/9 [187, 151] cosmological parameters. However, we have updated the parameters in the RHAPSODY_NewCosmo simulation to allow comparisons between the halo catalogs and zoom simulation results. We describe the running and processing of the simulations in more detail below.

Another set of halo catalogs and merger trees originates from simulations of the *Evolution and Assembly of GaLaxies and their Environments* simulation suite (EAGLE [279, 69, 216]) and is hosted by the Virgo consortium[1]. In particular, we provide access to the `Ref-L0025N0376` and the `Ref-L0100N1504` simulation that were run with full gravity, hydrodynamics and subgrid modeling, and their `L0025N0376` and `L0100N1504` DM-only counterparts. With the addition of

[1] http://www.virgo.dur.ac.uk/

		size $[h^{-1}\text{Mpc}]$	cosmo.	DM resolution $[h^{-1}M_\odot]$	[b]	snapshots $[z_{\max} - z_{\min}]$	structure finder	$N^e_{\min}$
local	150MPC	150	[P1]	2.70×10^8		101 [12 – 0]	ROCKSTAR	100
	150MPC_lowres	150	[P1]	2.16×10^9		101 [12 – 0]	ROCKSTAR	500
	300MPC	300	[P1]	2.14×10^9		101 [12 – 0]	ROCKSTAR	100
	300MPC_lowres	300	[P1]	1.71×10^{10}		101 [12 – 0]	ROCKSTAR	500
	AGORA	60	[W1]	1.21×10^8		101 [12 – 0]	ROCKSTAR	1000
	RHAPSODY	1000	[W2]	6.46×10^{10}		101 [12 – 0]	ROCKSTAR	1000
	RHAPSODY_NewCosmo	1000	[P1]	7.99×10^{10}		101 [12 – 0]	ROCKSTAR	1000
EAGLE	Ref-L0025N0376	16.94	[P2]	6.57×10^6	✓	29 [20.3 – 0]	FoF & SUBFIND	1000
	L0025N0376	16.94	[P2]	7.63×10^6		29 [20.3 – 0]	FoF & SUBFIND	1000
	Ref-L0100N1504	67.77	[P2]	6.57×10^6	✓	29 [20.3 – 0]	FoF & SUBFIND	1000
	L0100N1504	67.77	[P2]	7.63×10^6		29 [20.3 – 0]	FoF & SUBFIND	1000

Table 4.1: Available simulations with some key parameters, including the size of the simulated volume, the cosmological parameters that were used, dark matter mass resolution, the inclusion of baryonic physics in the simulation [b], the number and redshift range of snapshots, the structure finder that was used, and the minimum number of particles within the traceback-radius that was required to compute the minimum bounding ellipsoids ($N^e_{\min}$). [P1] and [P2] correspond to slightly different Planck 2015 [67] cosmologies, and [W1] and [W2] are derived from the WMAP 7 [187] and WMAP 9 [151] results. More details on the settings of the locally hosted simulation as well as the cosmological parameters can be found in appendix A.3, in particular table A.1. The EAGLE simulations are described in [279, 69, 216].

simulations including full baryonic physics, COSMICWEB users can also use galaxy properties to constrain their search for zoom simulation targets.

Locally hosted simulations

Initial conditions for the full simulations were generated using MUSIC [133] at redshift $z = 49$ (RHAPSODY & RHAPSODY_NewCosmo) and $z = 99$ (remaining simulations). Using a modified version of the GADGET-3 code [300], we evolved the simulations to redshift $z = 0$ and stored 100 snapshots between $z = 12$ and 0 (logarithmically distributed in scale factor units). Each snapshot was processed with the ROCKSTAR structure finder [30], which identifies halos and subhalos using a six-dimensional phase-space friend-of-friend algorithm and measures their intrinsic properties (cf. section 2.2). Using CONSISTENT TREES [28], we grouped halos from different snapshots together to merger trees containing information about spatial hierarchy (halo substructure) as well as temporal hierarchy (descendant and progenitor halos and merger events). In addition, we measure environmental parameters such as $D_{1,1}$ directly from the halo catalog.

The EAGLE database

The initial conditions of the EAGLE simulations were generated from white noise fields created with PANPHASIA [171] using the phase-descriptors specified in [279] as random seeds. The updated version of MUSIC includes the PANPHASIA random number generator, allowing us to create zoom simulations in the EAGLE volumes from a unified interface.

The eagle simulations were run with a modified version of the GADGET-3 code with a full gravity and hydrodynamics treatment, including a large number of subgrid modules accounting for physical processes below the resolution scale, such as radiative cooling and heating, star formation and evolution, metal enrichment, and feedback from supernovae and supermassive black holes [69]. Each simulation contains 29 snapshots distributed between $z = 20$ and $z = 0$. In the snapshots, halos are identified using a FoF algorithm (cf. section 2.2) with linking length $b = 0.2$ and a spherical over-density algorithm. Baryonic particles are then assigned to the FoF groups and all particle species within the group are further processed with the SUBFIND algorithm [301, 82] to separate self-bound structures and identify galaxies. The subhalo catalogs are linked across time by determining the descendant halos using D-TREES [172, 268], and the main progenitors defined by the largest "branch mass" [268].

4.2.2 Proto-halo computation

The proto-halo patch is defined by the Lagrangian volume that collapses to the halo of interest[2]. In an N-body simulation, it is traced by the particles that are within the traceback-radius $\boldsymbol{R}_{\mathrm{tb}}$ of the halo, which is often chosen as a multiple of the halo radius. The choice of $\boldsymbol{R}_{\mathrm{tb}}$ is a trade-off between the computational cost and the robustness of the zoom simulation against contamination of the high-resolution region by low-mass particles, which can bias final results. We will discuss these effects in more detail in chapter 5.

Once the particles within the traceback radius are identified, different techniques exist to describe their enclosing Lagrangian volume, such as a rectangular bounding box, minimum bounding ellipsoids, and convex hulls. A comparison of some commonly used methods can be found in [239]. To measure the quality and computational cost of a proto-halo patch, we define its efficiency as the ratio of the mass of the particles that were used in its construction to its enclosed mass:

$$\mathcal{E} = \frac{\boldsymbol{M}_{\mathrm{particles}}}{\boldsymbol{M}_{\mathrm{ellipsoids}}}. \tag{4.1}$$

In general, the efficiency increases with the complexity of the boundary description, e.g the rectangular bounding box requiring 6 coordinates is less efficient than the minimum bounding ellipsoid (9 parameters), which in turn is less efficient than the convex hull which is described by all the particles on the surface, see [239]. The variance of the efficiency is mass dependent and increases for low mass halos (cf. chapter 5). This is due to environmental effects such as strong tidal fields in the vicinity of small halos distorting the proto-halo shape as well as more anisotropic mass accretion.

For COSMICWEB, we decided to provide minimal bounding ellipsoids for our halos, since the storage of convex hulls for all halos in all snapshots and multiple traceback-radii would not be feasible, and since ellipsoids provide more robustness while still capturing the triaxial shape of a typical proto-halo patch. An ellipsoid is described by its center $\boldsymbol{q}_c$ and its shape matrix $\boldsymbol{A}$. The symmetric, positive definite matrix $\boldsymbol{A}$ can be normalized such that coordinates $\boldsymbol{q}$ that are within

[2] For high peak-height halos, the proto-halos correspond reasonable well to peaks in the initial Gaussian random field, cf. section 1.4 and [260, 206].

the ellipsoid satisfy

$$(\boldsymbol{q} - \boldsymbol{q}_c)^T A (\boldsymbol{q} - \boldsymbol{q}_c) < 1. \tag{4.2}$$

To compute the minimum bounding ellipsoid, we use Khachiyan's algorithm [177, 189], which iteratively optimizes the volume of the ellipsoid under the constraints that all particles are contained. We account for periodic boundary conditions by moving all particles to the same local coordinate system centered at the proto-halo center of mass. This requires that no axis of the proto-halo patch is longer than half the box size, which generally should not occur and for which a zoom simulation would only result in a marginal benefit.

For the locally hosted simulations, we provide minimal bounding ellipsoids for all host halos (i.e. no subhalos, since those will by definition be affected by contamination) at every snapshot and for four different traceback-radii $R_{\mathrm{tb}} = 1, 2, 4$, and 10 R_{vir} if the number of particles within R_{tb} is larger than the threshold N^e_{min} listed in table 4.1. The EAGLE simulations provide minimum bounding ellipsoids at $R_{\mathrm{tb}} = 1, 2$, and 4 R_{200c} for all FoF groups larger than 1000 particles. Note that in principle, intermediate size ellipsoids could be generated by interpolation. We will consider this in future versions of COSMICWEB.

4.2.3 Supported selectors

To allow users to find target halos to re-simulate, we store various intrinsic and environmental properties of the halos that can be used to constrain the set of potential candidates. Note that individual simulations may contain different information (e.g. baryons vs. DM-only) and the analysis of the original simulation can be performed with various structure finder tools (cf. section 2.2) that measure a varying set of properties and may use different conventions in their analysis. In the design of COSMICWEB, it is therefore essential to account for variable feature sets that can be configured separately for each simulation. The list of features also has to be easily extendable when additional simulations with new halo and galaxy properties will be added in the future.

Table 4.2 lists the selectors that have been added to COSMICWEB at the time of writing, and the support by the locally hosted simulations and the EAGLE simulations. In addition to intrinsic and environmental halo and galaxy properties, we also include temporal selectors (redshift of halo and redshift of last major merger) as well as properties of the proto-halo patch (number of particles used in the computation and the efficiency parameter). These parameters can be used to exclude poorly-converged minimum bounding ellipsoids. However, the filtering with these criteria may create a biased sample of proto-halos that are predominantly in less clustered environments. We will take a closer look at the correlation between the efficiency parameter and the environment in section 5.3.

4.3 Application architecture

Due to the diverse and potentially very large datasets, the COSMICWEB project is designed to be decentralized and modular. This allows us to host the merger trees and proto-halo patches on different servers than the application server, the user, and the publication data. We can therefore connect existing databases to COSMICWEB without the need of duplicating data. This decentralized approach however results in a more complex application design and requires a thorough

Table 4.2: List of currently available selectors, grouped by halo properties, galaxy properties, and further parameters including properties of available proto-halo patches. [L] and [E] mark the features that are currently supported for the locally hosted simulations and the EAGLE simulations respectively, cf. table 4.2.

	Parameter	Units	Description	[L]	[E]
halo	M_{200c} / M_{500c} / M_{2500c}	$h^{-1}M_\odot$	Mass within $\rho >= \Delta\rho_c$ contrast	✓	✓
	M_{200b} / M_{500b} / M_{2500b}	$h^{-1}M_\odot$	Mass within $\rho >= \Delta\bar{\rho}$ contrast	✓*	✓
	M_{vir}	$h^{-1}M_\odot$	Mass within the virial boundary using the definition of ρ_{vir} from Bryan & Norman [50]	✓	✓
	$R_{\Delta c}$ / $R_{\Delta b}$ / R_{vir}	h^{-1}kpc	Radius of the halo according to the mass definition	✓*	✓
	$c_{\Delta c}$ / $c_{\Delta b}$ / c_{vir}	—	concentration parameter $c_x = R_x/R_s$, where R_s is the scale radius of the NFW profile	✓*	
	$\lambda_{\mathrm{Peebles}}$	—	Spin parameter (Peebles definition [244], cf. eq. (1.108))	✓	
	$\lambda_{\mathrm{Bullock}}$	—	Spin parameter (Bullock definition [52], cf. eq. (1.109))	✓	
	f_{sub}	—	Substructure parameter $\sum_i M_{\mathrm{sub},i}/M_{\mathrm{host}}$	✓	
	virial ratio	—	Ratio between kinetic and potential energy $2T/U$	✓	
	x_{offset}	—	Normalized offset between center of mass and the most bound particle $x_{offset} = \lvert\lvert \boldsymbol{x}_{\mathrm{com}} - \boldsymbol{x}_{\mathrm{core}} \rvert\rvert / R_h$	✓	
	$D_{1,1}$	—	Normalized distance to the closest more massive neighbor $D_{1,1} = \lvert\lvert \boldsymbol{x}_h - \boldsymbol{x}_n \rvert\rvert / R_h$ (n: neighbor)	✓	
	last major merger	—	redshift of last major merger	✓	
galaxy	M_{star}	$h^{-1}M_\odot$	stellar mass in the central galaxy		✓**
	M_{gas}	$h^{-1}M_\odot$	gas mass in the central galaxy		✓**
	M_{BH}	$h^{-1}M_\odot$	black hole mass in the central galaxy		✓**
others	z	—	redshift (range)	✓	✓
	n_{part}	—	Number of particles used to construct the minimum bounding ellipsoid	✓	✓
	ϵ	—	Efficiency of the Lagrangian minimum bounding ellipsoid $\epsilon = n_{\mathrm{part}}/V_{\mathrm{ellipsoid}}$	✓	
	include substructure	—	boolean option to include substructure in the search	✓	

*: the local simulations currently do not support M_{500b}, M_{2500b} and the corresponding radii and concentration parameter.

**: only supported by the `Ref-*` subset of the EAGLE simulation that include baryonic physics.

specification of the communication protocols between the individual parts. In this section, we will discuss the structure of COSMICWEB, how the individual components interact, and what requirements need to be met to add additional external datasets. We will finish with a short overview on how we ensure data safety and prevent unauthorized to the various servers.

4.3.1 Overview

We will start with an outline of the project architecture. The COSMICWEB platform can be split into four main parts, visualized in fig. 4.2:

- the data servers providing access to the halo/galaxy catalogs and minimum bounding ellipsoids,
- the main server (application server) hosting the web application and storing user data, simulation meta-data, and access information to the API servers,
- the client web application running in the user's browser, and
- a plugin for the MUSIC initial condition generator.

The main application server, currently hosted on `https://cosmicweb.oca.eu`, is responsible for the user management, storage of collections and publications with references to the included halos, and provides information about the API server of each simulation. It also serves the actual website together with a collection of javascript functions and libraries, which we call, taken together, the *client application*. Using javascript and additional libraries and frameworks, we can design interactive webpages that load additional data from the application and API servers and updates the webpages accordingly. The actual implementations is discussed in detail in section 4.4. The simulation meta-data (e.g. the URL of the API server and feature list of the selected simulation) are included in the websites, allowing the client application to download the halo details and the Lagrangian ellipsoids directly from the API servers, as well as to submit halo-finder queries.

The data servers, which we will refer to as *API servers* (application programming interface), provide an interface between the actual datasets and the COSMICWEB application. This abstraction is necessary to support heterogeneous databases over a common protocol. In theory, an API server could be set up to read the data from text files on demand. However, specialized database software is preferred, as it provides easier methods to access the data, faster query rates through indexing, and helps ensuring data integrity with foreign keys and constraints.

Finally, the MUSIC plugin is a convenience tool that allows downloading initial condition configuration files directly on the command line. Using the plugin, downloading the files first on a local machine and then re-uploading them to a headless compute cluster can be avoided.

For the interaction between these four components to work, the requests to and answers from the API servers have to follow a specified protocol which we will discuss in more detail next.

4.3.2 The API

The communication between the COSMICWEB application and external databases is handled by API Servers following a predefined set of rules. Since these rules are subject to change over

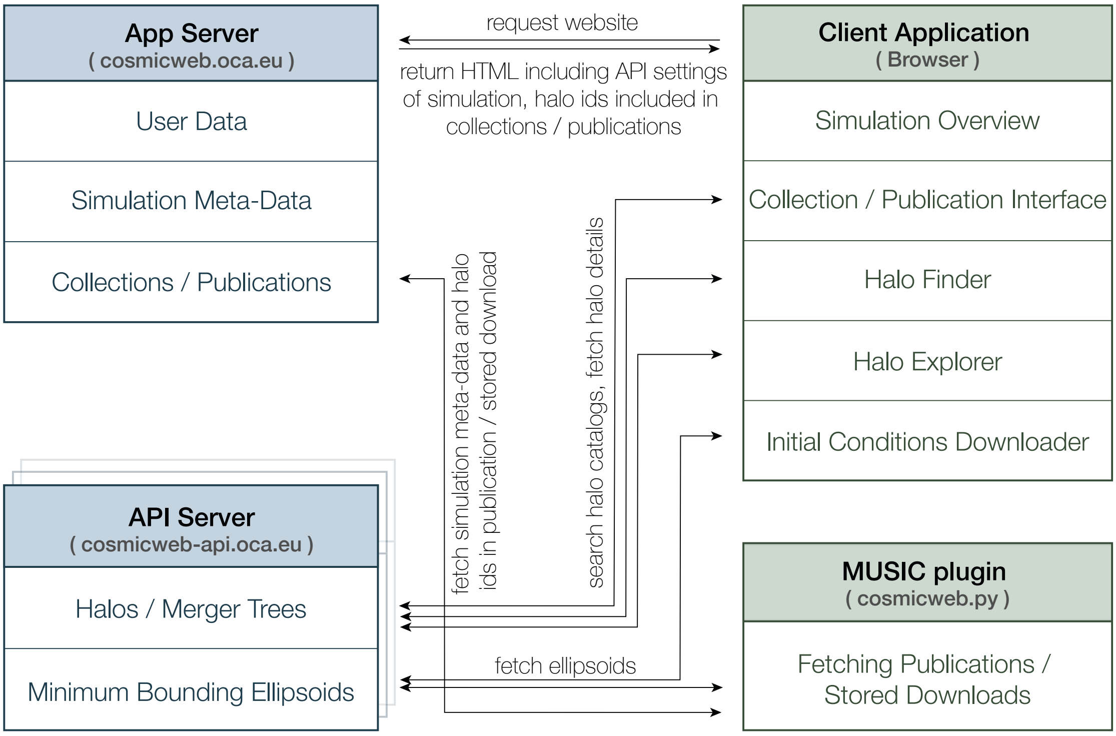

Figure 4.2: Sketch of the architecture of COSMICWEB. The server-side (left) is split into a main application server and data servers providing access to the simulations through an API. The main server hosts the webpage, provides user management and data storage (halo collections, publications, saved queries, etc.), and contains meta-data of the simulations and connection information to their associated API servers. The webpage served by the main server will fetch the requested data from the API servers and .

time, the API is versioned and the outline given here reflects the current state. Updated and more detailed specifications can be found directly on the webpage[3].

The API consists of several endpoints that receive requests from the client application and send the requested data back using the JSON[4] syntax. We list and explain these endpoints in table 4.3. Different simulations may not contain all data and support all features. This is why we differentiate between *required* and *optional* endpoints. The information on which features and properties are available for each simulation are stored on the central server.

The required endpoints are necessary for the basic functionality of COSMICWEB. They include information on the available snapshots, the halo-finding capability, basic information on individual halos, and their Lagrangian ellipsoids. The optional endpoints are mainly used for visualizations of the halo substructure, the formation history, and the local environment of the halo. For each simulation in COSMICWEB, individual features can be enabled, and the interface automatically adapts to show the available information.

[3] `https://cosmicweb.oca.eu/documentation/api`

[4] Specified in the ECMA-404 Standard, *The JavaScript Object Notation (JSON) Data Interchange Syntax* (2017).

Required endpoints		
/halo_finder	POST	Interface for halo queries, accepting a list of filters which include ranges for parameters, mass definitions, available ellipsoids, etc.
/snapshots	GET	List of available snapshots for the simulation, including redshifts and number of halos that were detected
/snapshots/<id>	GET	Details of a specific snapshot
/halo/<id>	GET	Details of a specific halo and associated galaxy (if available). The returned fields depend on the enabled properties for the simulation (cf. table 4.2).
/halo/<id>/ellipsoids	GET	List of Lagrangian ellipsoids measured at different traceback-radii, specified by the center, shape matrix and traceback-radius (optional: number of particles within $R_{\rm tb}$ and efficiency parameter).
/halo/<id>/ellipsoids/<id>	GET	Definition of a specific Lagrangian ellipsoid
Optional endpoints		
/snapshots/<id>/massfunction	GET	The halo mass function computed from all host halos in the snapshot
/halo/<id>/substructure	GET	Substructure tree of the halo
/halo/<id>/main_progenitors	GET	List of halos corresponding to the main progenitors sequence of the specified halo
/halo/<id>/mergertree	GET	Merger tree of the halo. The merger threshold can be specified by the request argument ?mm_fraction=<r>, where r is the ratio between merging and resulting halo, e.g. a 1:3 merger corresponds to $r = 0.25$.
/halo/<id>/surrounding	GET	All halos within a certain distance of the halo. The distance can be specified by the request argument ?box_size=<m>, where m is a multiplier to the halo radius.
/halo/<id>/tracking	GET	A list of coordinates of the main progenitors, normalized to the unit cube
/halo/<id>/images	GET	If there are images or graphics associated with the halo, return a list of image URLs and descriptions.

Table 4.3: List of API endpoints, split into required and optional features. The endpoints use the HTTP GET method with the exception of /halo_finder, for which the selectors will be transmitted by a POST request. The endpoint paths are relative to the simulation API URL stored on the COSMICWEB application server. The precise format of the request and JSON response is specified on the COSMICWEB website.

External datasets can be integrated in COSMICWEB by setting up a server[5] listening on the various endpoints, parsing incoming requests, querying the dataset, and returning the result in the specified format. For the locally hosted simulations, we are using the FLASK framework, but in general any web server that can parse and process the requests is suitable. We will discuss the API implementation for the local simulations in more detail in section 4.5.

4.3.3 The MUSIC plugin

To facilitate downloading initial conditions from COSMICWEB to computing facilities and local machines, we include a PYTHON command-line executable (compatible with PYTHON2 and PYTHON3) that interfaces the COSMICWEB API. It allows downloading individual IC configuration files as well as configuration files for collections and publication lists. The executable has two modes (`publication` and `get`) and is used as:

```
./cosmICweb.py [--output-path OUTPUT_PATH] [--common-directory]
     [publication [--traceback-radius TRACEBACK_RADIUS] PUBLICATION_TAG]
          OR
     [get DOWNLOAD_STRING]
```

`--output-path OUTPUT_PATH`: By default, the MUSIC configuration files are stored in the current working directory in a sub-directory named after the publication or the simulation of the halos. If `--output-path` is specified, the script stores the files in this directory instead without creating the subdirectory. Folders for each halo will be created however, unless the `--common-directory` flag is set.

`--common-directory`: If this option is set, all MUSIC configuration files will be stored in the same directory instead of individual directories for each halo.

`publication [--traceback-radius TRACEBACK_RADIUS] PUBLICATION_TAG`: The tag of the publication can be used to download zooms for all halos within the publication list. The traceback-radius for the proto-halo patches is set to 2 as default but can be changed. The executable will skip a halo if no minimum bounding ellipsoid with the specified traceback radius exists.

`get DOWNLOAD_STRING`: A download string can be generated from the download interface on COSMICWEB (cf. section 4.4). This string can then be used to download the MUSIC configuration files with this executable. Configuration settings from the download window will be applied during the process.

4.3.4 Security considerations

To protect confidential user data such as passwords and prevent unauthorized access and the injection of malicious code, several precautions have been taken. The communication between

[5] Since the API Server runs on a different address than the COSMICWEB server, it has to be configured to support *cross-origin resource sharing* (CORS).

the client and the application and API servers is encrypted with HTTPS, and no passwords are stored on the servers, but instead a secure hash is generated using the PBKDF2 algorithm and compared during the login process. All user input that is stored on the server and later visible on the page, such as title and descriptions of collections and publications, and names for halos, is sanitized to prevent cross-site scripting and injection of dangerous code.

To view halos and download initial conditions, no user account is currently required. However, to create collections and publications and to access the *Halo Finder* page, the user needs to be authenticated. We included the *Halo Finder* in this list, since queries can cause significant loads on the API servers which may require regulating user and web-crawler access. After logging in, the user's session is maintained through cookies in the client application.

Due to the decentralized design, the API servers do not have direct access to the user's session. To overcome this authentication limitation, we include a *JSON web token* (JWT) in each request that is sent from the client application to the API endpoints. This JWT is generated by the application server and includes the user's authentication status together with a signature that prevents modifications to the token. The API server can verify the authenticity of the JWT by using a shared secret key and deny the request if the authorization requirements are not met. With this approach, access to the API endpoints that do not originate from COSMICWEB can be prevented.

4.4 Details of the web interface

In this section, we present the main pages of COSMICWEB, discuss their functionality, and explain some of the implementation choices. The web interface is hosted using the FLASK framework[6], which routes and processes incoming requests, handles user sessions, and serves the web pages.

In general, pages with low interactivity, such as the landing page, simulation overview pages, and the documentation pages, are fully constructed on the application server, i.e. the server dynamically composes the page with user and simulation data and sends the complete and static HTML to the client. On the other hand, pages that change under the user interaction and pages that have to fetch additional data from the API servers only contain the skeleton of the webpage, into which components are dynamically inserted. For this purpose, we use the javascript-based REACT library[7], allowing us to write parts of a page as dynamical components with simple state and event handling. A schematic of the rendering of a REACT application and its insertion into the Document Object Model (DOM) of the browser is shown in fig. 4.3. The DOM is initially created when the browser receives the HTML skeleton and represents the tree structure of the webpage, with each node being an element of the page, such as an input field, table rows and cells, or text paragraphs. We include an empty container-node in the HTML, into which REACT inserts and updates its partial (virtual) DOM.

4.4.1 Halo Finder

The *Halo Finder* is the search page that allows the user to query the databases and find objects of interest to re-simulate. The page aims to provide an intuitive interface for selecting the target

[6] https://flask.palletsprojects.com
[7] https://reactjs.org/

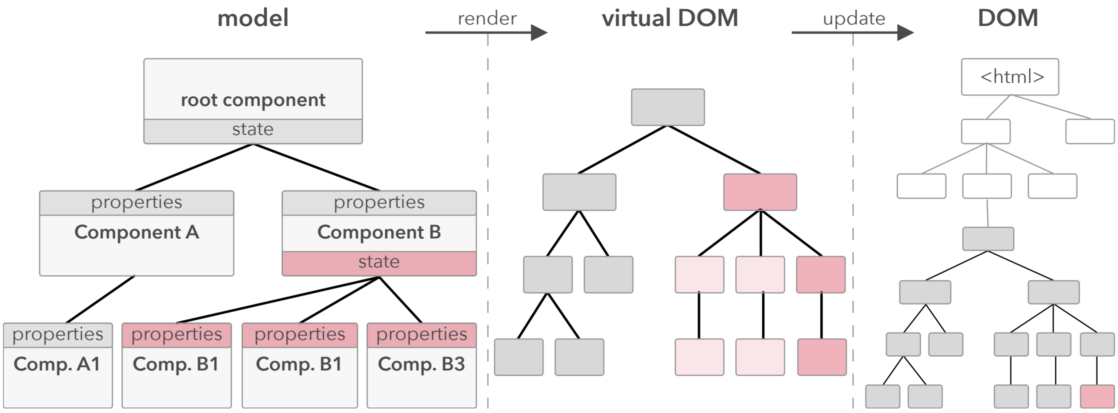

Figure 4.3: Illustration of the rendering process of a REACT application. The application is modeled as a tree consisting of REACT components, which can be stateful or stateless. Parameters can be forwarded through the property interface of the components. Each component defines a *render* function, containing other REACT components or HTML elements. The function is invoked during the initial construction and whenever the state or the properties change. The rendering builds a virtual DOM which is inserted to the real DOM. On re-renderings, the virtual and real DOM are compared in order to only update the differences, increasing the responsiveness of the application. As an example, we illustrate the procedure when the state of component B is changed (highlighted in red), e.g. after the user changed an input field. The state update causes a re-rendering of component B, altering the properties of components B1, B2, and B3 which in turn are also re-rendered. However, the updated properties only change the DOM representation of B3, hence only this node is updated in the real DOM.

simulation, setting up the query filters, and obtaining a preliminary overview of the returned results, without the need of knowing the database layout or SQL. To achieve this, the page needs to be able to dynamically adapt to the selected simulation, as different selectors may be supported for different projects (cf. table 4.2).

The interface consists of three parts: the simulation selection panel, the property filters, and the result display. In the simulation selection panel, a single simulation has to be selected which will set the corresponding API endpoint and security token in the application state. The choice of a snapshot is optional, as the redshift range can also be constrained in the filter window. The available filters are dynamic and adapt to the feature list of the selected simulation. The parameter ranges can either be edited in a textual interface or by using sliders, for which the available maximum range of is automatically set to a sensible default for the chosen simulation. Once a query has been committed and the response of the API server has arrived, the halos corresponding to the filter criteria are shown in the results panel, either as a list, where each element can be clicked to open the *Halo Explorer* for the corresponding halo, or as a scatter plot, where the parameters shown on the x and y axes can be chosen from the supported halo parameters. Halos can be further selected in either view in order to store them in a collection or for bulk-downloading the initial conditions configuration files directly from the halo finder.

Due to the high complexity of the *Halo Finder* page, with many components depending on the state of others, handling the application state directly in REACT components would become too complex and error-prone. We therefore decided to use the FLUX[8] design-pattern to manage the state, in particular the REDUX[9] implementation. The key idea is a unidirectional data flow with a central *store* managing the state of the application.

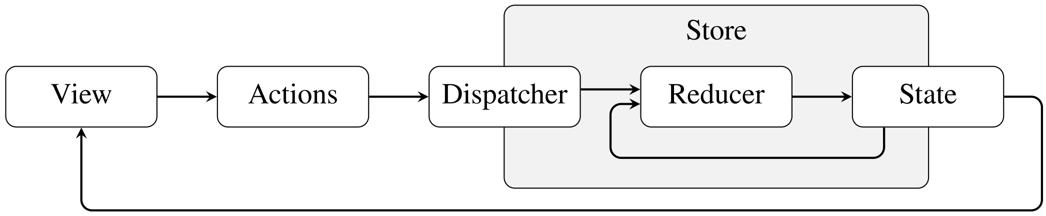

When the user interacts with the interface, or upon response from the API servers, an *action* is emitted and dispatched to the store. The store updates the state by combining the current state and the action with the help of the *reducer* functions. The interface components are then updated with the new state.

The clear separation of the interface, the state, and the update logic achieved by this design pattern greatly lowers the complexity of the *Halo Finder* page. Figure 4.4 shows the simplified website and a schematic diagram of the control flow and state management. Actions are for example emitted by

- selecting a simulation, which updates the state with the corresponding feature list and API server address and security token,
- changing the search options and filter ranges,
- clicking the search, reset, and save buttons,
- receiving a response from the API server,
- selecting individual halos in the result list or scatter plot.

As an example, we discuss the search action in more detail. The action is emitted after clicking the “search” button and dispatched to the store. First, the current parameter selection is validated, after which the result state is either updated to *error* or *loading*. In the latter case, a request with the query settings is sent to the API server corresponding to the selected simulation. This request is asynchronous, hence the state is updated and the interface updates to reflect the changed state (“loading”), completing the unidirectional flow cycle. Upon receiving the server’s response, a new action (“received”) is dispatched to the store. Depending on the status of the response, the result state is changed from *loading* to *error* with a description of the error, or updated with the returned list of matching halos. The interface updates to reflect the changed state. The other actions proceed in a similar order. By clicking the “reset” button for example, the dispatched action resets the simulation and filter settings to their default values and clears the result state.

[8] `https://facebook.github.io/flux/`
[9] `https://redux.js.org/`

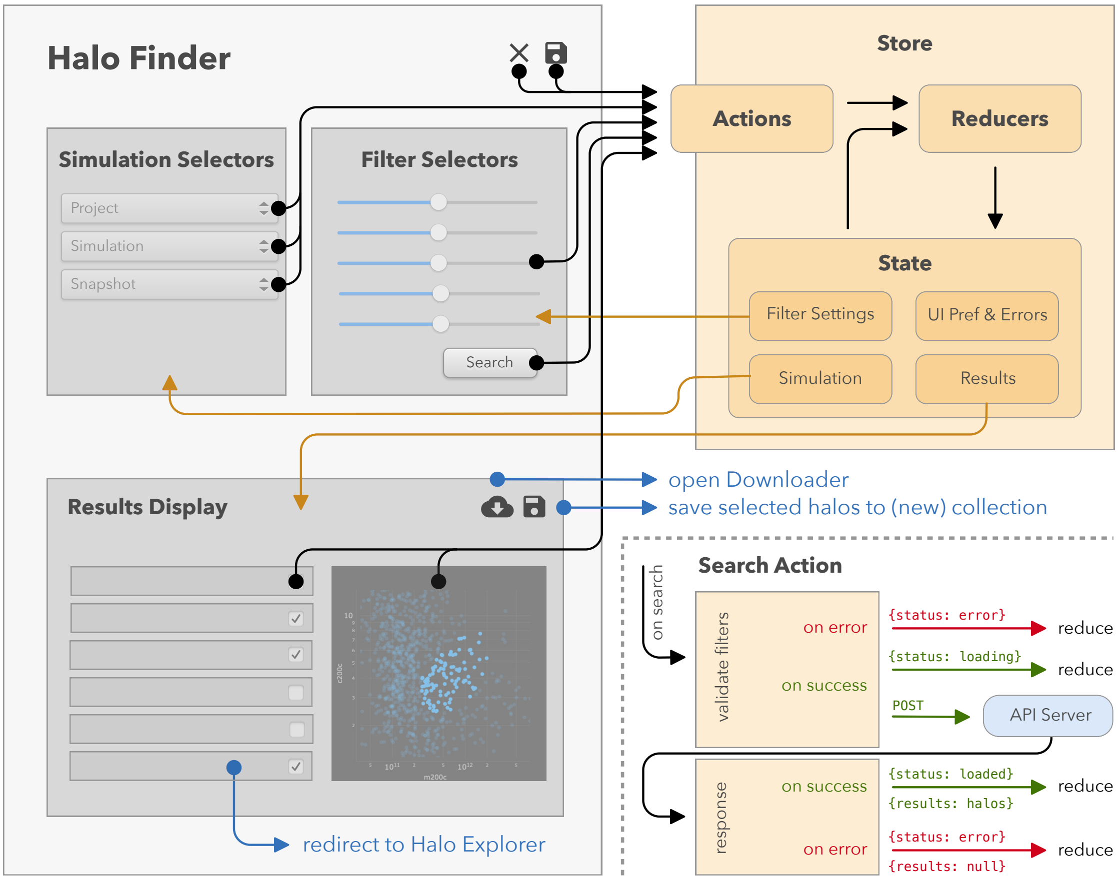

Figure 4.4: Schematic of the *Halo Finder* page. The state of the application, including UI settings, validation and server errors, the selected simulation and filters, and server responses, is managed using the FLUX design pattern described in the text. Interface interactions and callbacks from server responses (black arrows) emit actions which are dispatched to the central store and reduced with the current state to create the new state which is reflected in the updated UI (orange arrows). The search action is shown in more detail, with a description in the main text.

4.4.2 Halo Explorer

The *Halo Explorer* page provides an overview of the available details of a halo, enabling the user to confirm or exclude possible re-simulation targets. It displays valuable information on intrinsic parameters, the halos past, surrounding, and interior substructure. The design of the page is modular, and individual components are enabled depending on the feature set of the simulation to which the halo belongs to. Figure 4.5 shows a schematic overview over the different components and their corresponding API endpoints. The first row is always present and contains an overview over mass, radius, and further halo parameters, as well as links to related halos in the temporal and spatial hierarchy if available. The last row (*publications*) is also feature independent and indicates

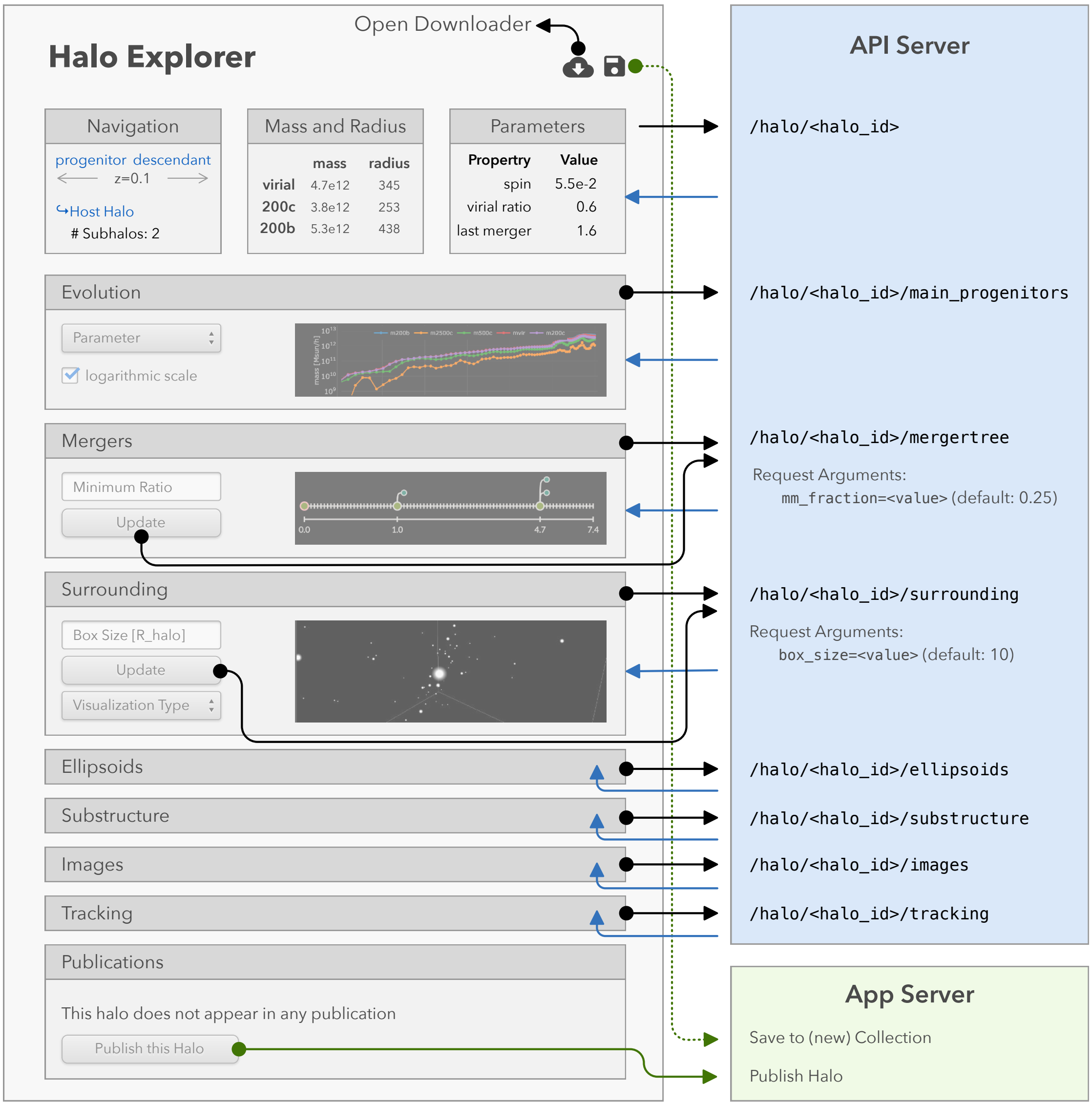

Figure 4.5: Schematic of the *Halo Explorer* page. Each panel is connected to an API endpoint to which a request is sent upon first opening the panel or upon refreshing the panel parameters (black arrows). Panels that are not supported by the corresponding simulation are automatically disabled. Additionally, the halo can be published or stored in a collection (green arrows), and initial conditions can be obtained through the *Downloader*.

if the halo is already part of a publication, with the possibility to create a new publication that will be visible for other users (more information in section 4.4.4). Using the buttons in the top right corner, the halo can be added to an existing or to a new collection, or the *Downloader* overlay can be opened to access the initial conditions configuration script for this halo.

The remaining panels contain additional information and visualizations that depend on the support of the corresponding simulation API. To avoid loading all the data at once and potentially overloading the API servers with several queries at once, the data retrieval is lazy, i.e. the panels start in a closed state and a request to the API endpoint is only sent when the panel is opened the first time. The response is then cached, so that closing and reopening the panel does not cause additional requests.

In addition to the schematic overview in fig. 4.5, screenshots of the visualization panels can be seen in fig. 4.6 and fig. 4.7. In the following, we will briefly discuss each panel.

Evolution visualization

The *evolution* panel retrieves the halo properties of the halo's main progenitor chain. It allows to visualize the evolution of any numerical parameter configured for that simulation. Different definitions of the same quantity, such as masses, radii, concentrations, and spin parameters, are shown together. The plot powered with PLOTLY[10] and is interactive and allows zooming, panning and hovering over data points to see the numerical values.

Merger visualization

The *merger* panel shows the past major mergers with an adjustable threshold for the ratio between the merging and resulting halo (i.e. a merger between two halos with a 1:3 mass ratio would correspond to a merger ratio of 0.25 for our definition). The graph shows the main progenitor branch and highlights halos associated with a merger above the threshold together with the merging halo. Each halo in the graph can be selected to show its mass and redshift and open its corresponding *Halo Explorer* page.

Halo Tracking

The *tracking* panel visualizes the (comoving) displacement of the halo from its first measured position during the course of the simulation, following the main progenitor branch. This can be useful to identify close-by interactions with neighboring massive halos altering the trajectory of the halo, and to set up parameters for "movie"-features included in various simulation codes that allow on-the-fly processing of a small simulation volume for visualization purposes. In that regard, we also provide a polynomial fit of selectable order to the halo coordinates, i.e. $x_i = \sum_k c_k a^k$, where a is the scale factor and c are the polynomial coefficients. Note that with default settings, MUSIC re-centers the simulation volume on the zoom center, hence the c_0 offsets need to be corrected for the shift before using the polynomial to track the movie center.

Substructure visualization

The *substructure* panel provides a broad overview of the halo's substructure tree with a *circle-packing* enclosure diagram. Note that the ratio of the circle radii of the subhalos roughly correspond to the halo radii, but the diagram does not represent the actual sizes or locations of the

[10] https://plot.ly/javascript/

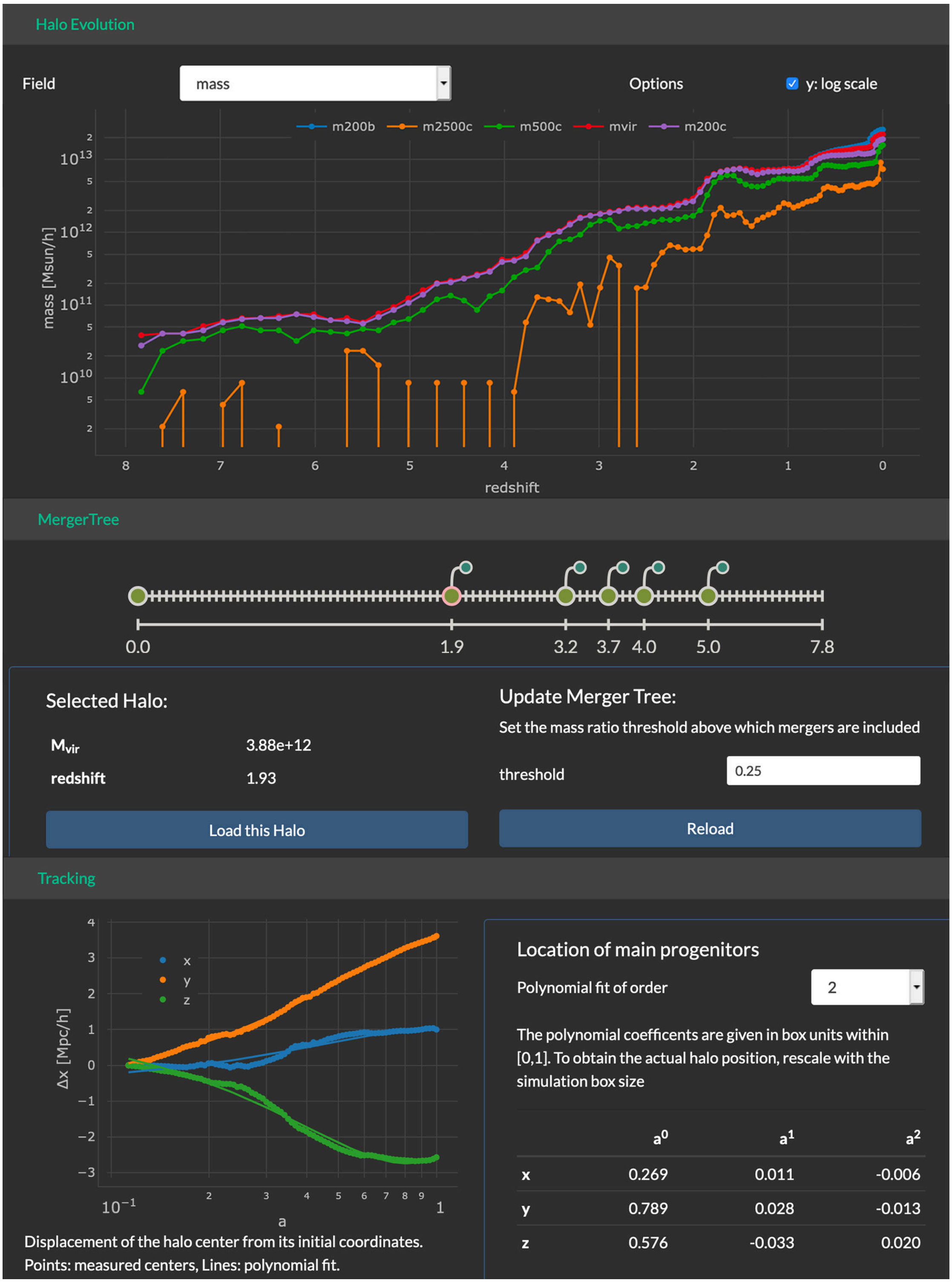

	a^0	a^1	a^2
x	0.269	0.011	-0.006
y	0.789	0.028	-0.013
z	0.576	-0.033	0.020

Figure 4.6: Screenshots of the *Halo Explorer* visualizations (Part 1: temporal)

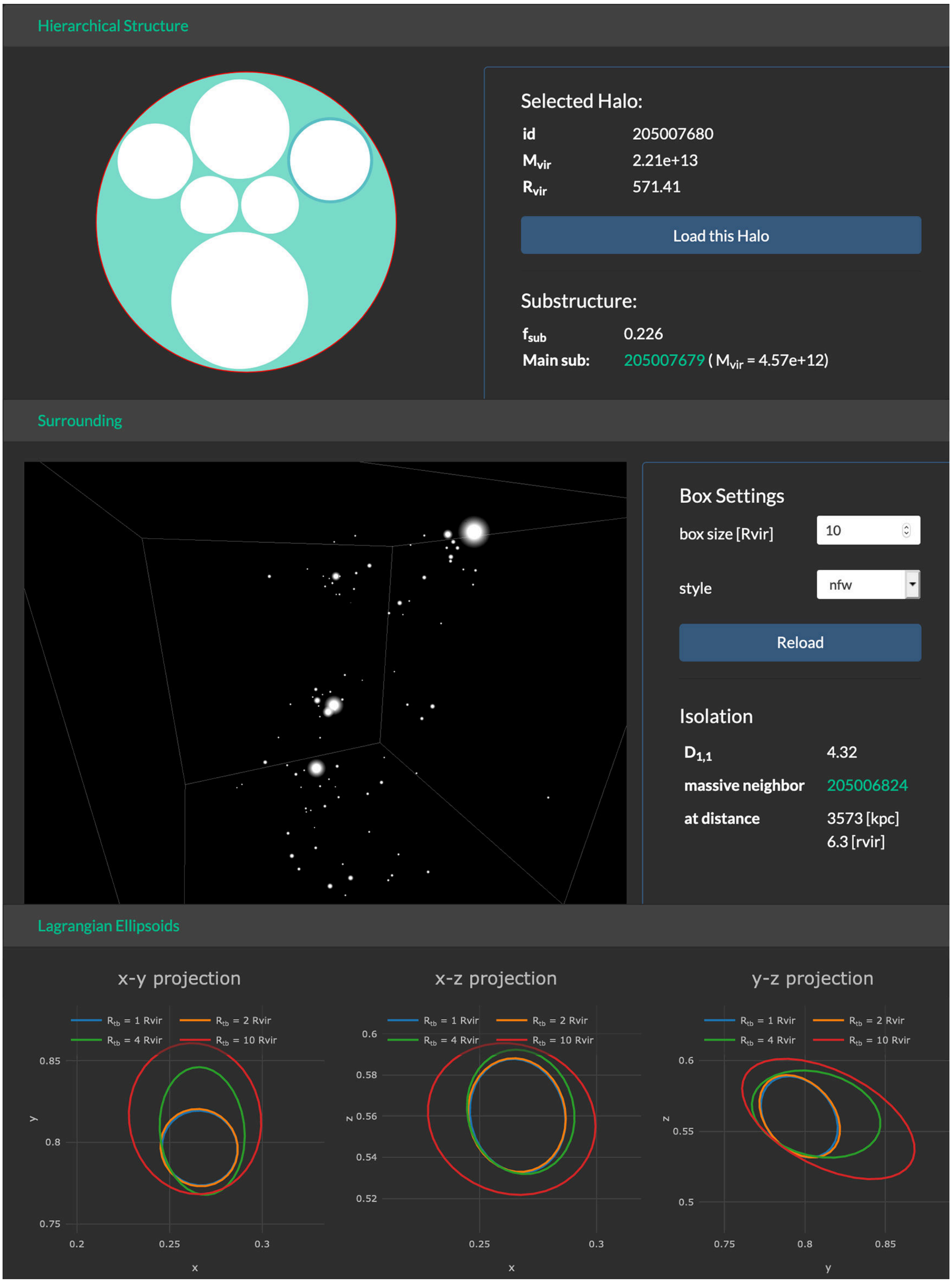

Figure 4.7: Screenshots of the *Halo Explorer* visualizations (Part 2: spatial and ellipsoids)

subhalos. However, it allows selecting subhalos to show more information on measured masses and radii.

Surrounding visualization

The *surroundings* panel shows all halos in the vicinity of the halo in a fully interactive and responsive 3d visualization built with WebGL[11]. The size of surrounding box can be chosen in multiples of the halo radius, and the display currently offers three different shaders for the halos: a disk and circle shader with the radii corresponding to the halo radius and a NFW-like surface density shader. The latter is adapted from the calculated surface density in [25]

$$\Sigma(x) = \frac{2\rho_s r_s}{x^2 - 1} f(x), \tag{4.3}$$

where $x = r/r_s = c(r/r_H)$ for a halo with radius r, scale radius r_H, and concentration parameter c, and $f(x)$ is defined as

$$f(x) = \begin{cases} 1 - \frac{2}{\sqrt{x^2-1}} \tan^{-1} \sqrt{\frac{x-1}{x+1}} & (x > 1) \\ 1 - \frac{2}{\sqrt{1-x^2}} \tanh^{-1} \sqrt{\frac{1-x}{1+x}} & (x < 1) \\ 0 & (x = 1). \end{cases} \tag{4.4}$$

For a clear visualization, we use a very low concentration parameter $c = 0.5$ for every halo and map the logarithmic density to a normalized luminosity scale. Additionally, if the information is available, the closest more massive neighbor and the separation is shown on the side.

Lagrangian ellipsoids overview

The *ellipsoid* panel visualizes the computed Lagrangian minimum bounding ellipsoids of the halo to allow for a comparison of the volume and shape of the Lagrangian patches associated with each traceback-radius. The projections are directly computed from the ellipsoid shape matrix by requiring the derivative of the ellipsoid boundary equation along the projection axis to vanish, i.e.

$$\frac{\partial(\boldsymbol{q}^T A \boldsymbol{q})}{\partial q_i} = 0. \tag{4.5}$$

Furthermore, the panel also lists the number of particles that were used for the ellipsoid computation to estimate the quality and convergence of the ellipsoid, the mass enclosed by the ellipsoid, and the efficiency parameter ϵ (cf. eq. (4.1)). Note that these quantities are not shown in the screenshots due to spatial constraints.

[11] https://www.khronos.org/webgl

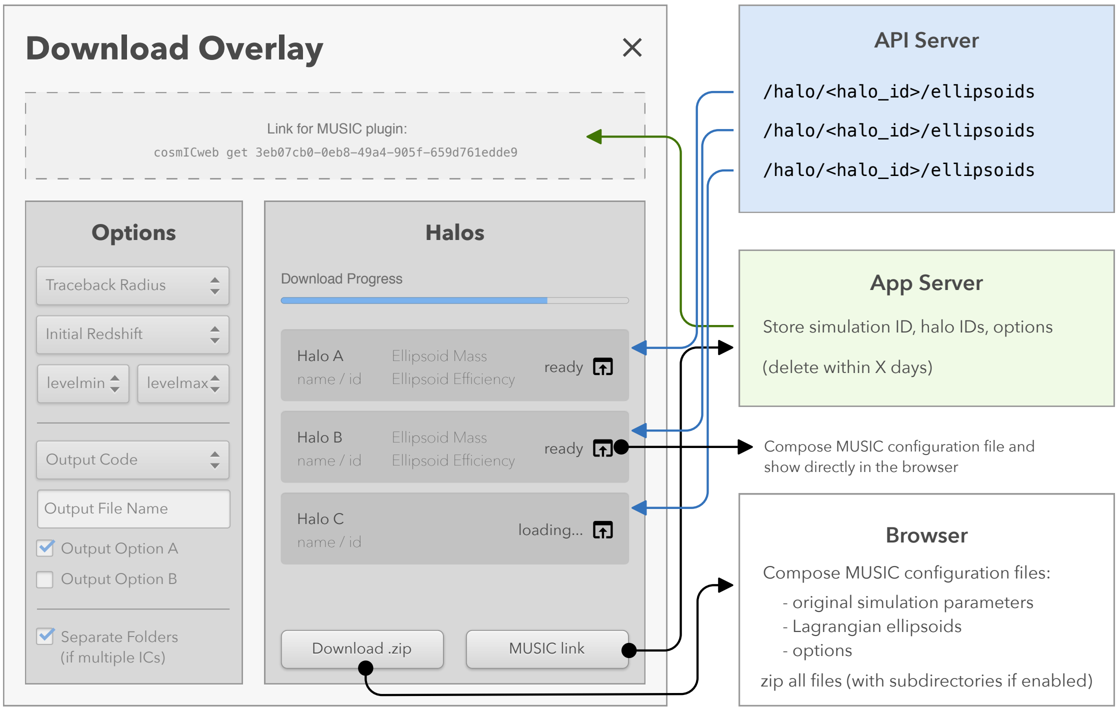

Figure 4.8: Schematic of the *initial conditions downloader* overlay. The overlay can be accessed from the *Halo Finder*, *Halo Explorer* and the collection and publication interfaces and allows configuring and downloading the initial conditions configuration files, either by opening them directly in the browser, downloading as an archive, or by generating a link which can be used with an external script directly on the server.

Images

Finally, the images panel will show already existing visualizations of the halo or associated galaxy. Mock images of the *gri* bands are for example provided for some galaxies in the publicly available EAGLE data [216]. This feature is currently is still under development, and the corresponding API backend for the EAGLE simulations has not been fully implemented yet. Future versions of COSMICWEB may also allow uploading images from re-simulations which will be shown in this panel.

4.4.3 Downloader

The *Downloader* is an overlay that can be opened from the *Halo Finder*, *Halo Explorer*, and the collection and publication views. It allows configuring and downloading the MUSIC initial condition configuration files for a single or multiple halos (from the same simulation) at once. A schematic overview is shown in fig. 4.8.

Upon opening the overlay, the *Downloader* is configured with the halos from the page of origin. For each halo, the *Downloader* proceeds with requesting its minimum bounding ellipsoids with the progress being shown in the overlay. If no ellipsoids are provided for a halo, the corresponding entry will be highlighted and ignored in the later processing.

The *options* menu allows selecting the traceback radius of the minimum bounding ellipsoid and specifying the starting redshift and the coarsest and finest particle resolution of the simulation, as well as the type of initial conditions file that will be generated by MUSIC. These options will be added to the configuration file, facilitating the batch processing of multiple zoom simulations. Depending on the selected output format, more options that are specific to that code will be shown in the list.

Finally, after the initial conditions are downloaded and the options specified, the interface offers three different ways of retrieving the initial conditions configuration files, either by clicking on the halo entry to open a single file directly in the browser, downloading an archive that contains all files, or storing the configuration online to later download the files with the separate PYTHON script that we provide with MUSIC. This allows downloading the initial conditions directly on the server where the full initial conditions will be generated.

4.4.4 Collections and Publications

When querying halos in the *Halo Finder*, a multitude of halos may fulfill the search requirements and be suitable for re-simulation. Narrowing the selection thus requires a more thorough investigation of the candidates, using the *Halo Explorer*, or maybe even running medium-resolution zoom simulations on a few targets. It is therefore convenient to temporary store the candidates and maybe share them with colleagues. Collections are designed to satisfy this requirement by providing an intuitive interface to group halos, with the capability of naming and describing the group and individual halos.

Collections can be created by selecting multiple halos in the *Halo Finder*, from the *Halo Explorer* by adding a single halo to an existing or new collection, or from a subset of halos in an existing collection. Once a collection has been created, it can be viewed and edited in the *Collection Editor*. We show a schematic overview of the viewer/editor in fig. 4.9. On the application server, we only store the simulation the collection belongs to, together with a list of halo identifiers associated with the group. To give an overview of the contained halos, the *Collection Editor* loads additional data from the API Server that can be viewed in a scatter plot or in a evolution plot, where the history of a selectable property along the main progenitor branch can be compared amongst the halos.

The editor allows changing the collection name and adding a descriptive text to the collection and individual halos. Halos can also be assigned names, for example to match the naming convention in a research article. If a halo is no longer being considered, it can be removed from the collection. Generally, a collection can only be accessed by the user who created it. To share a collection with colleagues, this restriction can be removed by checking the corresponding option, allowing other users to read but not modify the data. Since we use a random *universally unique identifier* (UUID[12], version 4) for each collection URL, with a total of 2^{122} possibilities, the probability of a third party guessing the URL is insignificant.

Once the re-simulations are complete and the results are ready for publication, the collection

[12] https://www.rfc-editor.org/info/rfc4122

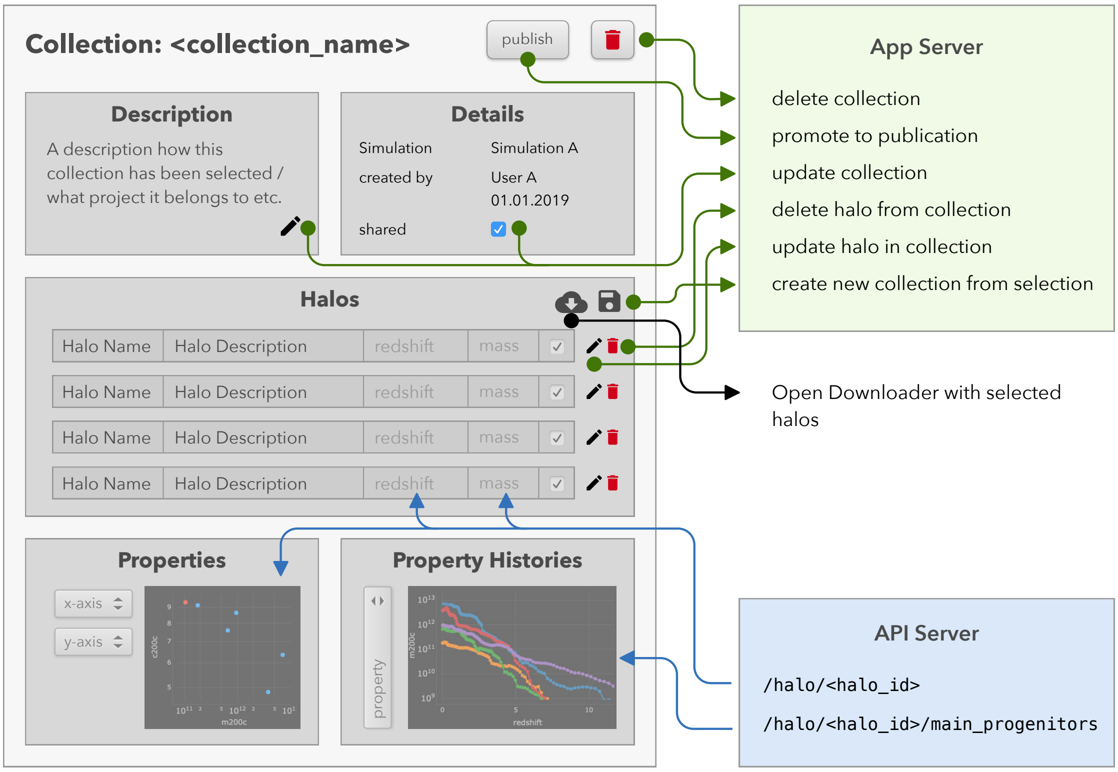

Figure 4.9: Schematic of the *Collection Editor*.

can be promoted to the publication status. During this process, the collection is assigned a permanent URL composed of the name that was given to the collection. This URL can then be added to the article, allowing other researches to easily retrieve the referenced halos and their initial conditions. Additionally, the collection appears under the list of publications shown on COSMICWEB, together with the description and a link to the research article, and the publication will also be highlighted in the *Halo Explorer* for the halos in the collection.

Sometimes, a study for a research article may target a single halo only. For this case, a permanent URL, together with a short description and a link to the article, can be created directly from the *Halo Explorer* page, without the detour of creating a single halo collection first.

4.5 Details of the local API implementation

In section 4.3, we have have discussed the requirements on the API servers in order that they can be integrated with the rest of the COSMICWEB application. How these requirements are best implemented has to be evaluated case-by-case and depends on the available data, its storage, the server infrastructure, etc. In this section, we will discuss the implementation for the local simulations as a case example.

The locally hosted simulations support all required and optional features listed in table 4.3 with the exception of images. The API server thus needs to be able to efficiently access halo

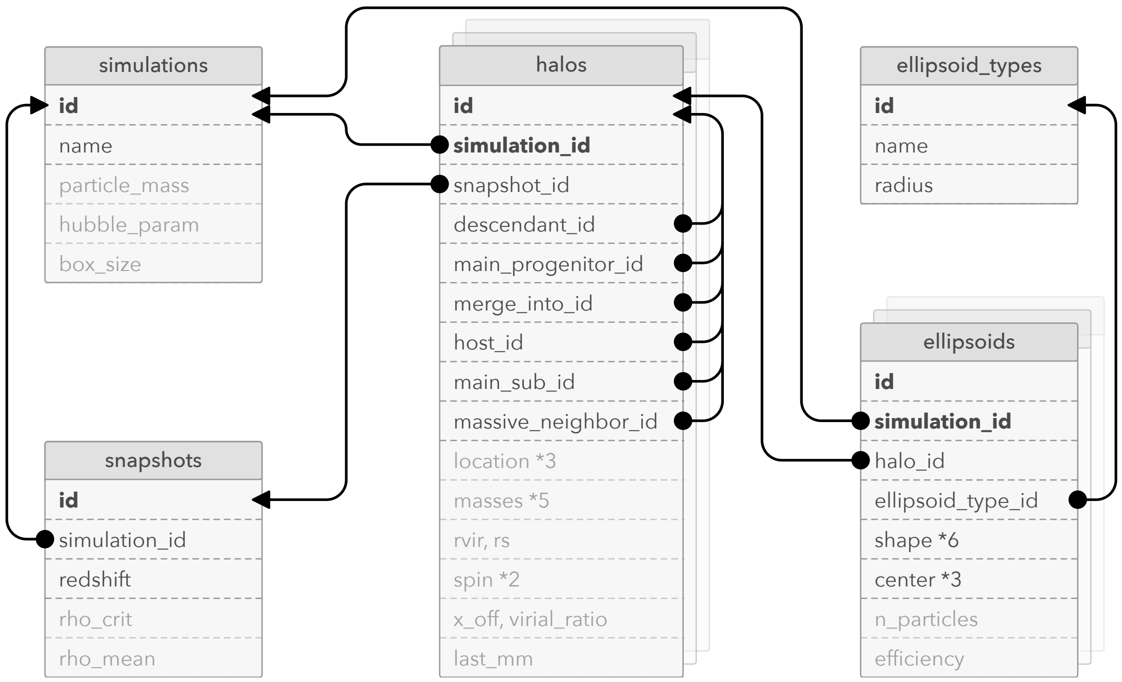

Figure 4.10: Schematic of the table layout of the local simulation database. Bold entries highlight the primary keys and arrows represent foreign keys. The *halos* and *ellipsoids* table have been partitioned by simulation for better performance. Additional halo and ellipsoid properties not relevant for the relationship graph have been grayed out. See table 4.2 for the abbreviations used for the properties.

catalogs with merger-tree information and associated Lagrangian ellipsoids. We therefore store the data in a SQL-database[13], which allows us to express relations, such as descendant halos, main progenitor halos, host halos, and main subhalo, as foreign keys between individual entities.

Figure 4.10 shows a schematic overview of the database layout. The lowest entity in the dependency graph is an *ellipsoid*, which is associated to a *halo*, which in turn belongs to a *snapshot*, associated to the top entity, a *simulation*. In theory, it would suffice to link a halo with a snapshot only. However, since the amount of data is fairly large and COSMICWEB requires low latencies to display the query results in the browser in a reasonable time frame, we use *partitioning* for the halos and ellipsoids table. This creates a sub-table for each simulation, basically removing the latency increase for queries after adding additional simulations.

To minimize storage requirements, some halo properties can be computed on-the-fly. For the halo boundary definitions following the critical and mean density threshold conventions, we for example only store the halo masses. The radii and concentration parameters can then be computed from the critical and mean densities stored with the associated snapshots and the scale radius stored with the halo. On the other hand, we decided to pre-compute the ellipsoid

[13] We use the open-source POSTGRESQL database, which provides advanced features such as data partitioning which is indispensable for large amounts of data such as with this project.

efficiencies from the shape matrix and the number of particles used to construct the ellipsoid, as an on-the-fly computation of the shape determinants would increase the query times for the /halofinder endpoint too much.

As mentioned previously, merger tree relations are implemented using foreign keys pointing to the related halo in the *halos* table. The full main progenitor branch, required for the /halo/<id>/main_progenitors endpoint, and merger list with variable merger thresholds, required for /halo/<id>/mergertree, can be efficiently constructed with recursive queries. Furthermore, quantities such as the mass fraction in substructures or distances to the closest more-massive halo can be computed dynamically from these relations. In theory, also the time of the last major merger could be calculated on-the-fly, but for performance reasons in the /halofinder endpoint, we decided to pre-compute the redshift of the last 1:3 merger for every halo.

As mentioned in section 4.2, the Lagrangian ellipsoids for the local simulations have been obtained from particles within 1, 2, 4, and 10 R_{vir} of the halos. Since we may add additional ellipsoid definitions in a future version of cosmICweb, we use an extra lookup-table for the ellipsoid type. Such additional Lagrangian ellipsoids may for example include ellipsoids obtained from only the bound particles within the traceback-radius, or by optimization of the shape by removing the outermost particles that increase the volume disproportionally. Having a lookup-table facilitates this step significantly, as one can simply add an additional entry.

To parse incoming API requests to the various endpoints, to dispatch queries to the database, and to format the response according to the API specifications, we use the Flask framework in combination with the SQLAlchemy library. Some complex and time-intensive queries, such as building merger trees or hierarchical trees, have been manually profiled and optimized to guarantee a reasonable execution time. To identify future bottlenecks in the API server, queries that take a disproportionate amount of time to process are logged on the server, allowing us to optimize the application where necessary.

4.6 Conclusions

In this chapter, we have presented the cosmICweb project, an online platform that aims to simplify the creation and sharing of zoom simulations. We have layed out the current work-flow for setting up and running zoom simulations and showed how cosmICweb integrates with this process. In particular, we address three key steps: i) finding and selecting targets for zoom simulations, ii) retrieving the zoom initial conditions with a high resolution region placed on the Lagrangian volume of the target, and iii), sharing the initial condition configuration in research publication, allowing the community to compare and verify scientific results. We envision the following workflow with cosmICweb:

1. select a suitable simulation for simulation target,
2. choose appropriate filters in the *Halo Finder* and query results,
3. preselect some halos using the property list and scatter plot and store them in a new collection,
4. take a closer look at individual halos in the *Halo Explorer*,

5. select the target halo(s) by either removing halos from the collection or by creating a new collection,
6. download the initial conditions configuration files for the halo(s) using the *Downloader* overlay,
7. create the initial conditions and run the zoom simulations,
8. when publishing the results, promote the collection to a publication, include the generated COSMICWEB link in the article, and add a link to the article in COSMICWEB.

The ability to access initial conditions from published research will allow the scientific community to easily verify results and compare and improve different models of baryonic physics and code implementations, which will ultimately help us to improve our overall understanding of the evolution of galaxies and clusters in our Universe.

Zoom simulations are and will remain an indispensable tool in numerical cosmology to perform high resolution simulations of individual gravitationally bound objects, study the formation and evolution of galaxies in great detail, and to compare different simulation codes and physical models on the same object.

State of COSMICWEB at the time of writing

Some parts of the COSMICWEB project are being finalized at the time of writing this thesis, after which the application will be ready to be released to the public. The development of the web frontend and the integration of the locally hosted simulation (cf. table 4.1) is mostly finished. There will be some minor changes, mostly affecting the documentation of COSMICWEB and small parts of the user interface to provide a more intuitive user guidance through the different components of the web application.

Some work is still required for the interface between the EAGLE simulation database and COSMICWEB, in particular to allow searching the halo catalogs through the halo-finder interface. At the moment, the *Halo Finder* (see below) is not yet working for EAGLE, but halos and their associated proto-halo patches can be retrieved if the EAGLE `galaxyID` is known. We hope to be able to finish the integration of EAGLE soon.

4.7 Outlook

As a public platform, the development of COSMICWEB will never be finished as such, since the data as well as the requirements will change over time, requiring adaptations and extensions to the project. The exact kind of improvements that we will consider highly depends on the feedback and requirements from the community. In this outlook, we will therefore only present some possibilities. Future development can be categorized into two classes: the addition of new data, in particular the integration of new simulations, and the addition of new features. We discuss them separately in the next two sections.

4.7.1 New simulations and data

New halo catalogs and proto-halos from additional simulations can either be directly hosted at the Observatoire de la Côte d'Azur, or from existing or new databases located outside. To facilitate the setting up of the API interface, we may publish our own implementation described in section 4.5 as a template in the future.

We are or are planning to get in contact with other collaborations that maintain large databases of simulation data, such as the ILLUSTRISTNG Collaboration [252, 232], the HORIZONAGN [90], and the MAGNETICUM project [83]. Adding cosmological volumes that contain halos that were studied in already published articles, such as the FIRE [157, 158] or C-EAGLE [21] simulations, may be a valuable addition to COSMICWEB. In addition, constrained simulations and reconstructions of the local Universe [37, 120] (e.g. [321, 296]) would provide interesting and unique possibilities to extend the available halo catalogs and initial conditions.

We are also planning to add new DM-only simulations to extend the mass range of halos for which we provide initial conditions. In particular, low mass halos are not well-represented at the moment, which will require high-resolution, low volume simulations. We are also planning to add halos from a "zoom-into-the-void" simulation, to allow studies of isolated, low mass objects, in even higher resolutions than the original zoom simulation.

We would also like to provide a platform for people to upload their own initial conditions, unrelated to simulations that are hosted on COSMICWEB. This would allow researchers to share the configurations of custom zoom simulations on COSMICWEB; however, the available features would obviously be very limited.

Running zoom simulations on targets in the COSMICWEB database will naturally improve the knowledge about this object, e.g. better mass estimates additional information on the galaxy forming inside the halo, and, most importantly, a better converged Lagrangian volume from which the halo originates. It would therefore be beneficial for future runs to collect this data and feed it back to the COSMICWEB database. How this "information loop" could be implemented is, however, unclear at the moment.

4.7.2 Additional functionality

As a result of the modular design, new *Halo Explorer* features and *Halo Finder* filters can be easily added in the future if required. Such features may include visualizations of the full halo merger tree with the ability to navigate different progenitor branches, animations of the halo growth, motion, and merger events using the already existing 3D framework for the visualization of the halo surrounding, or a tool to find similar halos in the database for statistical studies (e.g. by suggesting halos with similar properties).

For typical *Halo Finder* queries (e.g. Milky Way like halos), selector presets may be made available, with randomized ordering of the returned halos.

For initial conditions generation and proto-halos, we will add support for alternative generators to MUSIC, in particular for PANPHASIA [171] for the EAGLE simulations. We may also consider supporting additional descriptors of proto-halo shapes, such as convex hulls, for more optimized zoom simulations.

To guarantee the accessibility of initial conditions referenced in publications, even after the potential end of COSMICWEB, it would be advantageous to store these particular datasets on third-party services specialized on long-term storage of scientific data. We are considering using the CERN initiative ZENODO[14] to automatically create an entry upon the creation of a *publication* in COSMICWEB. In addition, this would provide the COSMICWEB users with unique, citable Digital Object Identifiers (DOI).

[14] `https://zenodo.org`

CHAPTER 5

Statistics of Proto-Halo Patches

For the COSMICWEB project presented in the previous chapter, we have computed a vast set of proto-halo patches from multiple simulations at various traceback-radii and at a large range of redshifts. This provides a large dataset connecting the linear density field with the non-linear collapsed structures across cosmic time, presenting a unique opportunity to study the origin of halos in the initial overdensity field and to find correlations between these initial patches and the objects they evolve into.

In section 1.4, we discussed some dynamical models that predict the non-linear collapse from the initial overdensity field, namely the spherical and ellipsoidal collapse model that associate halos to patches in the linear density field that have crossed a predicted density threshold, and the peaks theory which assumes that halos will form at local maxima of the linear density field. Both the ellipsoidal model and the peaks theory predict that in general, the gravitational collapse will be anisotropic, with larger ellipticities for lower peak heights and lower initial densities, generally associated with lower mass halos.

The mapping between the Lagrangian patch and the final halo encodes the entire formation history of the object. Its knowledge thus provides a unique opportunity to study how intrinsic properties of an object arise from initial fluctuations and how they are correlated with the environment at larger scales. For example, the triaxial nature of the collapse plays an important role in the initial growth of the halo's spin, modeled in *tidal torque theory* (e.g. [331, 24, 146]), which predicts that most of the angular momentum of halos is gained during the initial, linear collapse phase of the halo due to a miss-alignment between the proto-halos shape and the external tidal field. Of large interest are also secondary correlations of halo properties with the large scale environment, known as assembly bias [113, 324, 112, 47]. Such assembly bias is potentially problematic in LSS observations, as it can in principle induce a beyond mass dependent bias in measurements of cosmological clustering. Spatially correlated merger histories, reflected in spatially correlated proto-halo shapes, are a possible source of intrinsic alignments of galaxies, i.e. locally correlated orientations of galaxies, contaminating shear measurements in weak lensing studies [147, 71, 58, 152].

Studying proto-halo shapes may thus yield valuable information on the formation history and properties of the final halo and its surroundings. In this chapter, we will take a first look at the Lagrangian patches and their associated halos from the local COSMICWEB database. In particular, we will study the shape distribution of proto-halos, their alignment with the initial tidal and density field, and the impact of the halo environment on the proto-halo shape and the "goodness-of-fit" of the minimum bounding ellipsoid via the efficiency parameter. The massive amount of data will certainly allow for future in-depth studies (see the discussion in section 5.5). The chapter is structured as follows: In section 5.1, we describe the data that is used in the following analysis, measure how well the minimum bounding ellipsoids capture the shape of the proto-halo, and we take a closer look at some selected halos and their associated proto-halo. In section 5.2, we compute the shape distribution of halos depending on mass and on secondary environmental parameters. In section 5.3, we take a closer look at the minimum bounding as a description of the proto-halo and discuss important considerations when using them as zoom regions in simulations, such as the efficiency parameter and the choice of trace-back radius. We conclude in section 5.4 and provide an outlook on future projects in section 5.5

5.1 Overview

We will start with a brief discussion of the subset of simulations, halos, and associated proto-halos that we use in this chapter and then visually inspect a few halos and proto-halos of different masses.

5.1.1 Data

For this chapter, we use the 150MPC, 300MPC, and RHAPSODY_NewCosmo simulations already discussed in the previous chapter and summarized in appendix A.3. Since the only difference between these simulations is the simulated volume and the random seed, this choice allows us to extend the mass range of halos we have access to.

The primary factor that determines the shape distribution of halos is the halo mass (cf. [20] and section 1.4), and we will therefore study five mass bins in more detail. The mass bins and which simulation the data originates from is presented in table 5.1.

We will mainly use the minimum bounding ellipsoids evaluated at $R_{\rm tb} = 1R_{\rm vir}$ and look at larger trace-back radii in section 5.3. The ellipsoids in our database are defined by their center $\boldsymbol{q}_c$ and their shape matrix A, i.e.

$$(\boldsymbol{q} - \boldsymbol{q}_c)^T A(\boldsymbol{q} - \boldsymbol{q}_c) \leq 1. \tag{5.1}$$

mass range ($M_{\rm vir}$) $[h^{-1}M_\odot]$	sample size	simulation	redshift	particle numbers
$(3, 6) \times 10^{10}$	140736	150MPC	0	110 – 220
$(1, 2) \times 10^{11}$	51407	150MPC	0	370 – 740
$(1, 2) \times 10^{12}$	52030	300MPC	0	470 – 930
$(1, 2) \times 10^{13}$	6449	300MPC	0	4670 – 9340
$(1, 2) \times 10^{14}$	17803	RHAPSODY_NewCosmo	0	1250 – 2500

Table 5.1: Summary of halo mass bins used in this chapter, including the simulation the halos are obtained from, number of host halos in that mass range and corresponding number of particles (note that the number of particles within the ellipsoid is larger than the number of bound particles within the virial radius, since not all particles are gravitationally bound and proto-halos are not perfectly ellipsoidal).

The eigenvalues $\lambda_1 \geq \lambda_2 \geq \lambda_3$ of the shape matrix are related to the semi axes of the ellipsoid by $a_i = \lambda_i^{-1/2}$ (note that $a_1 \leq a_2 \leq a_3$). Equivalent to the shape of peaks (cf. section 1.4), we can define the ellipticity and prolateness of the ellipsoid by

$$e = \frac{a_3 - a_1}{2\sum a_i} \qquad\qquad p = \frac{a_1 + a_3 - 2a_2}{2\sum a_i}. \tag{5.2}$$

An often used alternative approach to measure the shape of a proto-halo patch L is the inertia tensor (e.g. [46, 184])

$$I_{ij} = \sum_{q\in L} \boldsymbol{q}^2\delta_{ij} - q_i q_j, \tag{5.3}$$

and its reduced and dimensionless form (e.g. [135])

$$\tilde{I}_{ij} = \sum_{q\in L} (\boldsymbol{q}^2\delta_{ij} - q_i q_j)/\boldsymbol{q}^2, \tag{5.4}$$

where $\boldsymbol{q}$ are the Lagrangian coordinates of particles associated with the halo, centered at the center of mass of the Lagrangian patch. The reduced form weighs the inner part of the profile more and is thus less affected by spurious particles in the outskirts of the proto-halo patch. Using the moment of inertia for a homogeneous ellipsoid with semi-axes $a_1 \geq a_2 \geq a_3$, which in the eigenframe of the ellipsoid corresponds to the diagonal matrix $\left(a_2^2 + a_3^2, a_1^2 + a_3^2, a_1^2 + a_2^2\right)/5$, we can relate the eigenvalues $\iota_1 \geq \iota_2 \geq \iota_3$ of the inertia tensor to the axes of the ellipsoid:

$$\begin{aligned} a_1^2 &= \frac{5}{2N}\left(\iota_1 + \iota_2 - \iota_3\right) \\ a_2^2 &= \frac{5}{2N}\left(\iota_1 - \iota_2 + \iota_3\right) \\ a_3^2 &= \frac{5}{2N}\left(-\iota_1 + \iota_2 + \iota_3\right), \end{aligned} \tag{5.5}$$

where N is the number of particles associated with the halo.

Compared to the minimum bounding ellipsoid, these methods, in particular the reduced inertia tensor, will be less affected by single outlier particles. However, on average, the shapes and orientations should agree with each other for all methods. To test this, we compute the ellipsoid shape from the inertia tensor and the reduced inertia tensor and compare them with the shape of the minimum bounding ellipsoid, using the two mass bins of the 300MPC simulation. The results are shown in fig. 5.1.

Comparing the ellipsoid derived from the full and from the reduced inertia tensor, we find a very good agreement. Naturally, the ellipticity and prolateness obtained from the reduced inertia tensor is lower compared to the full inertia tensor, since the outer particles, which define the proto-halo shape, contribute less to the tensor. We find that $e_{\mathrm{red}} \sim 0.6\, e_{\mathrm{full}}$ is a good fit to the ellipticity measurements. Similarly, the prolateness of the reduced inertia tensor is also damped to a similar degree and slightly stronger for lower mass halos at positive prolateness. The major and minor semi axes are strongly aligned: 80% of all major axes of proto-halos from the upper (lower) mass bin deviate less than 9° (13°), and 80% of all minor axes deviate less than 6° (9°).

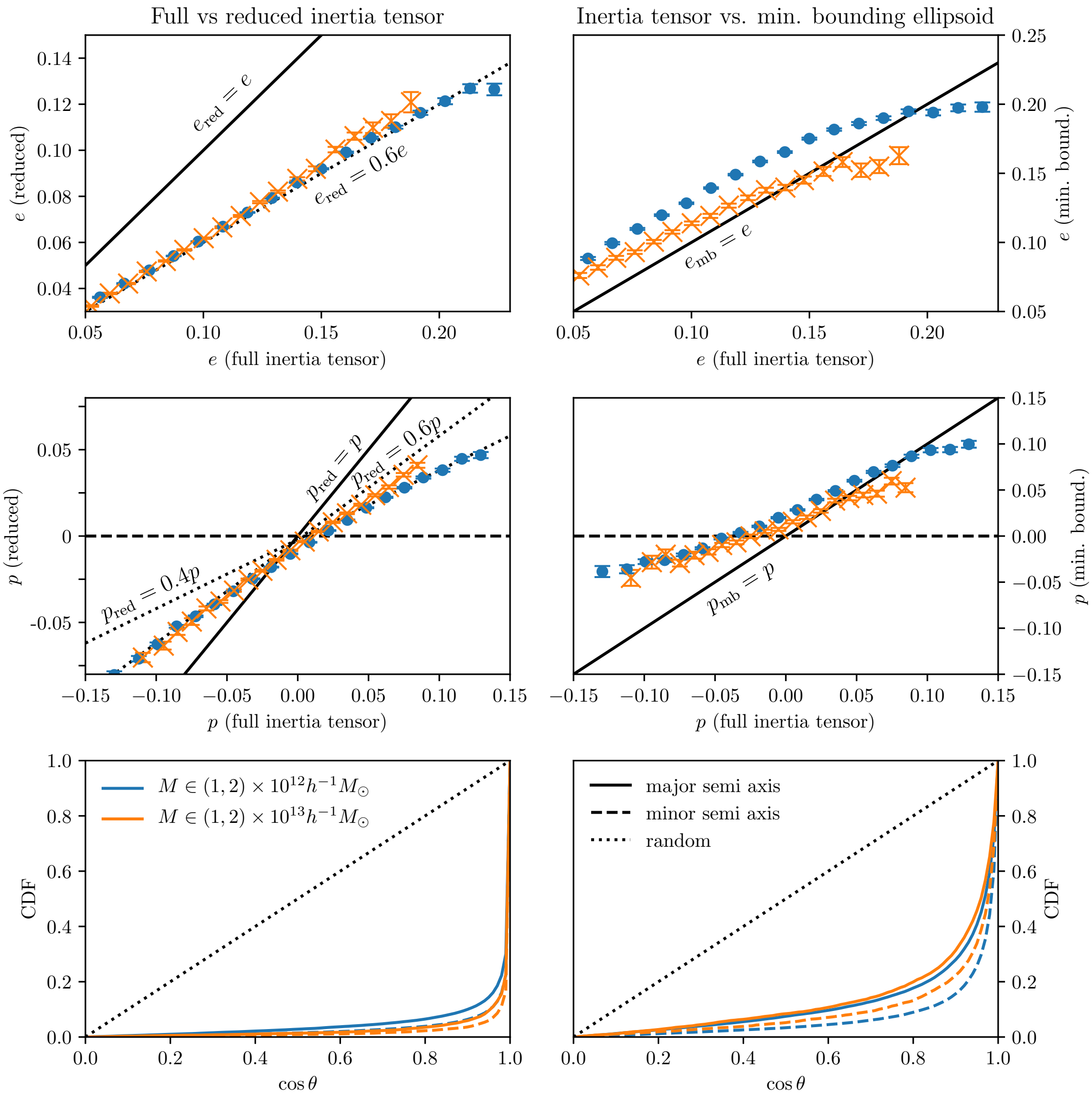

Figure 5.1: Comparison between the ellipticity, prolateness, and alignments of the major and minor axis of the proto-halo shape determined by the inertia tensor, reduced inertia tensor, and minimum bounding ellipsoid. We use proto-halos from two mass bins of the 300MPC simulation: $(1, 2) \times 10^{12}\, h^{-1} M_\odot$ (blue) and $(1, 2) \times 10^{13}\, h^{-1} M_\odot$ (orange). The left columns show the comparison between the ellipsoid obtained from the full inertia tensor $\boldsymbol{I}$ (eq. (5.3)) and the reduced inertia tensor $\tilde{\boldsymbol{I}}$ (eq. (5.4)), and the right columns the comparison between the full inertia tensors and the minimum bounding ellipsoids. Vertical bars indicate the standard error of the mean in the corresponding ellipticity and prolateness bin.

For the minimum bounding ellipsoid, we observe an overall larger scatter of ellipticities and prolateness, which is to be expected due to the large influence of outlier particles. On average, the ellipticity is slightly overestimated for low values and underestimated for larger ellipticities ($e \gtrsim 0.15$ for the higher, and $e \gtrsim 0.19$ for the lower mass bin). This is most likely due to the impact of outliers: if the patch is more spherical, an outlier will increase the ellipticity independently of its location. If the patch is already elliptic, there is a higher chance that the outlier will increase the minor semi axis, resulting in a more spherical minimum bounding ellipsoid. The prolateness of the minimum bounding ellipsoid is dampened, especially for oblate proto-halo patches. Major and minor semi axes are well aligned, with 80% of all major axes of proto-halos from the upper (lower) mass bin deviating less than 36° (33°), and 80% of all minor axes deviating less than 28° (21°).

Overall, the ellipsoid derived from the inertia tensor, the reduced inertia tensor, and the minimum boundary agree with each other to a reasonable degree. The inertia tensor may be preferred, as it is a more robust shape measurement of the proto-halo patch, assuming that the proto-halo patch is defined by only the particles within the halo boundary. For this chapter however, we will use the minimum bounding ellipsoids already precomputed for the COSMICWEB project. On average, the shapes should be consistent with the inertia tensor, but we expect that high ellipticities will be under-, and low ellipticities will be overestimated if one would directly compare the results with the inertia tensor method.

5.1.2 Visual Impression

Before we discuss the statistics of proto-halo shapes, we will take a visual look at some selected halos. Figure 5.2 illustrates the relation between proto-halos in Lagrangian space and the resulting halo at redshift $z = 0$. We choose six halos from the 300MPC simulation: two halos each around $M_{200c} \sim 10^{12}, 10^{13}$, and $10^{14}\ h^{-1} M_\odot$, where one is selected from an isolated and one from a more populated environment. The traceback radii at 1, 2, 4, and 10 R_{vir} are shown as circles in Eulerian space. All particles within the circles are traced back to the initial conditions and colored with the color corresponding to the radius. We note that while in isolated environments, the proto-halo patches are compact and do not grow significantly with increasing traceback radius (with the exception of $R_{\mathrm{tb}} = 10 R_{\mathrm{vir}}$), they are less spherical, more scattered, and grow significantly at larger radii in populated regions.

We outline the minimum bounding ellipsoids with the corresponding color. Note that the illustration is only a 2-dimensional slice through the center of the ellipsoid, hence the ellipsoids appear to be a bad fit in some cases since the 3-dimensional structure is not visible. However, we can already see that halos in isolated environments tend to have more efficient ellipsoids, with a higher fraction of particles within the ellipsoid boundaries collapsing into the traceback-radius. In section 5.3, we will measure this correlation between the environment and the efficiency parameter in more detail.

An interesting observation is the generally low increase in ellipsoid size between $R_{\mathrm{tb}} = 1 R_{\mathrm{vir}}$ and $R_{\mathrm{tb}} = 2 R_{\mathrm{vir}}$. This is particularly noticeable in the isolated 10^{13} and $10^{14}\ h^{-1} M_\odot$ examples, where the increase in ellipsoid size is barely visible and most of the added particles from the outer regions of the halo are within the proto-halo at $R_{\mathrm{tb}} = 1 R_{\mathrm{vir}}$. This is due to the splash-back radius, corresponding to the outer caustic that separates the infalling matter from the matter that

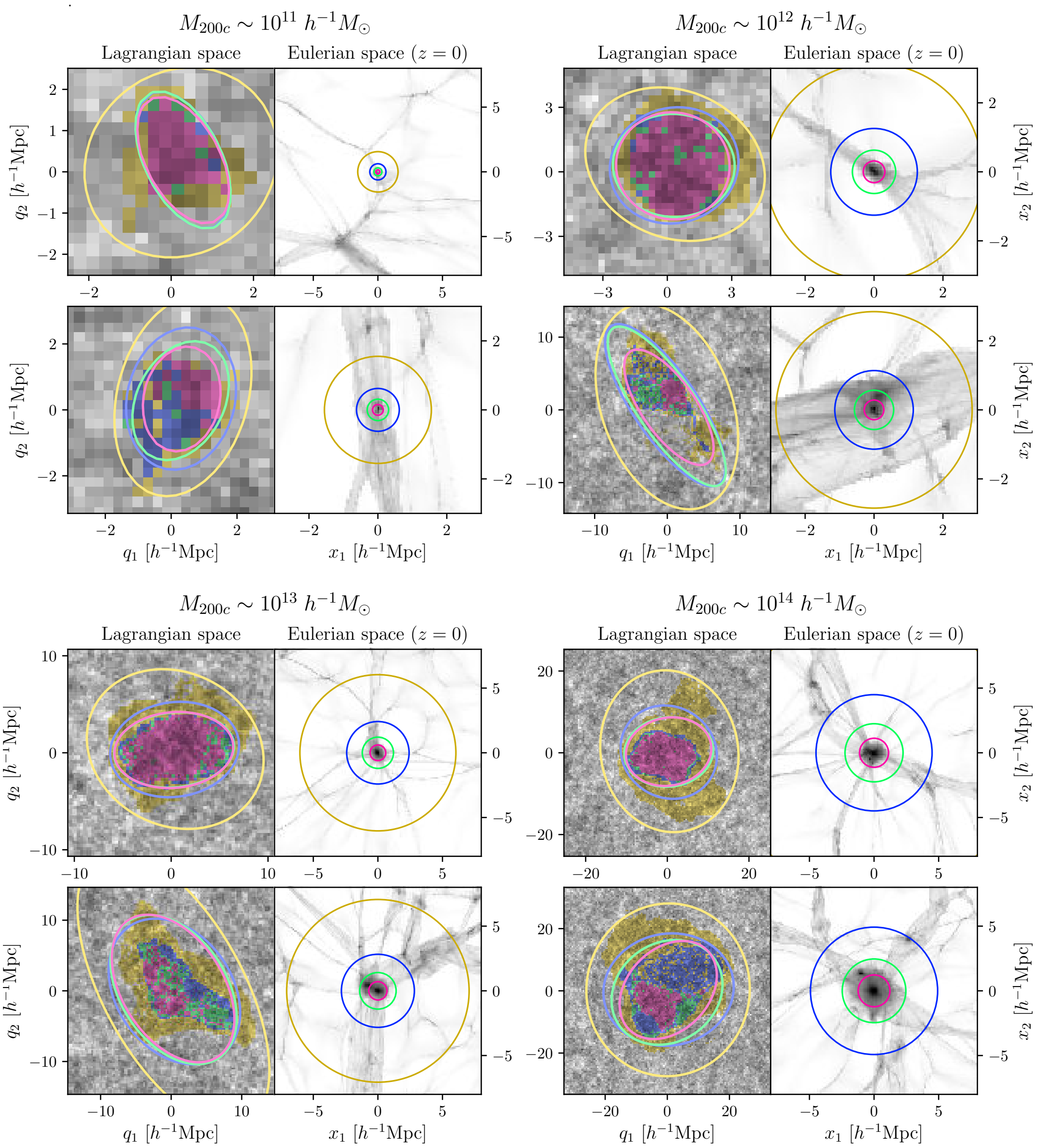

Figure 5.2: Slices through eight halos at redshift $z = 0$ (right side of the panels) and their proto-halo patches (left side). The halos are chosen from the 300MPC simulation around three halo mass values $M_{200c} \sim 10^{11}, 10^{12}, 10^{13}$ and $10^{14}\ h^{-1}M_\odot$ from an isolated environment (top) and more populated regions (bottom). The circles in Eulerian space correspond to traceback-radii of 1 (magenta), 2 (green), 4 (blue), and 10 R_{vir} (yellow) respectively. Particles within R_{tb} are traced back to Lagrangian space and colored correspondingly. The ellipses represent cuts through the minimum bounding ellipsoids and the background shades illustrate the density field (darker corresponds to higher density).

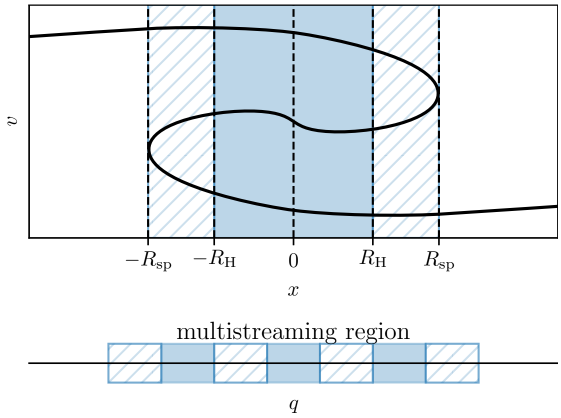

Figure 5.3: 1d illustration of the Lagrangian origin of the matter between the halo radius $R_{\rm H}$ and the splash-back radius $R_{\rm sp}$. The top panel shows the phase-space distribution of a plane-wave collapse (cf. fig. 1.3), with the multistreaming within the halo and splash-back radius highlighted. Note that the Lagrangian origin (the "unwrapped" phase-space spiral) of the region between $R_{\rm H}$ and $R_{\rm sp}$ is partially embedded within regions belonging to the central part of the halo.

has crossed the central halo region at least once [103, 35, 3]. The traceback radius is generally larger than conventional halo radii definitions and roughly between 1 and $2.5R_{\rm vir}$ [228]. The matter between 1 and 2 $R_{\rm vir}$ thus partially originates from the inner part of the proto-halo, which does not affect the minimum bounding ellipsoid. This effect is illustrated for a one-dimensional toy-example in fig. 5.3 and is also discussed in [135].

5.2 Shape distribution of proto-halos

In this section, we look at the statistical distribution of proto-halo ellipticities and prolateness. From peaks-theory, we expect that higher peaks, corresponding to more massive systems, will be more spherical (cf. section 1.4). We will therefore start by measuring the mass dependency of the proto-halo shape. Since halos in clustered environments are subject to stronger tidal fields, we will, in the second part, measure the environmental effect on the proto-halo shapes at fixed mass.

5.2.1 Shape distribution by halo mass

For all halos in the mass bins listed in table 5.1, we compute the ellipticity and prolateness of their associated Lagrangian minimum-bounding ellipsoid according to eq. (5.2). The resulting distributions are shown in fig. 5.4, with contours including 90%, 50%, and 10% of the proto-halo patches. In addition, we summarize the numerical values of the distributions in table 5.2.

We immediately notice that the more massive halos originate indeed from more spherical patches. The ellipticity increases towards lower masses, although there is no significant difference between the smallest two mass bins, most likely due to the smaller logarithmic mass gap

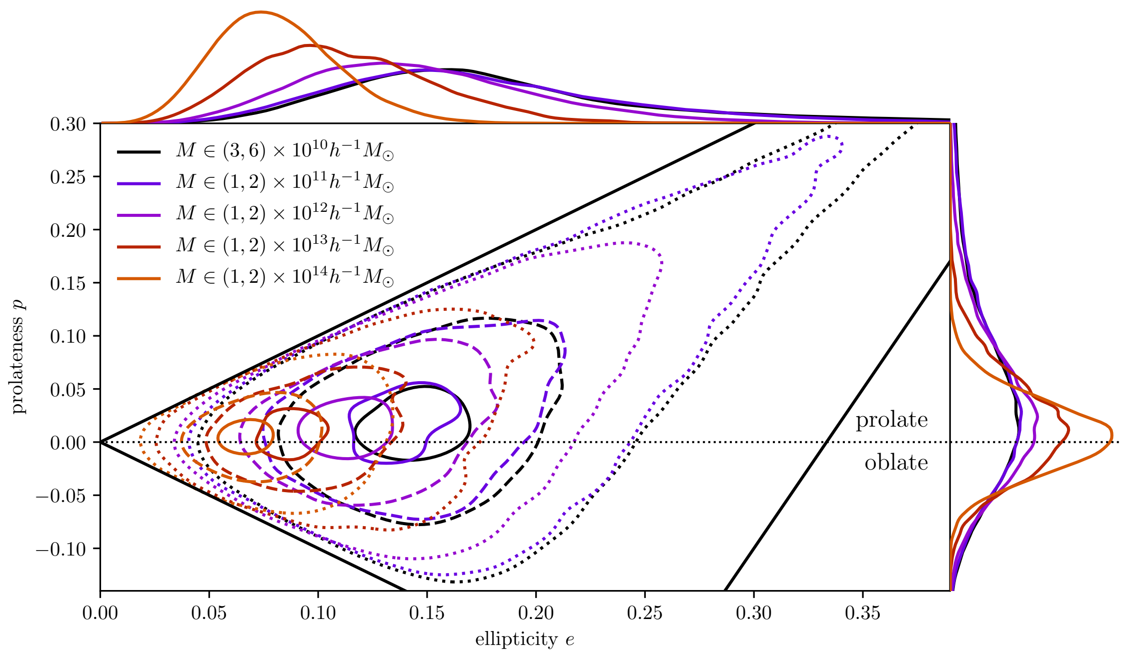

Figure 5.4: Ellipticity – prolateness distribution of proto-halos depending on the halo mass at $z = 0$. The proto-halos have been computed with $R_{\rm tb} = 1 R_{\rm vir}$. The contours include 10, 50, and 90% of the halos in the corresponding mass range. The proto-halos of the lowest two mass bins come from the 150MPC, the middle mass bin from the 300MPC, and the most massive two from the RHAPSODY_NewCosmo simulation.

between them.

The minimum bounding ellipsoids tend to be slightly prolate, especially for lower mass halos. One might expect slightly prolate proto-halos from the theoretical predictions of low mass peak-shapes (cf. fig. 1.7), but we will show below that the density peaks and the proto-halos are generally not aligned. We also note that the minimum bounding ellipsoids tend to be biased towards higher prolateness in comparison with the inertia tensor measurement (cf. fig. 5.1).

5.2.2 Shape distribution by environment

We will now focus on environmental influences on the proto-halo shape. Strong tidal fields will significantly affect the axes along which the initial perturbation can accrete mass, which in turn defines the proto-halo shape (see for example [193, 259, 260, 80, 207]). Tidal fields will be stronger in an already overdense environment (cf. fig. 1.6), and therefore we expect the proto-halo shape to be more distorted (i.e. elliptical) if the halo is in a clustered environment and in the vicinity of a more massive neighbor.

The local cosmICweb database (cf. section 4.5) currently offers two indicators to measure the halo environment: on the one hand, we store the $D_{1,1}$ parameter (see the definition in table 4.2), which measures the distance to the closest, more massive halo, normalized by the virial radius, and on the other hand, we store minimum bounding ellipsoids at 1, 2, 4, and 10 $R_{\rm vir}$ traceback-

mass range $[h^{-1} M_\odot]$	ellipticity $e \pm \sigma_e$	ellipticity 90% interval	prolateness $p \pm \sigma_p$	prolateness 90% interval
$(3,6) \times 10^{10}$	0.1828 ± 0.0002	(0.087, 0.333)	0.0523 ± 0.0003	(-0.081, 0.256)
$(1,2) \times 10^{11}$	0.1750 ± 0.0003	(0.081, 0.304)	0.0486 ± 0.0004	(-0.079, 0.225)
$(1,2) \times 10^{12}$	0.1469 ± 0.0002	(0.069, 0.244)	0.0315 ± 0.0003	(-0.072, 0.159)
$(1,2) \times 10^{13}$	0.1120 ± 0.0005	(0.053, 0.184)	0.0170 ± 0.0006	(-0.058, 0.104)
$(1,2) \times 10^{14}$	0.0809 ± 0.0002	(0.040, 0.130)	0.0070 ± 0.0003	(-0.048, 0.066)

Table 5.2: Mean, standard error of the mean, and 90% intervals of the ellipticity and prolateness distribution of proto-halos in the corresponding mass bin ($R_{\text{tb}} = 1R_{\text{vir}}$). The mass bins and their associated simulations are described in table 5.1.

radii, together with the number of particles that were used in their construction. The number of particles is proportional to the mass within the traceback radii and therefore, we can easily compute the relative mass increase with increasing radius from the halo center. For the following discussion, we use the $D_{1,1}$ parameter and the ratio

$$M_{10,1} \equiv \frac{N_p(R = 10R_{\text{vir}})}{N_p(R = R_{\text{vir}})} = \frac{M(R = 10R_{\text{vir}})}{M(R = R_{\text{vir}})}. \tag{5.6}$$

In fig. 5.5, we show the distribution of $D_{1,1}$ and $M_{10,1}$ for the mass bins described in table 5.1. $D_{1,1}$ tends to be smaller for lower mass halos, meaning that it is more likely for a low mass halo to be in the tidal influence of a more massive neighbor than it is for a high mass halo. The measured $D_{1,1}$ means and standard errors of the means for the mass bins in increasing order are: 9.09 ($\pm$0.02), 8.91 ($\pm$0.03), 9.01 ($\pm$0.03), 9.58 ($\pm$0.08), and 14.00 ($\pm$0.06). On the other hand, the relative mass increase from 1 to 10 traceback-radii peaks at lower values for low mass halos, but is distributed over a wider range than the mass increase of massive halos, meaning that low mass halos live in a larger variety of environments, from fairly isolated to very clustered. The means and standard errors of the means of $M_{10,1}$ for the mass bins in increasing order are: 27.89 ($\pm$0.14), 24.62 ($\pm$0.20), 15.83 ($\pm$0.11), 10.87 ($\pm$0.12), 8.54 ($\pm$0.03). Therefore, even though the distributions peak at lower values, the relative mass increase for low mass halos is on average larger than for massive halos.

To measure the effect of $D_{1,1}$ and $M_{10,1}$ on the ellipticity of the proto-halo, we focus on the $10^{11}\ h^{-1} M_\odot$ mass bin from the 150MPC and the $10^{13}\ h^{-1} M_\odot$ mass bin from the 300MPC simulation. We create subsets of each mass bin by splitting the sample along the 33rd and 67th percentile of the $D_{1,1}$ and $M_{10,1}$ distribution (indicated by vertical lines in fig. 5.5), and taking the lower and upper thirds to increase the contrast between low and high clustering. We show the ellipticity – prolateness distribution of these subsets in the two panels of fig. 5.6.

For both quantities indicating a more clustered environment, i.e. for low $D_{1,1}$ and for high $M_{10,1}$, we can clearly see from both mass bins that the ellipticity of the proto-halos is significantly larger than for isolated halos. The effect on the prolateness distribution is less evident. We list the means and 90% intervals of the measured ellipticities and prolateness in table 5.3.

Both the $D_{1,1}$ and $M_{10,1}$ filters separate the proto-halo ellipticities to a similar degree, indicating that they indeed measure the same property. The selection by $M_{10,1}$ produces a slightly

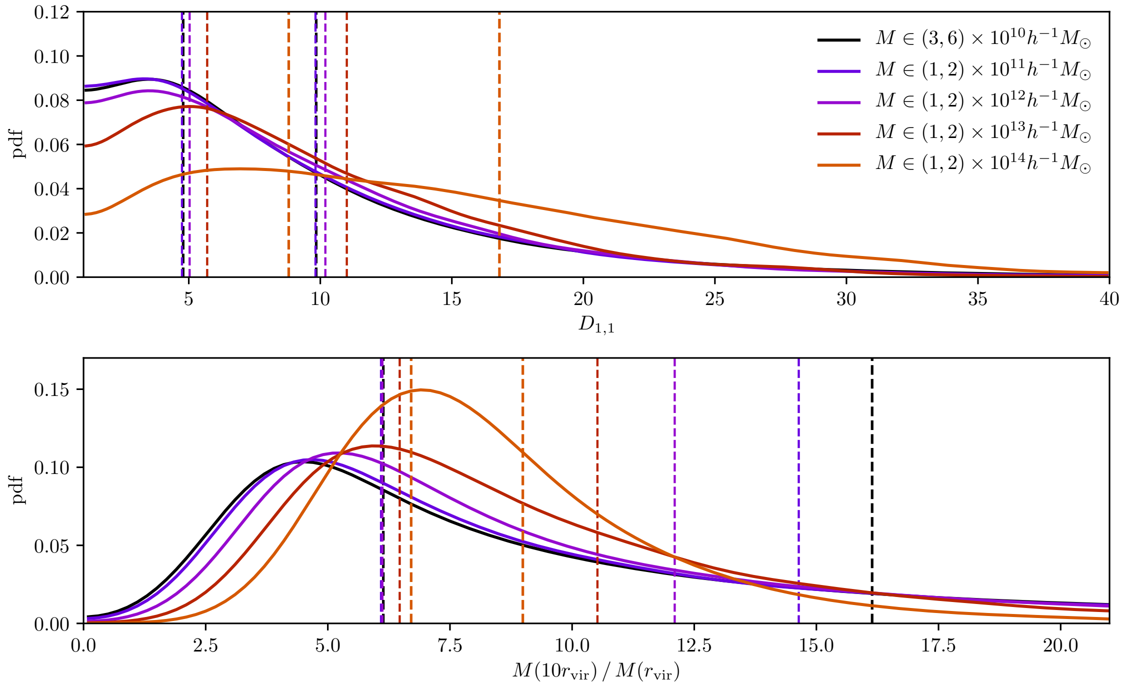

Figure 5.5: Distribution of the environmental parameter $D_{1,1}$ and mass increase between spheres of 1 and 10 R_{vir}, i.e. $M(10r_{\mathrm{vir}})\,/\,M(r_{\mathrm{vir}})$, measured from five different mass bins. The lower two mass bins have been obtained form the 150MPC, the middle bin from the 300MPC, and the upper two from the RHAPSODY_NewCosmo simulations. Horizontal lines show the 33rd and 67th percentile of the distribution, colored with respect to the mass bin.

mass range $[h^{-1} M_\odot]$	subset	ellipticity $e \pm \sigma_e$	ellipticity 90% interval	prolateness $p \pm \sigma_p$	prolateness 90% interval
$(1,2) \times 10^{11}$	$D_{1,1}$ low	0.1819 ± 0.0005	(0.082, 0.306)	0.0504 ± 0.0007	(-0.082, 0.226)
	$D_{1,1}$ high	0.1570 ± 0.0005	(0.075, 0.270)	0.0395 ± 0.0006	(-0.074, 0.189)
	$M_{10,1}$ low	0.1452 ± 0.0004	(0.072, 0.233)	0.0334 ± 0.0005	(-0.069, 0.156)
	$M_{10,1}$ high	0.1967 ± 0.0006	(0.086, 0.330)	0.0599 ± 0.0008	(-0.084, 0.254)
$(1,2) \times 10^{13}$	$D_{1,1}$ low	0.1208 ± 0.0009	(0.058, 0.193)	0.0187 ± 0.0011	(-0.061, 0.111)
	$D_{1,1}$ high	0.0977 ± 0.0007	(0.047, 0.160)	0.0129 ± 0.0009	(-0.052, 0.089)
	$M_{10,1}$ low	0.0960 ± 0.0007	(0.047, 0.155)	0.0124 ± 0.0009	(-0.052, 0.083)
	$M_{10,1}$ high	0.1265 ± 0.0009	(0.061, 0.199)	0.0212 ± 0.0012	(-0.063, 0.118)

Table 5.3: Mean, standard error of mean, and 90% intervals of the ellipticity and prolateness distribution of proto-halos in the corresponding mass bin and the environment subset.

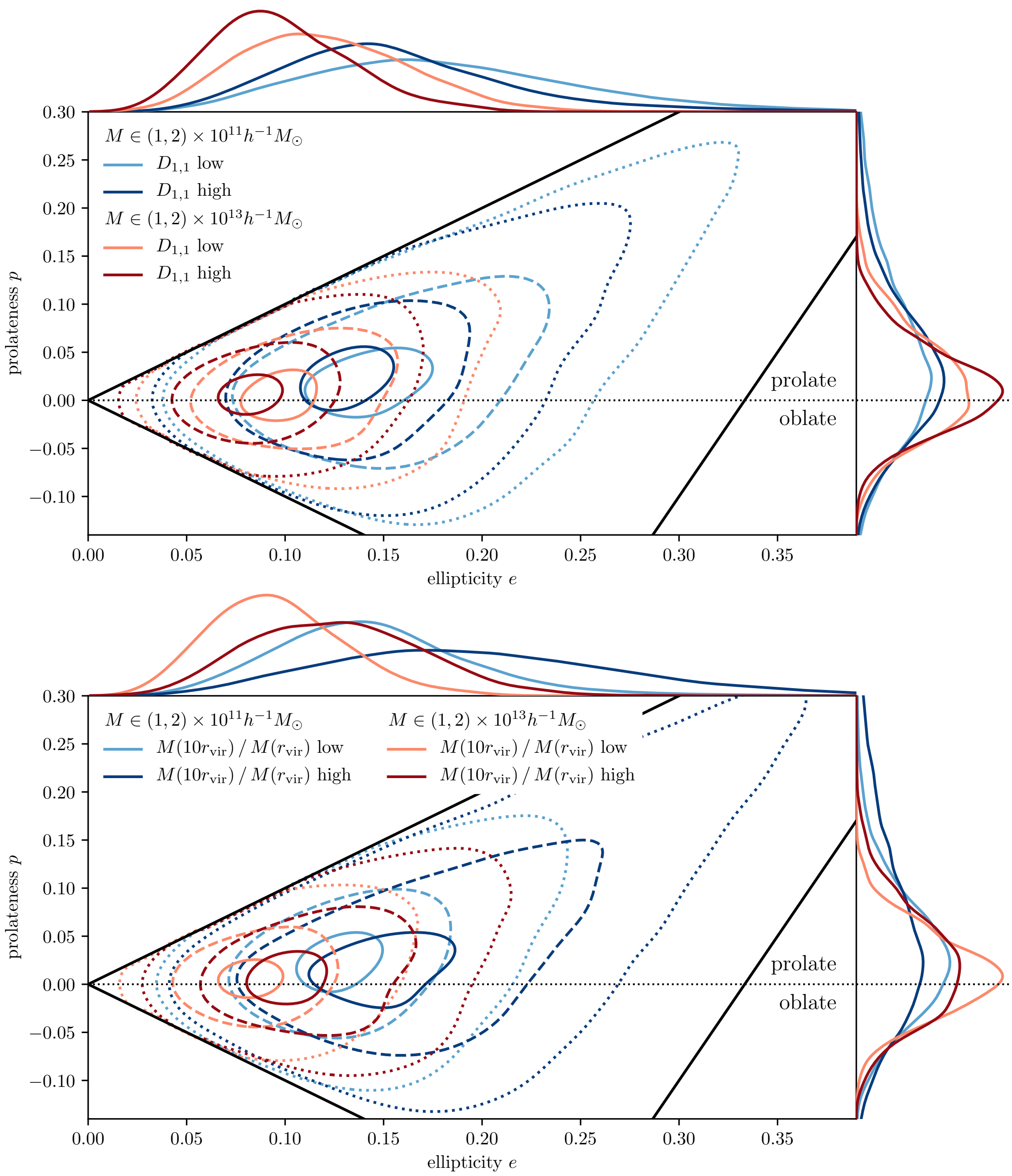

Figure 5.6: Ellipticity – prolateness distribution of proto-halos depending on the environmental parameter $D_{1,1}$ (**top**) and on the mass increase between a sphere of $1R_{\mathrm{vir}}$ and $10R_{\mathrm{vir}}$ of the halo at $z = 0$, $M_{10,1}$ (**bottom**). The distributions show the lower and upper third of the $D_{1,1}$ and $M_{10,1}$ distributions (cf. fig. 5.5), calculated from the 10^{11} and the $10^{13}\ h^{-1} M_{\odot}$ mass bins from the 150MPC and the 300MPC simulation respectively. The contours include 10, 50, and 90% of all halos in the corresponding mass bin.

stronger contrast between the subsets, in particular for the low halo mass bin, and we will therefore use this separation for the following analysis of the alignments of proto-halos with the tidal field and the density peaks.

5.2.3 Tidal field correlation

The ellipsoidal collapse model (cf. section 1.4) assumes that a Lagrangian sphere collapses anisotropically under the initial tidal field. We have seen that the assumption of spherical proto-halo patches is generally not true; the tidal field, however, still plays an important role in the collapse of the proto-halo, determining along which axes the Lagrangian patch is compressed (cf. e.g. [206]). We therefore expect a strong correlation between the direction of the tidal field and the proto-halo shape (also see [207]). Halos in highly clustered environments will additionally be affected by strong non-linear tidal fields at later times.

To measure the correlation between the initial tidal field and the proto-halo shape, we will again focus on the 10^{11} and 10^{13} $h^{-1}M_\odot$ mass bins. Using the initial conditions generator MUSIC, we output the initial density field of the 150MPC and 300MPC simulations and compute the (unnormalized) tidal tensor[1] via Fourier Transforms, i.e.

$$T_{ij} = \begin{cases} \mathcal{F}^{-1}\left(\frac{k_i k_j}{k^2}\tilde{\delta}_R(\boldsymbol{k})\right) & k \neq 0 \\ 0 & \text{else.} \end{cases} \tag{5.7}$$

In addition, we also compute the tidal tensors $T_{R,ij}$ from the density fields δ_R smoothed with a tophat window function of mass $M = 10^{11}$ and 10^{13} $h^{-1}M_\odot$ respectively.

To calculate the tidal field at the ellipsoid position, we use two commonly used methods: we once average the unsmoothed T_{ij} over the cells inside the ellipsoid, and once evaluate $T_{R,ij}$ at the ellipsoid center. We then determine the eigenvalues $\lambda_1 \geq \lambda_2 \geq \lambda_3$ and corresponding eigenvectors at every proto-halo location. Since the eigenvalues of the tidal tensor may be negative, we use the axes ratio λ_3/λ_1 instead of the ellipticity in the following discussion. Similarly, we can calculate the ratio a_3/a_1 of the semi axes $a_1 \geq a_2 \geq a_3$ of the minimum bounding ellipsoids.

The comparison between the ellipticity and orientation of the proto-halos, and the ellipticity and orientation of the tidal field is shown in fig. 5.7. The shape ratios are correlated for all mass bins, subsamples, and tidal field definitions. For a large positive tidal field ratio, i.e. $\lambda_3/\lambda_1 \gg 0$, there is no preferred direction of the tidal forces, and hence the collapse occurs more isotropically and mass can be accreted from all directions. With decreasing ratio, the relative accretion along the third axis becomes less efficient than along the first axis, resulting in an elongated, more elliptical proto-halo (see e.g. [207] for a detailed discussion and a similar measurement using the proto-halo inertia tensor). We note that the correlation is weaker for the high $M_{10,1}$ subset of the low mass bin. This is most likely due to non-linear tidal fields emerging during the collapse of the more clustered environments, erasing some of the “memory” of the halo’s birth place.

This phenomenon can also be seen in the alignment measurements of the proto-halo orientation in the tidal field. While the minor and major axes of the proto-halos in isolated environments are strongly aligned with the minor and major axes of the tidal field, this alignment is lowered for the high $M_{10,1}$ subset of both mass bins, but remains significant.

[1] The tidal tensor is sometimes also denoted as velocity shear tensor, since $T_{ij} \propto \nabla \boldsymbol{u}$.

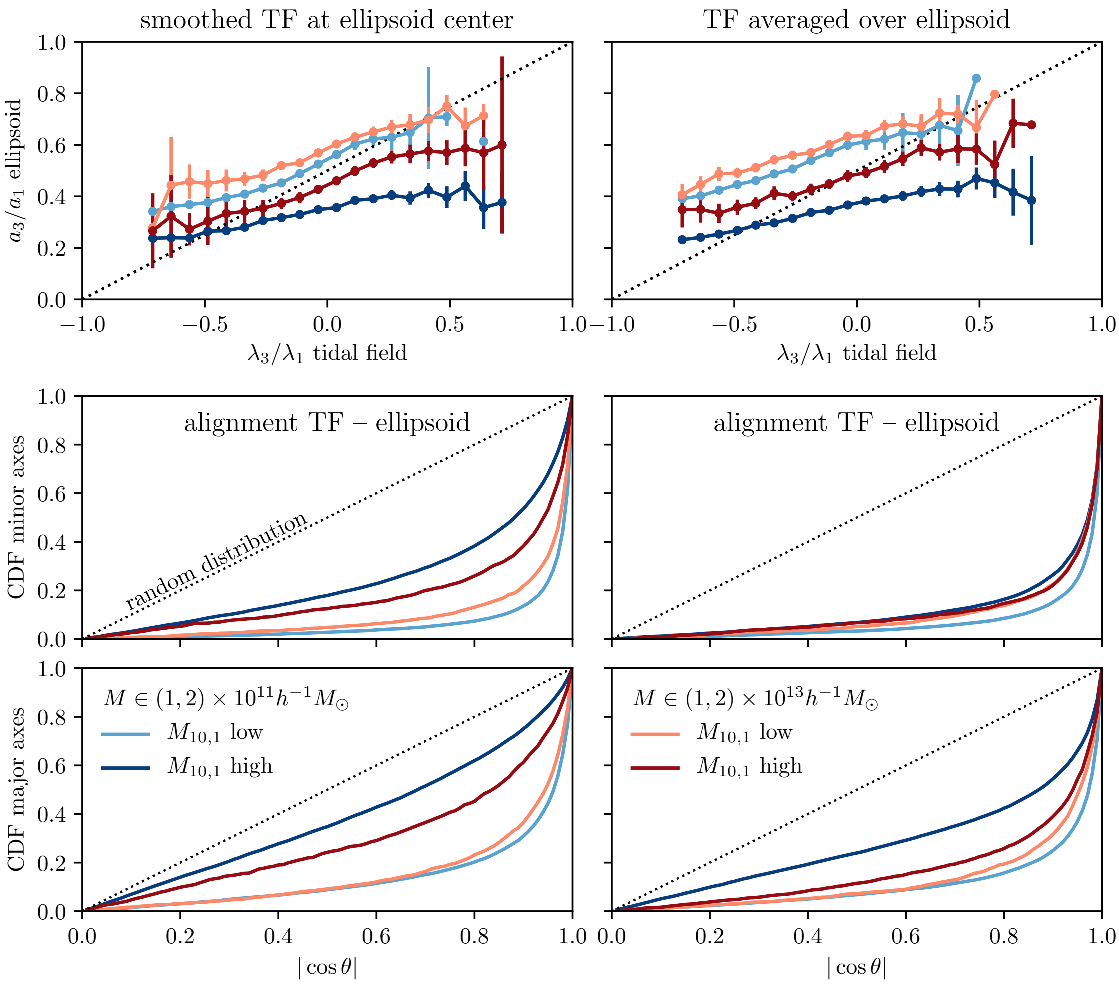

Figure 5.7: Comparison of the initial tidal field with the proto-halo shapes. **Top:** correlation between the tidal field axes ratio λ_3/λ_1 and the ellipsoid semi axes ratio a_3/a_1. The points show the mean ellipsoid shape ratio at fixed tidal field axis ratio, with vertical lines showing the standard error of the mean. **Bottom rows:** Cumulative distribution function of the alignment between the major and minor axes of the tidal field and the minimum bounding ellipsoid. We compare two measurements of the tidal field tensor: computed from the smoothed initial density and evaluated at the center of the ellipsoid (**left**) and computed from the initial density and averaged over the ellipsoid (**right**).

Comparing the two tidal field measurement methods, we observe that the averaging over the unsmoothed tidal field results in stronger alignments than evaluating the smoothed tidal field at the center of the ellipsoid. For future studies, this method is thus to be preferred.

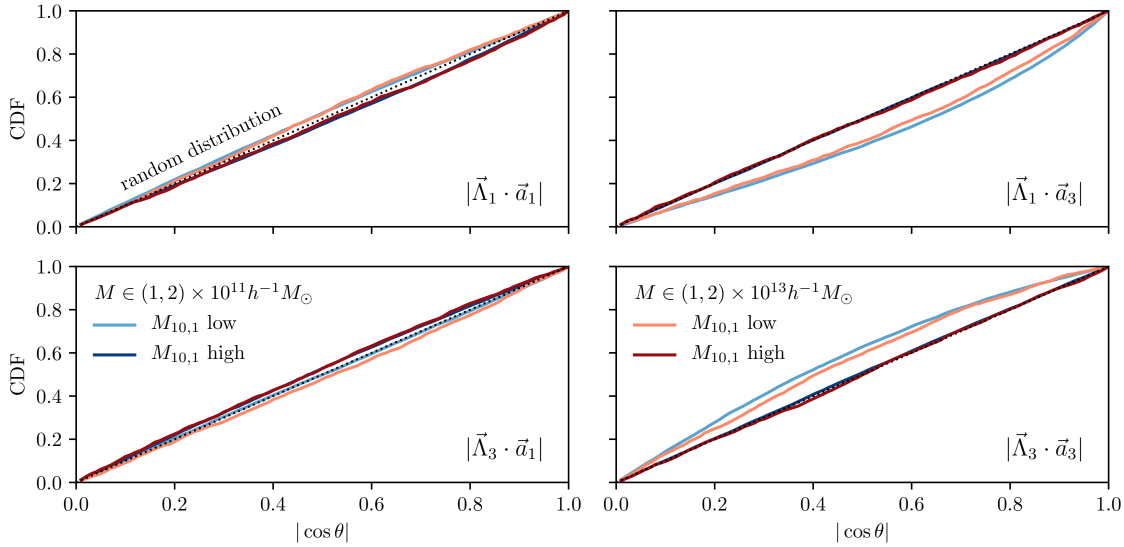

Figure 5.8: Alignment of the density field with the proto-halo shape. The plots show the cumulative distribution function of the alignment between the eigenvectors $\vec{\Lambda}_i$ of the Hessian of the smoothed density field and the major (a_1) and minor (a_3) semi axes of the ellipsoids. Note that on a peak, $\Lambda_i < 0$, and therefore, $\vec{\Lambda}_1$ indicates the shortest axis of the peak and $\vec{\Lambda}_3$ points along the elongated axis of the density peak.

We finish our discussion of the proto-halo shapes by measuring the alignment of the proto-halos with respect to the shapes of the peaks in the initial density field. For this purpose, we evaluate the Hessian H_{ij} of the smoothed δ_R at the ellipsoid centers[2] (cf. eq. (1.94)) and compute the eigenvalues $\Lambda_1 \geq \Lambda_2 \geq \Lambda_3$ and the corresponding eigenvectors $\vec{\Lambda}_i$. At a density peak, defined by its concave shape, all eigenvalues would be 0. We find, however, independently of the method used to determine H_{ij} and the mass samples, that this is only the case for 20% of the sample, but slightly lower (15%) for halos in clustered environments, and higher (25%) for isolated halos.

Figure 5.8 shows the alignments between the eigenvectors of Λ_1 and Λ_3 and the orientation of the proto-halo semi axes a_1 and a_3. For the clustered halo sample, there is almost no alignment between any axes, indicating that the proto-halos are basically randomly oriented with respect to the underlying density field, confirming previous results by Ludlow et al. [207]. However, we measure a slight positive alignment between the eigenvector of Λ_1 and the minor axis of the proto-halos in the isolated sample. This finding suggests that, in the absence of strong tidal forces, the shape of the local initial density field has a small impact on the regions that are accreted into the halo. Overall, however, the tidal field ultimately determines the shape and orientation of the proto-halo.

[2]The results have been verified against the evaluation by averaging the unsmoothed Hessian over the ellipsoid shape, yielding the same alignments.

5.3 Proto-halos for zoom simulations: efficiencies and traceback-radii

When running zoom simulations, one often targets a certain mass range and environment (e.g. cluster re-simulations [137, 21] or simulations of Milky-Way type halos [122]), with the goal of re-simulating a fair sample of halos in that parameter range. We have seen in the previous sections how the mass and environment affects the shape of the proto-halo. In this last section, we will focus on the efficiency parameter of the proto-halo ellipsoids, i.e. how well the minimum bounding ellipsoid described the proto-halo. The efficiency parameter is an important factor in determining how much computational resources are required to simulate the object in high resolution. We recall the definition of the efficiency parameter from eq. (4.1):

$$\mathcal{E} = \frac{M_{\text{particles}}}{M_{\text{ellipsoids}}}, \tag{5.8}$$

i.e. the ratio of the number of particles within the traceback radius of the halo and the number of particles within the minimum bounding ellipsoid. The lower the efficiency, the larger is the fraction of high resolution particles that have to be simulated, but which will not be part of the final halo.

We naturally expect that the more regular the shape of the traced-back particles, the better it will be described by an ellipsoid, and thus the higher the efficiency will be. In the previous section, we have seen that more compact and spherical proto-halos are associated with more massive and more isolated halos, so we expect that these halos will also be the most "efficient" to re-simulate. To determine this efficiency – mass and efficiency – environment correlation, we measure $\mathcal{E}$ at $R_{\text{tb}} = 1$ and $4R_{\text{vir}}$ at $z = 0$ for all halos in the 150MPC, 300MPC and RHAPSODY_NewCosmo simulation, and also at $z = 1$ and $z = 2$ for the 300MPC simulation to study the redshift dependency.

5.3.1 Efficiency distribution by halo mass

We start with the discussion of the efficiency – halo mass relation which is shown in fig. 5.9 for the three simulations at redshift $z = 0$ and at 1 and 4 R_{vir} traceback-radii. We also highlight the mass corresponding to 1000 $N - body$ particles. Above this threshold, the efficiency increases for all simulations, in agreement with the measurements in [239]. At the low mass end ($M_{vir} \sim 100m_p$, where m_p is the N-body particle mass), most of the ellipsoids have converged due to the low number of particles that are used to compute the ellipsoid, which can be seen by the substantial drop in efficiency.

For the $R_{\text{tb}} = 1R_{\text{vir}}$ ellipsoids, we observe an upturn in the efficiency between these lowest masses and the 1000 particle threshold. We suspect that this upturn is most likely due to a surface effect of the ellipsoid and may highlight an issue with our minimum bounding ellipsoid computation. To fit the minimum bounding ellipsoid to the Lagrangian particles, we use their Lagrangian coordinates, i.e. the center of the cells. On the surface of the ellipsoid, the optimized minimum bounding ellipsoid will therefore cut through cells belonging to particles within the traceback

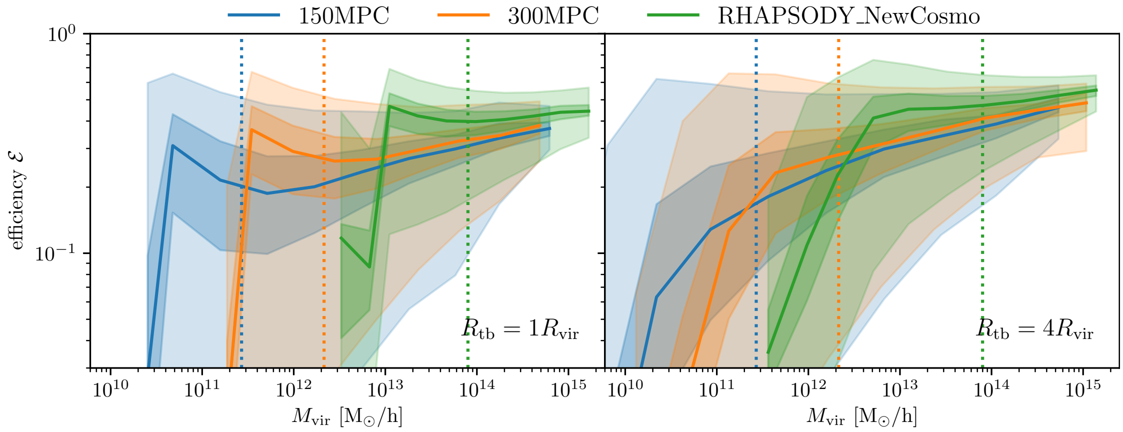

Figure 5.9: Efficiency of the Lagrangian minimum bounding ellipsoids as a function of the halo mass $M_{\rm vir}$. Shown is the median efficiency and the 66% and 90% contours. The minimal bounding ellipsoids are computed from particles within $R_{\rm tb} = 1$ and $4R_{\rm vir}$ of free halos in the 150MPC, 300MPC and the RHAPSODY_NewCosmo simulation at redshift $z = 0$. The dashed vertical lines show the mass of 1000 particles for estimating the convergence threshold.

radius. As a consequence, the ellipsoid volume and therefore mass decreases, and the apparent efficiency increases, as the ellipsoid does not contain the full Lagrangian volume associated with the traceback-radius (in theory, $\mathcal{E} > 1$ would be possible, but has not been observed in our database). With increasing halo mass, the number of particles within the traceback radius grows and the surface-to-volume fraction decreases, hence the effect becomes less apparent. However, we consider this to be a bug in the computation which will need to be addressed in future versions of cosmICweb, either by artificially upscaling the size of the ellipsoids by half a cell size in all directions, or by recomputing the ellipsoids and requiring that the entire Lagrangian cells are contained instead of only the centers.

When considering halos at different redshifts, objects of different mass occupy the nodes of the cosmic web where they can accrete surrounding mass relatively isotropically. Objects which are affected by massive neighbors must by definition be of smaller mass. We therefore expect the ellipsoid efficiency to strongly depend on cosmic time at fixed mass. To first order, this evolving mass scale is encoded in the peak height $\nu(M, z) = \delta_c/\sigma(M, z)$ (cf. section 1.4) of a perturbation. Specifically, one defines the non-linear mass as $\nu(M_{\rm NL}, z) = 1$ (cf. eq. (1.104)). Expressed in units of the non-linear mass, the HMF becomes (almost) universal (cf. e.g. [170, 97, 314]). Similarly, factoring out the growth of $M_{\rm NL}$ removes the evolution of the patch efficiency as shown in fig. 5.10 (with the exception of the increase and drop in measured efficiencies at low particle numbers that is present at all redshifts).

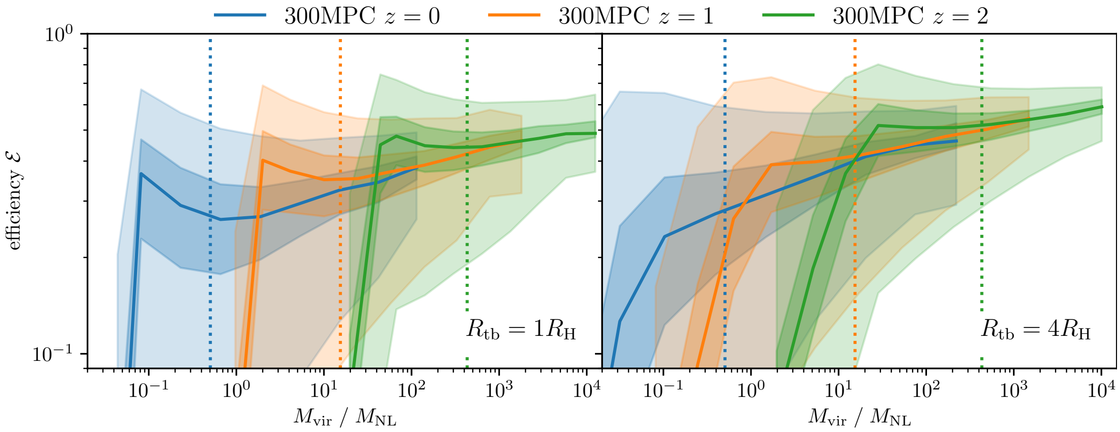

Figure 5.10: Efficiency of the Lagrangian minimum bounding ellipsoids of the 300MPC simulation at redshift $z = 0, 1$, and 2 as a function of the halo mass $M_{\rm vir}$ normalized by the non-linear mass $M_{\rm NL}$ (cf. eq. (1.104))

5.3.2 Efficiency distribution by secondary parameters

To investigate the influence of further parameters on the ellipsoid efficiency, we select halos from the five mass bins in table 5.1 and measure the distribution of efficiencies depending on the closest more-massive halo distance $D_{1,1}$, the mass increase ratio between 1 and $10R_{\rm vir}$ $M_{10,1}$, the proto-halo ellipticity $e_{\rm ellipsoid}$, the spin parameter $\lambda_{\rm Peebles}$, the concentration parameter $c_{\rm vir}$, and the redshift of the last major merger (defined with a minimum mass-ratio of 1:3) $z_{\rm last\_mm}$. While the first three parameters are a direct or strongly correlated measure of the environment (cf. previous section) and we therefore expect a strong correlation with the efficiency parameter, the other three parameters are at most connected to the environment via secondary effects.

Figure 5.11 visualizes the measured correlations between the six selected parameters and the efficiency at 1 and $4R_{\rm vir}$ traceback-radii. Additionally, we also show the distribution of the property for each mass bin to indicate in which parameter range we expect most halos. As expected, the three environmental parameters have the strongest influence on the efficiency of the proto-halo, with halos in clustered environments ($\Leftrightarrow$ low $D_{1,1}$ $\Leftrightarrow$ high $M_{10,1}$ $\Leftrightarrow$ high ellipticity) having a lower efficiency ($\mathcal{E} \sim 0.1 - 0.2$) on average than isolated halos ($\mathcal{E} \sim 0.4 - 0.6$). Since most halos, in particular low mass halos, live in rather clustered regions of the universe, selecting a re-simulation target by high efficiency will therefore create a strongly biased sample towards isolated halos. We note that this result is partially in tension with the results of Oñorbe et al. [239], detecting only a “mild correlation” between the Lagrangian volume and the environment.

The remaining three parameters show less correlation with the efficiency parameter. We can observe a weak trend to lower efficiencies with increasing spin parameter and decreasing concentration parameter, which is most likely related to the environmental correlation of these parameters. There is no visible dependence of the efficiency parameter on the time since the last major merger with the exception of the lowest mass bin. Perhaps a bit counter-intuitively, the efficiency drops significantly for low mass halos for which the last major merger event occurred

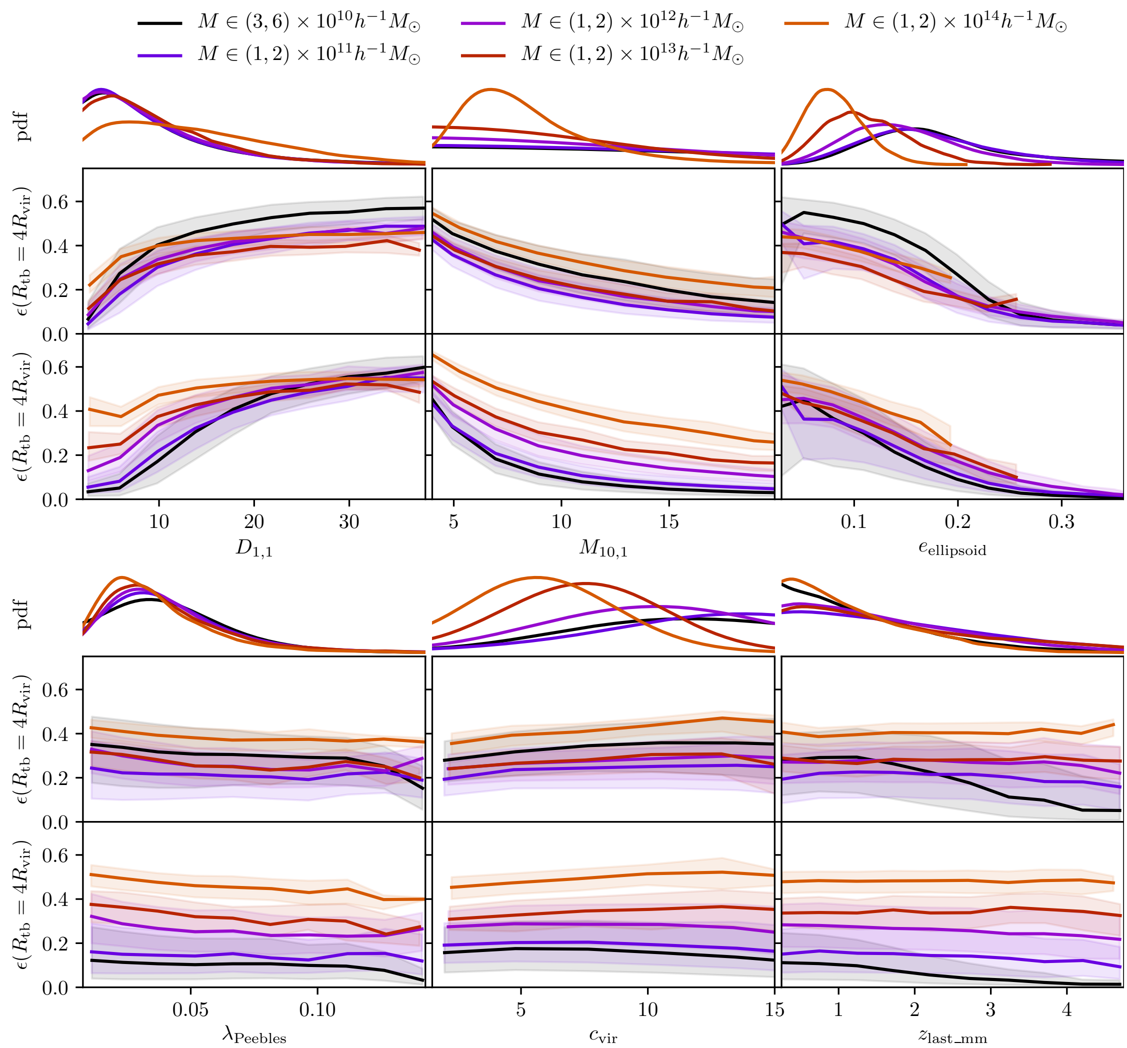

Figure 5.11: Efficiency of the Lagrangian minimum bounding ellipsoids as a function of the environmental parameters $D_{1,1}$, $M_{10,1}$, and the ellipticity $e_{\text{ellipsoid}}$, as well as the halo spin λ_{Peebles}, concentration c_{vir}, and redshift of the last major merger $z_{\text{last\_mm}}$. The plots show the median of the efficiency at 1 and 4 traceback-radii for the mass bins detailed in table 5.1. Shaded regions include 66% of the halos at the given parameter value. The top panels show the (normalized) distributions of the parameter for a each mass bin.

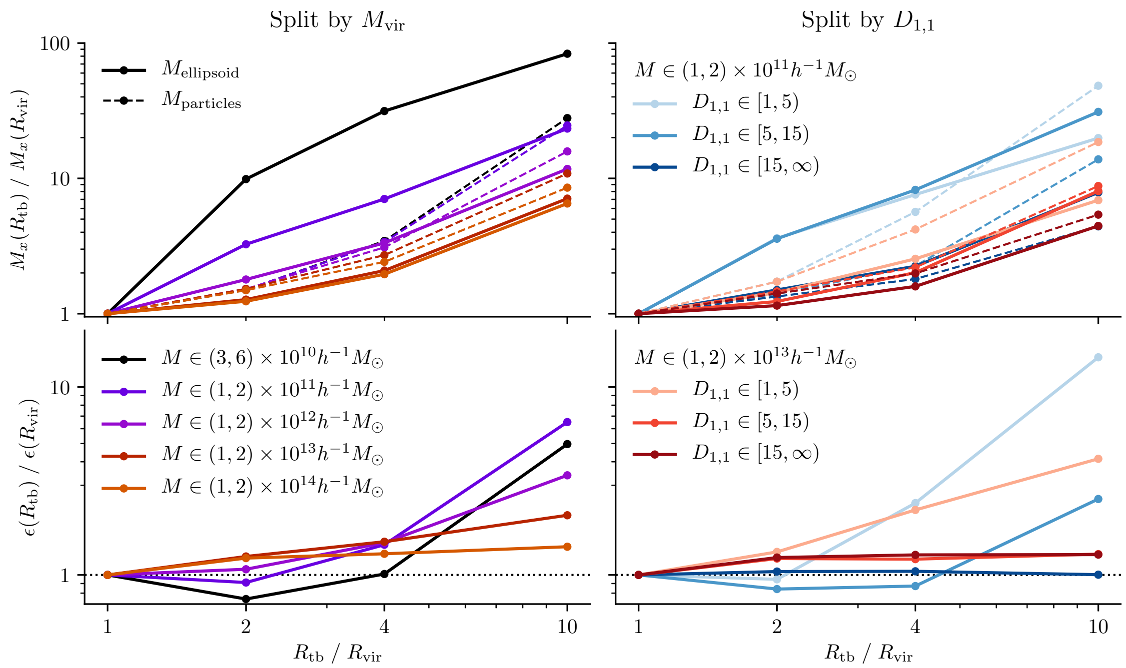

Figure 5.12: Relative change of mass of Lagrangian proto-halo patches (top) and the efficiency parameter (bottom) with increasing R_{tb} for halos in the mass bins detailed in table 5.1. For the mass increase, we plot the change in $M_{\mathrm{ellipsoid}}$ (dashed) and $M_{\mathrm{particles}}$ (solid) separately. In addition, we subdivide two mass bins according to the environmental parameter $D_{1,1}$, shown on the right.

at early times compared to low mass halos that had a more recent major merger. In previous studies, it has been shown that such halos with early last major merger are associated with regions of strong tidal fields which suppress mergers at later times [140, 29]. These halos may effectively be satellites of a host halo, but outside its virial radius and thus not counted as subhalos [119]. The strong tidal field influences the mass assembly (which in the most extreme cases includes mass loss) and thus leads to less regular proto-halo shapes, reflected in low efficiencies of the minimum bounding ellipsoid.

5.3.3 Mass increase and efficiency change with increasing traceback-radius

When running zoom simulations, one has to be aware of potential contamination of the target object with lower mass particles. It has been shown that such contamination will bias properties of the target significantly, e.g. by lowering the baryon fraction in the halo and causing artificial fragmentation of the gas [239]. To avoid contamination, a larger traceback-radius can be chosen. However, a larger traceback-radius will increase the volume of the minimal bounding ellipsoid, and therefore require more computational resources. The exact growth of the Lagrangian ellipsoid naturally depends on the environment of the halo: in a clustered environment, more mass will fall within the larger traceback-radii than for an isolated halo.

In order to measure the growth of the Lagrangian volume depending on the halo mass and environment, we compute the relative mass increase between 1, 2, 4, and $10R_{\mathrm{vir}}$ traceback-radii for the traceback-mass (i.e. the number of particles contained within R_{tb}) as well as the volume of the minimum bounding ellipsoids. We use the mass bins detailed in table 5.1 and subdivide the 10^{11} and 10^{13} $h^{-1}M_{\odot}$ bins into three subsets depending on the normalized distance to the closest more massive halo $D_{1,1}$.

The results are shown in the top panels of fig. 5.12. As expected, both the particles within R_{tb} and the volume of the minimal bounding ellipsoid increase faster for lower-mass halos and halos in more clustered environments. For halos in the lowest mass bin for example, the volume of the minimum bounding ellipsoid is on average more than ten times larger at $R_{\mathrm{tb}} = 2R_{\mathrm{vir}}$ compared to $1R_{\mathrm{vir}}$, whereas the ellipsoid volumes of the most massive halos in our sample only increase by a factor of 1.24 on average. We also note that for low mass halos and halos in clustered environments, the ellipsoid mass grows faster than the traceback mass between 1 and 2 R_{vir}. For these halos, it is very likely that neighboring halos contribute to the number of particles within a large R_{tb}, causing irregular proto-halo patches which lower the efficiency parameter and increase the volume of the ellipsoid fit. For isolated halos and massive halos dominating their surrounding on the other hand, the growth of the traceback-mass and the minimum bounding ellipsoid with increasing R_{tb} is lower and more regular.

This effect can also be seen from the average change in efficiency, shown in the lower panels of fig. 5.12. For halos in the lowest mass bin, the efficiency drops by $\sim 25\%$ from 1 to 2 R_{vir} traceback-radii. Only at larger R_{tb}, the efficiency increases significantly; however, so does the contained mass and therefore computational cost. For massive halos and halos in isolated environments, we measure a small increase of the efficiency with increasing traceback-radius. Note however, that the “base” efficiency of these halos is already higher than for less massive halos (cf. fig. 5.9 and fig. 5.11).

We conclude that for massive and isolated objects, the traceback-radius can be increased without a large penalty in computational cost. For halos in a dense and clustered environment, the high resolution volume increases more rapidly; however, this is to be expected, as the environment plays a more dominant role during the evolution of these objects than for isolated halos. With the exception of the lowest mass bin at $R_{\mathrm{tb}} = 2R_{\mathrm{vir}}$, the minimum bounding ellipsoids tend to provide a better fit to the proto-halos at larger traceback-radii, as can be seen by the increase of efficiency.

5.4 Conclusions

In this chapter, we took a first look at the proto-halo data contained in the cosmICweb database. Unlike previous studies of proto-halo shapes that use inertia tensors to infer ellipticity, prolateness, and orientation of the proto-halo (e.g. [259, 260, 135, 207, 46]), our database contains minimum bounding ellipsoids. We therefore first compared the shape and orientation measurements according to the inertia tensor, the reduced inertia tensor, and the minimum bounding ellipsoid descriptions, and we found good agreement between the various methods. However, to compare numerical values between the studies, one would have to take into account the discrepancies between the methods, e.g. the minimum bounding ellipsoid overestimates low and underestimates high ellipticities and is less sensitive to oblateness / prolateness compared to inertia tensors.

Visualizing the proto-halo and minimum bounding ellipsoids of six selected halos from the 300MPC simulation, we saw that halos in clustered environments tend to have less regularly shaped proto-halos and their bounding ellipsoids tend to be less spherical and less efficient, i.e. providing a worse fit than proto-halos of isolated halos.

We verified this observation by analyzing halos and their proto-halos from five mass bins between 3×10^{10} to 2×10^{15} $h^{-1} M_{\odot}$, taken from the 150MPC, the 300MPC, and the RHAPSODY_NewCosmo simulation of the COSMICWEB database. Our results mainly agree with previous studies [206, 207] and can be summarized as follows:

- more massive halos have on average a more spherical proto-halo shape, whereas proto-halos of low mass halos tend to be more elliptical and slightly prolate;
- however, triaxiality remains important throughout all tested mass-scales, invalidating the simple assumption of an initially spherical Lagrangian volume in the ellipsoidal collapse model (cf. section 1.4), and therefore predicting halo collapse requires a more sophisticated description;
- proto-halos of isolated halos are on average more spherical than the ones of halos in clustered environments;
- the proto-halos align mainly with the tidal field (the velocity shear) in the initial conditions, with the strongest compression along the major axis of the ellipsoid, and the lowest compression, or even expansion, along the minor semi axis. The alignment is stronger for proto-halos in isolated environments, hinting to non-linear effects erasing the "memory" of the initial condition in clustered environments;
- the proto-halos are almost randomly oriented with respect to the local density peaks. Only for the most isolated halos, we could measure a small alignment between peak shape and proto-halo shape.

We then shifted our focus towards the *efficiency* of the proto-halos, an important measure of the feasibility of the minimum bounding ellipsoid as a zoom-region for simulations. In agreement with [239], we found that proto-halos of more massive halos statistically have a higher efficiency and are thus better captured by an ellipsoid than proto-halos of lower masses. However, we found a strong correlation between the efficiency and the sphericity of the proto-halo shape as well as environmental parameters, indicating that the higher efficiency of more massive proto-halos is mainly due to their more compact, spherical shape that is less distorted by the tidal-field and non-linear interactions in clustered environments.

The strong correlation between the efficiency and environment calls for attention when selecting targets for zoom simulations, in particular for low mass halos. When requiring a high efficiency, desirable for high resolution simulation, one will be mainly selecting halos biased towards high isolation, which may not be representative of typical halos in that mass range. We also investigated correlations with additional halo parameters, and only found a weak relation between higher efficiency, lower spin parameter, and higher concentration.

For zoom simulations, one may prefer proto-halos at larger traceback radius to prevent contamination of the halo interior through lower mass particles. We saw that the increase in computational cost is low for high-mass and isolated halos, but becomes significant for low mass halos and halos in clustered environments, which is expected since the environment plays a more dominant role during the evolution of these halos. We also observed that with increasing traceback-radius, the minimum bounding ellipsoids provide a better fit to the proto-halos, and thus lead to a higher efficiency of these ellipsoids.

5.5 Outlook

This chapter provided merely a first glance at the proto-halo data contained in COSMICWEB. The large datasets will allow for more detailed studies of correlations between properties of the evolved halos and their place of origin. In our brief overview, we have only used halos at $z = 0$, but the availability of full merger trees with associated Lagrangian volume for each halo in this tree will allow us to study the evolution of the proto-halo patch as the halo accretes mass and merges with neighboring halos. Such measurements, if compared to different models and predictions of halo formation (e.g. [43, 135, 206, 145]), will hopefully be able to help our understanding of where and how structure forms from the initial perturbations.

Future large scale surveys require extensive sets of mock catalogs with varying cosmological parameters in order to estimate covariances, study systematics, and test data pipelines. However, the number of simulations required to generate these mocks becomes prohibitively large for full N-body simulations, and therefore, many approximate, accelerated methods have and are being developed [223]. These accelerated methods include *abridged particle-mesh methods* such as COLA [310, 160, 168] and FastPM [101], *generative methods* using trained neural networks (e.g. generative adversarial networks) to create new catalog realizations (e.g. [274, 273]), and *predictive methods*, which implement physical or machine learned models of gravitational collapse to find halos in the initial density field, which then can be moved to their final location using Lagrangian perturbation theory. This last category includes for example excursion sets and peak-patch methods [43, 303, 320], PINOCCHIO [225, 222], and the neural network code HALONET [33].

The large and detailed COSMICWEB datasets present an ideal testing and training ground to develop and improve such mock catalog generators. In particular, with the rising prevalence of machine learning techniques in cosmology, it would certainly be an interesting application to consider.

CHAPTER 6

Concluding remarks

Numerical simulations play an important role in cosmology by allowing us to connect theoretical models to observations, which in turn allows us to constrain parameters and to refine or reject models. Simulations also enable us to closely follow non-linear processes and study the mechanics behind the formation and evolution of halos and galaxies, and thus improve our understanding of the Universe. It is therefore crucial to further develop and improve numerical methods in order to keep up with the availability of larger and more accurate observational studies and to tackle current challenges in cosmology.

In this thesis, we focused on the connection between the initial perturbation field and the formed structures in N-body simulations by following the simulation particles during the evolution of the Universe. We used this *Lagrangian map* to reconstruct the continuous phase-space distribution of dark matter, allowing us to accurately measure the local velocity distribution function, and to determine the regions of origin which collapse to gravitationally bound dark matter halos. These regions, the proto-halos, are on the one hand an important ingredient for zoom simulations and on the other hand allow us to study correlations between the initial conditions, the properties of the final halos, and the tidal forces of the large scale environment.

In chapter 3, we used the tessellation method ([1, 285], section 2.3) to reconstruct the dark matter phase-space sheet which allowed us to accurately measure the velocity dispersion tensor field in the cosmic web. In the CDM paradigm, velocity dispersion vanishes per definition in the single-stream regime and emerges in collapsed structures where shell-crossing has occurred, carrying the anisotropic signature of collapse in its tensorial components. Using this property, we introduced a new cosmic web classification method based on the progress of the collapse along the three axes. We studied various aspects of the magnitude and the anisotropy of the velocity dispersion field in detail, such as their density dependence, spatial correlations, and alignments. Furthermore, we found a remarkable agreement between the DM velocity dispersion and the random motions in the shock-heated baryonic gas, opening an interesting research field for future studies.

In chapter 4, we presented COSMICWEB, a web application that aims to improve the zoom simulation workflow by providing a uniform interface to halo catalogs and merger trees from existing simulations, by allowing to download initial conditions refined on these halos, and by enabling users to easily reference these initial conditions in publications. The possibility to generate zoom initial conditions for halos from existing large and detailed datasets simplifies the creation of zoom simulations of objects that are well-suited for various research requirements. Furthermore, COSMICWEB provides the capabilities to easily batch-process a collection of zoom simulations, for example to run a statistical analysis on a number of halos from a certain parameter space, and the ability to access the zoom initial conditions from published articles allows to easily reproduce results and compare different codes and subgrid implementations.

In chapter 5, we studied the proto-halos computed for the COSMICWEB project, in particular the correlations between the shapes of the minimum bounding ellipsoids, the intrinsic properties of the formed halos, and their large-scale environment. We confirmed previous results that the tidal forces from the large scale environment play a significant role in determining the region that collapses to a halo. Furthermore, we verified the agreement of the minimum bounding ellipsoid shape with the inertia tensor, and we measured a strong correlation of the efficiency, i.e. the "goodness of fit" of the minimum bounding ellipsoid, with the halo mass and the environment. The environmental dependency of the proto-halo efficiency has to be taken into account when selecting targets for optimized zoom initial conditions, as considering high-efficiency proto-halos only will bias the selection to isolated halos.

Outlook

Each of the three main projects presented in this thesis provides many interesting and promising possibilities for future scientific studies. We have laid out several opportunities at the end of each chapter, and work on some of these projects has already been started.

Machine learning is becoming a more and more widely used technique in astrophysics and in cosmology in particular, covering a large variety of applications (see e.g. [55] for an overview of machine learning across physical sciences). Machine learning methods applied to and range from classifying strong lens systems [191], estimating photometric redshifts [45, 194] and cluster masses [235, 236, 234, 153], predicting cosmological parameters from the DM density fields [270]. Another category of applications focuses on creating mock observations for estimating covariances, testing pipelines, and studying systematic effects in observational surveys. The requirement of large quantities of test data can make N-body simulations and in particular full hydrodynamic simulations unfeasible, and accelerated, more approximate methods have to be used, such as "deep learning" models trained on the accurate models (full simulations). Applications of these generative models include enhancing DM-only simulations by "painting" baryonic features such as galaxies [345] and Sunyaev-Zel'dovich effect mock observations [315], predicting the non-linear particle evolution [145], creating halo mock catalogs from a linear density field [205, 204, 33], and generating new realizations of the large scale structure entirely [274].

Many of these applications are still in their infancy and sometimes merely a proof-of-concept. Substantial research efforts will be required to develop them into powerful and accurate tools in the future. In that regard, the projects presented in this thesis have great potential to be continued with a focus on machine learning, and to contribute to the ongoing effort in developing accurate mock observables using fast generative models.

On the one hand, the agreement between the DM velocity dispersion and the random motions in the baryonic gas measured in chapter 3 can be used to enhance DM-only simulations with baryonic features, specifically gas densities and temperatures in the intergalactic medium, and improve existing methods such as LYMAS [246] that predict Ly-α statistics from DM simulations. In fig. 3.15, we observed spatial differences between the DM velocity dispersion field and the baryonic temperature field, such as the larger extent of shock-heated regions compared to the

DM multistreaming environments. Convolutional networks would be the ideal tools to learn such discrepancies and accurately "paint" the baryonic properties onto the DM density and velocity distribution field.

On the other hand, the large number of proto-halos and associated merger trees from various different simulations in the COSMICWEB project present an ideal training ground for algorithms to learn i) predicting halo properties and entire merger trees from an initial proto-halo patch and its environment, and ii) identifying regions in the initial conditions that will collapse at a given time. Such machine learning algorithms could extend the currently available methods (e.g. [43, 303]), with less focus on physical processes and theoretical understanding, but fast and accurate predictions required for generating mock catalogs for upcoming surveys and instruments such as DESI [79], SKA [302], LSST [167], Euclid [192], WFIRST [299], and SPHEREx [86]. A further challenging but very rewarding task lies in inverting this problem and generate the proto-halo patch and environment of a halo, given certain constraints on intrinsic and external properties. This would allow creating constrained simulations of any kind of object or group of objects, such as the local Universe.

APPENDIX A

Appendix

A.1 Relativistic Perturbation Theory

In the early Universe and on large scales, we can treat the inhomogeneities as perturbations of the smooth FLRW background $\bar{g}_{\mu\nu}$ and write

$$g_{\mu\nu} = \bar{g}_{\mu\nu} + h_{\mu\nu}, \tag{A.1}$$

where $|h_{\mu\nu}| \ll g_{\mu\nu}$ is a symmetric 4-tensor. Due to gauge-freedom under the infinitesimal coordinate transformation $x^\mu \to \tilde{x}^\mu = x^\mu + \xi^\mu(x)$, only 6 of the 10 independent parameters of $h_{\mu\nu}$ are physical [221]. A choice of gauge has thus to be made, fixing 4 degrees of freedom.

We can decompose $h_{\mu\nu}$ in so-called *scalar-, vector- and tensor-perturbations* by writing

$$h_{00} = -E \tag{A.2}$$

$$h_{i0} = a\left[\frac{\partial F}{\partial x^i} + G_i\right] \tag{A.3}$$

$$h_{ij} = a^2\left[A\delta_{ij} + \frac{\partial B}{\partial x^i \partial x^j} + \frac{\partial C_i}{\partial x^j} + \frac{\partial C_j}{\partial x^i} + D_{ij}\right], \tag{A.4}$$

where A, B, E, F are scalars, C_i and G_i are divergence-less vector fields and D_{ij} is a traceless, symmetric and divergence-less tensor field. These different modes correspond to different physical phenomena: the gravitational potential (scalar mode), gravito-magnetism (vector mode) and gravitational radiation (tensor mode) (see e.g. [221]). In the linear regime, they are completely decoupled and evolve independently. It can be shown that the vector perturbations decay as the Universe expands while the tensor perturbations mainly play a role in the CMB polarization and would be an important probe to constrain inflation if detected [325].

In the following, we will be considering scalar modes only. Due to gauge-freedom, we can choose a coordinate system in which $B = F = 0$. Choosing $A = 2\Phi$ and $E = 2\Psi$, we recover the common notation of the Newtonian gauge in which the full metric becomes

$$g_{\mu\nu} = \begin{pmatrix} -1 - 2\Psi & \\ & a^2\delta_{ij}(1 + 2\Phi) \end{pmatrix}. \tag{A.5}$$

The Newtonian gauge has the advantage that it can easily be related to the Newtonian limit of gravity.

Analogously, we also perturb the stress-energy tensor $T_{\mu\nu} = \bar{T}_{\mu\nu} + \delta T_{\mu\nu}$. For photons, we parametrize the temperature inhomogeneities as $T = \bar{T}(t)(1+\Theta(\boldsymbol{x}, \hat{\boldsymbol{p}}, t))$ and label n-th multipole of Θ as Θ_n. Analogously for neutrinos, where we name the perturbations $\mathcal{N}$. For CDM, we write density perturbations as $\rho = \bar{\rho}(t)(1+\delta(\boldsymbol{x}, t))$ and peculiar velocities as $v(\boldsymbol{x}, t)$ and ignore all higher order moments due to the coldness of CDM[1] Similarly to CDM, the baryonic inhomogeneities can be parametrized by $\delta_b(\boldsymbol{x}, \boldsymbol{t})$ and $v_b(\boldsymbol{x}, t)$

To study the evolution of the perturbed metric and energy density, we can split the problem into two parts: studying the effect of the inhomogeneous potential on the content of the Universe via the Boltzmann equation, and the effect of the perturbed components on the metric via the EFE. Computing these reactions give rise to a system of coupled differential equations known as the Einstein-Boltzmann equations. Assuming the perturbations are small, the system can be simplified by only considering terms linear in perturbations and transforming the equations to Fourier space.

Using the conformal time η (see eq. (1.6)) and defining $\mu = \hat{\boldsymbol{p}}\hat{\boldsymbol{k}}$ as the cosine between the wave-vector $\boldsymbol{k}$ and the photon momentum $\boldsymbol{p}$, the linear Boltzmann equations can be written as [81]

$$\dot{\Theta} + ik\mu\Theta = -\dot{\Phi} - ik\mu\Psi - \dot{\tau}\left[\Theta_0 - \Theta + \mu v_{\mathrm{b}} - \frac{1}{2}\mathcal{P}_2(\mu)\Pi\right] \tag{A.6}$$

$$\Pi = \Theta_2 + \Theta_{P2} + \Theta_{P0} \tag{A.7}$$

$$\Theta_P + ik\mu\Theta_P = -\dot{\tau}\left[-\Theta_P + \frac{1}{2}\left(1 - \mathcal{P}_2(\mu)\right)\Pi\right] \tag{A.8}$$

$$\dot{\delta} + ikv = -3\dot{\Phi} \tag{A.9}$$

$$\dot{v} + \frac{\dot{a}}{a}v = -ik\Psi \tag{A.10}$$

$$\dot{\delta}_b + ikv_b = -3\dot{\Phi} \tag{A.11}$$

$$\dot{v}_b + \frac{\dot{a}}{a}v_b = -ik\Psi + \frac{\dot{\tau}}{R}\left[v_b + 3i\Theta_1\right] \tag{A.12}$$

$$\dot{\mathcal{N}} + ik\mu\mathcal{N} = -\dot{\Phi} - ik\mu\Psi, \tag{A.13}$$

where $\mathcal{P}_l$ is the Legendre polynomial of order l, τ is the optical depth, Θ_P the perturbations in the photon polarization field and $R = 3\rho_{b,0}/4\rho_{\gamma,0}$ is the baryon/photon ratio. Equation (A.6) determines the evolution of the photon temperature including Compton scattering between photons and baryons, eq. (A.8) describes the generation of photon polarization that can be observed in the CMB, eq. (A.9) and eq. (A.10) govern the evolution of CDM overdensities and peculiar velocities, and eq. (A.11) and eq. (A.12) the ones of baryons which unlike the CDM are coupled to the photons by Compton scattering. Equation (A.13) describes the evolution of the neutrino temperature inhomogeneities, assuming massless neutrinos.

The second part, the effects of the perturbations in the energy stress tensor on the potentials Φ and Ψ, are obtained from the EFE. We find in the linear approximation [81]

$$k^2\Phi + 3\frac{\dot{a}}{a}\left(\dot{\Phi} - \frac{\dot{a}}{a}\Psi\right) = 4\pi G a^2\left[\rho_{\mathrm{m}}\delta_m + 4\rho_r\Theta_{r,0}\right] \tag{A.14}$$

$$k^2(\Phi + \Psi) = -32\pi G a^2\rho_r\Theta_{r,2}, \tag{A.15}$$

[1] As discussed in section 1.2.3, this assumption is only valid before shell-crossing at early times.

where $\circ_m$ and $\circ_r$ indicates all non-relativistic matter and relativistic radiation respectively. Note that if the radiation quadrupole $\Theta_{r,2}$ is small, then $\Phi \simeq -\Psi$ is a good approximation. The difference between the potentials, the so-called gravitational slip, is predicted to be very small in GR but might arise in modified GR theories [34].

Perturbative solutions in limiting cases

With the exceptions of some limiting cases, the system of Einstein-Boltzmann equations has to be solved numerically. Various codes exist and are publicly available (e.g. CAMB [196] and CLASS [39]).

However, we can gain some useful insight by studying the Einstein-Boltzmann equations in some asymptotic cases and by taking some approximations. We assume that the photons are tightly coupled to the baryons and thus $\Theta_i = 0$ for $i > 1$ (valid before recombination) and thus also $\Psi = -\Phi$, but we neglect the baryonic matter density since DM is the dominant matter component. A thorough derivation can be found in [81].

After computing the zeroth and first moment of eq. (A.6), we are left with the equations [81]

$$\dot{\Theta}_0 + k\Theta_1 = -\dot{\Phi} \tag{A.16}$$

$$\dot{\Theta}_1 - \frac{k}{3}\Theta_0 = -\frac{k}{3}\Phi \tag{A.17}$$

$$\dot{\delta} + ikv = -3\Phi \tag{A.18}$$

$$\dot{v} + \frac{\dot{a}}{a}v = ik\Phi \tag{A.19}$$

$$k^2\Phi + 3\frac{\dot{a}}{a}(\dot{\Phi} + \frac{\dot{a}}{a}\Phi) = 4\pi G a^2 \left[\rho_m\delta + 4\rho_\gamma\Theta_0\right]. \tag{A.20}$$

Alternatively, we can use an algebraic version of the last equation without time derivatives

$$k^2\Phi = 4\pi G a^2 \left[\rho_m\delta + 4\rho_\gamma\Theta_0 + \frac{3aH}{k}\left(i\rho_m v + 4\rho_\gamma\Theta_1\right)\right]. \tag{A.21}$$

For modes that are much larger than the horizon and thus $k\eta \ll 1$, we can drop all terms containing k. Equation (A.16) and eq. (A.17) implicate that $\delta - 3\Theta_0 = \text{const}$. From the analysis of eq. (A.20), one finds that $\Phi = \Phi_P = \text{const}$ during the radiation dominated era with $a \ll a_{\text{eq},1}$ and once the universe becomes matter-dominated and $a \gg a_{\text{eq},1}$, the potential drops by 10%, hence $\Phi \to (9/10)\Phi_P$.

For subhorizon scales $k\eta \gg 1$ during the radiation era, one can ignore the matter contribution to the potential in eq. (A.21), and together with the radiation perturbation equations eq. (A.16) and eq. (A.17) one finds that

$$\Phi = 3\Phi_P \left(\frac{\sin(k\eta/\sqrt{3}) - (k\eta/\sqrt{3})\cos(k\eta/\sqrt{3})}{(k\eta/\sqrt{3})^3}\right), \tag{A.22}$$

where Φ_P is the primordial value of Φ. Hence, as soon as the mode enters the horizon ($k\eta = 1$), the potential starts to decay due to radiation pressure and after decaying oscillates. The photon temperature fluctuation Θ_0 oscillate with fixed amplitude and from the coupling with the potential one can derive that the matter perturbations grow logarithmically with η. Hence, perturbations in radiation (and also baryons since they are tightly coupled to photons in this era) do not grow in the radiation dominated era whereas dark matter perturbations can grow logarithmically.

Finally, during the matter era, we can safely ignore the radiation contribution. The equations we have to deal with are the matter density and velocity equations eq. (A.18) and eq. (A.19) and the Poisson equation eq. (A.21) without the radiation terms and the velocity term (since $k \gg \eta^{-1} \sim aH$ during the matter era). This Newtonian limit of matter perturbations is precisely the system of equations we studied in section 1.2.3. We found that the growth of perturbations δ is independent of the scale k and can be parametrized by the growing mode $D_+(a)$ and the decaying mode $D_-(a)$. Ignoring the decaying mode, we find using the Poisson equation that the evolution of the potential is determined by $\Phi \propto D_+(a)/a$. Since during the matter era $D_+(a) \propto a$, the potential is constant. During the dark energy dominated epoch however, it will decay due to the accelerated expansion of the Universe.

The different limits that we discussed are summarized in fig. 1.1. The scale dependent evolution during the radiation era and at horizon crossing is captured by the transfer function $T(k)$, which can either be obtained by the aforementioned numerical codes, or by fitting functions [20, 95]. The scale independent growth is decoded into the growth function $D_+(a)$. For late times (well after any scale-dependent effects take place), we can write the potential and the density perturbation as [81]

$$\Phi(\boldsymbol{k}, a) = \frac{9}{10}\Phi_P(\boldsymbol{k})T(k)\frac{D_+(a)}{a} \tag{A.23}$$

$$\delta(\boldsymbol{k}, a) = \frac{3}{5}\frac{k^2}{\Omega_m H_0^2}\Phi_P(\boldsymbol{k})T(k)D_+(a). \tag{A.24}$$

A.2 Spherical Collapse Model

Expressing eq. (1.86) with $k = +1$ in term of conformal time $\mathrm{d}\eta/\mathrm{d}t = r^{-1}$ and using the constant $r_\star = (4/3)\pi G\rho_0 r_0^3 = GM$ we find

$$\left(\frac{\mathrm{d}}{\mathrm{d}\eta}\frac{r}{r_\star}\right)^2 = 2\frac{r}{r_\star} - \left(\frac{r}{r_\star}\right)^2, \tag{A.25}$$

which has the simple solution

$$r(\eta) = r_\star(1 - \cos(\eta)) \tag{A.26}$$

$$t(\eta) = \int_0^\eta \mathrm{d}\eta'\ r(\eta') = r_\star(\eta - \sin(\eta)). \tag{A.27}$$

Note that for small η, we find $r \simeq r_\star\eta^2/2 \simeq (9GMt^2/2)^{1/3}$ which simply corresponds to the evolution of an EdS universe with $k = 0$. At very early times, the overdense patch thus grows at the same rate as the background is expanding. We can write the evolution of the background density as

$$\bar{\rho}(t) = \frac{3M}{4\pi r_b(t)^3} = \frac{1}{6\pi G t^2}, \tag{A.28}$$

where we used r_b to distinguish the evolution of the background radius from the radius r of the perturbation.

Looking at eq. (A.26), we see that the perturbation reaches its maximum expansion at $\eta = \pi$ or equivalently $t = GM\pi$. This is the so-called turnaround time, after which the sphere collapses. The density of the perturbation at the turnaround is

$$\rho_{\rm ta} = \frac{3M}{4\pi r_{\rm ta}^3} = \frac{3}{32\pi G^3 M^2}. \tag{A.29}$$

A comparison with the background density yields the patch overdensity at the time of turnaround:

$$1 + \delta_{\rm ta} = \frac{\rho_{\rm ta}}{\bar{\rho}(t_{\rm ta})} = \frac{9\pi^2}{16} \approx 5.55. \tag{A.30}$$

After the turnaround, the patch contracts and the overdensity increases. For a perfect spherically symmetric and perfect pressureless matter, the perturbation would collapse to a singularity at $\eta = 2\pi$. However, a realistic overdensity will never be perfectly spherical and the support from the angular momentum conservation will prevent the singularity from forming. It is therefore a good approximation to assume that eventually, a finite size, virialized structure (a dark matter halo) will form. Virial equilibrium requires

$$2E_{\rm kin}^{\rm vir} + E_{\rm pot}^{\rm vir} = 0, \tag{A.31}$$

and since the kinetic energy at the turnaround is zero, we find

$$E_{\rm tot} = E_{\rm kin} + E_{\rm pot} = E_{\rm pot}\Big|_{t=t_{\rm ta}} = \frac{1}{2}E_{\rm pot}^{\rm vir}, \tag{A.32}$$

assuming the total energy is conserved. Since $E_{\rm pot} \propto r^{-1}$ for a homogeneous sphere, we find that the virialized structure must have the radius $r_{\rm vir} = r_{\rm ta}/2 = r_\star$. Using eq. (A.26), the sphere contracts to the virial radius at $\eta_{\rm vir} = 3/2\pi$. However, virialization takes some extra time and one usually uses $\eta = 2\pi$ as the virialization time [185], i.e. when a perfect symmetric perturbation would have collapsed to a singularity. We thus calculate the overdensity of the system by evaluating the patch density at $\eta = 3\pi/2$ and the background density at $\eta = 2\pi$ and find for the virialization density threshold

$$1 + \delta_{\rm vir} = 18\pi^2 \simeq 178. \tag{A.33}$$

Note that this result is independent of the total mass of the overdense patch[2]. Encountering a region with an overdensity larger than $\delta_{\rm vir}$, we can thus assume that the structure it belongs to has virialized.

[2] This is however only true in an EdS universe. For a ΛCDM universe, the virial density can be approximated by the Bryan & Norman fitting function [50]

$$\frac{\rho_{\rm vir}}{\rho_c} = 18\pi^2 + 82x - 39x^2, \tag{A.34}$$

where $x = (1 + a^3\Omega_\Lambda/\Omega_m)^{-1} - 1$. Also see [159, 240] for general discussions of spherical collapse models with dark energy universes and characteristic signatures.

We can compute what densities these thresholds would compare to if we assume only linear growth. This will later allow us to identify non-linear, virialized structures in predictions from linear perturbation theory only. For this, we approximate the evolution of the patch density to the first non-vanishing order

$$1 + \delta(\eta) = \frac{\rho(\eta)}{\bar{\rho}(\eta)} = \frac{9(\eta - \sin\eta)^2}{2(1 - \cos\eta)^3} = 1 + \frac{3\eta^2}{20} + \mathcal{O}(\eta^4), \tag{A.35}$$

and expand η in terms of t to find

$$\delta_{\text{lin}}(t) = \frac{3}{20}\left(\frac{6t}{GM}\right)^{2/3} \propto t^{2/3} \propto a, \tag{A.36}$$

recovering the linear growth factor $D_+(a) \propto a$ in an EdS universe (cf. eq. (1.48) and the subsequent discussion). We therefore find the linear overdensity thresholds equivalents to the turnaround and virialization thresholds:

$$\delta_{\text{lin}}\Big|_{\text{ta}} = \frac{3}{20}(6\pi)^{2/3} \simeq 1.062 \tag{A.37}$$

$$\delta_c \equiv \delta_{\text{lin}}\Big|_{\text{vir}} = \frac{3}{20}(12\pi)^{2/3} \simeq 1.686. \tag{A.38}$$

Figure 1.5 visualizes the time evolution of the background and patch radii and the density contrast of the perturbation.

A.3 Simulation Details

This section provides a summary of the simulations that have been performed for this thesis. Some existing simulations that are used for COSMICWEB, such as the AGORA and RHAPSODY box, have been rerun with the original seed. The simulations are listed in table A.1 together with an overview over the most important parameters.

The N-body simulations have been performed with the tree-PM code GADGET-2 [300], with initial conditions generated with MUSIC [133]. For most of the simulations, we use the Eisenstein & Hu [95] transfer-function and cosmological parameters consistent with the Planck 2015 results [67] and denoted by [P1] in table A.1.

Additionally, a hydrodynamic simulation was run with the adaptive-mesh-refinement code RAMSES [312]. The 150CDM_H simulation uses the same random noise field as the 150CDM simulation, allowing a direct comparison of the collapsed structures between the dark-matter only and the hydrodynamic run. The mesh is initialized on level 10 and allowed to be refined to level 13 using the quasi-Lagrangian refinement strategy [188], spitting the cell if it contains more than 8 DM particles. Cooling and UV background heating have been turned off.

Furthermore, simulations with suppressed small-scale structures have been carried out by truncating the initial power spectrum. The truncation method is identical to the free-streaming in WDM models (cf. discussion in section 1.3.2). We used WDM masses of of 250eV and 500eV, leading to truncation scales $\alpha = 250h^{-1}$kpc and $\alpha = 113h^{-1}$kpc respectively. For the index parameter in eq. (1.81), we chose $\mu = 1$ [41]. For these WDM simulations, the amplitudes A_0 of

Table A.1: N-body simulations used in this thesis and the corresponding parameters: box size L_{box}, particle resolution N_P, particle mass m_P, force softening ϵ and WDM particle mass m_{WDM} used to truncate the initial power spectrum. The corresponding cosmological parameters of the ΛCDM model are listed below, where $h = H_0/(100\,\mathrm{km\,s^{-1}Mpc^{-1}})$. The AGORA [178] and RHAPSODY [336, 337, 137] re-simulation use the parameters and random seeds from the original projects, whereas the cosmological parameters have been updated for the RHAPSODY_NewCosmo simulation.

Chapter 3	Chapter 4	cosmology	L_{box} [h^{-1}Mpc]	z_{start}	N_p	m_p [$h^{-1}\mathrm{M}_\odot$]	ϵ [h^{-1}kpc]	m_{WDM} [eV]
300WDM1_10		[P1]	300	99	1024^3	2.142×10^{9}	15	250
300WDM1_9		[P1]	300	99	512^3	1.714×10^{10}	30	250
300WDM2_10		[P1]	300	99	1024^3	2.142×10^{9}	15	500
300WDM2_9		[P1]	300	99	512^3	1.714×10^{10}	30	500
300CDM_10	300MPC	[P1]	300	99	1024^3	2.142×10^{9}	6	-
300CDM_9	300MPC_lowres	[P1]	300	99	512^3	1.714×10^{10}	12	-
150CDM	150MPC	[P1]	150	99	1024^3	2.019×10^{8}	3	-
150CDM_H*		[P1]	150	99	1024^3	2.019×10^{8}	-	-
	150MPC_lowres	[P1]	150	99	512^3	2.156×10^{9}	6	-
	AGORA	[W1]	60	99	512^3	1.215×10^{8}	2.4	-
	RHAPSODY	[W2]	1000	49	1024^3	6.462×10^{10}	20	-
	RHAPSODY_NewCosmo	[P1]	1000	49	1024^3	7.986×10^{10}	20	-

* The 150CDM_H simulation includes hydrodynamics and was run with RAMSES [312], with minimal and maximal refinement levels 10 and 13, and cooling and UV background heating disabled.

cosmology	Ω_m	Ω_b	Ω_Λ	n_s	σ_8	h	origin
[P1]	0.307	0.0486	0.693	0.9667	0.816	0.6774	Planck 2015 [67]
[P2]	0.307	0.0425	0.693	0.9611	0.829	0.6777	Planck 2015 [67]
[W1]	0.272	0.0455	0.728	0.961	0.807	0.702	WMAP 7/9 [187, 151]
[W2]	0.25	0.04	0.75	1	0.8	0.7	WMAP 7/9 [187, 151]

the initial power spectrum (cf. eq. (1.77)) has been fixed to the corresponding CDM value, hence σ_8 alters from the assumed cosmological parameters. However, fixing the amplitude and using the same random seeds ensures that the large scale structure in the CDM and WDM simulations agree with each other up to non-linear back reaction of the small-scale structure.

A.4 Analytical model for one dimensional plane wave collapse

In this section we construct a very rough model to estimate the velocity dispersion of a plane wave right after the collapse time $a_\times$. A more thorough treatment including post-collapse corrections can be found in [309]. In order to be able to invert $\boldsymbol{x} = \boldsymbol{x}(\boldsymbol{q})$ analytically after shell-crossing, we expand the plane wave perturbation with mode k around $q = 0$ to the lowest order that leads to collapse,

$$x(q, a) = \left[1 - \frac{D_+(a)}{D_+(a_\times)}\right] q + \frac{k^2}{6} \frac{D_+(a)}{D_+(a_\times)} q^3 + \mathcal{O}(q^5). \tag{A.39}$$

This expression has one real root for $a < a_\times$ and three for $a > a_\times$, corresponding to the dark matter sheets crossing $x = 0$. In catastrophe theory (e.g. [261], but also [18, 150]), this is also called a *normal form*, describing the topological structure of the first shell-crossing, and such a system is referred to as the *cusp catastrophe*. We include this Taylor expansion in fig. A.1. It tightly follows the ZA around $q = 0$ but starts to deviate further away from the centre of collapse. This causes the approximation to underestimate the velocity dispersion (compared to ZA) at late times.

Focusing on the center $x = 0$ of the perturbation, we can express the velocity dispersion (in comoving velocity units) as

$$\sigma_c^2(x = 0, a) = \frac{3}{k^2} \left(1 - \frac{D_+(a_\times)}{D_+(a)}\right) \left(\frac{\dot{D}_+(a)}{D_+(a)}\right)^2, \tag{A.40}$$

for $a >= a_\times$. To get an estimate on σ_c^2 immediately after collapse, we evaluate this equation at $a = a_\times(1 + \Delta a)$ with $\Delta a \ll 1$. Furthermore, we assume an Einstein de-Sitter (EdS) universe ($\Omega_m = \Omega_{\mathrm{tot}} = 1$), for which the growth factor scales as $D_+(a) = a$ and $\dot{D}_+(a) = \dot{a} = H_0^2 a^{-1/2}$ and obtain

$$\sigma_c^2 \left(x = 0, a_\times(1 + \Delta a)\right) = \frac{3H_0^2}{k^2} \frac{\Delta a}{1 + \Delta a} \left(a_\times(1 + \Delta a)\right)^{-3}. \tag{A.41}$$

Recalling the shell-crossing time of a plane wave $a_\times = A^{-1}k^{-2}$, we find that at fixed Δa, the comoving velocity dispersion $\sigma_c^2 \propto A^3 k^4$. The typical amplitude of the potential is dependent on the scale k and related to the matter power spectrum as $A(k) \sim (P_{\delta\delta}(k)k^{-4})^{1/2}$. We therefore expect $\sigma_c^2 \propto P_{\delta\delta}^{3/2} k^{-2}$, which implies that for scales sufficiently smaller than the Hubble horizon at radiation-matter equality, $k > k_{\mathrm{eq}}$, small-scale perturbations are expected to have lower velocity dispersion at a fixed time after shell-crossing. Of course, this is only a very rough model of the actual physics, neglecting the three dimensional nature of collapse, the presence of perturbations on all scales and post-collapse corrections.

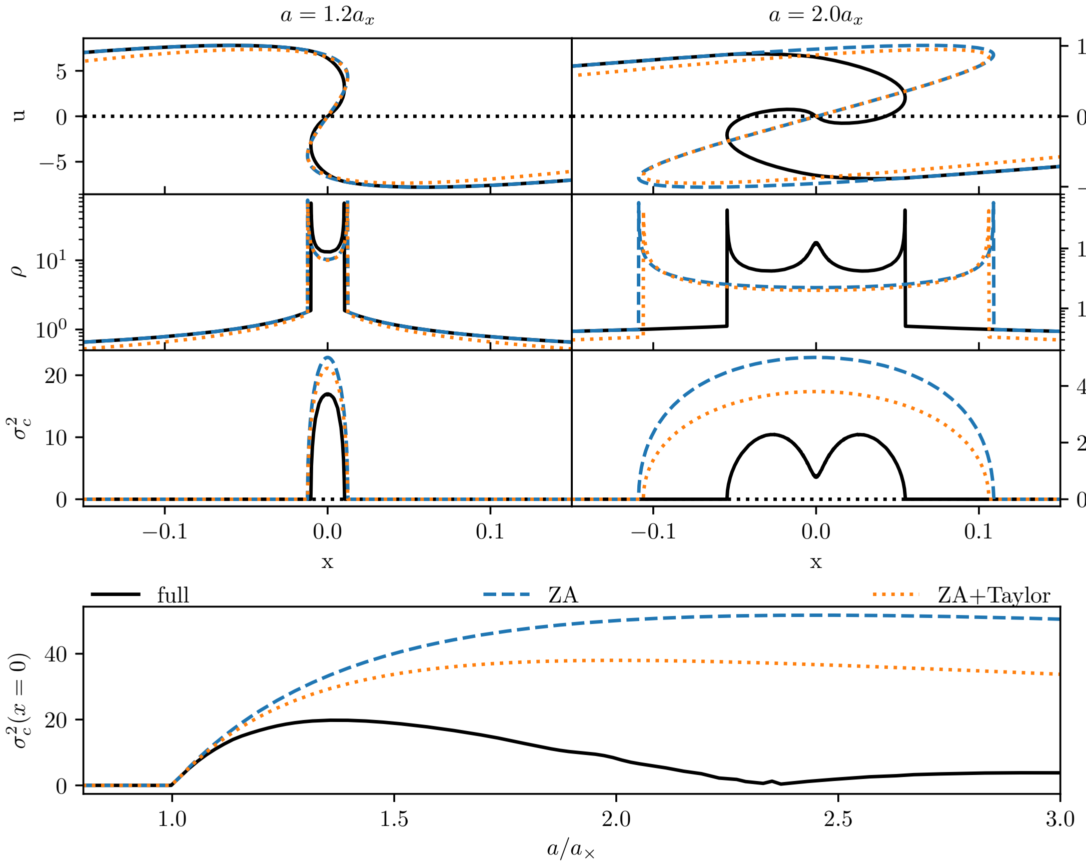

Figure A.1: One-dimensional plane-wave collapse model of the dark matter sheet showing the phase-space distribution, the local density and the (comoving) velocity dispersion. The left panels show the system shortly after shell-crossing ($a = 1.2a_\times$), whereas the system evolved further in the right panels ($a = 2a_\times$). We compare the results from numerical integration (black) with the ZA (blue) and the approximated plane wave perturbation (orange). The ZA is correct up to shell-crossing and starts to deviate at later times, overestimating the size of the collapsed region and the velocity dispersion within. The velocity dispersion at the center $x = 0.5$ in the fully evolved model peaks at $a \sim 1.4a_\times$ and decays afterwards due to the growing density after subsequent further shell-crossings in the central region. As the ZA does not model this secondary collapse, the velocity dispersion increases until the expansion of the universe dominates the velocity field.

Bibliography

[1] Tom Abel et al. "Tracing the dark matter sheet in phase space". In: *Monthly Notices of the Royal Astronomical Society* 427.1 (2012), pp. 61–76.

[2] P. A. R. Ade et al. "Planck 2015 results". In: *Astronomy & Astrophysics* 594 (2016), A13.

[3] Susmita Adhikari et al. "Splashback in accreting dark matter halos". In: *Journal of Cosmology and Astroparticle Physics* 2014.11 (2014), pp. 019–019.

[4] Andrew L. Alexander et al. "A geometric analysis of diffusion tensor measurements of the human brain". In: *Magnetic Resonance in Medicine* 44.2 (2000), pp. 283–291.

[5] B. Allgood et al. "The shape of dark matter haloes: dependence on mass, redshift, radius and formation". In: *Monthly Notices of the Royal Astronomical Society* 367.4 (2006), pp. 1781–1796.

[6] Ralph A. Alpher & Robert Herman. "Evolution of the Universe". In: *Nature* 162.4124 (1948), pp. 774–775.

[7] A. Amara et al. "Simulations of strong gravitational lensing with substructure". In: *Monthly Notices of the Royal Astronomical Society* 367.4 (2006), pp. 1367–1378.

[8] Raul E. Angulo et al. "How closely do baryons follow dark matter on large scales?" In: *Monthly Notices of the Royal Astronomical Society* 434.2 (2013), pp. 1756–1764.

[9] Raul E. Angulo et al. "Towards noiseless gravitational lensing simulations". In: *Monthly Notices of the Royal Astronomical Society* 444.3 (2014), pp. 2925–2937.

[10] M. A. Aragon-Calvo & Lin Forrest Yang. "The hierarchical nature of the spin alignment of dark matter haloes in filaments". In: *Monthly Notices of the Royal Astronomical Society: Letters* 440.1 (2014), pp. L46–L50.

[11] M. A. Aragon-Calvo et al. "Locally cold flows from large-scale structure". In: *Monthly Notices of the Royal Astronomical Society: Letters* 415.1 (2011), pp. L16–L20.

[12] M. A. Aragon-Calvo et al. "Unfolding the hierarchy of voids". In: *Monthly Notices of the Royal Astronomical Society: Letters* 404.1 (2010), pp. L89–L93.

[13] M. A. Aragón-Calvo et al. "The multiscale morphology filter: identifying and extracting spatial patterns in the galaxy distribution". In: *Astronomy & Astrophysics* 474.1 (2007), pp. 315–338.

[14] M. A. Aragón-Calvo et al. "The multiscale morphology filter: identifying and extracting spatial patterns in the galaxy distribution". In: *Astronomy & Astrophysics* 474.1 (2007), pp. 315–338.

[15] Miguel A. Aragon-Calvo et al. "The Spine of the Cosmic Web". In: *The Astrophysical Journal* 723.1 (2008), pp. 364–382.

[16] Miguel A. Aragón-Calvo et al. "Multiscale phenomenology of the cosmic web". In: *Monthly Notices of the Royal Astronomical Society* 408.4 (2010), pp. 2163–2187.

[17] V. I. Arnold. "Evolution of singularities of potential flows in collisionless media and transformations of caustics in three-dimensional space". In: *Tr. Semin. imeni G Petrovskogo* 8 (1982), pp. 21–57.

[18] V. I. Arnold et al. "The large scale structure of the universe I. General properties. One-and two-dimensional models". In: *Geophysical & Astrophysical Fluid Dynamics* 20.1-2 (1982), pp. 111–130.

[19] Jeremy Bailin & Matthias Steinmetz. "Internal and External Alignment of the Shapes and Angular Momenta of ΛCDM Halos". In: *The Astrophysical Journal* 627.2 (2005), pp. 647–665.

[20] J M Bardeen et al. "The statistics of peaks of Gaussian random fields". In: *The Astrophysical Journal* 304 (1986), p. 15.

[21] David J. Barnes et al. "The Cluster-EAGLE project: global properties of simulated clusters with resolved galaxies". In: *Monthly Notices of the Royal Astronomical Society* 471.1 (2017), pp. 1088–1106.

[22] David J Barnes et al. "Enhancing AGN efficiency and cool-core formation with anisotropic thermal conduction". In: *Monthly Notices of the Royal Astronomical Society* 488.3 (2019), pp. 3003–3013.

[23] Josh Barnes & Piet Hut. "A hierarchical O(N log N) force-calculation algorithm". In: *Nature* 324.6096 (1986), pp. 446–449.

[24] Joshua Barnes & George Efstathiou. "Angular momentum from tidal torques". In: *The Astrophysical Journal* 319 (1987), p. 575.

[25] M Bartelmann. "Arcs from a universal dark-matter halo profile." In: *Astronomy and Astrophysics* 313 (1996), pp. 697–702. arXiv: `astro-ph/9602053 [astro-ph]`.

[26] Harry Bateman. "Some recent researches on the motion of fluids". In: *Monthly Weather Review* 43.4 (1915), pp. 163–170.

[27] Daniel Baumann et al. "Cosmological non-linearities as an effective fluid". In: *Journal of Cosmology and Astroparticle Physics* 2012.07 (2012), pp. 051–051.

[28] Peter S. Behroozi et al. "Gravitationally consitent halo catalogs and merger trees for precision cosmology". In: *The Astrophysical Journal* 763.1 (2013), p. 18.

[29] Peter S. Behroozi et al. "Mergers and mass accretion for infalling halos both end well outside cluster virial radii". In: *The Astrophysical Journal* 787.2 (2014), p. 156.

[30] Peter S Behroozi et al. "The ROCKSTAR phase-space temporal halo finder and the velocity offsets of cluster cores". In: *The Astrophysical Journal* 762.2 (2013), p. 109.

[31] Claus Beisbart & Martin Kerscher. "Luminosity- and Morphology-dependent Clustering of Galaxies". In: *The Astrophysical Journal* 545.1 (2000), pp. 6–25.

[32] C. L. Bennett et al. "First-Year Wilkinson Microwave Anisotropy Probe (WMAP) Observations: Foreground Emission". In: *The Astrophysical Journal Supplement Series* 148.1 (2003), pp. 97–117.

[33] Philippe Berger & George Stein. "A volumetric deep Convolutional Neural Network for simulation of mock dark matter halo catalogues". In: *Monthly Notices of the Royal Astronomical Society* 482.3 (2019), pp. 2861–2871.

[34] E. Bertschinger. "One gravitational potential or two? Forecasts and tests". In: *Philosophical Transactions of the Royal Society A: Mathematical, Physical and Engineering Sciences* 369.1957 (2011), pp. 4947–4961.

[35] E. Bertschinger. "Self-similar secondary infall and accretion in an Einstein-de Sitter universe". In: *The Astrophysical Journal Supplement Series* 58 (1985), p. 39.

[36] Edmund Bertschinger. "Multiscale Gaussian Random Fields for Cosmological Simulations". In: *The Astrophysical Journal Supplement Series* 137.1 (2001), p. 38.

[37] Edmund Bertschinger. "Path integral methods for primordial density perturbations - Sampling of constrained Gaussian random fields". In: *The Astrophysical Journal* 323 (1987), p. L103.

[38] Diego Blas et al. "Cosmological perturbation theory at three-loop order". In: *Journal of Cosmology and Astroparticle Physics* 2014.01 (2014), pp. 010–010.

[39] Diego Blas et al. "The Cosmic Linear Anisotropy Solving System (CLASS). Part II: Approximation schemes". In: *Journal of Cosmology and Astroparticle Physics* 2011.07 (2011), pp. 034–034.

[40] Paul Bode & Jeremiah P. Ostriker. "Tree Particle-Mesh: An Adaptive, Efficient, and Parallel Code for Collisionless Cosmological Simulation". In: *The Astrophysical Journal Supplement Series* 145.1 (2003), pp. 1–13.

[41] Paul Bode et al. "Halo Formation in Warm Dark Matter Models". In: *The Astrophysical Journal* 556.1 (2001), pp. 93–107.

[42] J. R. Bond et al. "Excursion set mass functions for hierarchical Gaussian fluctuations". In: *The Astrophysical Journal* 379 (1991), p. 440.

[43] J. Richard Bond et al. "How filaments of galaxies are woven into the cosmic web". In: *Nature* 380.6575 (1996), pp. 603–606.

[44] Nicholas A. Bond et al. "Crawling the cosmic network: identifying and quantifying filamentary structure". In: *Monthly Notices of the Royal Astronomical Society* 409.1 (2010), pp. 156–168.

[45] C. Bonnett et al. "Redshift distributions of galaxies in the Dark Energy Survey Science Verification shear catalogue and implications for weak lensing". In: *Physical Review D* 94.4 (2016), p. 042005.

[46] Mikolaj Borzyszkowski et al. "The formation of cold dark matter haloes – II. Collapse time and tides". In: *Monthly Notices of the Royal Astronomical Society* 445.4 (2014), pp. 4124–4136.

[47] Mikolaj Borzyszkowski et al. "ZOMG I: How the cosmic web inhibits halo growth and generates assembly bias". In: *MNRAS* 000 (2016), pp. 1–17. arXiv: 1610.04231.

[48] Frank C van den Bosch & Go Ogiya. "Dark matter substructure in numerical simulations: a tale of discreteness noise, runaway instabilities, and artificial disruption". In: *Monthly Notices of the Royal Astronomical Society* 475.3 (2018), pp. 4066–4087.

[49] Achi Brandt. "Multi-Level Adaptive Solutions to Boundary-Value Problems". In: *Mathematics of Computation* 31.138 (1977), p. 333.

[50] Greg L. Bryan & Michael L. Norman. "Statistical Properties of X-Ray Clusters: Analytic and Numerical Comparisons". In: *The Astrophysical Journal* 495.1 (1998), pp. 80–99.

[51] Michael Buehlmann & Oliver Hahn. "Large-scale velocity dispersion and the cosmic web". In: *Monthly Notices of the Royal Astronomical Society* 487.1 (2019), pp. 228–245.

[52] J. S. Bullock et al. "A Universal Angular Momentum Profile for Galactic Halos". In: *The Astrophysical Journal* 555.1 (2001), pp. 240–257.

[53] James S. Bullock & Michael Boylan-Kolchin. "Small-Scale Challenges to the Λ CDM Paradigm". In: *Annual Review of Astronomy and Astrophysics* 55.1 (2017), pp. 343–387.

[54] J.M. Burgers. "A Mathematical Model Illustrating the Theory of Turbulence". In: 1948, pp. 171–199.

[55] Giuseppe Carleo et al. "Machine learning and the physical sciences". In: (2019). arXiv: 1903.10563.

[56] John Joseph M. Carrasco et al. "The effective field theory of cosmological large scale structures". In: *Journal of High Energy Physics* 2012.9 (2012), p. 82.

[57] Sean M. Carroll. "Lecture Notes on General Relativity". In: (1997). arXiv: 9712019 [gr-qc].

[58] P. Catelan et al. "Intrinsic and extrinsic galaxy alignment". In: *Monthly Notices of the Royal Astronomical Society* 320.1 (2001), pp. L7–L13.

[59] Marius C Cautun & Rien van de Weygaert. "The DTFE public software - The Delaunay Tessellation Field Estimator code". In: (2011). arXiv: 1105.0370 [astro-ph.IM].

[60] Marius Cautun et al. "Evolution of the cosmic web". In: *Monthly Notices of the Royal Astronomical Society* 441.4 (2014), pp. 2923–2973.

[61] Marius Cautun et al. "NEXUS: tracing the cosmic web connection". In: *Monthly Notices of the Royal Astronomical Society* 429.2 (2013), pp. 1286–1308.

[62] Subrahmanyan Chandrasekhar. *Ellipsoidal Figures of Equilibrium*. New Haven, London: Yale University Press, 1969.

[63] Michał J. Chodorowski & Paweł Ciecielag̨. "Local Group velocity versus gravity: the coherence function". In: *Monthly Notices of the Royal Astronomical Society* 331.1 (2002), pp. 133–140.

[64] P. Ciecielag et al. "Gaussianity of cosmic velocity fields and linearity of the velocity–gravity relation". In: *Monthly Notices of the Royal Astronomical Society* 339.3 (2003), pp. 641–651.

[65] Jörg M. Colberg et al. "The Aspen–Amsterdam void finder comparison project". In: *Monthly Notices of the Royal Astronomical Society* 387.2 (2008), pp. 933–944.

[66] P. Coles et al. "Testing approximations for non-linear gravitational clustering". In: *Monthly Notices of the Royal Astronomical Society* 260.4 (1993), pp. 765–776.

[67] Planck Collaboration. "Planck 2015 results. XIII. Cosmological parameters". In: *arXiv* (2015). arXiv: 1502.01589.

[68] M Colless et al. "The 2dF Galaxy Redshift Survey: Final Data Release". In: *arXiv Astrophysics e-prints* (2003).

[69] Robert A. Crain et al. "The EAGLE simulations of galaxy formation: calibration of subgrid physics and model variations". In: *Monthly Notices of the Royal Astronomical Society* 450.2 (2015), pp. 1937–1961.

[70] Martín Crocce & Román Scoccimarro. "Renormalized cosmological perturbation theory". In: *Physical Review D* 73.6 (2006), p. 063519.

[71] Rupert A. C. Croft & Christopher A. Metzler. "Weak-Lensing Surveys and the Intrinsic Correlation of Galaxy Ellipticities". In: *The Astrophysical Journal* 545.2 (2000), pp. 561–571.

[72] M. Davis et al. "The evolution of large-scale structure in a universe dominated by cold dark matter". In: *The Astrophysical Journal* 292 (1985), p. 371.

[73] G. De Lucia & J. Blaizot. "The hierarchical formation of the brightest cluster galaxies". In: *Monthly Notices of the Royal Astronomical Society* 375.1 (2007), pp. 2–14.

[74] W. Dehnen & J. I. Read. "N-body simulations of gravitational dynamics". In: *The European Physical Journal Plus* 126.5 (2011), p. 55.

[75] Walter Dehnen. "A Very Fast and Momentum-conserving Tree Code". In: *The Astrophysical Journal* 536.1 (2000), pp. L39–L42.

[76] Walter Dehnen. "Towards optimal softening in three-dimensional N -body codes - I. Minimizing the force error". In: *Monthly Notices of the Royal Astronomical Society* 324.2 (2001), pp. 273–291.

[77] A. Dekel et al. "Cold streams in early massive hot haloes as the main mode of galaxy formation". In: *Nature* 457.7228 (2009), pp. 451–454.

[78] Erwan Deriaz & Sébastien Peirani. "Six-Dimensional Adaptive Simulation of the Vlasov Equations Using a Hierarchical Basis". In: *Multiscale Modeling & Simulation* 16.2 (2018), pp. 583–614.

[79] DESI Collaboration et al. "The DESI Experiment Part I: Science,Targeting, and Survey Design". In: (2016). arXiv: `1611.00036`.

[80] Giulia Despali et al. "Ellipsoidal halo finders and implications for models of triaxial halo formation". In: *Monthly Notices of the Royal Astronomical Society* 431.2 (2013), pp. 1143–1159.

[81] Scott Dodelson. *Modern Cosmology*. Elsevier, 2003.

[82] K. Dolag et al. "Substructures in hydrodynamical cluster simulations". In: *Monthly Notices of the Royal Astronomical Society* 399.2 (2009), pp. 497–514.

[83] K. Dolag et al. "SZ effects in the Magneticum Pathfinder simulation: comparison with the Planck , SPT, and ACT results". In: *Monthly Notices of the Royal Astronomical Society* 463.2 (2016), pp. 1797–1811.

[84] P Domínguez-Fernández et al. "Dynamical evolution of magnetic fields in the intracluster medium". In: *Monthly Notices of the Royal Astronomical Society* 486.1 (2019), pp. 623–638.

[85] J. Donnert et al. "Magnetic Field Amplification in Galaxy Clusters and Its Simulation". In: *Space Science Reviews* 214.8 (2018), p. 122.

[86] Olivier Doré et al. "Cosmology with the SPHEREX All-Sky Spectral Survey". In: (2014). arXiv: `1412.4872`.

[87] A. G. Doroshkevich. "Spatial structure of perturbations and origin of galactic rotation in fluctuation theory". In: *Astrophysics* 6.4 (1973), pp. 320–330.

[88] A. G. Doroshkevich. "The space structure of perturbations and the origin of rotation of galaxies in the theory of fluctuation." In: *Astrofizika* 6 (1970), p. 581.

[89] A. G. Doroshkevich et al. "Astrophysical Implications of the Neutrino Rest Mass - Part Two - the Density Perturbation Spectrum and Small-Scale Fluctuations in the Microwave Background". In: *Soviet Astronomy Letters* 6 (1980), pp. 252–259.

[90] Y. Dubois et al. "Dancing in the dark: galactic properties trace spin swings along the cosmic web". In: *Monthly Notices of the Royal Astronomical Society* 444.2 (2014), pp. 1453–1468.

[91] Yohan Dubois & Benoît Commerçon. "An implicit scheme for solving the anisotropic diffusion of heat and cosmic rays in the RAMSES code". In: *Astronomy & Astrophysics* 585 (2016), A138.

[92] Yohan Dubois et al. "Shock-accelerated cosmic rays and streaming instability in the adaptive mesh refinement code Ramses: methods and tests". In: (2019). arXiv: `1907.04300`.

[93] G. Efstathiou et al. "Numerical techniques for large cosmological N-body simulations". In: *The Astrophysical Journal Supplement Series* 57 (1985), p. 241.

[94] Albert Einstein. "The basics of general relativity theory". In: *Annalen der Physik* 49.7 (1915), pp. 769–822.

[95] Daniel J. Eisenstein & Wayne Hu. "Baryonic Features in the Matter Transfer Function". In: *The Astrophysical Journal* 496.2 (1998), pp. 605–614.

[96] Pascal J. Elahi et al. "Peaks above the Maxwellian Sea: a new approach to finding substructures in N-body haloes". In: *Monthly Notices of the Royal Astronomical Society* 418.1 (2011), pp. 320–335.

[97] A. E. Evrard et al. "Galaxy Clusters in Hubble Volume Simulations: Cosmological Constraints from Sky Survey Populations". In: *The Astrophysical Journal* 573.1 (2002), pp. 7–36.

[98] P. P. Ewald. "Die Berechnung optischer und elektrostatischer Gitterpotentiale". In: *Annalen der Physik* 369.3 (1921), pp. 253–287.

[99] Bridget L. Falck et al. "ORIGAMI: delineating halos using phase-space folds". In: *The Astrophysical Journal* 754.2 (2012), p. 126.

[100] Job Feldbrugge et al. "Caustic Skeleton & Cosmic Web". In: *Journal of Cosmology and Astroparticle Physics* 2018.05 (2018), pp. 027–027.

[101] Yu Feng et al. "FastPM: a new scheme for fast simulations of dark matter and haloes". In: *Monthly Notices of the Royal Astronomical Society* 463.3 (2016), pp. 2273–2286.

[102] Christian Fidler et al. "General relativistic weak-field limit and Newtonian N-body simulations". In: *Journal of Cosmology and Astroparticle Physics* 2017.12 (2017), pp. 022–022.

[103] J. A. Fillmore & P. Goldreich. "Self-similar gravitational collapse in an expanding universe". In: *The Astrophysical Journal* 281 (1984), p. 1.

[104] J. E. Forero-Romero et al. "A dynamical classification of the cosmic web". In: *Monthly Notices of the Royal Astronomical Society* 396.3 (2009), pp. 1815–1824.

[105] Etienne Forest & Ronald D. Ruth. "Fourth-order symplectic integration". In: *Physica D: Nonlinear Phenomena* 43.1 (1990), pp. 105–117.

[106] C. S. Frenk et al. "Nonlinear evolution of large-scale structure in the universe". In: *The Astrophysical Journal* 271 (1983), p. 417.

[107] C.S. Frenk & S.D.M. White. "Dark matter and cosmic structure". In: *Annalen der Physik* 524.9-10 (2012), pp. 507–534.

[108] Carlos S. Frenk et al. "The formation of dark halos in a universe dominated by cold dark matter". In: *The Astrophysical Journal* 327 (1988), p. 507.

[109] A. Friedman. "Über die Krümmung des Raumes". In: *Zeitschrift für Physik* 10.1 (1922), pp. 377–386.

[110] A. Friedman. "Über die Möglichkeit einer Welt mit konstanter negativer Krümmung des Raumes". In: *Zeitschrift für Physik* 21.1 (1924), pp. 326–332.

[111] U. Frisch et al. "Singularities and the distribution of density in the Burgers/adhesion model". In: *Physica D: Nonlinear Phenomena* 152-153 (2001), pp. 620–635.

[112] L. Gao & S. D. M. White. "Assembly bias in the clustering of dark matter haloes". In: *Monthly Notices of the Royal Astronomical Society: Letters* 377.1 (2007), pp. L5–L9.

[113] L. Gao et al. "The age dependence of halo clustering". In: *Monthly Notices of the Royal Astronomical Society: Letters* 363.1 (2005), pp. L66–L70.

[114] L. Gao et al. "The Phoenix Project: the dark side of rich Galaxy clusters". In: *Monthly Notices of the Royal Astronomical Society* 425.3 (2012), pp. 2169–2186.

[115] Liang Gao et al. "The redshift dependence of the structure of massive Λ cold dark matter haloes". In: *Monthly Notices of the Royal Astronomical Society* 387.2 (2008), pp. 536–544.

[116] Enrico Garaldi et al. "ZOMG - III. The effect of halo assembly on the satellite population". In: *Monthly Notices of the Royal Astronomical Society* 473.2 (2018), pp. 2234–2250.

[117] Shy Genel et al. "The halo merger rate in the millennium simulation and implications for observed galaxy merger fractions". In: *The Astrophysical Journal* 701.2 (2009), pp. 2002–2018.

[118] Howard Georgi & S. L. Glashow. "Unity of All Elementary-Particle Forces". In: *Physical Review Letters* 32.8 (1974), pp. 438–441.

[119] Stuart P. D. Gill et al. "The evolution of substructure - III. The outskirts of clusters". In: *Monthly Notices of the Royal Astronomical Society* 356.4 (2005), pp. 1327–1332.

[120] Stefan Gottloeber et al. "Constrained Local UniversE Simulations (CLUES)". In: (2010). arXiv: 1005.2687.

[121] Fabio Governato et al. "The Local Group as a test of cosmological models". In: *New Astronomy* 2.2 (1997), pp. 91–106.

[122] Robert J. J. Grand et al. "The Auriga Project: the properties and formation mechanisms of disc galaxies across cosmic time". In: *Monthly Notices of the Royal Astronomical Society* (2017), stx071.

[123] L Greengard & V Rokhlin. "A fast algorithm for particle simulations". In: *Journal of Computational Physics* 73.2 (1987), pp. 325–348.

[124] Brendan F. Griffen et al. "THE CATERPILLAR PROJECT: A LARGE SUITE OF MILKY WAY SIZED HALOS". In: *The Astrophysical Journal* 818.1 (2016), p. 10.

[125] Thomas Guillet & Romain Teyssier. "A simple multigrid scheme for solving the Poisson equation with arbitrary domain boundaries". In: *Journal of Computational Physics* 230.12 (2011), pp. 4756–4771.

[126] S. N. Gurbatov & A. I. Saichev. "Probability distribution and spectra of potential hydrodynamic turbulence". In: *Radiophysics and Quantum Electronics* 27.4 (1984), pp. 303–313.

[127] S. N. Gurbatov et al. "The large-scale structure of the Universe in the frame of the model equation of non-linear diffusion". In: *Monthly Notices of the Royal Astronomical Society* 236.2 (1989), pp. 385–402.

[128] Sergei N Gurbatov et al. "Large-scale structure of the Universe. The Zeldovich approximation and the adhesion model". In: *Physics-Uspekhi* 55.3 (2012), pp. 223–249.

[129] Alan H. Guth. "Inflationary universe: A possible solution to the horizon and flatness problems". In: *Physical Review D* 23.2 (1981), pp. 347–356.

[130] Francesco Haardt & Piero Madau. "Radiative transfer in a clumpy universe IV: New synthesis models of the cosmic UV/X-ray background". In: *The Astrophysical Journal* 746.2 (2012), p. 125.

[131] Salman Habib et al. "HACC: Simulating sky surveys on state-of-the-art supercomputing architectures". In: *New Astronomy* 42 (2016), pp. 49–65.

[132] O. Hahn et al. "Properties of dark matter haloes in clusters, filaments, sheets and voids". In: *Monthly Notices of the Royal Astronomical Society* 375.2 (2007), pp. 489–499.

[133] Oliver Hahn & Tom Abel. "Multi-scale initial conditions for cosmological simulations". In: *Monthly Notices of the Royal Astronomical Society* 415.3 (2011), pp. 2101–2121.

[134] Oliver Hahn & Raul E. Angulo. "An adaptively refined phase–space element method for cosmological simulations and collisionless dynamics". In: *Monthly Notices of the Royal Astronomical Society* 455.1 (2016), pp. 1115–1133.

[135] Oliver Hahn & Aseem Paranjape. "The locations of halo formation and the peaks formalism". In: *Monthly Notices of the Royal Astronomical Society* 438.1 (2014), pp. 878–899.

[136] Oliver Hahn et al. "A new approach to simulating collisionless dark matter fluids". In: *Monthly Notices of the Royal Astronomical Society* 434.2 (2013), pp. 1171–1191.

[137] Oliver Hahn et al. "Rhapsody-G simulations I: the cool cores, hot gas and stellar content of massive galaxy clusters". In: *Monthly Notices of the Royal Astronomical Society* (2017), stx001.

[138] Oliver Hahn et al. "The evolution of dark matter halo properties in clusters, filaments, sheets and voids". In: *Monthly Notices of the Royal Astronomical Society* 381.1 (2007), pp. 41–51.

[139] Oliver Hahn et al. "The properties of cosmic velocity fields". In: *Monthly Notices of the Royal Astronomical Society* 454.4 (2015), pp. 3920–3937.

[140] Oliver Hahn et al. "Tidal effects and the environment dependence of halo assembly". In: *Monthly Notices of the Royal Astronomical Society* 398.4 (2009), pp. 1742–1756.

[141] Jiaxin Han et al. "Resolving subhaloes' lives with the Hierarchical Bound-Tracing algorithm". In: *Monthly Notices of the Royal Astronomical Society* 427.3 (2012), pp. 2437–2449.

[142] Steen H. Hansen et al. "An Alternative to Grids and Glasses: Quaquaversal Pre-Initial Conditions for N -Body Simulations". In: *The Astrophysical Journal* 656.2 (2007), pp. 631–635.

[143] Steen H Hansen et al. "A universal velocity distribution of relaxed collisionless structures". In: *Journal of Cosmology and Astroparticle Physics* 2006.01 (2006), pp. 014–014.

[144] E. R. Harrison. "Fluctuations at the Threshold of Classical Cosmology". In: *Physical Review D* 1.10 (1970), pp. 2726–2730.

[145] Siyu He et al. "Learning to predict the cosmological structure formation". In: *Proceedings of the National Academy of Sciences* 116.28 (2019), pp. 13825–13832.

[146] A. Heavens & J. Peacock. "Tidal torques and local density maxima". In: *Monthly Notices of the Royal Astronomical Society* 232.2 (1988), pp. 339–360.

[147] A. Heavens et al. "Intrinsic correlation of galaxy shapes: implications for weak lensing measurements". In: *Monthly Notices of the Royal Astronomical Society* 319.2 (2000), pp. 649–656.

[148] Katrin Heitmann et al. "HACC Cosmological Simulations: First Data Release". In: (2019). arXiv: 1904.11966.

[149] C. Heymans et al. "Potential sources of contamination to weak lensing measurements: constraints from N-body simulations". In: *Monthly Notices of the Royal Astronomical Society* 371.2 (2006), pp. 750–760.

[150] Johan Hidding et al. "The Zel'dovich approximation: key to understanding cosmic web complexity". In: *Monthly Notices of the Royal Astronomical Society* 437.4 (2014), pp. 3442–3472.

[151] G. Hinshaw et al. "Nine-year Wilkinson Microwave Anisotropy Propbe (WMAP) observations: cosmological parameter results". In: *The Astrophysical Journal Supplement Series* 208.2 (2013), p. 19.

[152] Christopher M. Hirata & Uroš Seljak. "Intrinsic alignment-lensing interference as a contaminant of cosmic shear". In: *Physical Review D* 70.6 (2004), p. 063526.

[153] Matthew Ho et al. "A Robust and Efficient Deep Learning Method for Dynamical Mass Measurements of Galaxy Clusters". In: (2019). arXiv: 1902.05950.

[154] R .W. Hockney & James W. Eastwood. *Computer Simulation Using Particles*. Bristol: IOP Publishing Ltd, 1988.

[155] Yehuda Hoffman et al. "A kinematic classification of the cosmic web". In: *Monthly Notices of the Royal Astronomical Society* 425.3 (2012), pp. 2049–2057.

[156] Philip F. Hopkins et al. "Cluster Alignments and Ellipticities in ΛCDM Cosmology". In: *The Astrophysical Journal* 618.1 (2005), pp. 1–15.

[157] Philip F. Hopkins et al. "Galaxies on FIRE (Feedback In Realistic Environments): stellar feedback explains cosmologically inefficient star formation". In: *Monthly Notices of the Royal Astronomical Society* 445.1 (2014), pp. 581–603.

[158] Philip F Hopkins et al. "FIRE-2 simulations: physics versus numerics in galaxy formation". In: *Monthly Notices of the Royal Astronomical Society* 480.1 (2018), pp. 800–863.

[159] Cathy Horellou & Joel Berge. "Dark energy and the evolution of spherical overdensities". In: *Monthly Notices of the Royal Astronomical Society* 360.4 (2005), pp. 1393–1400.

[160] Cullan Howlett et al. "L-PICOLA: A parallel code for fast dark matter simulation". In: (2015). arXiv: 1506.03737.

[161] F. Hoyle. "The origin of the rotations of the galaxies". In: *Symposium on the Motion of Gaseous Masses of Cosmological Dimensions*. Paris: Central Air Documents Office, Ohio, 1949, pp. 195–197.

[162] F. Hoyle & R. J. Tayler. "The Mystery of the Cosmic Helium Abundance". In: *Nature* 203.4950 (1964), pp. 1108–1110.

[163] E. Hubble. "A relation between distance and radial velocity among extra-galactic nebulae". In: *Proceedings of the National Academy of Sciences* 15.3 (1929), pp. 168–173.

[164] E. P. Hubble. "A spiral nebula as a stellar system, Messier 31." In: *The Astrophysical Journal* 69 (1929), p. 103.

[165] L. Hui & N. Y. Gnedin. "Equation of state of the photoionized intergalactic medium". In: *Monthly Notices of the Royal Astronomical Society* 292.1 (1997), pp. 27–42.

[166] V Icke. "Formation of Galaxies inside Clusters". In: *Astronomy and Astrophysics* 27 (1973), p. 1.

[167] Željko Ivezić et al. "LSST: from Science Drivers to Reference Design and Anticipated Data Products". In: (2008).

[168] Albert Izard et al. "ICE-COLA: towards fast and accurate synthetic galaxy catalogues optimizing a quasi- N -body method". In: *Monthly Notices of the Royal Astronomical Society* 459.3 (2016), pp. 2327–2341.

[169] Goran Jelic-Cizmek et al. "The generation of vorticity in cosmological N-body simulations". In: *Journal of Cosmology and Astroparticle Physics* 2018.09 (2018), pp. 006–006.

[170] A. Jenkins et al. "The mass function of dark matter haloes". In: *Monthly Notices of the Royal Astronomical Society* 321.2 (2001), pp. 372–384.

[171] Adrian Jenkins. "A new way of setting the phases for cosmological multiscale Gaussian initial conditions". In: *Monthly Notices of the Royal Astronomical Society* 434.3 (2013), pp. 2094–2120.

[172] Lilian Jiang et al. "N-body dark matter haloes with simple hierarchical histories". In: *Monthly Notices of the Royal Astronomical Society* 440.3 (2014), pp. 2115–2135.

[173] Y. P. Jing. "Correcting for the Alias Effect When Measuring the Power Spectrum Using a Fast Fourier Transform". In: *The Astrophysical Journal* 620.2 (2005), pp. 559–563.

[174] Rahul Kannan et al. "Increasing Black Hole Feedback-induced Quenching with Anisotropic Thermal Conduction". In: *The Astrophysical Journal* 837.2 (2017), p. L18.

[175] I. D. Karachentsev et al. "The very local Hubble flow". In: *Astronomy & Astrophysics* 389.3 (2002), pp. 812–824.

[176] S. Kaviraj et al. "Galaxy merger histories and the role of merging in driving star formation at z > 1". In: *Monthly Notices of the Royal Astronomical Society* 452.3 (2015), pp. 2845–2850.

[177] Leonid G. Khachiyan. "Rounding of Polytopes in the Real Number Model of Computation". In: *Mathematics of Operations Research* 21.2 (1996), pp. 307–320.

[178] Ji-hoon Kim et al. "The AGORA high-resolution galaxy simulations comparison project". In: *The Astrophysical Journal Supplement Series* 210.1 (2013), p. 14.

[179] Juhan Kim et al. "The horizon run N-body simulation: baryon acoustic oscillations and topology of large-scale structure of the universe". In: *The Astrophysical Journal* 701.2 (2009), pp. 1547–1559.

[180] L. J. King et al. "Cluster mass profiles from weak lensing: The influence of substructure". In: *Astronomy & Astrophysics* 378.3 (2001), pp. 748–755.

[181] Anatoly A. Klypin et al. "Dark matter halos in the standard cosmological model: results from the Bolshoi simulation". In: *The Astrophysical Journal* 740.2 (2011), p. 102.

[182] Alexander Knebe et al. "Haloes gone MAD: The Halo-Finder Comparison Project". In: *Monthly Notices of the Royal Astronomical Society* 415.3 (2011), pp. 2293–2318.

[183] Alexander Knebe et al. "Structure finding in cosmological simulations: the state of affairs". In: *Monthly Notices of the Royal Astronomical Society* 435.2 (2013), pp. 1618–1658.

[184] Alexander Knebe et al. "The impact of baryonic physics on the shape and radial alignment of substructures in cosmological dark matter haloes". In: *Monthly Notices of the Royal Astronomical Society* (2010).

[185] Christian Knobel. "An Introduction into the Theory of Cosmological Structure Formation". In: (2012). arXiv: `1208.5931`.

[186] E. Komatsu & U. Seljak. "Universal gas density and temperature profile". In: *Monthly Notices of the Royal Astronomical Society* 327.4 (2001), pp. 1353–1366.

[187] E. Komatsu et al. "Seven-year Wilkinson Microwave Anisotropy Probe (WMAP) observations: cosmological interpretation". In: *The Astrophysical Journal Supplement Series* 192.2 (2011), p. 18.

[188] Andrey V. Kravtsov et al. "Adaptive Refinement Tree: A New High-Resolution N -Body Code for Cosmological Simulations". In: *The Astrophysical Journal Supplement Series* 111.1 (1997), pp. 73–94.

[189] P. Kumar & E. A. Yildirim. "Minimum-Volume Enclosing Ellipsoids and Core Sets". In: *Journal of Optimization Theory and Applications* 126.1 (2005), pp. 1–21.

[190] Cedric Lacey & Shanu Cole. "Merger rates in hierarchical models of galaxy formation – II. Comparison with N-body simulations". In: *Monthly Notices of the Royal Astronomical Society* 271.3 (1994), pp. 676–692.

[191] François Lanusse et al. "CMU DeepLens: deep learning for automatic image-based galaxy–galaxy strong lens finding". In: *Monthly Notices of the Royal Astronomical Society* 473.3 (2018), pp. 3895–3906.

[192] R. Laureijs et al. "Euclid Definition Study Report". In: (2011). arXiv: `1110.3193`.

[193] Jounghun Lee & Ue-Li Pen. "Cosmic Shear from Galaxy Spins". In: *The Astrophysical Journal* 532.1 (2000), pp. L5–L8.

[194] Boris Leistedt et al. "Hierarchical Modeling and Statistical Calibration for Photometric Redshifts". In: *The Astrophysical Journal* 881.1 (2019), p. 80.

[195] G. Lemaître. “Un Univers homogène de masse constante et de rayon croissant rendant compte de la vitesse radiale des nébuleuses extra-galactiques”. In: *Annales de la Société Scientifique de Bruxelles* 47 (1927), p. 49.

[196] Antony Lewis et al. “Efficient Computation of Cosmic Microwave Background Anisotropies in Closed Friedmann-Robertson-Walker Models”. In: *The Astrophysical Journal* 538.2 (2000), pp. 473–476.

[197] Shihong Liao. “An alternative method to generate pre-initial conditions for cosmological N-body simulations”. In: *Monthly Notices of the Royal Astronomical Society* 481.3 (2018), pp. 3750–3760.

[198] Noam I. Libeskind et al. “The cosmic web and the orientation of angular momenta”. In: *Monthly Notices of the Royal Astronomical Society: Letters* 421.1 (2012), pp. L137–L141.

[199] Noam I Libeskind et al. “Tracing the cosmic web”. In: *Monthly Notices of the Royal Astronomical Society* 473.1 (2018), pp. 1195–1217.

[200] Andrew R Liddle. “An introduction to cosmological inflation”. In: (1999). arXiv: 9901124 [astro-ph].

[201] E. M. Lifshitz. “On the gravitational stability of the expanding universe”. In: *Zhurnal Eksperimentalnoi i Teoreticheskoi Fiziki* 16 (1946), pp. 587–602.

[202] A.D. Linde. “A new inflationary universe scenario: A possible solution of the horizon, flatness, homogeneity, isotropy and primordial monopole problems”. In: *Physics Letters B* 108.6 (1982), pp. 389–393.

[203] Pablo López et al. “Deviations from tidal torque theory: environment dependences on halo angular momentum growth”. In: *Monthly Notices of the Royal Astronomical Society* 485.4 (2019), pp. 5244–5255.

[204] Luisa Lucie-Smith et al. “An interpretable machine learning framework for dark matter halo formation”. In: (2019). arXiv: 1906.06339.

[205] Luisa Lucie-Smith et al. “Machine learning cosmological structure formation”. In: *Monthly Notices of the Royal Astronomical Society* 479.3 (2018), pp. 3405–3414.

[206] Aaron D. Ludlow & Cristiano Porciani. “The peaks formalism and the formation of cold dark matter haloes”. In: *Monthly Notices of the Royal Astronomical Society* 413.3 (2011), pp. 1961–1972.

[207] Aaron D. Ludlow et al. “The formation of CDM haloes – I. Collapse thresholds and the ellipsoidal collapse model”. In: *Monthly Notices of the Royal Astronomical Society* 445.4 (2014), pp. 4110–4123.

[208] Aaron D Ludlow et al. “Numerical convergence of simulations of galaxy formation: the abundance and internal structure of cold dark matter haloes”. In: *Monthly Notices of the Royal Astronomical Society* 488.3 (2019), pp. 3663–3684.

[209] Roger Lynds. “The Absorption-Line Spectrum of 4c 05.34”. In: *The Astrophysical Journal* 164 (1971), p. L73.

[210] Hareth S. Mahdi et al. “MATTER IN THE BEAM: WEAK LENSING, SUBSTRUCTURES, AND THE TEMPERATURE OF DARK MATTER”. In: *The Astrophysical Journal* 826.2 (2016), p. 212.

[211] R. G. Mann et al. “The richness dependence of cluster correlations”. In: *Monthly Notices of the Royal Astronomical Society* 263.3 (1993), pp. 798–816.

[212] Philip Mansfield et al. “Splashback Shells of Cold Dark Matter Halos”. In: *The Astrophysical Journal* 841.1 (2017), p. 34.

[213] Yao-Yuan Mao et al. "HALO-TO-HALO SIMILARITY AND SCATTER IN THE VELOCITY DISTRIBUTION OF DARK MATTER". In: *The Astrophysical Journal* 764.1 (2013), p. 35.

[214] Federico Marinacci et al. "First results from the IllustrisTNG simulations: radio haloes and magnetic fields". In: *Monthly Notices of the Royal Astronomical Society* (2018).

[215] Federico Marinacci et al. "The large-scale properties of simulated cosmological magnetic fields". In: *Monthly Notices of the Royal Astronomical Society* 453.4 (2015), pp. 4000–4020.

[216] S. McAlpine et al. "The eagle simulations of galaxy formation: Public release of halo and galaxy catalogues". In: *Astronomy and Computing* 15 (2016), pp. 72–89.

[217] C McBride et al. "LasDamas Mock Galaxy Catalogs for SDSS". In: *American Astronomical Society Meeting Abstracts #213*. Vol. 41. Bulletin of the American Astronomical Society. 2009, p. 253.

[218] Patrick McDonald et al. "The Lyα Forest Power Spectrum from the Sloan Digital Sky Survey". In: *The Astrophysical Journal Supplement Series* 163.1 (2006), pp. 80–109.

[219] Matthew McQuinn & Phoebe R. Upton Sanderbeck. "On the intergalactic temperature–density relation". In: *Monthly Notices of the Royal Astronomical Society* 456.1 (2016), pp. 47–54.

[220] Matthew McQuinn et al. "He II REIONIZATION AND ITS EFFECT ON THE INTERGALACTIC MEDIUM". In: *The Astrophysical Journal* 694.2 (2009), pp. 842–866.

[221] Houjun Mo et al. *Galaxy Formation and Evolution*. Cambridge: Cambridge University Press, 2010.

[222] P. Monaco et al. "An accurate tool for the fast generation of dark matter halo catalogues". In: *Monthly Notices of the Royal Astronomical Society* 433.3 (2013), pp. 2389–2402.

[223] Pierluigi Monaco. "Approximate methods for the generation of dark matter halo catalogs in the age of precision cosmology". In: (2016). arXiv: `1605.07752`.

[224] Pierluigi Monaco. "Dynamics in the Cosmological Mass Function (or, why does the Press-Schechter work?)" In: *Observational Cosmology: The Development of Galaxy Systems*. Ed. by G Giuricin et al. Vol. 176. Astronomical Society of the Pacific Conference Series. 1999, p. 186. arXiv: `astro-ph/9811085 [astro-ph]`.

[225] Pierluigi Monaco et al. "The pinocchio algorithm: pinpointing orbit-crossing collapsed hierarchical objects in a linear density field". In: *Monthly Notices of the Royal Astronomical Society* 331.3 (2002), pp. 587–608.

[226] J. J. Monaghan & J. C. Lattanzio. "A refined particle method for astrophysical problems". In: *Astronomy and Astrophysics* 149 (1985), pp. 135–143.

[227] Surhud More et al. "The overdensity and masses of the friends-of-friends halos and universality of halo mass function". In: *The Astrophysical Journal Supplement Series* 195.1 (2011), p. 4.

[228] Surhud More et al. "The splashback radius as a physical halo bondary and the growth of halo mass". In: *The Astrophysical Journal* 810.1 (2015), p. 36.

[229] Dipak Munshi et al. "Nonlinear approximations to gravitational instability: A comparison in the quasi-linear regime". In: *The Astrophysical Journal* 436 (1994), p. 517.

[230] J. F. Navarro et al. "The inner structure of ΛCDM haloes - III. Universality and asymptotic slopes". In: *Monthly Notices of the Royal Astronomical Society* 349.3 (2004), pp. 1039–1051.

[231] Julio F. Navarro et al. "The Structure of Cold Dark Matter Halos". In: *The Astrophysical Journal* 462 (1996), p. 563.

[232] Dylan Nelson et al. "The IllustrisTNG simulations: public data release". In: *Computational Astrophysics and Cosmology* 6.1 (2019), p. 2.

[233] Mark C. Neyrinck. "zobov: a parameter-free void-finding algorithm". In: *Monthly Notices of the Royal Astronomical Society* 386.4 (2008), pp. 2101–2109.

[234] M. Ntampaka et al. "A Deep Learning Approach to Galaxy Cluster X-Ray Masses". In: *The Astrophysical Journal* 876.1 (2019), p. 82.

[235] M. Ntampaka et al. "A Machine Learning Approach for Dynamical Mass Measurements of Galaxy Clusters". In: *The Astrophysical Journal* 803.2 (2015), p. 50.

[236] M. Ntampaka et al. "Dynamical Mass Measurements of Contaminated Galaxy Clusters Using Machine Learning". In: *The Astrophysical Journal* 831.2 (2016), p. 135.

[237] Adi Nusser & Avishai Dekel. "Filamentary structure from Gaussian fluctuations using the adhesion approximation". In: *The Astrophysical Journal* 362 (1990), p. 14.

[238] Julian Onions et al. "Subhaloes going Notts: the subhalo-finder comparison project". In: *Monthly Notices of the Royal Astronomical Society* 423.2 (2012), pp. 1200–1214.

[239] Jose Oñorbe et al. "How to zoom: Bias, contamination and lagrange volumes in multimass cosmological simulations". In: *Monthly Notices of the Royal Astronomical Society* (2013).

[240] F. Pace et al. "Spherical collapse model in dark-energy cosmologies". In: *Monthly Notices of the Royal Astronomical Society* (2010), no–no.

[241] Daeseong Park & Jounghun Lee. "Void Ellipticity Distribution as a Probe of Cosmology". In: *Physical Review Letters* 98.8 (2007), p. 081301.

[242] J. A. Peacock. "Statistics of cosmological density fields". In: *New Insights into the Universe. Lecture Notes in Physics, vol 408*. Ed. by V. J. Martinez et al. Berlin, Heidelberg: Springer Berlin Heidelberg, 1992.

[243] P. J. E. Peebles. "Origin of the Angular Momentum of Galaxies". In: *The Astrophysical Journal* 155 (1969), p. 393.

[244] P. J. E. Peebles. "Rotation of Galaxies and the Gravitational Instability Picture". In: *Astronomy and Astrophysics* 11 (1971), p. 377.

[245] P. J. E. Peebles. *The large-scale structure of the universe*. New Jersey, United States: Princeton University Press, 1980, p. 440.

[246] Sébastien Peirani et al. "LyMAS: Predicting large-scale Lya forest statistics from the dark matter density field". In: *The Astrophysical Journal* 784.1 (2014), p. 11.

[247] Ue-Li Pen. "Generating Cosmological Gaussian Random Fields". In: *The Astrophysical Journal* 490.2 (1997), pp. L127–L130.

[248] A. A. Penzias & R. W. Wilson. "A Measurement of Excess Antenna Temperature at 4080 Mc/s." In: *The Astrophysical Journal* 142 (1965), p. 419.

[249] S. Perlmutter et al. "Measurements of Ω and Λ from 42 High-Redshift Supernovae". In: *The Astrophysical Journal* 517.2 (1999), pp. 565–586.

[250] Christophe Pichon et al. "Why do galactic spins flip in the cosmic web? A Theory of Tidal Torques near saddles". In: *Proceedings of the International Astronomical Union* 11.S308 (2014), pp. 421–432.

[251] J J Pillai. *Functional Brain Tumor Imaging*. Springer New York, 2013.

[252] Annalisa Pillepich et al. "Simulating galaxy formation with the IllustrisTNG model". In: *Monthly Notices of the Royal Astronomical Society* 473.3 (2018), pp. 4077–4106.

[253] Alice Pisani et al. "Counting voids to probe dark energy". In: *Physical Review D* 92.8 (2015), p. 083531.

[254] Planck Collaboration et al. "Planck 2018 results. X. Constraints on inflation". In: (2018). arXiv: 1807.06211.

[255] E. Platen et al. "A cosmic watershed: the WVF void detection technique". In: *Monthly Notices of the Royal Astronomical Society* 380.2 (2007), pp. 551–570.

[256] Erwin Platen et al. "Alignment of voids in the cosmic web". In: *Monthly Notices of the Royal Astronomical Society* 387.1 (2008), pp. 128–136.

[257] H. C. Plummer. "On the Problem of Distribution in Globular Star Clusters: (Plate 8.)" In: *Monthly Notices of the Royal Astronomical Society* 71.5 (1911), pp. 460–470.

[258] Dmitry Pogosyan et al. "Cosmic Web: Origin and Observables". In: *Wide Field Surveys in Cosmology*. Ed. by Stephane Colombi et al. Vol. 14. 1998, p. 61. arXiv: 9810072 [astro-ph].

[259] Cristiano Porciani et al. "Testing tidal-torque theory - I. Spin amplitude and direction". In: *Monthly Notices of the Royal Astronomical Society* 332.2 (2002), pp. 325–338.

[260] Cristiano Porciani et al. "Testing tidal-torque theory - II. Alignment of inertia and shear and the characteristics of protohaloes". In: *Monthly Notices of the Royal Astronomical Society* 332.2 (2002), pp. 339–351.

[261] T Poston & I N Stewart. *Catastrophe Theory and Its Applications*. Pitman, 1978.

[262] D Potter et al. "PKDGRAV3: beyond trillion particle cosmological simulations for the next era of galaxy surveys". In: *Computational Astrophysics and Cosmology* 4 (2017), p. 2.

[263] C. Power et al. "The Inner Structure of LambdaCDM Halos I: A Numerical Convergence Study". In: *Monthly Notice of the Royal Astronomical Society* 338.1 (2002), pp. 14–34.

[264] William H. Press & Paul Schechter. "Formation of Galaxies and Clusters of Galaxies by Self-Similar Gravitational Condensation". In: *The Astrophysical Journal* 187 (1974), p. 425.

[265] Iu. P Pskovskii. "Light curves, color curves, and expansion velocity of type I supernovae as functions of the rate of brightness decline". In: *Soviet Astronomy* 21 (1977), p. 675.

[266] Ewald Puchwein et al. "Consistent modelling of the meta-galactic UV background and the thermal/ionization history of the intergalactic medium". In: *Monthly Notices of the Royal Astronomical Society* 485.1 (2019), pp. 47–68.

[267] Sebastián Pueblas & Román Scoccimarro. "Generation of vorticity and velocity dispersion by orbit crossing". In: *Physical Review D* 80.4 (2009), p. 043504.

[268] Yan Qu et al. "A chronicle of galaxy mass assembly in the EAGLE simulation". In: *Monthly Notices of the Royal Astronomical Society* 464.2 (2017), pp. 1659–1675.

[269] Nesar S. Ramachandra & Sergei F. Shandarin. "Multi-stream portrait of the cosmic web". In: *Monthly Notices of the Royal Astronomical Society* 452.2 (2015), pp. 1643–1653.

[270] Siamak Ravanbakhsh et al. "Estimating Cosmological Parameters from the Dark Matter Distribution". In: (2017). arXiv: 1711.02033.

[271] Darren Reed et al. "Evolution of the mass function of dark matter haloes". In: *Monthly Notices of the Royal Astronomical Society* 346.2 (2003), pp. 565–572.

[272] Adam G. Riess et al. "Observational Evidence from Supernovae for an Accelerating Universe and a Cosmological Constant". In: *The Astronomical Journal* 116.3 (1998), pp. 1009–1038.

[273] Sandra Robles et al. "A Halo Merger Tree Generation and Evaluation Framework". In: (2019). arXiv: 1906.09382.

[274] Andres C. Rodríguez et al. "Fast cosmic web simulations with generative adversarial networks". In: *Computational Astrophysics and Cosmology* 5.1 (2018), p. 4.

[275] Emilio Romano-Díaz et al. "ZOMG – II. Does the halo assembly history influence central galaxies and gas accretion?" In: *Monthly Notices of the Royal Astronomical Society* 469.2 (2017), pp. 1809–1823.

[276] Varun Sahni & Peter Coles. "Approximation Methods for Non-linear Gravitational Clustering". In: *Physics Reports* 262.1-2 (1995), pp. 1–135.

[277] Varun Sahni et al. "The evolution of voids in the adhesion approximation". In: *The Astrophysical Journal* 431 (1994), p. 20.

[278] W. E. Schaap & R van de Weygaert. "Continuous fields and discrete samples: reconstruction through Delaunay tessellations". In: *Astronomy and Astrophysics* 363 (2000), pp. L29–L32.

[279] Joop Schaye et al. "The EAGLE project: simulating the evolution and assembly of galaxies and their environments". In: *Monthly Notices of the Royal Astronomical Society* 446.1 (2015), pp. 521–554.

[280] Aurel Schneider et al. "Halo mass function and the free streaming scale". In: *Monthly Notices of the Royal Astronomical Society* 433.2 (2013), pp. 1573–1587.

[281] Aurel Schneider et al. "Non-linear evolution of cosmological structures in warm dark matter models". In: *Monthly Notices of the Royal Astronomical Society* 424.1 (2012), pp. 684–698.

[282] R. Scoccimarro. "Transients from initial conditions: a perturbative analysis". In: *Monthly Notices of the Royal Astronomical Society* 299.4 (1998), pp. 1097–1118.

[283] E Sefusatti et al. "Accurate estimators of correlation functions in Fourier space". In: *Monthly Notices of the Royal Astronomical Society* 460.4 (2016), pp. 3624–3636.

[284] S. F. Shandarin & Ya. B. Zeldovich. "The large-scale structure of the universe: Turbulence, intermittency, structures in a self-gravitating medium". In: *Reviews of Modern Physics* 61.2 (1989), pp. 185–220.

[285] Sergei Shandarin et al. "Cosmic web, multistream flows, and tessellations". In: *Physical Review D* 85.8 (2012), p. 083005.

[286] P. R. Shapiro et al. "Pancakes and the formation of galaxies in a neutrino-dominated universe". In: *The Astrophysical Journal* 275 (1983), p. 413.

[287] Jiajian Shen et al. "An Excursion Set Model of the Cosmic Web: The Abundance of Sheets, Filaments, and Halos". In: *The Astrophysical Journal* 645.2 (2006), pp. 783–791.

[288] Ravi K Sheth & Giuseppe Tormen. "Large-scale bias and the peak background split". In: *Monthly Notices of the Royal Astronomical Society* 308.1 (1999), pp. 119–126.

[289] Ravi K Sheth et al. "Ellipsoidal collapse and an improved model for the number and spatial distribution of dark matter haloes". In: *Monthly Notices of the Royal Astronomical Society* 323.1 (2001), pp. 1–12.

[290] Ravi K Sheth et al. "Marked correlations in galaxy formation models". In: *arXiv* (2005). arXiv: 0511773 [astro-ph].

[291] Edwin Sirko. "Initial Conditions to Cosmological N -Body Simulations, or, How to Run an Ensemble of Simulations". In: *The Astrophysical Journal* 634.2 (2005), pp. 728–743.

[292] Ramin A. Skibba et al. "Measures of galaxy environment – II. Rank-ordered mark correlations". In: *Monthly Notices of the Royal Astronomical Society* 429.1 (2013), pp. 458–468.

[293] Ramin Skibba et al. "The luminosity-weighted or 'marked' correlation function". In: *Monthly Notices of the Royal Astronomical Society* 369.1 (2006), pp. 68–76.

[294] G. F. Smoot et al. "Structure in the COBE differential microwave radiometer first-year maps". In: *The Astrophysical Journal* 396 (1992), p. L1.

[295] Rachel S. Somerville & Romeel Davé. "Physical Models of Galaxy Formation in a Cosmological Framework". In: *Annual Review of Astronomy and Astrophysics* 53.1 (2015), pp. 51–113.

[296] Jenny G Sorce & Elmo Tempel. "Galaxy clusters in simulations of the local Universe: a matter of constraints". In: *Monthly Notices of the Royal Astronomical Society* 476.4 (2018), pp. 4362–4371.

[297] Daniele Sorini et al. "Modeling the Lya forest in collisionless simulations". In: *The Astrophysical Journal* 827.2 (2016), p. 97.

[298] T. Sousbie. "The persistent cosmic web and its filamentary structure - I. Theory and implementation". In: *Monthly Notices of the Royal Astronomical Society* 414.1 (2011), pp. 350–383.

[299] D. Spergel et al. "Wide-Field InfraRed Survey Telescope-Astrophysics Focused Telescope Assets WFIRST-AFTA Final Report". In: (2013). arXiv: `1305.5422`.

[300] Volker Springel. "The cosmological simulation code gadget-2". In: *Monthly Notices of the Royal Astronomical Society* 364.4 (2005), pp. 1105–1134.

[301] Volker Springel et al. "Populating a cluster of galaxies - I. Results at z=0". In: *Monthly Notices of the Royal Astronomical Society* 328.3 (2001), pp. 726–750.

[302] Square Kilometre Array Cosmology Science Working Group et al. "Cosmology with Phase 1 of the Square Kilometre Array; Red Book 2018: Technical specifications and performance forecasts". In: (2018). arXiv: `1811.02743`.

[303] George Stein et al. "The mass-Peak Patch algorithm for fast generation of deep all-sky dark matter halo catalogues and its N -body validation". In: *Monthly Notices of the Royal Astronomical Society* 483.2 (2019), pp. 2236–2250.

[304] Dietrich Stoyan. "On Correlations of Marked Point Processes". In: *Math. Nachr.* 116.1 (1984), pp. 197–207.

[305] Dietrich Stoyan & Helga Stoyan. *Fractals, Random Shapes, and Point Fields : Methods of Geometrical Statistics*. Wiley, New York, 1994.

[306] Jens Stücker et al. "The median density of the Universe". In: *Monthly Notices of the Royal Astronomical Society* 477.3 (2018), pp. 3230–3246.

[307] D. Syer & S. D. M. White. "Dark halo mergers and the formation of a universal profile". In: *Monthly Notices of the Royal Astronomical Society* 293.4 (1998), pp. 337–342.

[308] Satoshi Tanaka et al. "Multidimensional Vlasov–Poisson Simulations with High-order Monotonicity- and Positivity-preserving Schemes". In: *The Astrophysical Journal* 849.2 (2017), p. 76.

[309] Atsushi Taruya & Stéphane Colombi. "Post-collapse perturbation theory in 1D cosmology – beyond shell-crossing". In: *Monthly Notices of the Royal Astronomical Society* 470.4 (2017), pp. 4858–4884.

[310] Svetlin Tassev et al. "Solving large scale structure in ten easy steps with COLA". In: *Journal of Cosmology and Astroparticle Physics* 2013.06 (2013), pp. 036–036.

[311] Max Tegmark et al. "The Three-Dimensional Power Spectrum of Galaxies from the Sloan Digital Sky Survey". In: *The Astrophysical Journal* 606.2 (2004), pp. 702–740.

[312] R. Teyssier. "Cosmological hydrodynamics with adaptive mesh refinement". In: *Astronomy & Astrophysics* 385.1 (2002), pp. 337–364.

[313] Jeremy L. Tinker et al. "The Large-Scale Bias of Dark Matter Halos: Numerical Calibration and Model Tests". In: *The Astrophysical Journal* 724.2 (2010), pp. 878–886.

[314] Jeremy Tinker et al. "Toward a Halo Mass Function for Precision Cosmology: The Limits of Universality". In: *The Astrophysical Journal* 688.2 (2008), pp. 709–728.

[315] Tilman Tröster et al. "Painting with baryons: augmenting N-body simulations with gas using deep generative models". In: *Monthly Notices of the Royal Astronomical Society: Letters* 487.1 (2019), pp. L24–L29.

[316] U. Trottenberg et al. *Multigrid*. Academic Press, 2001, p. 631.

[317] M.A. Troxel & Mustapha Ishak. "The intrinsic alignment of galaxies and its impact on weak gravitational lensing in an era of precision cosmology". In: *Physics Reports* 558 (2015), pp. 1–59.

[318] Patrick Valageas & Francis Bernardeau. "Density fields and halo mass functions in the geometrical adhesion toy model". In: *Physical Review D* 83.4 (2011), p. 043508.

[319] Matteo Viel et al. "Constraining warm dark matter candidates including sterile neutrinos and light gravitinos with WMAP and the Lyman-a forest". In: *Physical Review D* 71.6 (2005), p. 063534.

[320] Rodrigo Voivodic et al. "Excursion Set Halos – ExSHalos: A New Parameter Free Method for Fast Generation of Halo Catalogues". In: (2019). arXiv: `1906.06630`.

[321] Huiyuan Wang et al. "ELUCID - Exploring the local Universe with reconstructed initial density field. III. Constrained simulation in the SSSD volume". In: *The Astrophysical Journal* 831.2 (2016), p. 164.

[322] Jie Wang & Simon D. M. White. "Discreteness effects in simulations of hot/warm dark matter". In: *Monthly Notices of the Royal Astronomical Society* 380.1 (2007), pp. 93–103.

[323] Michael S. Warren et al. "Precision Determination of the Mass Function of Dark Matter Halos". In: *The Astrophysical Journal* 646.2 (2006), pp. 881–885.

[324] Risa H. Wechsler et al. "The Dependence of Halo Clustering on Halo Formation History, Concentration, and Occupation". In: *The Astrophysical Journal* 652.1 (2006), pp. 71–84.

[325] Steven Weinberg. *Cosmology*. Oxford University Press, 2008, p. 593.

[326] Pieter Wesseling. *An introduction to multigrid methods*. Wiley, 1992, p. 284.

[327] Rien van de Weygaert & Erwin Platen. "Cosmic Voids: Structure, Dynamics and Galaxies". In: *International Journal of Modern Physics: Conference Series* 01 (2011), pp. 41–66.

[328] Rien van de Weygaert & W Schaap. "The Cosmic Web: Geometric Analysis". In: *Data Analysis in Cosmology, Lecture Notes in Physics, vol. 665.* Ed. by V. J. Martinez et al. Berlin: Springer, 2009, pp. 291–413.

[329] Rien van de Weygaert et al. "The Zeldovich Universe: Genesis and Growth of the Cosmic Web". In: *Proceedings of the International Astronomical Union* 11.S308 (2014), f1–f27.

[330] Martin White. "A marked correlation function for constraining modified gravity models". In: *Journal of Cosmology and Astroparticle Physics* 2016.11 (2016), pp. 057–057.

[331] S. D. M. White. "Angular momentum growth in protogalaxies". In: *The Astrophysical Journal* 286 (1984), p. 38.

[332] S. D. M. White. "Formation and Evolution of Galaxies". In: *Cosmology and Large Scale Structure*. Ed. by Richard Schaeffer et al. Amsterdam: Elsevier Scientific Publishing Company, 1996, p. 349.

[333] S. D. M. White. "Further simulations of merging galaxies". In: *Monthly Notices of the Royal Astronomical Society* 189.4 (1979), pp. 831–852.

[334] Gerald Beresford Whitham. *Linear and nonlinear waves*. John Wiley & Sons, 2011.

[335] B. G. Williams et al. "Exact hierarchical clustering in one dimension". In: *Monthly Notices of the Royal Astronomical Society* 250.2 (1991), pp. 458–476.

[336] Hao-Yi Wu et al. "Rhapsody I: Structural properties and formation history from a statistical sample of re-simulated cluster-size halos". In: *The Astrophysical Journal* 763.2 (2013), p. 70.

[337] Hao-Yi Wu et al. "Rhapsody II. Subhalo Properties and the impact of tidal stripping from astatistical sample of cluster-size halos". In: *The Astrophysical Journal* 767.1 (2013), p. 23.

[338] Guohong Xu. "A New Parallel N-Body Gravity Solver: TPM". In: *The Astrophysical Journal Supplement Series* 98 (1995), p. 355.

[339] Kazuhiro Yamamoto et al. "Evolution of Small-Scale Cosmological Baryon Perturbations and Matter Transfer Functions". In: *The Astrophysical Journal* 501.2 (1998), pp. 442–460.

[340] Christophe Yèche et al. "Constraints on neutrino masses from Lyman-alpha forest power spectrum with BOSS and XQ-100". In: *Journal of Cosmology and Astroparticle Physics* 2017.06 (2017), pp. 047–047.

[341] Haruo Yoshida. "Construction of higher order symplectic integrators". In: *Physics Letters A* 150.5-7 (1990), pp. 262–268.

[342] Kohji Yoshikawa et al. "Direct Integration of the Collisionless Boltzmann Equation in six-dimensional Phase Space: Self-Gravitating Systems". In: *The Astrophysical Journal* 762.2 (2013), p. 116.

[343] Ya. B. Zel'dovich. "Gravitational instability: An approximate theory for large density perturbations." In: *Astronomy and Astrophysics* 5 (1970), pp. 84–89.

[344] Y. B. Zeldovich. "A Hypothesis, Unifying the Structure and the Entropy of the Universe". In: *Monthly Notices of the Royal Astronomical Society* 160.1 (1972), 1P–3P.

[345] Xinyue Zhang et al. "From Dark Matter to Galaxies with Convolutional Networks". In: (2019). arXiv: `1902.05965`.

List of Abbreviations

API Application programming interface (Page 97)

CDM Cold dark matter (Page 3)

CMB Cosmic microwave background (Page 1)

DE Dark energy (Page 3)

DM Dark matter (Page 3)

EdS Einstein-de Sitter (Page 5)

EFE Einstein field equations (Page 3)

EOS Equation of state (Page 3)

FE Friedman equations (Page 4)

FLRW Friedman-Lemaître-Robertson-Walker (Page 1)

GR General relativity (Page 1)

HMF Halo mass function (Page 25)

IGM Intergalactic medium (Page 80)

LSS Large scale structure (Page 1)

PM Particle-mesh (Page 36)

PS Press and Schechter (Page 25)

SO Spherical overdensity (Page 39)

VDF Velocity distribution function (Page 11)

WDM Warm dark matter (Page 18)

ZA Zel'dovich approximation (Page 13)

Acknowledgements

The last three years have passed by at an incredible speed. I clearly remember arriving at the Faculty Club in Nice and there was no time to unpack, as Oliver had already organized a trip to the Ramses User Meeting the same week. It was a fascinating introduction to the world of astrophysical simulations, and I felt excited (and also a bit overwhelmed) by the large variety of topics presented at the conference. During the last years, I had the opportunity to work on many different aspects of the research field and it has been an exiting and highly rewarding time.

That I have the opportunity to write these concluding words of my thesis is to large parts thanks to many people who accompanied, guided, and supported me on my path. Among these people are some excellent teachers and professors who sparked my interest for mathematics and physics and motivated me to delve deeper into the mysteries of our Universe. In particular, I would like to thank Armin Barth for sharing his excitement for the beauty of mathematics and his efforts to teaching his passion every day in the most approachable way. I would also like to thank Alex Refregier and Adam Amara for the opportunity to do my semester project and master thesis in their group and for their support and advice throughout this time, and I'm particularly grateful to Andrina, who has been the most dedicated and most awesome teaching assistant and project supervisor that I could have wished for, and for whose support I will never be able to thank enough.

I am deeply grateful to Oliver for the opportunity of being his first PhD student and for the continuous support throughout my entire PhD. Thank you very much for the interesting projects I was able to work on, for all the small and big discussions, for the confidence and encouragements during the sometimes more difficult times, and for your open ears also for personal matters.

I also want to thank all the PhD students, postdocs, and staff at the observatory for making these three years a great time. Thank you Go for being a great office mate and for all the times I could just ask you for advice. I wish you and your family all the best at your new position in Canada. Thank you Michael III, Jolanta, and Alisson for making our group feel like a big family, for all the scientific and non-scientific discussions during the coffee breaks, and for the many skiing and hiking trips. Your arrival has brought much life to CION and our group.

I am very thankful to Govind, Michael I, Marina, Remi, and Gerardo for introducing me to Nice and making me feel welcome during my first months at the Côte d'Azur. Thank you Francesco, Gabriele, Annelore, Emma, and Pablo for being great friends during my time at the observatory and all the fun memories, and Nastia, Clement, and Adrien for having been awesome climbing partners.

Merci Khaled et toute l'équipe du restaurant pour tous ces repas magnifiques. Sans vous, l'Observatoire ne serrait pas le même. J'éspère avoir montré que tous les Suisses ne sont pas pareils $\ddot{\smile}$.

Thank you Surabhi for all the small and big adventures and the beautiful memories from our time in Nice, Europe, and in the US. I could always call you and talk to you, and I'm very thankful for your support throughout the years. Finally, I want to thank my mom for always being there for me through the highs and lows, and for always believing in me. I know it is not easy that I'm barely home, and I appreciate the support and encouragement throughout my life.

This PhD project has received funding from the European Research Council (ERC) under the European Union's Horizon 2020 research and innovation programme (grant agreement No. 679145, project 'COSMO-SIMS')